Doctoral Dissertation
Doctoral Program in Chemical Engineering (35th Cycle)

The manifold roles of zinc oxide nanocrystals in interaction with acoustic waves

By

Veronica Vighetto

Supervisor(s):
Prof.ssa Valentina Alice Cauda, Supervisor
Prof. Davide Fissore, Co-Supervisor

Politecnico di Torino
2022

Declaration

I hereby declare that the contents and organization of this dissertation does not compromise in any way the rights of third parties, including those relating to the security of personal data. This dissertation is my own work and work done in collaboration with others.

Most chapters of this dissertation are based on research published in scientific journals:

Chapter 2: **V. Vighetto**, A. Ancona, L. Racca, T. Limongi, A. Troia, G. Canavese, V. Cauda. "*The synergistic effect of nanocrystals combined with ultrasound in the generation of reactive oxygen species for biomedical applications*", Frontiers Bioeng. Biotechnol, 2019, DOI: 10.3389/fbioe.2019.00374.

Chapter 3: G. Tamboia, M. Campanini, **V. Vighetto**, L. Racca, L. Spigarelli, G. Canavese, V. Cauda. "*A comparative analysis of low intensity ultrasound effects on living cells: from simulation to experiments*". Biomed Microdevices, 2022, DOI: 10.1007/s10544-022-00635-x

Chapter 4: **V. Vighetto**, A.Troia, M. Laurenti, M. Carofiglio, N. Marcucci, G. Canavese, V Cauda. "*Insight into Sonoluminescence Augmented by ZnO-Functionalized Nanoparticles*". ACS Omega 2022, DOI: 10.1021/acsomega.1c05837.

Chapter 5: L. Racca, T. Limongi, **V. Vighetto**, B. Dumontel, A. Ancona, M, Canta, G. Canavese, N. Garino, V. Cauda. "*Zinc Oxide Nanocrystals and High-Energy Shock Waves: A New Synergy for the Treatment of Cancer Cells*". Front. Bioeng. Biotechnol.,2020, DOI: 10.3389/fbioe.2020.00577.

Chapter 6: B. Dumontel, F. Susa, T. Limongi, **V. Vighetto**, D. Debellis, M. Canta, V. Cauda. "*Nanotechnological engineering of extracellular*

vesicles for the development of actively targeted hybrid nanodevices". CELL & BIOSCIENCE, 2022, DOI: 10.1186/s13578-022-00784-9.

Veronica Vighetto

Torino, 2022

A mamma e papà,

Acknowledgment

First and foremost, I would like to thank my supervisor Prof. Valentina Cauda, for letting me be part of her lab, supporting me, kindly guiding me throughout these three years of PhD, and above all believing in me.

The research work presented in this thesis comes from the dedication of many people, who teach me, help me and support me. So, special thanks go to all TNH lab members, to Luisa, Marta, Bianca, and Andrea (who were there at the beginning and were so patient with me), to Marzia, Giada, Nicolò, Giulia, Federica and Maria Cristina (who are here now, supporting us at the end of this chapter). Than Marco, who started this journey with me, with whom I share almost everything (maybe too much), good news, bad news and research troubles: a gigantic thank you. It wouldn't be the same without you.

Thanks also to Giancarco Canavese for each fruitful and interesting discussion, to Marco Laurenti for help and kindess, to Adriano Troia for his work and to Francesca Susa and Tania Limongi for their collaboration.

Abstract

Nanoparticles (NPs) are a wide class of new materials, representing an innovative branch of scientific research, able to address various challenges in different scientific areas. The unique nano-dimension of particles provides them with specific physical and chemical properties, related to their size, shape, crystalline structure and surface-to-volume ratio. Within this frame of reference, zinc oxide has become one of the most popular metal oxide nanoparticles for biological applications. This material is characterized by an excellent biocompatibility, hemocompatibility, high surface reactivity, and it is a semiconductor with a wide band gap, which makes it excellent for optical imaging purposes.

This dissertation focuses its attention on the interaction between zinc oxide nanoparticles and ultrasound irradiation. Ultrasound exposure of ZnO NPs solution causes the occurrence of complex mechanisms, comprising stable and inertial cavitation, microstreaming and the generation of photons as well as radiation forces, having as consequences synergistic physical and chemical processes. These phenomena can be exploited for different paramount proposes, from imaging to anticancer treatment.

The use of zinc oxide combined with ultrasound (US), in accordance with numerical simulation, shows the ability to enhance and control the production of Reactive Oxygen Species (ROS), anticipating their potential as therapeutic agent. Furthermore, the combination of US and ZnO NPs reveals to increase the sonoluminescence (SL) emission, together with the ability to modify the SL spectrum when compared to the pure water behavior, making ZnO NPs very good candidates as efficient nanocontrast agents for SL imaging for biological and biomedical applications.

As first proof of concept of therapeutic application, cytotoxicity and internalization of ZnO NPs were evaluated in cervical adenocarcinoma (KB) cells, as well as the safety of the highly intense mechanical pressure waves (SW) treatment alone. The remarkably high cytotoxic combination of ZnO NP and SW was demonstrated, comparing the effect of multiple (3 times/day) SW treatments toward a single one, highlighting the killing efficiency of the combined strategy here proposed.

To overcome the problems derived from the interaction of nanoparticles with the human body, different shielding approaches for ZnO NPs were investigated. At first, re-engineered extracellular vesicles derived from healthy B-lymphocytes donor cells were studied as shell for ZnO NPs. They were decorated with monoclonal antibody (anti-CD20) to target $CD20^{+}$ cells, as Burkitt's lymphoma cells (Daudi). The hybrid nanoconstructs demonstrate to be characterized by high biocompatibility, targeting specificity and cytotoxic capability when remotely activated with SW. An important aspect of this nanotool is the significantly higher selectivity, and consequently the selective cytotoxicity, demonstrated towards the targeted cancerous Daudi cell line compared to the $CD20^{-}$ cancerous myeloid cells (HL60) and the healthy cell line.

A diverse strategy for ZnO NPs encapsulation was adopted and tested on the same hematological cell lines. Artificial, less time consuming, and self-assembled liposomes were designed and decorated with fragments of anti-CD38 antibody, as targeting agent toward cancerous Daudi cells. The biosafety of the construct itself was here proved in both healthy (B-lymphocytes) and cancerous cell lines. The remote activation of the nanoconstruct by ultrasound exposure makes it become toxic for cancerous cells, without having any significant impact on healthy cells. The mechanism of killing was examined, determining that mechanical damages were created at first, then apoptotic pathways were activated increasing the therapeutic efficiency against cancerous cells.

In conclusion, this work demonstrates the multifaced potential of nanosized zinc oxide as biomedical imaging agent and therapeutic nanotool for anticancer applications

Contents

List of Figures

List of Tables

Chapter 1

Introduction

During the last decade, nanotechnology has increasingly gained attention for its beneficial role in several scientific areas[1], among them nanomedicine is one of the most studied. Nanomedicine can be defined as the application of nanotechnologies for medical proposes, as diagnosis, monitoring, prevention, and therapy[2], or even the simultaneous combination of them, named nanotheranostic[3].

Nanomedicine results to be particularly appealing for cancer applications, which is today a leading cause of death worldwide[4]. This is due to the ability of nanomaterials to deliver drugs, be tools for diagnosis and imaging, create nano medical devices and even be therapeutic agents themselves[5]. In particular, nanoparticles (NPs) have been widely studied, trying to address various medical challenges faced with conventional medicine, as poor target specificity, systemic and organic toxicity and lack of efficiency[6]. The unique nano-dimension of particles provides them with specific physical and chemical properties, related to their size, shape, crystalline structure and surface-to-volume ratio[7]. They can be excellent carriers for different types of therapeutic molecules[8], their surface reactivity can be exploited for bio mimicking and targeting purposes[9], or they can be considered the therapy itself taking advantage of the chemical nature of NPs[10,11] or their effects under external stimuli[12,13].

Among the large variety of nano materials, zinc oxide has become one of the most popular metal oxide nanoparticles for biological applications[14]. This material is characterized by an excellent biocompatibility, as it is defined as Generally

Recognized as Safe (GRAS) by FDA[15]. Furthermore, it is hemocompatible and characterized by a high surface reactivity and high surface to volume ratio[15], making it suitable for cargo loading for drug delivery purposes. It is as a semiconductor, with a wide band gap (3.37 ev at room temperature)[16], which makes it excellent for optical imaging purposes. Finally, it is a piezoelectric and pyroelectric materials, thanks to its fundamental crystalline cell structure (tetragonal).

Zinc Oxide nanoparticles are also considered as a therapeutically active material when externally stimulated by ultrasounds (US). Nowadays, ultrasounds are largely employed in diagnosis and therapy[17], but combined to ZnO NPs different phenomena are generated, suitable for both imaging and therapy. In particular, the acoustic cavitation induced by ultrasound (and broadly discussesd in details in the next chapters) can be favoured by the presence of nanoparticles. As a consequence, the generation of Reactive Oxygen Species (ROS) is one of the main effects produced by US irradiation of ZnO NPs. The role of ROS, and consequently the redox cellular homeostasis, is fundamental in cells: low levels of ROS are responsible for the activation of the signaling system, while high levels of ROS can induce oxidative stress and cellular damages[18]. The ability to regulate the amount of ROS generated by ZnO NPs and US inside cells can play a fundamental role, driving the cell survival or the cell death[19]. Thus ROS generation mediated by US and ZnO NPs can be exploited for therapeutic purposes against cancer cells. On the other hand, the ability of ZnO NPs to generate photons when exposed to ultrasounds[20], also called sonoluminescence, and create specific and recognizable light emission patterns. This interesting effect makes ZnO perfectly suitable also for imaging purposes in the biomedical field.

Aim of the work and Thesis structure

The work presented in this dissertation deeply focuses on the effects generated by the exposure of zinc oxide nanoparticles solutions to ultrasound, and the possible involvement of the developed combined strategy in the biomedical field.

Chapter 2 describes in details how ZnO NPs are synthetized, functionalized, and characterized. The generation of ROS by ZnO was investigated under different US conditions not only in pure water, but also in biological media with

the aim to understand how this ROS production can be tuned for therapeutic purposes.

The ultrasound acoustic and pressure fields generated inside a solution and in presence of ZnO was studied in Chapter 3, together with the assessment of ROS generation. The driving idea was to understand not only the main effect of US exposure of ZnO NPs (i.e. ROS generation), but also characterize the internal acoustic field, which also depends on the sample holder. This aspect is fundamental for moving toward the application of US *in vitro*, to find the right condition able to efficiently couple US to a sample holder and then generate ROS, allowing an easy tuning of cells damages or cell survival.

In Chapter 4 another possible biomedical application of ZnO NPs under US exposure is investigated. ZnO NPs are here proven able to generate light with specific and precise emission patterns when stimulated with ultrasounds, not only in pure water but also in biological media. These results suggest the application of ZnO NPs for bio-imaging purposes.

Chapter 5 is the first *in vitro* application of the system studied in the previous chapters. ZnO NPs functionalized with amino-propyl groups is here presented as a therapeutic agent in combination with US against cervical adenocarcinoma cells.

Further advancements are presented in Chapter 6 and Chapter 7. In Chapter 6 ZnO NPs are made biomimetic, being encapsulated inside extracellular vesicles derived from healthy cells and targeted with antiCD20 to be selectively internalized by cancerous cells. The targeted nanoconstruct is than remotely activated by US, demonstrating its efficiency in selective killing of Burkitt's lymphoma cells. Chapter 7 focuses the attention on a different type of biomimetic shell in which ZnO NPs are enveloped. In this study, a fully artificial lipidic shell is self-assembled on ZnO NPs, and fragments of antiCD38 antibody are conjugated to functional lipids, being part of the shell, with targeting purposes against Burkitt's lymphoma cells. This new nanoconstruct is then remotely activated by US, demonstrating also in this case the efficacy of the proposed strategy. The selective killing mechanism is deeply analyzed to unravel the combined effects generated by the combination of US and ZnO NPs in inducing cancer cells to death while sparing healthy ones.

Chapter 8 reports the general conclusion of the dissertation.

Chapter 2

The combined effect of nanocrystals and ultrasound in the generation of reactive oxygen species for biomedical applications

This chapter has been taken from the open-access publication [19], as stated in the declaration of this dissertation.

2.1 Introduction

Acoustic cavitation is a phenomenon that involves formation and growth of gas bubble[21], caused by the time-varying sinusoidal pressure cycles applied to the liquid, corresponding to expansion and contraction phases. Two possible conditions can be distinguished: stable cavitation, which is characterized by permanent bubbles that oscillate for many cycles of pressure variation, and transient or inertial cavitation. In this last condition, the gas bubbles expand enormously with respect to their original size and then violently collapse releasing a large amount of energy[22]. During such collapse, very high temperatures (above 5000 K) and pressures (above 800 atm) are generated locally causing the

ionization of gas, microjet streaming, and thermal dissociation of water molecules into hydroxyl radicals (HO·) and hydrogen atoms (H·), the cleavage of dissolved oxygen, O_2, leading to the formation of several Reactive Oxygen Species (ROS)[23,24]. The hydroxyl radical (HO·) is one of the strongest radicals ever described[25] and it possesses the highest reduction potential of all the ROS that are physiologically relevant: due to its nature it can react with a large variety of different type of biological molecule[26].

Nevertheless, oxygen is the fundamental element needed for the normal metabolic activity of every aerobic organism, and so ROS are inevitably produced inside living organisms, as cells. Reactive oxygen species are normally involved in different cell functions as signaling system, induction of mitogenic response, and mitochondria activity[26]. Nonetheless, the survival of cells is related to the ability of maintaining the redox homeostasis[25] during all this processes. An instability in this equilibrium results in a variety of possible different disease. When chronic low levels of ROS occurs in a biological living system indeed, it has been demonstrated that gene mutation and malignant cell transformation can appear, or a large variety of vascular diseases can be promoted[27]. In addition, Shafique et al[28] established that the increase in ROS levels can have a protective role in endothelial homeostasis, improving the vascular function in patients affected by cardio vascular disease (CDV). It is also been proven that the ROS generation achieved by the external activation of membrane-bound NADPH oxidase can induce angiogenesis and other essential functions of endothelial cells, such as hemostasis[26,29]. The activation of angiogenesis caused by an increase in ROS production to restore ROS physiological levels, can be beneficial not only for CVD, as occurs after ischemia[30], but can also contribute to wound healing[31]. On the other hand, an excessive production of ROS leads to a disequilibrium redox state, where the antioxidant defenses of the cell have been overcome, being responsible for damaging cellular components, as lipids, proteins and DNA. Acute high levels of ROS cause the activation of different signal pathways, involving cytokines, transcription factors and mediators, responsible for cell death, causing ROS-mediated apoptosis or necrosis. These effects generated by cellular oxidative stress can be exploited for cancer therapeutic applications[32–34].

Therefore, it is clear that the ability to regulate the amount of ROS generated inside cells plays a fundamental role in the survival or death of cells. During last years thus different ways to produce ROS in a controlled manner were investigated. Nanomaterials (NM) are largely studied with the aim to apply them

in biomedical field, and one of the principal mechanisms of nanotoxicity is the production of oxidative stress due to ROS generation. It has also been demonstrated that the level of generated ROS is dependent on the physical and chemical properties of the considered engineered nanomaterial, as size, surface to volume ratio and surface reactivity[35,36]. Carlson et al[37] measured the amount of ROS produced in cells when Ag nanoparticles with different dimensions were present: 10-fold increase of ROS levels was measured in cells exposed to the smallest dimension nanoparticles. In the same work, it has been assessed that not all nanomaterials with equal dimensions can produce the same amount of ROS, supporting the idea that the ROS generation from NM depends also on their chemical nature.

Oxidative stress can also be achieved by an external activation of nanomaterials to generate ROS, leading to tumor cell death under specific conditions. An example of this mechanism is photodynamic therapy (PDT)[25]. It has been previously[38] proposed hybrid nanoparticles able to produce intracellular ROS only when remotely activated by UV light irradiation. The photogeneration of electrons (e^-) and holes (h^+) have the ability to react with the environment forming superoxide radical anions (O_2^-) when e^- reduce oxygen molecules while hydroxyl radicals (HO·) and hydrogen peroxide (H_2O_2) molecules are produced when h^+ oxidize water molecules. In the last two decades the use of photosensitizer materials in PDT was largely applied to cancer therapy[39–41], but there are some limitations, as the limited tissue penetration depth of UV light used to excite the photosensitizer, that confine the application of PDT to treat superficial tumors[25].

Ultrasound (US) is another external stimulus investigated to activate the production of ROS, and sonodynamic therapy (SDT) is recently emerged as an alternative to PDT due to the higher penetration depth of ultrasound with respect to UV light[42]. Under ultrasound excitation additionally, cavitation bubbles are generated, and their violent oscillation and collapse let them act as nano-chemical reactors, leading to the formation of ROS in water media. The compounds that promote ROS formation, chemically reacting or introducing a larger number of bubbles, are named sonosensitizers[43]. Most of the sonosensitizers, such as porphyrins, are characterized by an easy aggregation in physiological environment due to their hydrophobic nature, decreasing the therapy effectiveness, by an

intrinsic toxicity and by minor selectivity to cancer tissue[44]. The effectiveness of SDT is related to the ability of efficiently generating ROS, without major drawbacks related to the nature of the implied sonosensitizer material.

In this chapther, Zinc Oxide nanocrystals with a functionalized surface of aminopropyl groups (ZnO- NH_2 NCs) have been proved able to produce ROS in a controlled manner, when stimulated by US generated by an already approved medical device (LipoZero G39).

Nanosized ZnO is a metal oxide well known for its safety in biomedical fields[45]. Here, it is demonstrated that our customized ZnO-NH_2 NCs specific monocrystalline structure, size, shape and functionalization, are able to generate a tunable quantity of ROS according to the intensity of administered US. More in details, the ultrasound is generated through the use of a safe medical device able to generate cavitation phenomena in human tissues. Several parameters like US output power, frequency, duty cycle, sonication time, as well as ZnO-NH_2 NCs concentration in water media, were systematically examined. To push our study forward up to a possible *in vivo* application, it has also been verified that a larger amount of controllably cavitation and ROS generation occur also when tissue mimicking materials have been employed.

2.2 Materials and methods

2.2.1 ZnO- NH_2 NCs synthesis and functionalization

ZnO nanoparticles were synthesized through a microwave-assisted synthesis, as previously reported[46]. The reaction path is based on the hydrolysis of the zinc precursors (zinc acetate dihydrate) due to the presence of sodium hydroxide as the base in methanol. In details, the solution of zinc precursor, i.e., zinc acetate dihydrate (99.99% Sigma Aldrich) 0.1 M in methanol, was stirred directly in the microwave-reactor vessel. 0.48 mL of bidistilled (bd) water were added to initiate the nucleation and then a KOH solution (≥85% pellets, Sigma-Aldrich, 0.2 M in methanol) was rapidly added. The resulting solution, with an overall pH of 8, was put in the microwave oven (Milestone START-Synth, Milestone Inc) at 60 °C for 30 min, under temperature and pressure control and with a maximum microwave power of 150 W. Upon completion of the reaction, the obtained colloidal suspension was cooled down to room temperature (RT) and centrifuged (3500 g for 10 min) to remove the unreacted compounds. The obtained pellet was

dispersed in fresh ethanol through sonication and the washing step was repeated two more times.

The as-synthesized ZnO were then functionalized with amino-propyl groups with a post-grafting approach using 3-(AminoPropyl)-TriEthoxySilane (APTMS), as in refs [46,47]. The functionalization with amino-propyl groups allows to bound to the nanocrystals other useful compounds, as for example different type of dyes for microscopy purposes or for cytofluorimetric analysis.
Briefly, the synthesized ZnO NCs dispersed in ethanol were heated to 70 °C in a round glass flask under continuous stirring and nitrogen gas flow. After approximately 15 min, the functionalizing agent, was added in a molar ratio of 10 mol% with respect to the total ZnO amount. The reaction was carried out in reflux condition under nitrogen atmosphere for 6 h and then washed twice, in to order to remove unbound APTMS molecules, by centrifuging (10,000 g for 5 min).

The obtained nanostructures are amine-functionalized zinc oxide nanocrystals (ZnO- NH_2 NCs) stable colloidal suspensions in ethanol.

2.2.2 ZnO- NH_2 NCs characterization

ZnO NCs were characterized by X-Ray Diffraction (XRD) with a Cu-Kα source of radiation, operating at 40 kV and 30 mA in configuration θ-2θ Bragg-Brentano (Panalytical X'Pert diffractometer). For this analysis, several drops of the colloidal ZnO NCs solution were deposited on a silicon wafer and allowed to dry at room temperature (RT). The XRD spectrum was collected in the range of 20°-65° with a step size of 0.02° (2θ) and an acquisition time of 100 s.

High-resolution transmission electron microscopy (HRTEM) was used to characterize the morphological and structural features of the different materials. HRTEM was performed by using a FEI Titan ST microscope working at an acceleration voltage of 300 kV, equipped with a S-Twin objective lens, an ultra-bright field emission electron source (X-FEG) and a Gatan 2k x 2k CCD camera. All the ZnO NCs samples were diluted in ultrapure ethanol (99%) down to a concentration of 100 μg/mL. One drop of each sample was deposited on a holey carbon copper grid with 300-carbon mesh and left to dry overnight, prior to imaging.

Dynamic Light Scattering (DLS) and Z-Potential measurements were carried out with Zetasizer Nano ZS90 (Malvern Instruments). The size of pristine and amino-propyl functionalized ZnO NC was measured in both ethanol and double distilled (dd) water at a concentration of 100 μg/mL. Z-Potential measurements were performed in dd water at a concentration of 100 μg/mL.

2.2.3 Evaluation of ROS production

Ultrasound excitation was carried out with LipoZero G39 (GLOBUS) and the evaluation of ROS production was provided by Electron Paramagnetic Resonance (EPR) Spectroscopy (EMXNano X-Band spectrometer from Bruker) assisted by a spin-trapping technique. The formation of hydroxyl and superoxide anion radicals was actually detected in double distilled water using as a spin trap the 5,5-dimethyl-L-pyrroline-N-oxide (DMPO, Sigma) and each tested sample contained DMPO 10mM. This compound is suitable for the study of ROS generation due to its capability to trap both hydroxy and superoxide anion radicals. After the ultrasound irradiation, the sample was promptly transferred into a quartz microcapillary tube and inserted in the EPR cavity. The spectra were recorded with the following measurement conditions: center field 3428 G, sweep time 160.0 s, sample g-factor 2.00000, number of scans 15. After acquisition, the spectrum was processed using the Bruker Xenon software (Bruker) for baseline correction. Analysis of recorded spectra was executed using the Bruker SpinFit software.

To perform sonication, 1 mL of sample was placed in a 24 well plate (Thermo Scientific) which was positioned in contact with LipoZero transducer through a thin layer of coupling gel (Stosswellen Gel Bestelle, ELvation Medical GmbH). Formation of hydroxyl and superoxide anion radicals was evaluated under a large range of different conditions. Samples were tested for three different sonication times (2, 5, and 10 min), five Duty Cycle conditions (10%, 20%, 30%, 40%, 50%), three distinct working frequencies (150 KHz, 526 KHz, 1 MHz) and different output powers of the LipoZero device (0.3, 0.6, 0.9, 1.2 and 1.5 W/cm^2 corresponding to 10%, 20%, 30%, 40% and 50% of the maximum output power). In addition to these conditions, different concentrations of amino-functionalized ZnO- NH_2 NCs were also tested (50, 100 and 200 μg/mL) for oxygen radicals production.

2.2.4 Needle cavitometer measurements

The acoustic cavitation activity in presence or absence of nanocrystals was monitored by recording the broad band acoustic emissions generated by collapsing bubbles by using a needle hydrophone Dapco NP 10-3 coupled to a spectrum analyzer (Agilent N9320B) and integrating the FFT area for a frequency range of 0.8-5.0 MHz. Analyses were performed at least on three spectra for each experiment.

2.2.5 B-mode ecographic imaging

Ultrasound imaging was performed with a research ultrasonic scanner (Ultrasonix Sonic Touch) equipped with linear probe (L14-5/38) operating at 10 MHz in high resolution mode. It was coupled with the sample holder using ultrasound coupling gel and positioned along the axis of a single plastic well filled with 1 mL of solution. The imaging transducer was focalized to the excitation transducer focus. Real-time videos of the system response to ultrasound irradiation were recorded and videos were analysed using MATLAB script which calculated the relative average intensity of the bright spots in the region of interest (ROI) of each frame of the videos. Three videos were recorded for each sample.

2.2.6 Tissue mimiking and ultrasound irradiation

In order to evaluate the attenuation of ultrasound effects in the presence of tissue mimicking media, different materials, as phantom and *ex vivo* chicken-breast tissue, were interposed between the transducer and the sample.

To conduct these tests, the ultrasound source was immersed in a plexiglass tank filled up with demineralized water and a single well, previously cut and polished from a 24 well plate (Thermo Scientific), was placed at a distance of 1 cm from the transducer surface and exposed to ultrasound, as shown in Figure 1.

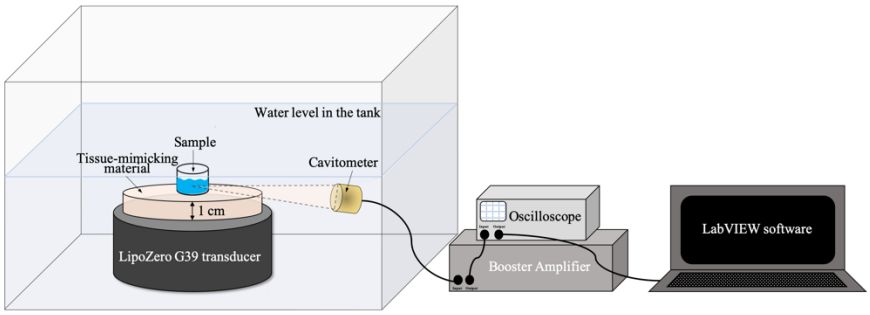

Figure 1 Schematic illustration of ultrasound irradiation set up for the measurements with tissue-mimicking materials.

Therefore, the measurements were performed using a tissue-mimicking homogeneous phantom (based on 3% in weight of agarose and 0.4 M zinc acetate, $Zn(CH_3COOH)_2$, with an ultrasound attenuation of 0.5 dB/cm·MHz, which matches the attenuation of muscle tissue as reported in 25) with a diameter of 40 mm and an ex vivo tissue (chicken breast); both materials were characterized by a thickness of 1 cm. As a reference, the effects of ultrasound irradiation on the sample were also evaluated considering only the water bath, where the system is immersed, as medium between the piezoelectric transducer and the sample well.

Ultrasound excitation was provided by LipoZero and measurements were conducted with a frequency of 1 MHz, 50% of Duty Cycle, and a power of 3 W/cm^2 for 20 min. During each experiment the acoustic signal generated inside the well was recorded using a focused piezo-detector (Precision Acoustic) as a cavitometer, coupled to the Booster Amplifier (Precision Acoustic) and connected to a digital oscilloscope (TDS 2012B, Tektronix). To store the data, LabVIEW software was used and 100 µs were recorded every 2 s if the signal measured by the oscilloscope was higher than 0.001 V. Data were successively analyzed with MATLAB software. The time-domain signal was transformed in the frequency-domain by Fourier Transform and the cavitation dose was quantified with MATLAB by calculating the area subtended by the curve. The area measurements considered only values from a frequency of 2.5 MHz to 12 MHz, in order to eliminate the initial 1 MHz driving signal.

At the end of sonication, EPR spectroscopy assisted by a spin-trapping technique was performed as previously described. In this set of tests, EPR

measurement conditions were as follows: center field 3428 G, sweep time 60.0 s, sample g-factor 2.00000, number of scans 15.

To evaluate the increase of ROS production in presence of ZnO- NH_2, two conditions were tested for each tissue-mimicking material and, as a reference, for water: milliQ water with 10 mM content of DMPO and milliQ water with 10 mM content of DMPO and a concentration of NCs equal to 200 µg/mL.

SigmaPlot 14.0 software was used for all statistical analyses. Data are expressed as the mean ± standard error mean (S.E.M.). Asterisks denoting P-values (*$p<0.05$ and **$p<0.001$) and sample sizes are indicated in each figure legend.

2.3 Results and discussion

ZnO NCs, prior to the functionalization, were analyzed with XRD, shown in Figure 2-A, and compared with the standard XRD pattern of ZnO (JCPDS card n. 36-1451) confirming that the pristine ZnO NCs showed the typical hexagonal wurtzite crystalline structure, with diffraction peaks corresponding to the Miller's index indicated in Figure 2-A.

The HRTEM results (Figure 2-B,C) additionally displayed that both the pristine and amino-functionalized NCs had a spherical morphology with size ranging from 15 to 25 nm and a single crystalline nature, in particular a wurtzite hexagonal structure, as already observed in previous publication[16].

The grafting of the amino-functional groups imparted to ZnO NCs a strong positive Z-potential in bd water (+22 mV), higher than the Z-potential recorded for pristine ZnO NCs (+15 mV), as shown in Figure 2-D. DLS analyses were performed in both ethanol and bd water showing that amino-functionalized ZnO NCs hydrodynamic size was 79 nm in ethanol and 164 nm in bd water (Figure 2-F), thus smaller than the hydrodynamic size of pristine ZnO NCs (91 nm in ethanol and aggregated in dd water, with 531 nm in size, Figure 2-E). The positive charge of amino-functionalized ZnO NCs thus improves their colloidal stability in solution and can also possibly increase their uptake in cells, characterized mainly by negatively-charged cell membranes[48]. Additionally, the amino functionalization allows the conjugation with different fluorescent dyes[49] for their

further characterization at flow cytometry to test the internalization rate in cancer cells.

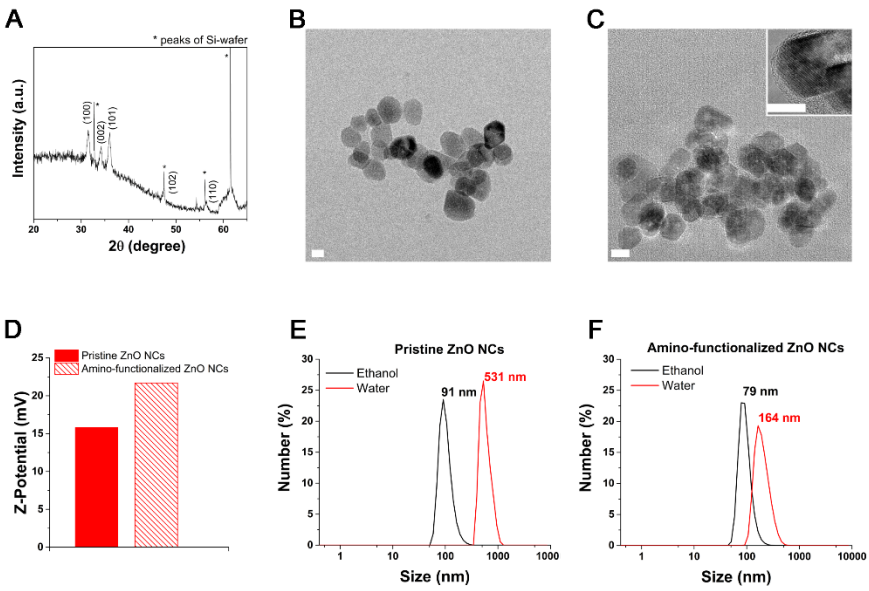

Figure 2 (A) XRD analysis. (B) HRTEM of pristine ZnO NCs and (C) amino-functionalized ZnO NCs, scale bar = 10 nm. The inset in C represents a higher magnification image of amino-functionalized ZnO NCs. (D) Z-potential of pristine and amino-functionalized ZnO. DLS measurements of (E) pristine and (F) amino-functionalized ZnO NCs both in ethanol (black curve) and dd water (red curve).

The EPR spectroscopy was used to evaluate the enhancement of ROS production when ZnO- NH_2 NCs are present in water (with a concentration of 200 µg/mL) and according to different US power. The results are shown in Figure 3. Samples were irradiated with US for 10 min, at a frequency of 1 MHz and the ultrasound stimulation was pulsed, with a Duty Cycle of 10%, Pulse Repetition Frequency 1Hz. The concentration of DMPO-OH was then evaluated since it is directly correlated to the ROS production, in particular to the hydroxyl and superoxide anions production.

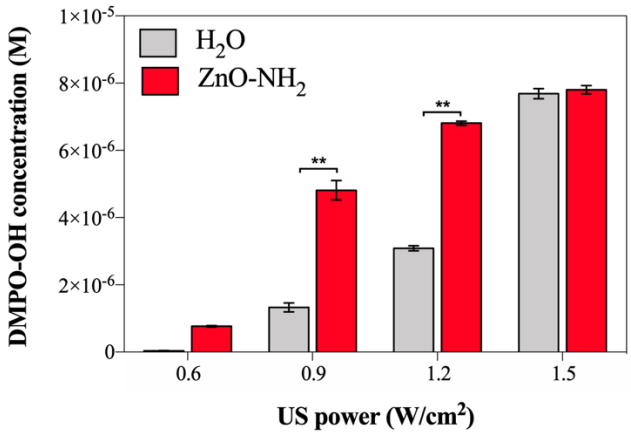

Figure 3 DMPO-OH concentration (M) to evaluate ROS production after 10 min of US irradiation according to different US powers, in presence of ZnO-NH_2 NCs (200 µg/mL). All measurements were conducted in triplicate with 10% DC, 1 MHz frequency, using the LipoZero

When 0.3 W/cm^2 (corresponding to 10% of the maximum output US power) was delivered, the threshold for ROS generation was not reached, meaning that inertial cavitation did not occur in the sample during the US irradiation. Otherwise, with 0.6 W/cm^2 (corresponding to the 20% of the maximum output power), a small amount of hydroxyl and superoxide anions were detected, and even if the amount of DMPO-OH was greater in presence of ZnO- NH_2 NCs (red bar) with respect to pure water (black bar), it can be noted that the 20% of power was not enough to obtain a statistical difference between samples. A different scenario is depicted when 0.9 and 1.2 W/cm^2 were utilized. In both cases a significant difference (both with $p<0.001$) between the amount of ROS produced in pure water and the one obtained in the presence of ZnO- NH_2 NCs is clearly observed. The results achieved with these conditions indicate the efficacy of our ZnO- NH_2 NCs to act as a ultrasound responding nano-agent. It is interesting to observe that the power doses of 0.9 and 1.2 W/cm^2, corresponding to the 30 and 40% of the maximum power output of the Lipozero transducer, were too low to generate high amount of ROS when the sonicated sample in the well was the pure water. Strikingly, both these low intensities ultrasound conditions are enough to elicit an activation of the ZnO- NH_2 NCs, widely increasing the amount of ROS produced.

The last US power tested for the sonication was 1.5 W/cm^2 (corresponding to the 50% of the maximum output power): the delivered intensity of US was

sufficiently high to activate the inertial cavitation in the water alone, leading to a large amount of ROS produced, comparable with the one obtained in presence of ZnO- NH_2 NCs.

From the results in Figure 3, it is assessed that 0.9 W/cm^2 (30% of US power) is the optimal condition to have ZnO- NH_2 NCs working as ultrasound responsive nano-agent: the significant difference ($p<0.001$) in ROS production suggests that, at that power, the US irradiation was not enough intense to cause a large production of hydroxyl and superoxide anions in the water, but it was sufficiently high to initiate the acoustic cavitation in the sample containing ZnO- NH_2 NCs due to the presence of nanobubbles the NCs surface, which act as nuclei for inertial cavitation and consequently leads to a larger ROS production.

To support these results, other parameters such as ZnO- NH_2 NCs concentration in water, time of US treatment, frequency of the US were tested to ensure the efficacy of the ZnO- NH_2 NCs, as reported in Figure 4.

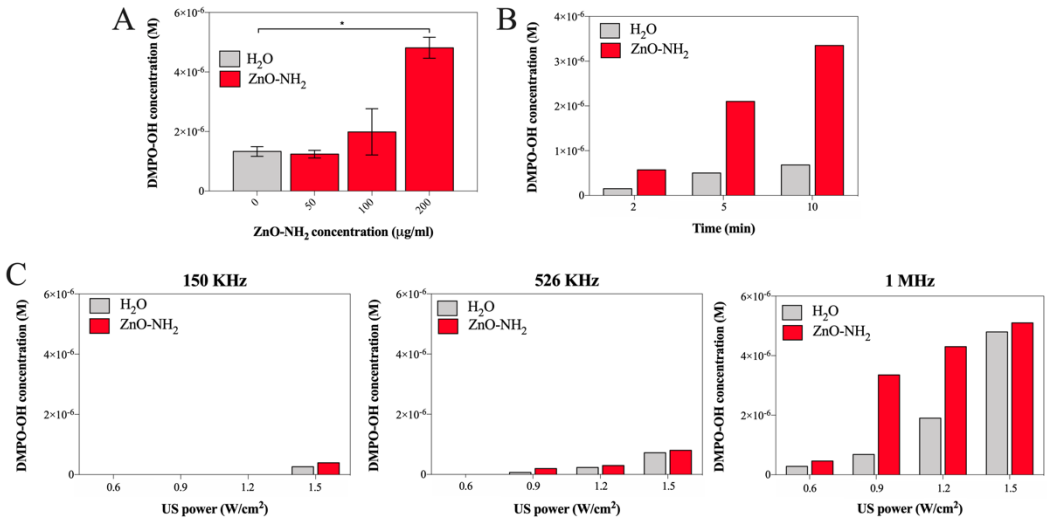

Figure 4 (A) Effects on ROS production at different concentration of ZnO-NH_2 NC; measurements were conducted in duplicate with 10% DC, 0.9 W/cm^2, 10 min of treatment time, 1 MHz. One-way ANOVA was performed to determine statistical significance (*$p < 0.05$ and **$p < 0.001$). (B) Evaluation of the optimal amount of treatment time, with 10% DC, 0.9 W/cm^2, 1 MHz, and 200 µg/mL of ZnO NC. (C) Comparison between different excitation frequency for all the tested US power, with 10% of DC, 10 min as treatment and time 200 µg/mL of ZnO NC

To assess the optimal concentration of ZnO- NH_2 NCs, 50 µg/mL, 100 µg/mL and 200 µg/mL of NCs were examined (Figure 4-A), suggesting that the highest concentration tested, as used in all the other experiments, is the optimal one.

Three different treatment times were thus evaluated, 2, 5 and 10 min, keeping fixed all the other parameters (0.9 W/cm^2 of power, 10% of DC and 1 MHz of excitation frequency and 200 µg/mL of ZnO- NH_2 NCs in water). The insonation time of 10 min was confirmed to be the best treatment time condition to enhance the ultrasound responsive nano-agent capabilities of ZnO- NH_2 NCs with respect to pure water. In Figure 4-C three excitation frequency were also screened: 150 KHz, 526 KHz and 1 MHz at different US output powers, with 10% DC and 200 µg/mL as NCs concentration. With the lowest frequency, a large amount of power (50% with respect to the maximum output) was needed to obtain a detectable signal with EPR instrument and DMPO spin adducts. The frequency of 1 MHz, which is the most used frequency for biomedical applications, is here confirmed to enhance the production of ROS in the presence of the ZnO- NH_2 NC under ultrasound excitation.

An hypothesis for the explanation of ROS generation capabilities of ZnO-NH_2 NCs is related to the NC surface: the high surface-to-volume ratio of ZnO-NH_2 NCs, showing a large surface area of 60 m^2/g (as measured by Nitrogen Sorption isotherm elsewhere[16]) and the surface functionalization of amino-propyl groups are both capable to immobilize and promote the inertial cavitation of tiny gas nanobubbles under such US power conditions. As inertial cavitation is produced, ROS are generated: the EPR technique detected OH· radicals, which are one of the most reactive and potentially dangerous species of ROS.

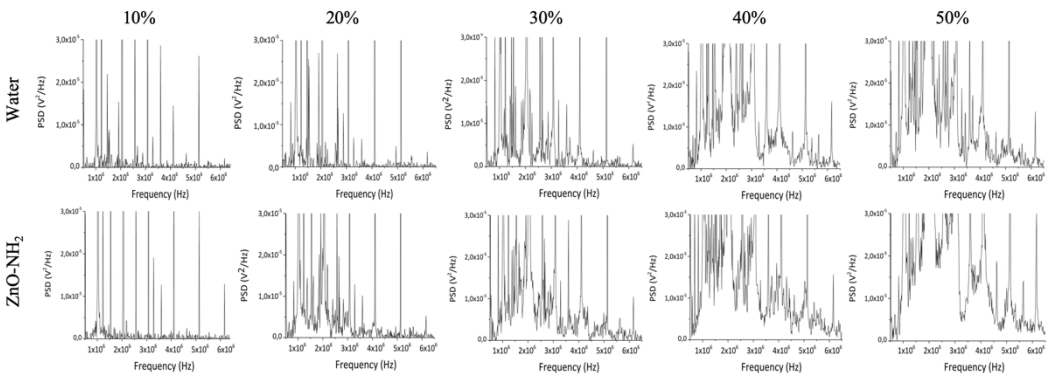

Figure 5 Frequency spectra recorded by needle cavitometer in order to evaluate cavitation of water and ZnO-NH_2 NCs water suspensions. The comparison between the two solutions was carried out at 1 MHz, 100% of DC, 10 min of insonation with 0.3, 0.6, 0.9, 1.2, and 1.5 W/cm^2, which correspond to 10, 20, 30, 40, and 50% of maximum available US power

To evaluate the role of acoustic cavitation on the generation of ROS by the ultrasound exposure of ZnO- NH_2 NCs passive cavitation detection (PCD) technique was used. Figure 5 shows the frequency spectra of the acoustic signals obtained at different ultrasound intensities with and without ZnO- NH_2 NCs in solution. At low ultrasound intensities, only harmonics and sub-harmonics signals are present: since these signals are recorded for both water and NCs samples, they are probably due to oscillation of large gas bubbles trapped in the plastic wells of the sample holder. At increasing ultrasound intensities (above 1.2 W/cm^2), acoustic broadband noise typical of inertial cavitation was recorded for the water solution. When ZnO- NH_2 NCs were added to the solution, broadband noise signal was recorded at lower ultrasound intensities, suggesting that our NCs acted as nucleation site inducing inertial cavitation, thus decreasing the cavitation threshold. Since it has been shown both theoretically and experimentally that collapsing cavitating bubbles can generate sufficiently high temperatures and pressures able to induce generation of ROS in aqueous solution (The Acoustic Bubble, Leighton), PCD and EPR experiments together suggest that ZnO- NH_2 NCs generate ROS by inducing inertial cavitation upon ultrasound exposure

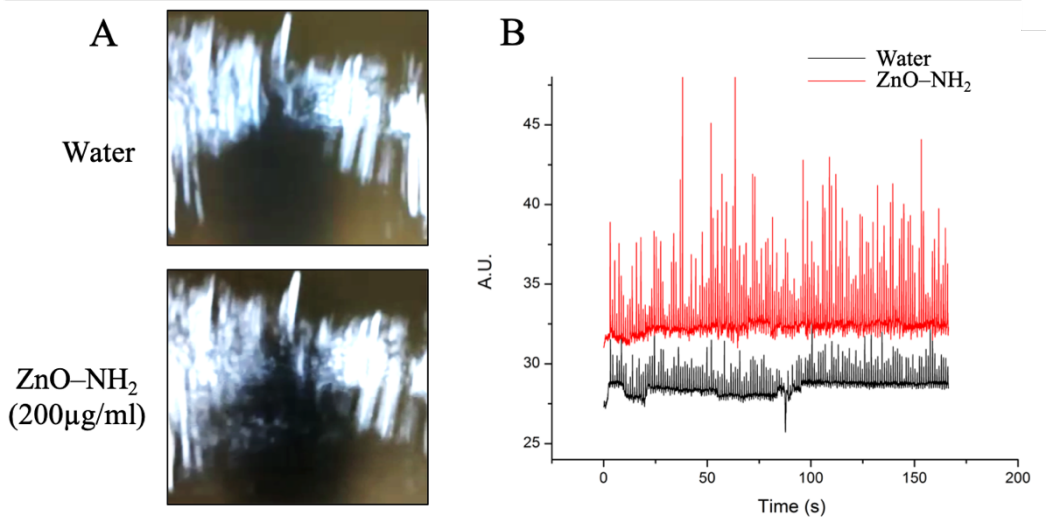

Figure 6 (A) B-mode ecographic imaging of the corresponding (B) scattering signal related to bubble cavitation events obtained when 50% of maximum available US power was applied at 10% of DC, 1 MHz, and 170 s.

In order to further study the generation of inertial cavitation by ZnO- NH_2 NCs, ultrasound B-mode imaging was used. Figure 6-A shows the ecographic images obtained for water and ZnO- NH_2 NCs containing solutions exposed to 40% intensity ultrasound. Cavitating bubble generated by ZnO- NH_2 NCs led to

bright spots in the solution, while in the absence of NCs the ecographic signal did not increase. Figure 6-B shows the quantification of ecographic contrast obtained during the pulsed ultrasound exposure (170 s), as previously described in the Material and Methods. section 2.2.5. ZnO- NH_2 NCs generated higher ecographic contrast over all the sonication period compared with the water containing solution. Together these results further confirm the ability of ZnO- NH_2 NCs in inducing inertial cavitation under pulsed ultrasound exposure.

Reactive oxygen species exert a multitude of biological effects[45,50], which also comprehend the creation of molecular damages inside cells, leading to antitumoral application[16].

In order to evaluate the future applicability of ZnO-NH_2 NCs in the biomedical field, in particular to subcutaneous *in vivo* applications, the generation of ROS, and the effects of our NCs as ultrasound responsive nano-agent was tested when different tissue mimicking materials were interposed during the insonation between the LipoZero US transducer and the sample well.

The evaluation of the cavitation and ROS generation related to the interposition of tissue-mimicking materials between the ultrasound source and the samples are shown in Figure 7. Different materials were tested, and for all of them the amount of cavitation of water and water with the combined effect of ZnO-NH_2 NCs (200 µg/mL) were evaluated. All the measurements were performed for 20 min, with a frequency of 1 MHz, 50% of Duty Cycle and 100% of US power available from LipoZero transducer.

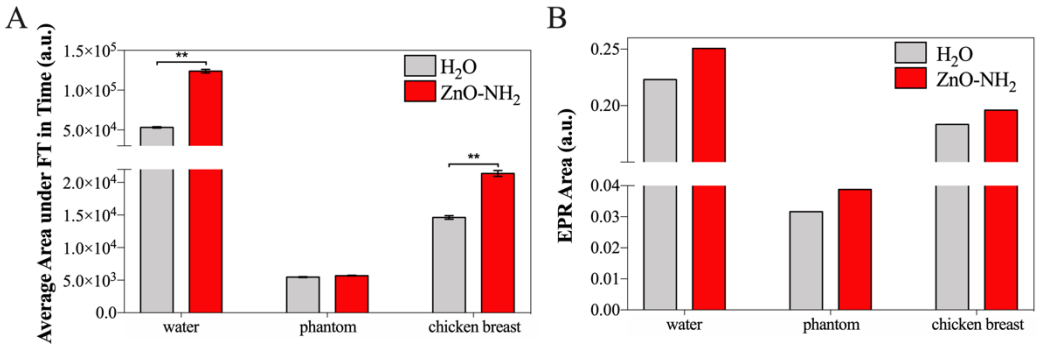

Figure 7 (A) Average area under Fourier Transform, calculated with MATLAB, of signals recorded in time by cavitometer during ultrasound irradiation. One-way ANOVA was performed to determine statistical

significance (*$p < 0.05$ and **$p < 0.001$). (B) Area under the EPR spectrum curve measured with Bruker SpinFit software.

Figure 7-A exhibits the results of cavitometer measurements during 20 min of insonation, which are the average area under the Fourier Transform (FT) of each measured signal over time. These data correlate with the amount of occurred cavitation, and the S.E.M. is reported. It can be appreciated that, when the ultrasound propagation medium was water, the amount of cavitation detected by the cavitometer was higher than the one measured when tissue mimicking materials were interposed. This effect can be explained considering the attenuation of power perceived inside the sample well. When the phantom and the ex vivo tissue are used, the real amount of US energy inside the well is lower, and the measured broadband noise, which correlates to cavitation, reflects this reduction. Nevertheless, a significant increase of cavitation is noticeable when ZnO- NH_2 NCs are present, not only when water is the transmission medium, but also when ex vivo tissue is interposed as the propagation medium. Even if there is not a significant difference in the presence of phantom, an increase of 4% in the generated cavitation can still be noticed when ZnO- NH_2 NCs are used.

At the end of 20 min of insonation, the amount of hydroxyl and superoxide anion radicals produced were evaluated for all the different conditions using a spin-trapping technique involving DMPO.

Figure 7-B shows areas under the EPR spectrum curve, corresponding to the integrated intensity of the radical species and reflecting the concentration of DMPO-OH, index of ROS generation. As similarly reported in Figure 7-A, the results in Figure 7-B demonstrate that a larger amount ROS were produced when the irradiation medium is distilled water, with respect to phantom and ex vivo tissue. Despite there is an increased ROS production when ZnO-NH_2 NCs are present in all the cases, these results are not significative, probabily due to the attenuation of power perceived inside the sample well and the different nature of the analysis.

The results obtained lead to the conclusion that we successfully generated ROS in a controlled manner even in presence of two different tissue-mimicking materials. The data open the possibility to apply this technology *in vivo* for subcutaneous ROS generation using an already approved medical device.

Despite the general difference between the attenuating media, in all the cases a largest amount of ROS was detected in presence of ZnO- NH_2 NCs, suggesting that our nanocrystals enhance the production of free radicals under ultrasound stimulation. This phenomenon is proved here also when tissue mimicking materials were interposed between the stimulation source and the sample, suggesting the possibility of *in vivo* applications.

2.4 Conclusion

In this chapter is reported the ability of ZnO-NH_2 nanocrystals in inducing inertial cavitation under pulsed ultrasound exposure. In details, it is assessed that 0.9 W/cm^2 (30% of US power) is the optimal condition to have ZnO-NH_2 NCs working as ultrasound responsive nano-agent and showing the significant large production of ROS, specifically of hydroxyl and superoxide anions in the water. Here, it is proposed, as mechanism of ROS generation, that this US conditions are sufficient to initiate the acoustic cavitation of tiny gas nanobubbles trapped at the ZnO- NH_2 NCs surface. This inertial cavitation consequently leads to a large ROS production. Strikingly in the same insonating condition, lower cavitation and consequently largely lower amount of ROS are generated from the pure water control sample.

Ultrasound B-mode imaging was also used proving the enhanced ecographic signal generation of the ZnO- NH_2 NCs containing solutions exposed to 40% intensity ultrasound with respect to pure water.

To evaluate the future applicability of ZnO-NH_2 NCs in the biomedical field, the generation of ROS and the effects of NCs as ultrasound responsive nano-agent agent were tested when different tissue mimicking materials were interposed during the insonation between the US transducer and the sample well. A significant increase of cavitation is noticeable when ZnO- \NH_2 NCs are present, with respect to pure water, when phantoms and, in a larger amount, *ex vivo* tissue are interposed as the propagation medium.

Chapter 3

A comparative analysis of low intensity ultrasound effects on living cells: from simulation to experiments

This chapter has been taken from the open-access publication, as stated in the declaration of this dissertation[51].

3.1 Introduction

The recent advancement in research has proposed the use of various types of nanoparticles, which can be better dispersed in water-based media and can be efficiently targeted to cancer cell[52]. The mechanism of interaction among ultrasound and organic or inorganic nanoparticles (NPs) in water solution exposed to such acoustic irradiation can lead to different effects. Depending on their nature, NPs of organic polydopamine or inorganic one like cerium oxide can scavenge the produced ROS from water, reducing the oxidative stress[53,54].On the other hand, semiconductor nanoparticles like zinc oxide or titania[55] can support the ROS generation, typically lowering the inertial cavitation threshold. In particular, it is supposed that their surface roughness and porosity, as well as the presence of organic functional groups imparting a hydrophobic milieu to their surface, can immobilize nanosized gas bubbles and provide nucleation sites for their cavitation[56,57] .Furthermore, the emission of photon in the ultraviolet-visible

region during inertial cavitation is supposed to photoexcite large band gap semiconductor NPs, such as ZnO and TiO_2[20].

Several groups have applied different types of NPs as sonosensitizer or, more in general, as acoustically-activated nanomaterials under ultrasound stimulation at low intensity, towards a therapy called sonodynamic (SDT)[52,58]. The use of SDT with solid-state NPs is still under study, due to the poor comprehension of the mechanisms under which NPs and ultrasound cooperate to induce cell death or spare healthy tissues and to possible side effect on the NPs use.

The possible mechanisms of cell death induced by ultrasound and in particular by NP-assisted ultrasound are manifold and depends on the US figures of merit and on the type and nature of the nanomaterial used[52]. Very generally, both thermal and non-thermal effects of US can induce toxicity and even death on the cancer cell. The presence of NPs can then increase temperature and ROS production, while the sonoluminescence can activate NPs to produce radicals and other toxic species. Furthermore, NPs motion in the US filed can create mechanical injury to cells, and also ion release should be considered, as well as electric or even piezoelectric stimulations with consequent nanomaterial polarization and cell charge imbalance[52]. In this chapter, the acoustic field of the water had been simulated to properly estimate the US field intensity and pressure across the water solution, with spatial resolution throughout the sample volume. For this purpose, simulations were implemented in COMSOL® Multiphysics.

Secondly, experimental studies were carried out to validate the numerical simulations, and sonochemiluminescence (SCL)[59] and Electron Paramagnetic Resonance (EPR) spectroscopy has been exploited to quantify the production of ROS in water solution at the previously simulated conditions[19,59–62]. Clearly, the simulation set-up was maintained as much close as possible to the experimental one, so that a clear comparison can be made. Previous studies were reported in the literature trying to compare the simulated pressure field with experimental data obtained from US transducers in a low frequency range. More in details, these works proposed to compare either the simulated pressure field with acoustic pressure measurements[63,64] or with indirect effect caused by US, like the SCL emission.

The above evaluations were then combined with biological data, i.e. the measurement of cell viability of two different cancer cell lines, treated with the same ultrasound irradiation parameters. In particular, a cervical adenocarcinoma (KB cell line) and a Burkitt's lymphoma (Daudi cell line) were used to investigate the cytotoxic role of the generated ROS.

To further advance the knowledge in the field of nanomedicine, semiconductor zinc oxide nanocrystals (ZnO NCs) stabilized with amino-propyl functional

groups were considered in the presented system, in view also of the results described in the previous chapter and in literature[16,19,20,56,65]. A possible enhancement in ROS production was evaluated from these NCs in combination with US at various power densities and treatment times. Furthermore, ZnO-NH_2 NCs were also administered to cell in a sub-toxic concentration, in order to investigate their possible combined effects related cell death.

The proposed evaluations aim thus to shed light on the effect of ultrasound in a living system *in vitro* and increase the level of knowledge on the different key parameters to help the advancement in the field of physical therapies and nanotherapeutics against cancer.

3.2 Materials and methods

3.2.1 Acoustic field simulations

The acoustic field was induced in 2 mL of a water solution contained in a well and simulated with COMSOL® Multiphysic (version 5.5, COMSOL Inc.), using the *Pressure Acoustic Frequency domain* interface. By means of this interface, the linearly approximated form of the acoustic wave equation for a time-harmonic pressure wave was solved for the specific frequency (*f*) of 1MHz, the same applied with the transducer in the experiments.

As done in previous works[59,66,67], some assumptions were implemented: (1) all the thermoviscous effects were neglected: the simulated system was adiabatic, with an equilibrium temperature equal to the standard ambient one (298.15 °K); (2) the fluid (water) was homogeneous, isotropic, in quiescence and unperturbed from any background pressure field; (3) the US wave propagated linearly through the fluid; (4) the presence and the generation of cavitation bubbles in the fluid was not simulated; (5) the system was simulated by using the COMSOL® *Viscous Fluid* model.

Therefore, the acoustic wave equation solved by the software for the acoustic pressure field *p* had the following form (Eq. 1)[66]:

$$\nabla \cdot \left(-\frac{1}{\rho_c}(\nabla p \quad - q_d)\right) - \frac{k_{eq}^2 p}{\rho_c} = Q_m \quad (1)$$

where $k_{eq} = \frac{\omega}{c_c}$ is the wave number, equal to the ratio between the wave angular frequency $\omega = 2\pi f$ and the complex speed of sound in water $c_c = c(1 + i\omega\frac{\delta}{c^2})^{0.5}$, whose real part is represented by c = 1497 m/s [21], while the imaginary

part, which takes into account the damping of the US wave due to viscous losses, contains the sound diffusivity $\delta = \frac{1}{\rho}(\frac{4}{3}\mu + \mu_b)$, where ρ is the water density, μ is the water dynamic viscosity and μ_b is the water bulk viscosity. Then, $\rho_c = \frac{\rho c^2}{c_c^2}$ is the complex water density, q_d and Q_m are the dipole and the monopole domain source respectively, both of them set to 0 since no kind of source was assumed to be present inside the system, and p is the acoustic pressure, computed by the software at each point of the domain.

Since only the fluidic domain was included in the simulations, the polystyrene walls of the well were modeled by implementing at the lateral surface of the domain the *Impedance* boundary condition[68] (Eq. 2), where the value of the polystyrene acoustic impedance ($Z_{ps} = \rho_{ps} \cdot c_{ps}$) was set in the right-hand side of the equation; the same kind of boundary condition, this time using the air acoustic impedance ($Z_{air} = \rho_{air} \cdot c_{air}$), was imposed at the domain top surface (Eq. 3), in order to model the contact of the upper surface of the solution with the air. The sinusoidal displacement generated by the oscillating US transducer at the bottom basis of the fluid was modeled by adding the *Normal Displacement* boundary condition[68](Eq. 4) at the domain bottom surface: the displacement amplitude (L_D), inserted on the right-hand side of the equation, was determined from the intensity value of the incident wave to the system (I_0), defined according to Eq. 5[69]. This value was calculated by considering the exponential reduction of the US intensity caused by the wave propagation from the transducer (generating its acoustic intensity I_{input}) through the 1.3 mm thick polystyrene basis (t) of the well, characterized by its attenuation coefficient α (Eq. 6) [69], considered at 298.15 K and US frequency of 1MHz.

$$-n \cdot \left(-\frac{1}{\rho_c}(\nabla p - q_d)\right) = -\frac{pi\omega}{Z_{ps}} \quad \text{on the lateral surface,} \qquad (2)$$

$$-n \cdot \left(-\frac{1}{\rho_c}(\nabla p - q_d)\right) = -\frac{pi\omega}{Z_{air}} \quad \text{on the top surface,} \qquad (3)$$

$$-n \cdot \left(-\frac{1}{\rho_c} (\nabla p \quad - q_d) \right) = (i\omega)^2 L_D \quad \text{on the bottom surface,} \tag{4}$$

$$I_0 = 1/2\rho c\omega^2 {L_D}^2 \rightarrow L_D = \sqrt{\frac{2I_0}{\rho c\omega^2}} \tag{5}$$

$$I_0 = I_{input} e^{-2\alpha t} \tag{6}$$

where **n** is the outward normal vector to the domain.

The domain was discretized with the COMSOL model of *Mapped* quadrilateral mesh in the boundaries, which was reproduced even at each point of the bulk by applying the *Swept* discretization method. The maximum mesh element size was imposed equal to 1/8 of the wavelength of the applied US, and the minimum one to 1/10, since 8-10 mesh elements within the wavelength are enough to simulate acoustic fields[66], providing a sufficiently accurate solution of the acoustic wave equation.

The simulation parameters whose values have not already been expressed are listed in Table 1 and the geometrical features of the well containing the water volume as well as the position of the US transducer are depicted in Figure 8.

Parameter	Value	Description
μ	0.890 [mPa·s]	Water dynamic viscosity[21]
μ_B	2.485 [mPa·s]	Water bulk viscosity[21]
ρ	998 [Kg·m^{-3}]	Water density[21]
α	0.108 [cm^{-1}]	Polystyrene attenuation coefficient[15, X]
Z_{ps}	2.5·10^6 [Pa·s·m^{-1}]	Polysterene acoustic impedance[21]
Z_{air}	4.017·10^2 [Pa·s·m^{-1}]	Air acoustic impedance[22, 23]
r	7.950 [mm]	Well basis radius
H	10.78 [mm]	Solution height
$L_{D,\,0.30}$	10.09 [nm]	Bottom wall displacement at I_{input} = 0.30 W/cm^2
$L_{D,\,0.45}$	12.36 [nm]	Bottom wall displacement at I_{input} = 0.45 W/cm^2
$L_{D,\,0.60}$	14.27 [nm]	Bottom wall displacement at I_{input} = 0.60 W/cm^2

Table 1 . Some of the parameters used in the simulation. The ones related to water, polystyrene and air are referred to a temperature of 298.15 °K. The polystyrene attenuation coefficient was determined from the formula present in Reference[70] and by using the values reported by Spigarelli et al.[59,66,67] In the calculation of

the air acoustic impedance, the speed of sound in the air and the air density have been taken respectively from the work of Dhiren M Joshi and Shih[71,72].

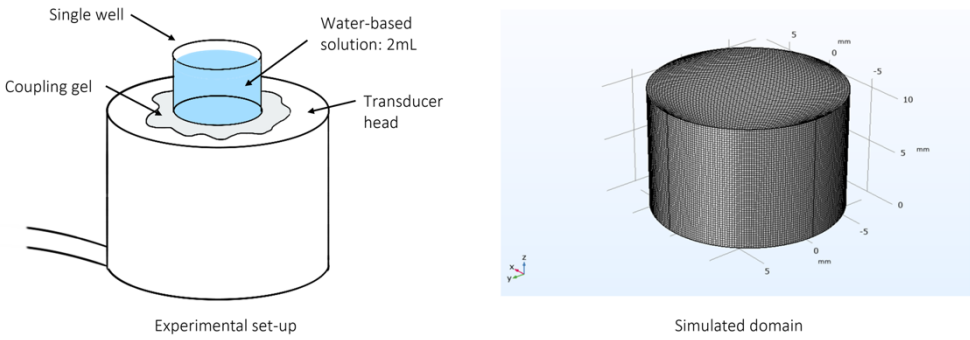

Figure 8 Scheme of the experimental set-up (left) and simulated domain (right), whose description and characteristic dimensions are reported in Table 1

3.2.2 Synthesis, functionalization and preliminary characterization of zinc oxide nanocrystals

ZnO nanocrystals (NCs) were synthesized through a hydrothermal microwave-assisted approach developed by Garino et al.[16]. More details on synthesis and ammino-propyl functionalization and NCs characterization are reported in 2.2.1 and 2.2.2 section.

3.2.3 Experimental acoustic stimulation of solutions

Ultrasounds were generated by using the LipoZero G39 (GLOBUS) unfocused transducer. Each sample was composed of a water-based solution in a single well of a 24 well plate of polystyrene (PS, Thermo Scientific) and positioned on the Us transducer (Figure 8). To ensure the contact between the sample and the transducer, a thin layer of coupling gel (ELvation Medical GmbH) was interposed. The experiments were performed by setting the following parameters: ultrasound frequency of 1 MHz, Duty Cycle (DC) of 100%, power densities of 0.3, 0.45 and 0.6 W/cm^2 and sonication times of 5 s, 10 s, 15 s, 30 s, 1 min, 2 min. The ROS generation was analyzed in pure bidistilled (bd) water solutions (from Milli Q, Millipore-Merck) or in water-containing ZnO-NH_2 NCs at 200 μg/mL concentration.

The amount of ROS was evaluated with two different detection techniques: the induction and successive analysis of sonochemiluminescence (SCL) from luminol solutions and the Electron Paramagnetic Resonance (EPR) Spectroscopy assisted by a spin-trapping technique, as detailed below.

3.2.4 ROS evaluation with sonochemiluminescence method

As described in the work of McMurray et al.[23], SCL is the emission of blue light (λ = 430 nm) by Luminol molecules in an alkaline solution caused by their interaction with hydroxyl radicals (OH·), generated by acoustic cavitation. This oxidative chemiluminescence of Luminol develops through a complex reaction pathway of the molecule, which undergoes many intermediate reaction steps before emitting the blue light. For a given concentration of luminol molecules in the solution, the light intensity emitted (and then detected) by SCL, denoted as I_{SCL}, is proportional to the amount of cavitation-generated hydroxyl radicals in water.

To ensure a proper activation of the SCL process, a solution composed of 80 mM luminol (97% by Sigma-Aldrich), 0.1 M sodium hydroxide (NaOH) and 0.5 mM hydrogen peroxide (H_2O_2, from a stock solution of 0.02 M) in a total volume of 2 mL of bd water was placed in a well of the 24-well plate. Furthermore, in case of nanoparticles-assisted US study, ZnO-NH_2 NCs were added leading to a final concentration of 200 µg/mL. The prepared solutions were treated within 4 hours from their preparation.

The SCL intensity emitted by each solution during the sonication was detected by using a Nikon D80 digital camera, set with ISO = 1250, f-stop = f/4 and with an exposure time that, for the shorter sonication times (as 5s, 10s, 15s) is at least of 30s, while, for the longer sonication times (as 30s, 1min, 2 min), it is set equal to the sonication time. Thus, by fixing the camera on a tripod and positioning it right above the well (approximately at a height around 20 cm from the well), images of the blue colored solutions were acquired, showing a visible circle corresponding to the well shape (Figure 9-A). Following the work of Tiong et al.[59], to avoid the acquisition of noisy light coming from the environment (due to the long exposure times) and remove the thermal noise inside the camera, the experiments were performed in a dark room and a frame image was taken in absence of sonication (background) before each experiment. After the experiments, the obtained images were analyzed and processed with the open-

source software ImageJ: firstly, the background was subtracted to the acquired images in a pixel-by-pixel approach; then, the area of the images showing blue light pixels (Figure 9-A) was selected as Region Of Interest (ROI, Figure 9-B) and spatial average blue intensity was calculated over all the intensity values of the pixels inside the ROI. The processed images were set as 24-bit RGB color images and since Luminol emits blue light, only the intensity of the blue channel was computed.

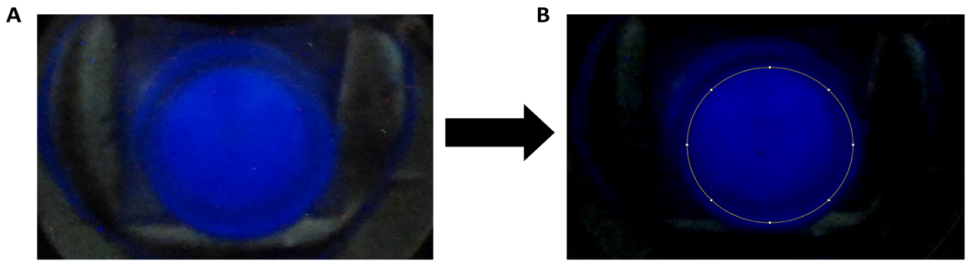

Figure 9 Acquired image from the 24-well plate and its processing. The image resulting from the sonication (A) is subjected to subtraction of the background image and the selection of a specific circular ROI (B). These images refer to the particular sonication condition with US power = 0.6 W/cm2 and sonication time 3min

3.2.5 ROS evaluation by Electron Paramagnetic Resonance (EPR) Spectroscopy

A quantitative evaluation of ROS production by US-induced cavitation in a water-based solution was provided by means of the Electron Paramagnetic Resonance (EPR) Spectroscopy, performed with the EMXNano X-Band spectrometer (Bruker).

The samples were prepared according to protocol reported in section 2.2.3, instrument settings and data analysis were also described in the same section.

3.2.6 Cells line and treatments

The human Burkitt Lymphoma cell line Daudi (ATCC® CCL-213TM), as a suspension cell line, was cultured in RPMI-1640 Medium (ATCC30-2001)

supplemented with 10% of heath inactivated fetal bovine serum (ATCC-302020), 100 units/mL penicillin and 100 µg/mL streptomycin (Sigma-Aldrich, Schnelldorf, Germany) and maintained at 37 °C under a 5% CO_2 atmosphere.

To evaluate the effects of ultrasound irradiation on this hematological cancer cell line, samples containing 2 x10^5 cell/mL were plated into 24 well plate (Nunc) with 2 mL per well, treated with different conditions of ultrasounds and promptly seeded in a 96 well plate (Greiner Bio-One). Each 96 well contained 100 µl per well of sample solution, in three replicates for viability assay. After 24h indeed, 10 µl/well of cell proliferation reagent WST-1 (Roche) was added and after additional 4h of incubation, the formazan absorbance was detected at 450 nm by the Multiskan Go microplate spectrophotometer (Thermo Fisher Scientific Waltham, MA, USA) using a 620 nm reference.

The effects of ultrasound and the further combined action of US and amino-functionalized ZnO nanocrystals were tested on another cancer cell line. i.e. cervical adenocarcinoma KB cell line (ATCC CCL17TM), which grows in adhesion as a 2D monolayer. KB cells were grown in Eagle's Minimum Essential Medium (EMEM, Sigma) supplemented with 10% heat inactivated fetal bovine serum (FBS, Sigma), 100 units/mL penicillin and 100 µg/mL streptomycin (Sigma), and maintained as reported for Daudi cell line[65,73].

Before treating the KB cancer cells with US, cells were trypsinized, counted, and 5x10^5 cells were plated in 1 mL of complete medium/well into 24 well plates (Nunc). In this way, KB cell were in suspension in cell culture media and thus exposed to ultrasound irradiation. Different experimental groups were considered: untreated cells, cells treated with US, and cells pre-treated for 24 h with ZnO-NH_2 NCs with or without the subsequent US treatment. In the case of cells pretreated with ZnO-NH_2 NCs, cells were preincubated with 10 µl/mL ZnO-NH_2 NCs for 24h then trypsinized and counted following the same protocol as before. After the treatment, cells were promptly seeded in a 96 well plate (Greiner Bio-One), i.e. at 2x10^3 cells in 100 µl medium per well in replicates, for the viability assay. After 24h from the treatment, proliferation activity of KB cells was measured by WST-1 assay, as previously reported for Daudi cells.

All cells were treated with LipoZero ultrasound transducer, with US frequency equal to 1MHz, 100% of Duty Cycle, and different condition of power densities (0.3, 0.45 and 0.6 W/cm^2) and exposure times, as detailed above.

All the reported results are expressed as percentage of cell viability with respect to untreated cells, assessed as 100% viable. Data are shown as mean ± standard deviation.

3.3 Results and discussion

3.3.1 Acoustic field simulations

The simulations allowed to model the acoustic pressure field and the acoustic intensity distribution inside the well due to the propagation of the US wave through the solution. In Figure 10 both entities are computed at I_0 = 0.45 W/cm^2 of the US transducer input power density.

The acoustic pressure field and the acoustic intensity distribution inside the well are visualized along three vertical planes (Y-Z planes, Figure 10-A and 10-C), selected at x = 0 (well central section), x = 3.98 mm (half of the well basis radius along the X axis) and x = 7.9499 (0.0001 mm from the well wall along the X axis). These vertical planes allowed to study the US behaviour along the wave propagation direction (i.e. the vertical axis, Z) and when moving radially (X and Y axes). A second set of planes was selected horizontally (X-Y planes, Figure 10-B and 10-D), chosen at z = 0 (well bottom surface), z = 2.5 mm (one quarter of the well height), z = 7.5 mm (three quarters of the well height) and z = 10.7 mm (well top surface).

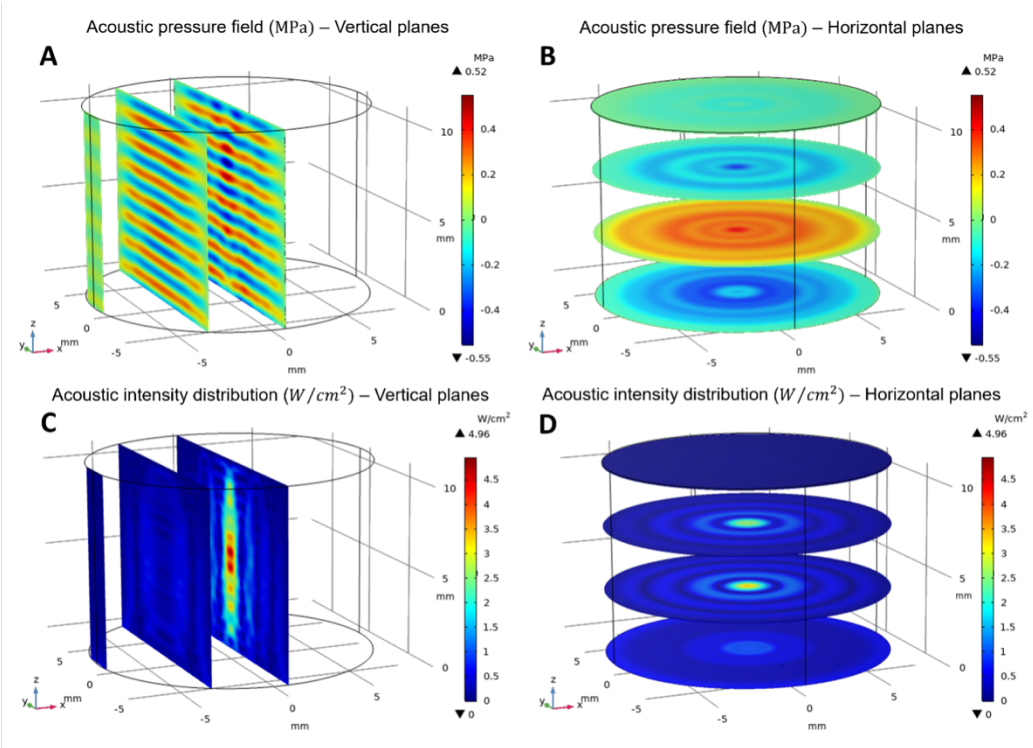

Figure 10 Acoustic pressure field (top panels) and acoustic density distributions (bottom panels) within the well simulated with COMSOL® Multiphysics for I_{input} = 0.45 W/cm^2, along vertical (A and C) and horizontal (B and D) planes of the sample well containing water. The darkest red and blue colors in panels A and C indicate the maximum and the minimum values, respectively, that the acoustic pressure can assume, equal to + 0.52 MPa and - 0.55 MPa. The darkest blue and red colors of the acoustic density (panels C and D) correspond to 0 W/cm^2 and 4.96 W/cm^2, respectively.

The acoustic pressure field on the vertical planes (Figure 10-A) highlights the alternation of compression and rarefaction cycles along the Z axis, according to the propagation direction of US. This trend is sinusoidal, characterized by highly varying and pronounced peaks around the vertical central axis, in particular at the well center, and then tend to decrease and to assume a more regular and homogeneous shape when moving radially towards the walls. Also from the acoustic pressure field on the horizontal planes (Figure 10-B), it can be observed that the peaks around the central vertical axis gradually decrease along the radial direction, following an oscillatory trend of symmetrical pressure phases. This behavior may be caused by the scattering of the propagating US wave inside the fluid and by its interaction (transmission and reflection phenomena) with the cylindrical lateral surfaces of polystyrene walls and with the air at the top surface, generating specific interference effects. In fact, Figure 10-A demonstrates that the region around the central vertical axis appears to be subjected to strong

constructive and destructive interference effects, originating diversified local maxima and minima pressure peaks which decrease along the radial direction. Moreover, it can be supposed that the particular axis-symmetric geometry of the well favors the formation of a symmetric and tapered focus along the central vertical axis, composed by the highest pressure amplitude values.

Further information about the behavior of the US field inside the well can be gained from the acoustic intensity distribution on the vertical (Figure 10-C) and horizontal planes (Figure 10-D): as previously noticed, a symmetric and tapered focus along the central vertical axis is clearly visible, showing the highest acoustic intensity values (at about 4.5 W/cm^2) around the center of the well. From this region, the intensity slowly decreases moving towards the top and bottom surfaces, while it sharply reduces radially. Moreover, interference effects can be distinctly observed, represented by a pattern of concentric fringes, whose variations are strong around the vertical central axis and attenuate along the radial direction.

The same trends of the acoustic pressure field and the acoustic intensity distribution on the vertical and the horizontal planes were obtained also for I_0 equal to 0.60 W/cm^2 and 0.30 W/cm^2, even if they were characterized by different values, as expected by the different US input power densities used and thus by the different bottom wall displacements of the well.

Finally, a comprehensive analysis was carried out by computing the average acoustic pressure amplitude and acoustic intensity on each of the three vertical planes, for all the three US input power densities (0.3, 0.45 and 0.6 W/cm^2 in Table 2). The obtained data show that for each US power density in input, both acoustic pressure and intensity decrease along the radial direction, in agreement with the previous color maps of Figure 10. A higher reduction is achieved by approaching the well lateral surface. At the same time, for each vertical plane, the average acoustic pressure amplitude and acoustic intensity increase proportionally to the transducer power density, as expected. It is worth to note that the average acoustic intensity calculated in the central plane of the well is higher than the power density of the transducer. This local value provides the highest contribution to the average intensity over the whole domain, but it is counterbalanced by the much lower acoustic intensities calculated when moving towards the well boundaries. As a result, the average intensity over the whole solution volume is

actually lower than the input one. This outcome can be attributed both to the viscous losses of the fluid (which are taken into account in the used *Viscous Fluid* model) and to the acoustic pressure and intensity trends described above.

Input power density [W/cm²]	**0.3**	**0.45**	**0.6**
Bottom wall displacement [nm]	9.95	12.19	14.06
Intensity average central [W/cm²]	0.414	0.621	0.826
Intensity average r/2 [W/cm²]	0.193	0.290	0.386
Intensity average wall [W/cm²]	0.070	0.105	0.140
Intensity average whole solution [W/cm²]	0.236	0.355	0.472
Pressure ampl average central [MPa]	0.152	0.187	0.215
Pressure ampl average r/2 [MPa]	0.125	0.154	0.178
Pressure ampl average wall [MPa]	0.043	0.052	0.061

Table 2 Average acoustic intensity and acoustic pressure amplitude computed on the three considered vertical planes and at different US power densities in input from the transducer.

3.3.2 Experimental measurements

With the aim to validate the acoustic pressure and density simulations with experimental data, the central average acoustic pressure was evaluated in the center of the 24-well at each US input power densities, as used for the mathematical simulations, by hydrophone measurements. The collected data showed that the same values of acoustic pressure inside the well are achieved with

both simulation and experimental tests, and thus perfectly validating the output results and the correctness of the used mathematical model.

Furthermore, the measurements of ROS production was investigated in the well volume under US irradiation at the selected input conditions and measured through the SCL and EPR methods[19,74]. Initially, the ROS measurements were conducted in pure water, as previously considered for the simulations, and afterwards the same US input power densities and times were applied to living cancer cells, i.e. KB and Daudi cell lines, both in suspension in their culture media. The effect of ROS in living cell is multifaced, due to their role in the cell signaling system[75]. An imbalance, i.e. an overproduction, of ROS levels in cells can result in the activation of apoptotic pathways, which in turns lead to cell deaths[25]. Therefore, the evaluation of cell viability can be a meaningful tool to indirectly assess the absence or the presence of abnormal ROS production in an US irradiated cell culture solution, further supporting the EPR and SCL measurements and the simulation results.

In a second set of experiments, the role played by ZnO-NH_2 NCs dispersed in water was evaluated in terms of ROS generation and thus on the possible amplification of US effects. Ultimately, the analysis of the KB cancer cells viability after 24 hours of incubation with NCs and consequent US treatment was examined, trying to propose a correlation among ROS generation and the cell viability, also depending on the presence of nanoparticles. It is worth to mention that the selected US power densities used to run both simulations and experiments are dictated mainly by the cell viability: actually, preliminary experiments showed that US input densities higher than 0.6 W/cm^2 relied on a rapid increase of the temperature of the water media and on a high percentage of cell death, even without the presence of NCs. Since these effects prevented to evaluate the non-thermal effects of US on the cell fate, higher US powers than 0.6 W/cm^2 were not considered.

3.3.2.1 Measurement of acoustic cavitation in pure water and on living cancer cells

Figure 11 compares the production of ROS, evaluated by SCL of Luminol and EPR measurements of DMPO-OH molar concentrations, with the cell viability essays on two different cencer cell lines (KB cells, a cervical adenocarcinoma and

Daudi cells, a Burkitt lymphoma) at different US input power densities and irradiation times. Studying the effect of US on two so different cancer cell lines, allow to test also the biological variability, enabling us to verify the hypothesis of a potential therapeutic system.

Both the spatial average SCL blue intensity detected from the well (Figure 11-A) and the molar concentration of DMPO-OH spin adducts found through EPR measurements (Figure 11-B) globally show an increasing trend proportional to longer sonication times and higher US power densities in input. Considering firstly the lowest US power density (0.3 W/cm^2), the related SCL intensity assumes negligible values for all the sonication times, in agreement with the null molar concentration of DMPO-OH obtained by EPR. This result corresponds to a negligible production of ROS during sonication. At the same power density, a high cells viability is obtained for both cell lines. In particular, at the lowest applied US power of 0.3 W/cm^2, KB cells are not affected by the US treatment (Figure 11-C), even for the longest sonication times (up to 2 min). Daudi cells also report a viability close to 100% for 30 s and 1 min, and a slight decrease of their metabolic activity is exhibited for 2 min sonication condition (Figure 11-D). The unvaried cell viability for almost all the tested conditions supports the EPR and SCL measurements in which ROS production is negligible.

Concerning the results obtained by applying the intermediate US power, 0.45 W/cm^2, a negligible Luminol intensity is observed for 30s sonication time (Figure 11-A), while it gradually increases from 1 to 2 minutes. In particular, at 0.45 W/cm^2, a treatment of 1 min represents the shortest sonication time able to produce a detectable SCL blue light, even if its value is relatively very low. This result is consistent with the EPR results (Figure 11-B), showing a similar increasing trend of ROS production as the sonication time increases, i.e. from 30 s to 1 min and to 2 min of sonication time.

Concerning the cells viability, the first signs of modest cytotoxicity are obtained at 0.45 W/cm in KB cells at 2 minutes of sonication (around 78% cell viability in Figure 11-C), while are already visible at the shortest sonication time of 30 s in Daudi cell line (Figure 11-D). It is hypothesized that the applied power density of 0.45 W/cm^2 may impact on the cell viability, even slightly, while the dose of this treatment, which depends also on the application time, may vary depending on the cell type. More in general, the cell viability trend (Figure 11-C and 11-D) appears to be globally lower at 0.45 W/cm^2 than at 0.3 W/cm^2 power density, and seems to be in line with the higher ROS production, increasingly proportional to the applied US power densities and times.

A remarkable behavior is presented by the measurements at 0.60 W/cm^2 of applied US power density. Both the SCL intensity histogram (dark blue bars in Figure 11-A) and the molar concentration of DMPO-OH adducts (dark blue bars in Figure 11-B) show non-negligible and increasing values of ROS production as a function of the treatment time. This behavior is reflected by the average cell viability values below 30% (see dark blue bars in Figure 11-C and D) in both cancer cell lines, indicating an evident cytotoxic effect of 0.60 W/cm^2 power density at any sonication time. In particular, the recorded cell viability of Daudi cell line is null at the highest tested time, i.e. 2 minutes.

Considering that the both cell lines are dispersed homogeneously inside the solution volume, it can be hypothesized that they are continuously moved by the convective forces generated by US during the irradiation time. It can be supposed that during the treatment, the majority of cells are exposed one or more times to the strongest sonication activities occurring in the central region of the well, as highlighted by the simulation results. Actually, the simulation revealed the presence of a central tapered region in the well with the highest values of acoustic pressure and intensity. From the experimental data of SCL intensity and DMPO-OH molar concentration, a consistent ROS production can be also noticed. All the above considerations can be used to possibly motivate the reduced cell viability recorded at the highest US power density used, i.e. 0.6 W/cm^2.

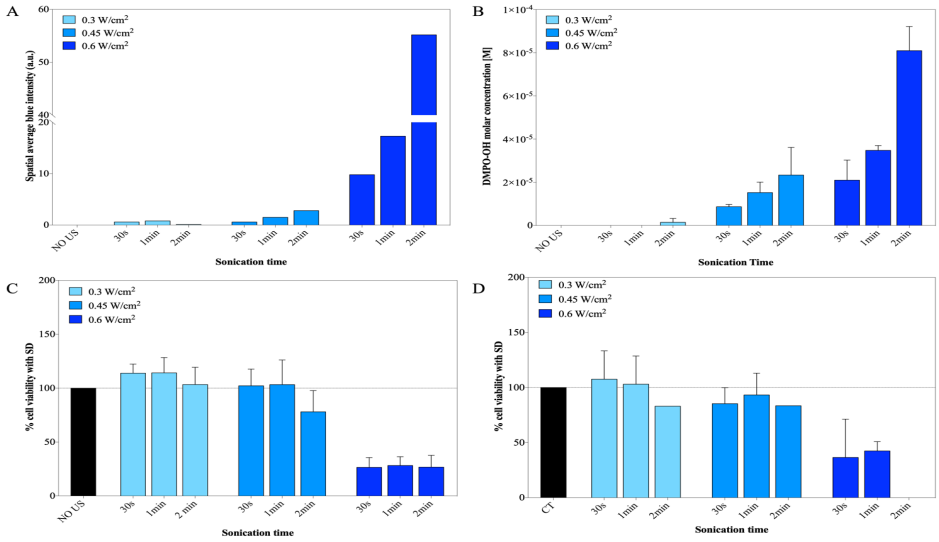

Figure 11 The generation of ROS in bd water volumes and the possible effects on living cell cultures: (A) Spatial average blue intensity of luminol due to sonochemiluminescence (SCL); (B) Molar concentration of DMPO-OH spin adducts obtained during EPR measurements; (C) KB cancer cell viability and (D) Daudi cell viability after 24 hour from US irradiation. In these experiments, UT means untreated cells, and the presence of ZnO-NH_2 NCs is not considered

3.3.2.2 Measurements of acoustic cavitation mediated by ZnO-NH_2 NCs

The previous measurements allowed to set a base of understanding about the possible interaction among acoustic irradiation and living cell systems. Further comprehension of this mechanism can be done by challenging the overall system with the addition of inorganic metal oxide nanoparticles in the water solution, providing a direct evidence of the effect of solid-state inorganic nanoparticles compared to the pure water solutions. Furthermore, the ZnO-NH_2 NCs were exploited in the cell culture media, allowing their internalization in KB cancer cells and providing a base of understanding in combination with US irradiation. In these experiments, the lowest US powers, equal to 0.3 and 0.45 W/cm^2, were applied since they have per se a non-toxic behavior towards cells, as demonstrated in Figure 11-C. For similar reasons, the ZnO-NH_2 NCs concentration of 10 µg/mL was incubated with the KB living cancer cells, as it resulted from a previous study (which are reported in this thesis in Chapter 5, Figure 21)[65] to do not cause any cytotoxicity to the cells (in absence of US), and to provide a sufficiently high amount of NCs internalized (98.0±0.4% at 24h also reported in chapter 5, Figure 22) into the cells[65]. However, for the sake of completeness, also the results associated to an input power of 0.60 W/cm^2 are reported in this study.

Figure 12 shows an overview among the effect of US irradiation combined with the presence of NCs leading to the generation of ROS in water-based media (red bars), and a possible comparison with the cell viability, by analyzing the influence of different sonication times and input power densities. Control measurements in the absence of ZnO-NH_2 NCs (blue bars) are also inserted for reference and refer to experiments already reported in Figure 4.

An initial consideration can be done in absence of US irradiation, where the sole presence of ZnO-NH_2 NCs is not sufficient for generating ROS, thus neither blue light emission in SCL (Figure 12-A), nor DMPO-OH adducts in EPR spectroscopy (Figure 12-B) are measured. These preliminary data are consistent with high cell viability of the NCs-incubated cells in absence of US (red dotted bar in Figure 12-C) very similar to the untreated cell control (black bar).

SCL measurements at 0.3 W/cm^2 and 0.45 W/cm^2 (Figure 12-A) show a slight increased spatial average blue intensity in presence of ZnO-NH_2 NCs, in accordance with the augmented amount of free radicals detected, i.e. EPR measurements (Fig 12-B), when NCs are in solution. A different behavior is displaced in SCL at 0.6 W/cm^2. The presence of NCs reduces the detected light compared to pure water under identical US irradiation conditions. As reported in literature[20,76] and in the next chapter, ZnO NCs are characterized by an absorption spectrum which partially overlap with blue light emission by SCL. It is possible to state that for 0.6 W/cm^2, even though there is an increased ROS production with NCs (Fig 12-B) attributable to an increased inertial cavitation, the absorption by ZnO NCs of the photon produced by SCL become a dominant phenomenon and it is responsible for the diminished blue signal detected due to the close proximity between the NC and point of photon generation[20,77,78].

EPR measurements (Fig. 12-B) show a monotonic increase of DMPO-OH concentration values in presence of ZnO NCs (red bars in Figure 12-B) with respect to the values from pure water at the same conditions (blue bars in Figure 12-B). Therefore, a clear trend of the ROS generation as function of the sonication time and the US output power density can be observed and is enhanced by ZnO-NH_2 nanocrystals. The trend of radical production, visible for all the power densities tested, suggests a constructive interaction between US and NCs, which possibly facilitated inertial cavitation in water, responsible for ROS production, and lowers the cavitation threshold, as also previously reported[19,56].

In accordance with the results presented above, the US powers at lowest input densities, i.e. 0.3 and 0.45 W/cm^2, did not impact significantly on the cancer cell viability in either presence or absence of NCs. While the presence of ZnO NCs resulted to increase the ROS production, this effect was not sufficient enough to induce cytotoxicity. Specifically, nor the used US power densities and times, neither the ZnO-NH_2 NCs co-incubation, were sufficient to generate an irreversible damage to cells, (including the generated ROS or any mechanical effects) to cause a consistent cell death. Cell viability of the preliminary data reported in Figure 12-C actually remained well above 90%.

Different considerations can be done for the highest US input power density, 0.6 W/cm^2: at increasing irradiation times from few seconds (5-10 s) up to 30 s, a negative effect on cell viability is recorded, decreasing the cell viability down to 25-30% at 0.6 W/cm^2 for 30 s, both in presence and absence of ZnO-NH_2 NCs. The contribution of the NCs remains however unclear and the responsibility of the observed cell death mechanism can be mainly reconducted to the US input power density used and to a specific time of US application. Both can lead to ROS production, however, as mentioned above, ROS are not the only responsible for cell death, as far as also mechanical damages can be obtained and are here not measured.

The obtained finding however highlights the adequacy of the mathematical modelling and of both SCL and EPR experiments in pure water, all useful to quantify a certain “dose” of US given to a system and to hypothetically predict the possible biological consequences. In particular we highlight that the measurement of the luminol sonochemiluminescence, although not quantitative, may represent a useful qualitative method to rapidly and directly estimate the presence of ROS produced in an US irradiated solution and screen out conditions which could be applied to living cancer cell aiming at killing them. Clearly, the final proof of the identification and quantification of the produced ROS has to be achieved with a more robust technique, like the EPR spectroscopy, mandatory in presence of optically responsive materials, which is however much more time consuming and laborious, and the biological results proofed by robust cell viability tests.

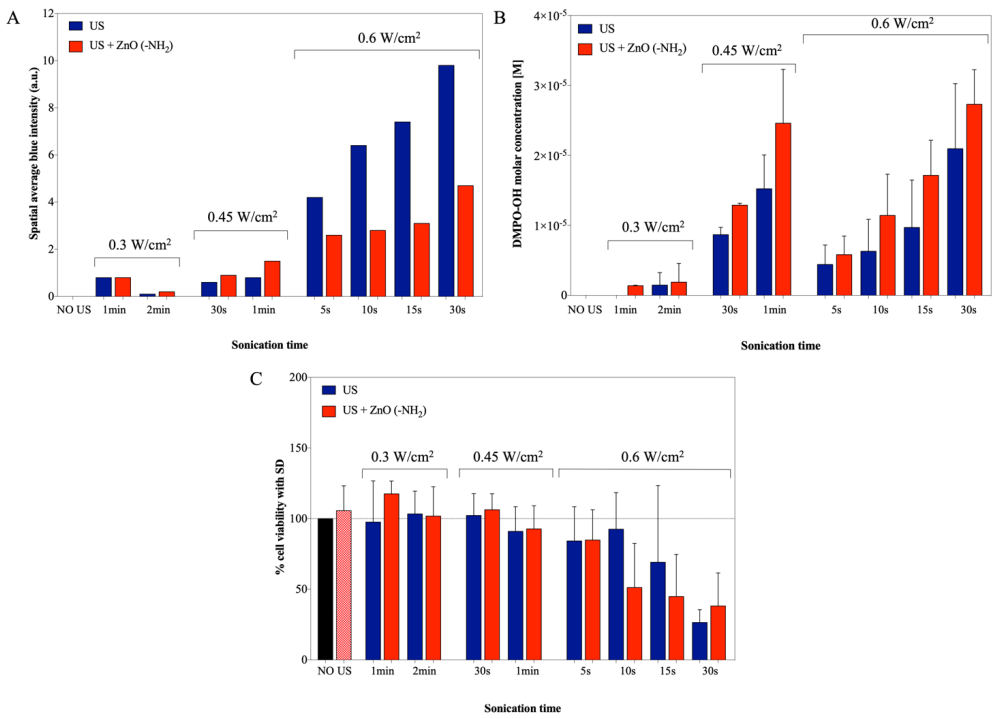

Figure 12 Overview of the ROS generation and related cell viability in a system comprising inorganic metal oxide nanoparticles (ZnO-NH_2 NCs) and ultrasound irradiation in a well from a 24-multiwell plate. (A) Luminol blue intensity from SCL measurements with 200 µg/mL of ZnO-NH_2 NCs; (B) DMPO-OH adduct concentration measurements from EPR spectroscopy to evaluate ROS production (with 200 µg/mL of ZnO-NH_2 NCs), and (C) KB cancer cell viability according to different US power densities and sonication times (with 24 hours preincubation of cell with 10 µg/mL of ZnO-NH_2 NCs), test was performed at least in duplicate; black bar and red dotted bar correspond respectively to untreated KB cell and cells incubated with NCs without US exposure.

3.4 Conclusion

In this chapter it is set a mathematical model able to predict the acoustic pressure field and acoustic density distribution in the analyzed water volume. Despite the used US were non-focused, the formation of a symmetric and tapered focus along the central vertical axis of the water sample volume was observed, having the highest pressure amplitude values and acoustic densities.

The simulated data are here validated with experimental measurements, detecting the reactive oxygen species generation with two different techniques, sonochemiluminescence and electron paramagnetic resonance spectroscopy. Both

methods indicated a negligible value of produced ROS once US input power density are low enough, i.e. at 0.3 W/cm^2, for any of the application time studied. An increasing trend of produced ROS is consistently observed once US power densities in input are increased and at increasing values of irradiation times, as also reported in chapter 1 for different conditions. A parallel evaluation of two different cancer cell line viability was also performed. High cell viability was indeed accounted at the lowest US power densities in input, while a decrease in cell viability was recorded at higher power densities and increasing application times. In these conditions, the 0.6 W/cm^2 US power density resulted to produce the highest amount of ROS and the strongest cytotoxic effect, especially for the longest treatment time of 2 minutes.

To further challenge the use of US in combination with nanoparticles, towards the direction of US-assisted nanomedicines, the interplay among US and amine-functionalized ZnO NCs was analyzed for any of the US power densities and times considered. Also in this chapter it has been proven that the amount of ROS generated in presence of NCs is higher than the respective amount produced pure water.

The cell viability measurements were conducted first internalizing the nanoparticles for 24 hour in KB adenocarcinoma cell line and then exposing the cells to US. Since the ZnO-NH_2 NCs were adopted with cells in a sub-toxic concentration, a very good cell viability was observed both in absence of US irradiation and at the lowest US input power density, 0.3 W/cm^2, irrespectively to the applied sonication time. In contrast at increasing US input densities of 0.45 and 0.6 W/cm^2 and related increasing application times, more evident signs of cytotoxicity were observed, however the presence of ZnO-NH_2 NCs did not give a clear contribution improving the cell cytotoxicity. These results evidence that the interplay among US and NPs in biological living system is more complex than in pure water and more conditions have to be explored prior to achieve a univocal answer. In our contest, it seems that US power densities and application times on a biological system plays the major role in dictating the cell viability.

As a whole, the obtained results fairly show that mathematical simulation of an acoustically treated water system can be also experimentally validated with simple measurements, like ROS production. In particular, the qualitative SCL measurements are confirmed in pure water by more robust and quantitative EPR technique and allow to estimate the amount of produced ROS in the system. In a

further step, the amount of produced ROS can fairly correlate to the cancer cell viability measurements.

Particular attention should be paid when optically responsive materials, as ZnO NCs, where involved in the studied system.

Chapter 4

Insight into Sonoluminescence Augmented by ZnO-Functionalized Nanoparticles

This chapter has been taken from the open-access publication[20], as stated in the declaration of this dissertation.

4.1 Introduction

In recent years, the development of diagnostic tools has seen considerable progress in the anticancer field and, in this regard, the design of sophisticated contrast agents is at the frontiers of modern research[79–81].These agents allow us to obtain high sensitivity and specificity toward organs or tissues of interest and are capable of providing a visual aid to assess the presence of a disease.

At present, a large number of nanosized materials have been studied for their potential use in optical diagnostic purposes[82,83]. The most interesting and recent applications of optical imaging rely on molecular imaging applied to *in vitro* and *in vivo* systems. These techniques aim at high-resolution applications at the single-cell level and for real-time molecular processes to study cancer biology, holding promise in clinical translation for prognosis and treatment[84,85]. Many types of semiconductor nanomaterials have been prepared, and the best known is quantum dots (e.g., CdS, CdSe, CuS, and other composites or core−shell

nanomaterials[86,87]). However, they present some disadvantages, such as poor biodistribution or accumulation in target organs with persistent effects (e.g., poisoning, local and/ or systemic toxicity, and a lack of final biodegradation in nontoxic products)[88].

At the current state of knowledge, various approaches have been attempted to replace QDs with less toxic nanostructures as well as to modify their surface chemistry using organic materials such as polymers, lipids, or functional molecules with selective targeting[89–91].

To this purpose, biodegradable and biocompatible semiconductor nanomaterials, also equipped with targeting agents, have shown their abilities in therapeutic and imaging applications [52,92–95]. One of the most recent examples is a semiconducting metal oxide in the form of zinc oxide nanocrystals (ZnO NCs) chemically functionalized with organic functional molecules and lipid bilayers from both artificial and natural origin[10,96,97].

In this chapter Sonoluminescence (SL) augmented by ZnO NCs is exploited to produce light for imaging purposes. SL is acknowledged as the emission of light resulting from the implosion of cavitating bubbles that form in a liquid when irradiated by US[98].

In the literature, sonoluminescent signals, proven not to be quenched by body temperature[99], should also correlate with the amount of biological damages achieved during the ultrasound exposure of cells. The work of Dezhkunov et al. identified four different stages of cavitation development based on the presence or absence of SL and sound absorption[100]. Furthermore, SL could be related with other biological parameters. Cochran et al. indeed established a correlation between the cellular uptake of calcein and viability with SL[101]. The presence of nanoparticles (irrespective of their nature) in the liquid medium reduces the dose of US necessary to obtain acoustic inertial cavitation[56]. Indeed, nanoparticles tend to carry gas pockets thanks to their structure, roughness, and surface porosity, as we also recently proved[56].

SL has a broad emission spectrum that ranges from the ultraviolet (UV) to visible wavelengths and can vary with emission peaks depending on the presence

of dissolved gas or salts[102]. However, the intensity of SL is per se very low and barely visible, requiring a specific setup for its detection.

It is possible to modify or even amplify the SL emission spectrum by means of particular types of nanoparticles, having well-defined optical properties. In particular, it is supposed that such nanoparticles can act as imaging contrast agents, first by increasing the effects of inertial cavitation and therefore improving the SL signal intensity. Second, in view of their nanometric size, such nanoparticles can allow a better spatial resolution of SL, improving the diagnostic detection. Third, the presence of nanoparticles characterized by specific optical absorption and emission properties can produce well-defined spectral emission in SL, allowing the increase of optical emission peaks or reduction of others in the SL spectral range.

In this chapter is reported an imaging contrast effect that arises from the combination of ultrasonic irradiation of an aqueous medium with semiconductor ZnO nanocrystals functionalized with aminopropyl groups. This imaging method is not based on echographic contrast but on the sonoluminescence emission supported by ZnO nanocrystals, providing bright luminescence emission and reducing the cavitation threshold at which this phenomenon takes place, decreasing the US dose to be able to produce contrasted images. Furthermore, being ZnO, a semiconductor material, photons of SL can be optically absorbed by the nanoparticles and may be re-emitted at different energies. This optical modification of the SL spectrum can thus generate particular spectral signatures determined by the optical properties of the ZnO semiconductor nanocrystals.

Nanoparticle-assisted SL phenomenon can be exploitable to provide control over the spectral emission features and, more in general, to enhance SL even using mild ultrasounds, thus avoiding diffuse thermal effects. Sonoluminescence is investigated in water and in biological solutions while spectral information is recorded and analyzed.

To get further insights into the phenomenon and moving toward biomedical applications, optical images are presented both in pure water and in biologically relevant buffers and media. The results of this analysis confirm that in presence of ZnO NCs, the US power needed for SL evidence is reduced considerably and underline the role of these NCs as nanocontrast agents to enhance and further tune the spectral emission of SL.

4.2 Materials and methods

4.2.1 ZnO-NH_2 NCs synthesis, functionalization, and characterization

ZnO nanoparticles were synthesized through a microwave- assisted synthesis, as reported in ref[16,97], and detailed synthesis and functionalization process are reported in section 2.2.1. The morphological characterization of ZnO-NH_2 NCs is described in detail in section 2.2.2

4.2.2 SiO_2-NH_2 NPs synthesis and characterization

Silica (SiO_2) nanoparticles of approximately 20 nm diameter, used as optically inert control, were obtained exploiting the Stober̈ method[103,104]. 0.558 mL of tetraethyl orthosilicate (TEOS, ≥99% from Sigma-Aldrich) was added to 25 mL of absolute ethanol (99%, Merck). After 15 min of vigorous stirring, 1.018 mL of ammonium hydroxide solution (NH4OH, ACS reagent, 28−30% purchased from Sigma- Aldrich) was rapidly dropped in the solution. The system was left in moderate agitation for 24 h, and the particles were collected afterward by centrifugation. Several washing in ethanol was performed to obtain the final particle suspension.

Silica nanoparticles (SiO_2-NPs) were also functionalized with APTMS following the same procedure exploited for ZnO NCs (Section 4.2.1) to obtain the final SiO_2-NH_2 nanoparticles. Also, the characterization of these NPs was performed by field- emission scanning electron microscopy (FESEM) and DLS.

4.2.3 SL with a photomultiplier tube

A photomultiplier tube was positioned in front of a well (obtained from a 24-well polystyrene plate from Thermo Scientific) containing 1 mL of the sample consisting of Milli Q bidistilled water or the water suspension of amine-functionalized ZnO NCs at different concentrations of 50, 100, and 200 μg/mL. To perform sonication, the sample well was placed in contact with a commercial ultrasonic transducer with a planar geometry (LipoZero G39, Globus) through a thin layer of ecographic coupling gel (Stosswellen Gel Bestelle, ELvation Medical GmbH). The ultrasonic transducer was operated at a frequency of 1 MHz, duty

cycle (DC) of 100%, and different output powers (0.3, 0.6, 0.9, and 1.2 W/cm^2 corresponding to 10, 20, 30, and 40% of the maximum output power, respectively). The sonoluminescence-derived light emission was detected after few seconds of irradiation using a Hamamatsu R7400 photomultiplier tube (PMT) driven by a high voltage power supply (800 V). To exclude any possible temperature increase, each sample was stored in a fridge at 4 °C until use.

4.2.4 SL spectroscopic signal with a UV−Vis Spectrometer

The light emission produced from the well containing b.d. water, ZnO-NH_2 NCs (200 μg/mL) water solution or SiO_2-NH_2 NPs (200 μg/mL) water suspensions, was acquired using a multicore optical UV−vis fiber connected to a monochromator (Acton SP 2300), with the setup depicted in Figure 13-a. The well was coupled to the US probe with ecographic gel. The monochromator was equipped with a grating blazed at 300 nm (150 g/mm), giving a final wavelength resolution of 1.2 nm; the spectral signal was collected by a CCD camera (Princeton LN) operating at −90 °C. To optimize the signal/noise ratio, 120 s acquisition was collected for each spectrum. The ultrasound irradiation power was varied from 20 to 80% of the maximum power of the ultrasonic transducer, i.e., from 0.6 to 2.4 W/cm^2, duty cycle (DC) equal to 100%, and 1 MHz of frequency. SL spectra were measured from the beginning of sonication.

The same apparatus and spectrometer settings were used to measure the light generation from the well when the water solution was saturated with gaseous argon. The cold (4 °C) b.d. water solution was saturated, fluxing Ar for 2 min, and then 2 mL was placed in the well. The solution was irradiated with US for 120 s at 0.9, 1.2, 1.5, 1.8 W/cm^2 and 100% DC at 1 MHz. An identical procedure was used when the water solutions contained ZnO-NH_2 NCs at a concentration of 200 μg/mL. he light spectra of SL emitted photons were collected for various media, i.e., physiologic solution (0.9 wt % NaCl), phosphate-buffered saline (PBS, Sigma), live-cell imaging solution (LCI, Molecular Probes, Invitrogen), complete cell culture medium (RPMI-1640, ATCC with 10 vol % fetal bovine serum, ATCC, and 1 vol % penicillin−streptomycin) for culturing cells *in vitro*, in the presence and absence of ZnO- NH_2 NCs at a concentration of 200 μg/mL. Measurements were conducted at 1.2, 1.5, and 1.8 W/cm^2, with 2 mL of liquid in the well and 120 s acquisition; each sample solution was maintained at 4 °C right before US irradiation. Each spectrum was analyzed with MATLAB software.

4.2.5 SL imaging

An imaging setup was also implemented to get more reliable data about the total (i.e., quantitative) emission produced by SL in these media. As depicted in Figure 13-b, in this case, all of the lights produced into the well were recorded directly on the CCD camera operating in a full chip mode to substantially perform an image of the emitted SL. The image of the well was collected onto the cooled CCD by means of an objective (Yashika lens, ML 28 mm 1:2.8), placed at the proper focal distance, and a mirror was positioned at 45°. Exposure time was set to 120 s, a volume of 2 mL of sample solutions was placed in the well and irradiated with US at different powers (from 0.9 to 1.5 W/cm^2) and 100% DC at 1 MHz. The tested samples were b.d. water, phosphate-buffered saline (PBS, Sigma), live-cell imaging solution (LCI, Molecular Probes, Invitrogen), and complete cell culture medium (RPMI-1640 with 10% fetal bovine serum, ATCC), as reported above. Each liquid was tested in the presence and absence of ZnO-NH_2 NCs. Each set of data was analyzed with MATLAB software to set the same reference scale to all of the images. For all of the images, the amount of illuminated pixels was calculated with MATLAB, considering a specific intensity range for each medium considered.

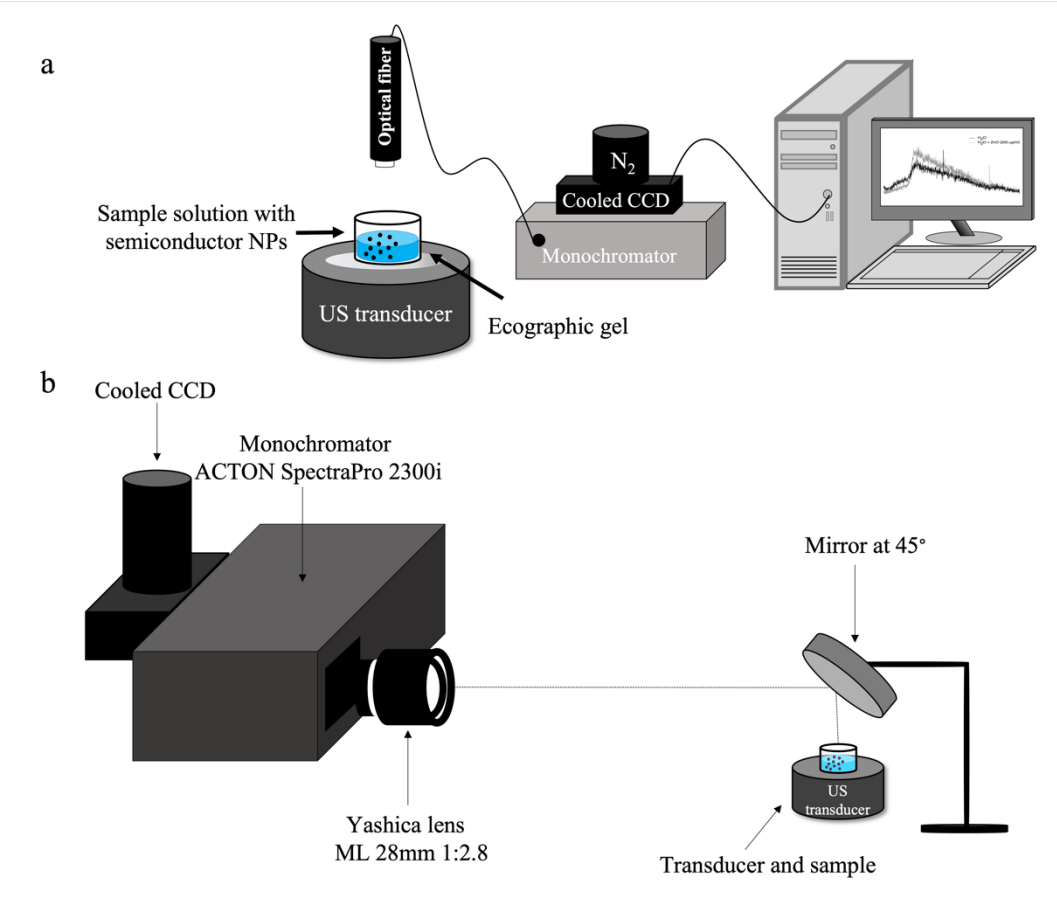

Figure 13 Scheme of the used setup for (a) sonoluminescence spectroscopy and (b) imaging

4.3 Results and discussion

ZnO NCs were synthesized by means of a microwave-assisted hydrothermal routeand the surface was then decorated with aminopropyl functional groups and characterized by conventional techniques like X- ray diffraction, TEM, DLS in ethanol, as well as ζ-potential measurements in water. All of these characterization results were already reported in section 2.3 and in previous publications[16,19,56,65] .

Monodispersed spherical SiO_2 NPs were obtained through the Stöber method[103] with a diameter of approximately 20 nm evaluated by FESEM and hydrodynamic diameter in ethanol of 70 nm, as shown in Figure 14, while ζ-potential in water was −22.4 mV.

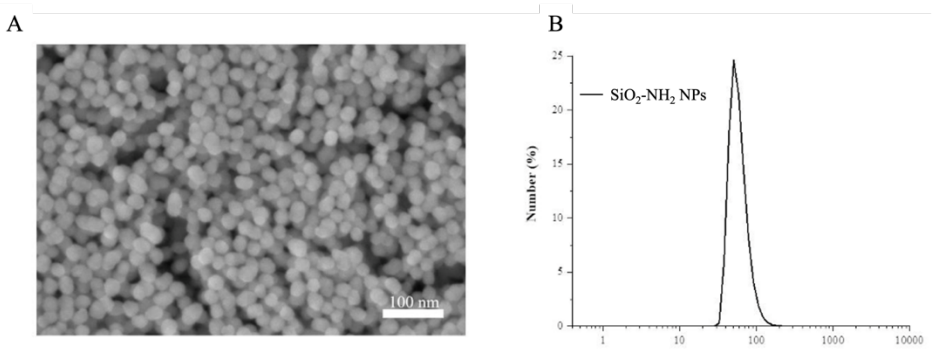

Figure 14 (A) FESEM image of SiO_2-NH_2 NPs. (B) DLS in ethanol of SiO_2-NH_2 NPs

4.3.1 Sonoluminescence experiments with photomultiplier tube

A first series of experiments were performed under dark conditions for the detection of light emission given by the irradiation of water-based solutions with the ultrasonic transducer. They were performed using a photomultiplier tube positioned in front of the well containing either simple water or the colloidal solution of amine-functionalized ZnO NCs.

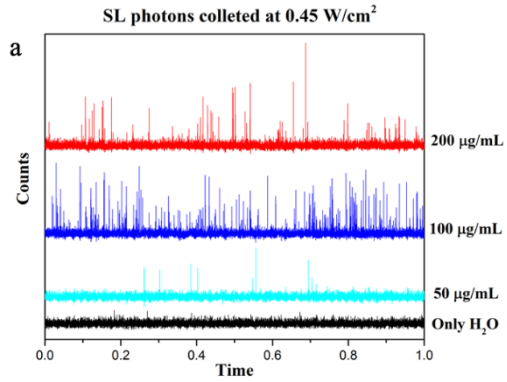

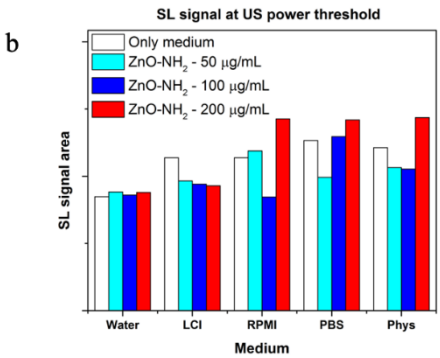

c

	H_2O	LCI	RPMI	PBS	Physiological Solution
ZnO-NH_2 0 µg/mL	0.6 W/cm²	0.45 W/cm²	0.6 W/cm²	0.6 W/cm²	0.6 W/cm²
ZnO-NH_2 50 µg/mL	**0.57 W/cm²**	0.45 W/cm²	0.6 W/cm²	0.6 W/cm²	**0.57 W/cm²**
ZnO-NH_2 100 µg/mL	**0.45 W/cm²**	0.45 W/cm²	0.6 W/cm²	0.6 W/cm²	**0.45 W/cm²**
ZnO-NH_2 200 µg/mL	**0.45 W/cm²**	0.45 W/cm²	0.6 W/cm²	0.6 W/cm²	**0.45 W/cm²**

Figure 15 (a) SL photons collected by the photomultiplier tube in water at different concentrations of ZnO-NH_2 NCs. (b) Area under the SL spectra collected with the photomultiplier tube in different media at the US power threshold and different concentrations of ZnO-NH_2 NCs. (c) US power threshold (data in red) measured for different media and for different ZnO-NH_2 NC concentrations.

We defined the threshold of cavitation as the US intensity at which we start to measure spikes in the recorded spectrum due to light emission. The threshold for detecting the light emission in pure water was around 20% of the maximum power of the ultrasonic transducer (corresponding to 0.6 W/ cm^2). As expected, the presence of ZnO-NH_2 NCs is able to lower the cavitation threshold, as previously reported[56]. This effect allows us to detect the light emission at a lower power intensity (around 0.45 W/cm^2) with respect to pure water (Figure 15-a). By increasing the ZnO-NH_2 NC concentration, the detected photon counts increase. Some differences can also be observed in different media (either water, physiologic solution 0.9 wt % NaCl, phosphate-buffered saline, PBS, live- cell imaging fluid, LCI, or cell culture medium, RPMI), always depending on the NC concentrations (Figure 15-b). The different US power thresholds vary depending on the used medium and NC concentrations. For example, it has to be noted from Figure 15-c that the lowering threshold effect expected by ZnO NCs was almost absent when using PBS and cell culture medium RPMI as solutions. Further comments on the SL emission above 20% of the maximum power, i.e., above 0.6

W/cm^2, are unreliable since the data collected with the photomultiplier tube refer to very short timescales. Substantially, no differences can be found on the light emission obtained in water or with the ZnO-NH_2 nanocrystals. Moreover, the ZnO-NH_2 NC concentration seems to display a threshold at 0.45 W/cm^2, as observed in Figure 15-a, the maximum number of light events is obtained when the ZnO- NH_2 NC concentration is equal to 100 μg/mL. This effect can be ascribed to the formation of a bubble population with bigger dimensions than in the previous cases at lower ZnO-NH_2 NC concentrations. It could be promoted by the high number of nucleation sites and consequent coalescence phenomena, which, in turn, lead to a reduction of the sonoluminescent bubbles. This intriguing phenomenon was observed in almost all tested, except in RMPI. We propose that this different behavior in RPMI on the light emission, where no threshold of ZnO-NH_2 NC concentration is found, can be attributed to the limited number of nucleation sites, which are shadowed by proteins and other biomolecules present in this medium or adsorbed at the nanoparticle surface as a protein corona[105].

Focusing the attention on the SL signal obtained for each media at their respective US threshold, 200 μg/mL was the concentration at which the highest overall signal was obtained for three out of five tested solutions, as can be observed in Figure 15-b, which also confirms data showed in chapter 1 and 2. In view of these results, further experiments were conducted to investigate the UV−vis emission spectra of the detected sonoluminescence, using a fixed concentration of 200 μg/mL.

4.3.2 SL Spectra using a UV−Vis spectrometer

To get more insights on the SL emission in the presence of ZnO-NH_2 nanocrystals, an ad hoc setup for acquiring the UV−visible spectra of the SL was implemented, as schematized in Figure 13-a.

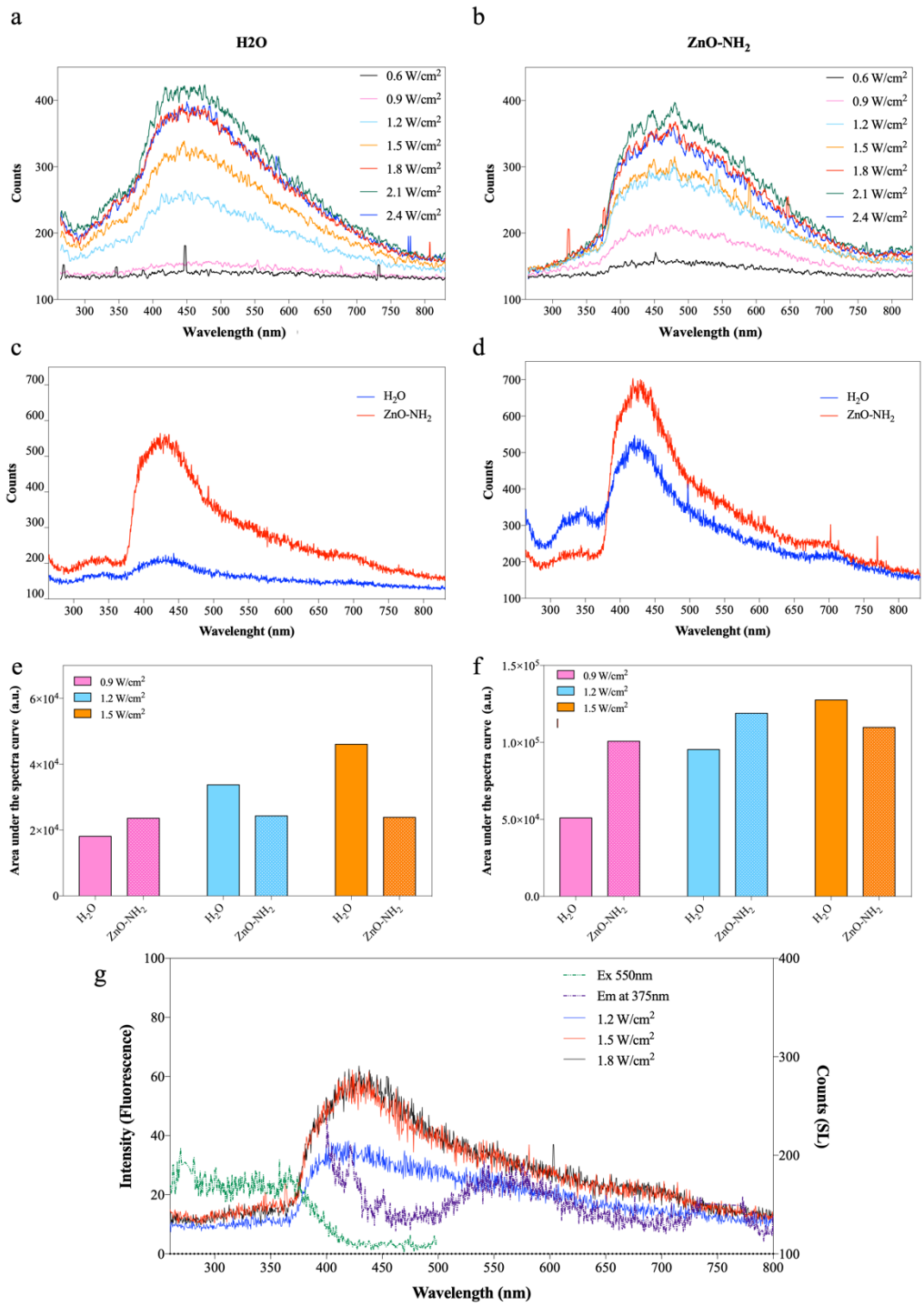

Figure 16 SL spectra in (a) pure water and (b) water-containing $ZnO\text{-}NH_2$ NCs at 200 µg/mL concentration for different US powers. SL spectra under argon-saturated conditions at (c) 0.9 W/cm^2 and (d) 1.2 W/cm^2, underlining the differences in the presence or absence of $ZnO\text{-}NH_2$ NCs. (e) Area under the

argon-saturated SL spectrum curve from 250 to 350 nm at different US powers with and without ZnO-NH2 NCs. (f) Area under the argon-saturated SL spectrum curve from 400 to 700 nm at different US powers with and without ZnO-NH_2 NCs. (g) SL spectra of water containing 200 μg/mL of ZnO-NH_2 NCs at different US powers related to the optical properties of NCs

To record the SL spectra, the ultrasonic power needed was increased from 20 to 80% of the maximum power, i.e., from 0.6 to 2.4 W/cm^2. In Figure 16-a, the SL spectra in pure water as a function of different US powers are shown, reporting a broad peak covering the whole UV and visible range with a maximum centered around 450 nm. A clear spectrum is visible from the US power intensity of 1.2 W/cm^2 (corresponding to 40% of the maximum US power).

In the presence of ZnO-NH_2 NCs, it is evident that already in the range 0.9−1.2 W/cm^2 of US power, the spectra are more intense with respect to the water case. Interestingly, the UV light component of SL is clearly absorbed by the ZnO-NH_2 semiconductor (Figure 16-b), showing a clear cut of the UV light range emission (from 250 to 350 nm) measured at all ultrasonic powers. It was thus decided to further examine this effect, investigating if the SL intensity increment due to the presence of ZnO-NH_2 NCs could be accomplished not only by a complete absorption in the UV range but also by a possible re-emission in the visible light region.

To verify this hypothesis, similar experiments were conducted under an argon-saturated atmosphere to get more intense light emissions. The obtained spectra in Figure 16-c,d strongly confirm the strong UV light absorption by ZnO-NH_2 NCs; however, a process of reemission is barely visible and, if present, is covered up with the remaining emission spectrum.

As a further analysis in this regard, both fluorescence excitation and emission spectra collected by a conventional spectrofluorimeter of the ZnO-NH_2 NCs in water were superimposed to the SL emission spectra obtained in the presence of ZnO-NH_2 in water at various US powers (from 1.2 to 1.8 W/cm^2 as US power). As shown in Figure 16-g, it is clear that the ZnO-NH_2 excitation range from 200 to 400 nm fairly coincides with the strong SL emission reduction. In contrast, the ZnO-NH_2 fluorescence emission in the range from 500 to 650 nm superimposes with the characteristic SL emission from the water system. By measuring the UV absorption spectrum of ZnO-NH_2 NCs in water, the band gap value is computed to be 3.32 eV, which is in fair agreement with the literature[10]. This result clearly

shows that ZnO-NH_2 is a wide band gap semiconductor and is able to absorb light in the UV range.

To further analyze the phenomenon, the areas underneath the SL emission spectra were calculated and evaluated in the different emission regions (i.e., UV, from 250 to 350 nm, and visible one, from 400 to 700 nm). Figure 16-e shows the area calculated under the curve of the SL spectra from 250 to 350 nm, which overlaps with the portion of the spectrum characterized by ZnO absorption. By increasing the US power, a direct increment of the SL signal in pure water is obtained, which likely corresponds to an increase of the absorption phenomena by ZnO-NH_2 NCs, which, in turn, could explain the reduction of the area under the curve in the presence of NCs (and in this portion of the spectrum) for 1.2 and 1.5 W/cm^2 irradiation power. For 0.9 W/cm^2 instead, we observe a threshold. Here, the generation of SL photons in pure water is very low; therefore, the addition of 200 μg/mL of ZnO-NH_2 NCs increases the SL emission but the absorption of the generated photons cannot be appreciated. The threshold observed at 0.9 W/cm^2 is particularly evident looking at the portion of the spectrum corresponding to the emission of ZnO, i.e., from 500 to 650 nm. In Figure 16-f, the areas under the SL spectrum are also calculated for different US powers from 400 to 700 nm. At 0.9 W/cm^2, the amount of SL photons produced is weak when compared to the one in the presence of the NCs under the same operating conditions. This effect means that in pure water, it is difficult to reach the threshold for SL, but when ZnO-NH_2 NCs are in solution, the SL signal increases. The same behavior can be appreciated at 1.2 W/cm^2. At 1.5 W/cm^2, the SL signal generated from pure water is higher, and the SL threshold is largely reached and comparable with the one obtained in the presence of ZnO-NH_2 NCs; therefore, the difference between the SL produced in the two cases is no longer visible.

The specific role of ZnO-NH_2 NCs as the semiconductor nanoparticles is more evident when considering different materials. ZnO-NH_2 NCs were thus substituted with silica nanoparticles (SiO_2-NH_2) dispersed in water, using the same US irradiation conditions and spectral acquisition parameters. It should also be noted that SiO_2 nanoparticles were functionalized with aminopropyl groups.

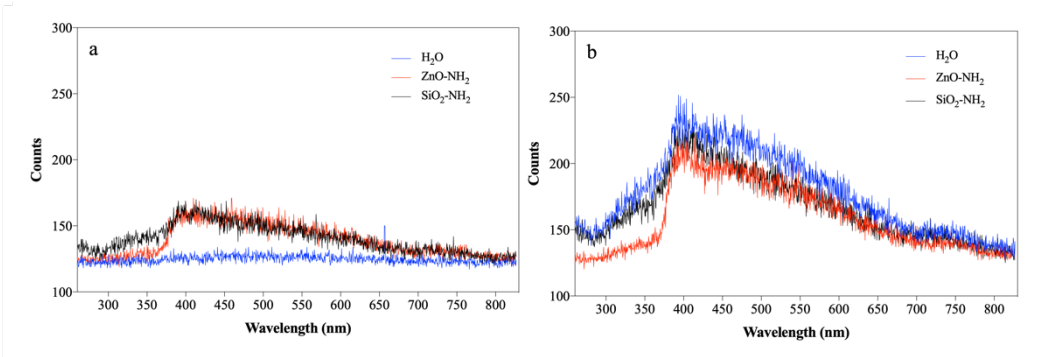

Figure 17 Sonoluminescence emission spectra acquired at (a) 0.9 W/cm^2 and (b) 1.8 W/cm^2 for 2 min comparing 2 mL solutions of pure water (black curves), water-containing ZnO-NH2 NCs at 200 µg/mL concentration (red curves), and water-containing silica (SiO_2-NH_2) nanoparticles at 200 µg/mL concentration (blue curves).

The recorded spectra are reported in Figure 17 at both 0.9 and 1.8 W/cm^2 as US power, as representative examples. It is clear that the SiO_2-NH_2 nanoparticles also act as cavitation enhancers since they generally increase the SL detection at low US powers (Figure 17-a). However, no particular differences in the SL spectrum features can be observed between pure water and the SiO_2-NH_2 colloidal dispersion (see Figure 17-b), as opposed to the dispersion with ZnO-NH_2 NCs, where the cutoff of the SL emission in the UV range is evident.

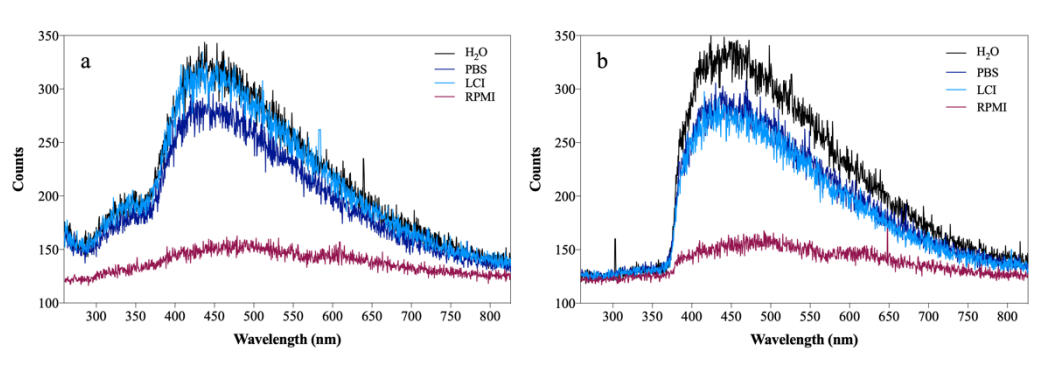

Figure 18 SL spectra obtained from various biologically relevant media like phosphate-buffered saline (PBS) and live-cell imaging (LCI) used under fluorescence microscopy for imaging of living cells and cell culture medium (RPMI) in comparison with SL from pure water (a) in the absence of nanoparticles dispersed in the solution and (b) with ZnO-NH_2 NCs at 200 µg/mL concentration. US power = 1.5 W/cm^2.

To explore the potential applications of SL for biological imaging, in Figure 18, we report several spectra obtained in different biologically relevant media irradiated at 1.5 W/cm^2 of US power both with (Figure 18-b) and without (Figure

18-a) ZnO-NH_2 NCs. Irrespective of the medium used, the cutoff in the UV range produced by the presence of semiconducting NCs is evident. It is thus possible to confirm the capability to have not only an SL emission from various water-based media but also that the presence of ZnO-NH_2 NCs can impart a clear signature to the SL spectrum. Again, this is a verification of the potentialities in using the ZnO-NH_2 NCs as contrast agents for sonoluminescence.

As already observed in the previous experiments with the photomultiplier tube, the emission intensity decreases and its spectrum modifies when using complex media rich in proteins and other biomolecules, such as cell culture media, while comparable high intensities and spectra profiles are obtained with buffers such as PBS and LCI. This is another proof supporting the idea that ZnO-NH_2 nanocrystals can be used as contrast agents to produce enhanced sonoluminescence signals in biologically relevant fluids, and further experiments in the presence of living cells can be carried out in the future to prove this concept.

4.3.3 Sonoluminescence imaging

The data obtained with the CCD camera connected to the spectrofluorimeter give information on the spectral distribution of SL photons generated during a few seconds of ultrasound irradiation. Despite the fact that the single sonoluminescence phenomen- on occurs in a very short period of time, i.e., less than 1 ns, recording the amount of SL photons produced during a larger amount of time could be useful to evaluate the overall generation of light and its spatial distribution inside the sample, giving quantitative information on SL in the tested samples.

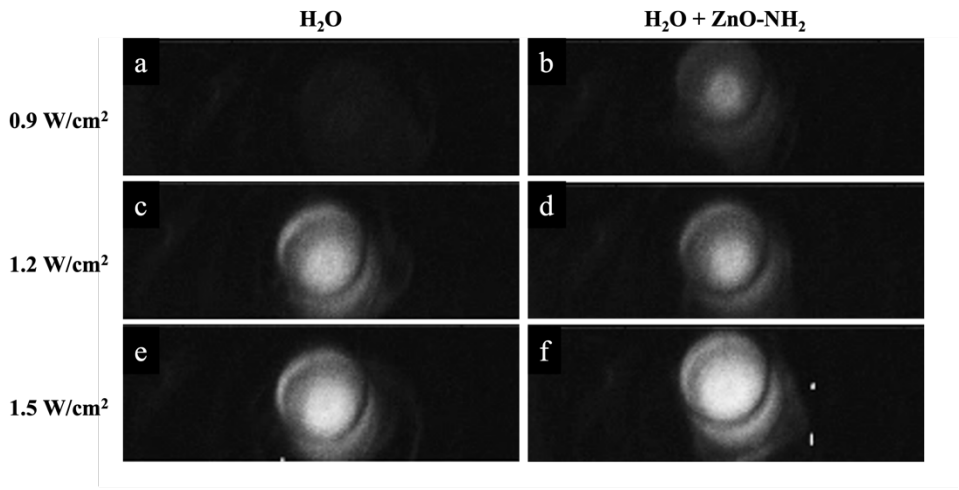

Figure 19 SL imaging in pure water at (a) 0.9 W/cm^2, (c) 1.2 W/cm^2, and (e) 1.5 W/cm^2, and in water-containing ZnO-NH_2 NCs (concentration: 200 µg/mL) at (b) 0.9 W/cm^2, (d) 1.2 W/cm^2, and (f) 1.5 W/cm^2

To perform these measurements, a different experimental configuration has been set, as schematized in Figure 13-b. To acquire an image of the sample well, the SL emitted light was collected using the cooled CCD camera as an imaging recorder. A mirror tilted at 45° above the sample and a standard camera objective allowed us to create an image of the well on the CCD sensor. By design, camera objectives filter out ultraviolet light, therefore the images acquired refer only to the visible portion of the spectrum. By comparing the acquired images at different US power intensities, it is evident how the SL light emitted in the presence of ZnO-NH_2 NCs is higher than that in their absence. Indeed, Figure 19 clearly shows the threshold of SL at 0.9 W/cm^2 of US power, where sonoluminescence is actually visible only for the nanocrystal water dispersion. This finding is also supported by the total number of illuminated pixels calculated for the images obtained at 0.9 W/cm^2 US power, which is four times higher in the presence of ZnO-NH_2 NCs (435 pixels) than the total number of pixels in pure water (1 pixel).

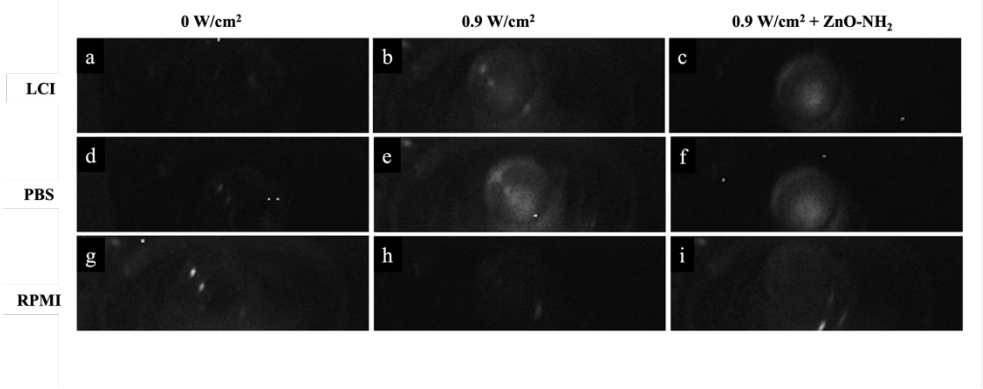

Figure 20 SL imaging in biologically relevant fluids: (a) Live-cell imaging buffer without US irradiation (0 W/cm^2) at (b) 0.9 W/cm^2 and (c) 0.9 W/cm^2 in the presence of ZnO-NH_2 NCs at 200 µg/mL concentration; (d) PBS at no US irradiation (0 W/cm^2); (e) at 0.9 W/cm^2 and (f) 0.9 W/cm^2 in the presence of ZnO-NH_2 NCs at 200 µg/mL concentration; (g) cell culture medium RPMI at no US irradiation (0% power) at (h) 0.9 W/ cm^2 and (i) 0.9 W/cm^2 in the presence of ZnO-NH_2 NCs at 200 µg/mL concentration

We also acquired the images in different biological media, such as cell culture media RPMI, live-cell imaging, and PBS buffers (Figure 20). We observed SL emission differences even in these cases with or without the ZnO-NH_2 NCs. The major difference has been found using the live-cell imaging buffer, where the number of illuminated pixels is twice higher in the presence of ZnO-NH_2 NCs with respect to the pure media.

This is attributed to the limit of the experimental condition, i.e., only 30% of the maximum US power (0.9 W/cm^2) was tested, and the presence of various salts in the medium. For example, using PBS, the SL light emission is already high without ZnO-NH_2 NCs, revealing that, for each medium, different operating conditions have to be set to exploit the SL generation enhancement and exploit ZnO-NH_2 nanocrystals as nanocontrast agents.

4.4 Conclusions

Biological applications of SL have been debated over the last 20 years[106], and more recently, studies on ultrasonic activation of light-sensitive nanoparticles for therapy have been published[107].However, the first data were not too accurate and, till now, a careful analysis of the light emission spectra and absorption effect from nanoparticles or organic molecules in biological media is still lacking. In this chapter, it is demonstrated the ability of ZnO-NH_2 NCs to enhance the SL

emission under low-intensity ultrasound irradiation revealing their potential use as a nanocontrast agent for therapeutic applications.

The measurements reported here evidenced the increase of SL emission, as the ZnO-NH_2 NC concentration in aqueous solutions increases, and the decrease of the US power necessary to detect the SL signal when NCs are present. Furthermore, this phenomenon has been observed also in biological cell culture media like LCI. An influence of the ZnO-NH_2 NC concentration on the light emission detected by PMT has been observed and it could be explained by the well-known effects occurring in liquids exposed to higher intensity ultrasounds (i.e., formation of bigger cluster of bubbles, the consequent acoustic absorption/shielding of the collapsing events, lowering or threshold appearance on the total light emission as the case for the acoustic emissions, noise spectra, and so on). The concentration of 200 μg/mL was the one at which the highest overall signal was measured for three out of five tested solutions for a fixed value of US power (0.9 W/cm^2), which confirms the result obtained in chapter 1 and 2.

SL spectra displayed a specific shape in the presence of our ZnO-NH_2 NCs: the UV light component of SL is evidently absorbed by the semiconductor, resulting in a cutoff of the UV range emission. However, at very low acoustic intensities, a slight increase of visible contribution seems to be present and, to confirm it, experiments with the Ar saturate solution have been carried out. This phenomenon was observed in water as well as in different media for biological applications, such as LCI and PBS.

Finally, the elaboration of the SL optical images recorded in the visible region allowed to get more insights into this effect. As expected, looking also at the spectra in Figure 16-a,b at the intensity range of 0.9−1.5 W/cm^2, the SL emission was more intense, or even “visible only”, when ZnO-NH_2 NCs were present in the solution.

These results clearly indicate an SL generation enhancement by ZnO-NH_2 NCs, proposing them as nanocontrast agents not only in water solution but also in buffered media like PBS and LCI. The ability of NCs to increase the SL emission at low acoustic intensities and their potential uptake[65,97,108] by living cells open the use of these nanocontrast agents in the biomedical field.

Chapter 5

Zinc Oxide nanocrystals combined with high-energy shockwaves: new combined treatment for cancer cells

This chapter has been taken from the open-access publication[65], as stated in the declaration of this dissertation.

5.1 Introduction

Among various innovative new approaches to fight cancer, nanomedicine has attracted many interests[109]. The application of nanomaterials for health and medicine can lead successful advancements in diagnosis and therapy[110], particularly in the delivery of cargo molecules[111], or through their direct use to damage cancer cells[112]. Such nanotools indeed could be intrinsically toxic[113], e.g., through the release of metal ions, or could be remotely activated to achieve cell death, as in the photothermal and photodynamic therapies[114]. Zinc Oxide (ZnO) in particular has raised researchers' interest thanks to its biocompatibility and peculiar piezoelectric and semiconductive properties[15,115], useful for its exploitation for imaging[116] , as underlined in the previous chapter, biosensing[117–119], tissue engineering[120] and drug delivery[121,122] purposes. Remarkably, ZnO

nanoparticles are also studied for their intrinsic anticancer properties thanks to their selective toxicity toward cancer cells[113]. ZnO cytotoxicity indeed is related to ROS, as largely described above, and production and Zn^{2+} ions release[15,113,115,123]

SDT is based on the activation through US of an organic molecule, called sonosensitizer, to induce cells to death. US is a mechanical pressure wave with the outstanding properties of deep tissue penetration and focusing[21,124]. The passage of an US wave through a tissue can exert two different consequences: thermal and non-thermal effects. Even though US thermal effects can be exploited to achieve tumor thermoablation, as in the high intensity focused US (HIFU) therapy, SDT investigations are generally based on the non-thermal ones[44]. Non-thermal effects consist in a vast group of phenomena, as acoustic cavitation[44].

Some groups proposed to employ high-energy SW to activate the organic molecular sonosentizer minimizing the US-related thermal effects, enhancing instead non-thermal ones[124]. SW indeed are sonic pulses characterized by a first very rapid positive pressure phase (up to 100 MPa) that lasts for 0.5– 3 μs, followed by a tensile wave characterized by a negative pressure (−10 MPa) for 2–20 μs, then recovering ambient values[124,125]. SW has been evaluated to enhance the intracellular drug delivery[126,127] and for the activation of various porphyrin complexes[126,128–130]. However, to our knowledge there are no investigations exploiting the non-thermal effect of SW assisted by solid nanoparticles. The combined use of SW with solid nanoparticles can induce the great above-mentioned advantages, i.e., improve the SW efficacy. This is achieved thanks to the enhanced cavitation effects produced by the presence of solid nanoparticles, as described in previous chapters. Furthermore, the use of ZnO nanoparticles and SW to induce cancer cell death has not already been reported in the literature.

The highly efficient killing capability of amino-propyl functionalized ZnO nanocrystals (ZnO NCs) in combination with SW for the treatment of cancer in an *in vitro* study is demonstrated in this chapter.

The cytotoxicity and internalization of ZnO NCs were evaluated in cervical adenocarcinoma KB cells, as well as the safety of the SW treatment alone. Then, the remarkably high cytotoxic combination of ZnO NCs and SW was demonstrated, comparing the effect of multiple (3 times/day) SW treatments to a single one. At last, preliminary tests to undertake the mechanism of the observed

combined effect were carried out. The obtained results highlight the effective anticancer applicability of the proposed nanomedicine treatment, based on the combined effect of ZnO NCs and highly intense and focalized mechanical pressure waves.

5.2 Materials and methods

5.2.1 ZnO-NH_2 NCs synthesis and functionalization

Zinc Oxide Nanocrystals were synthesized, functionalized and characterized as reported in sections 1.2.1 and 2.2.2.

5.2.2 Cell lines

Cervical adenocarcinoma KB cell line (ATCC® CCL17TM) was grown in Eagle's Minimum Essential Medium (EMEM, Sigma) supplemented with 10% heath inactivated fetal bovine serum (FBS, Sigma), 100 units/mL penicillin and 100 µg/mL streptomycin (Sigma) and maintained at 37 °C, 5% CO_2 atmosphere.

5.2.3 Cytotoxicity test

$1.5x10^3$ cells/well were plated in replicates (n=4) into 96-well culture plates (TC-Treated, Corning) and incubated at 37 °C, 5% CO_2. 24 h later, the culture medium was replaced with fresh medium containing different concentrations of ZnO NCs (5, 10, 15, 20, 25, 50 µg/mL). The ZnO NCs stock solution (1 mg/mL) was sonicated in a water bath (Labsonic LBS 2-10, Falc Instrument) at 40 kHz for 10 minutes before the preparation of the aliquots. After the incubation time, cell proliferation was assessed by the WST-1 cell proliferation assay. 10 µL of the WST-1 reagent (Roche) were added to each well and after 2 h incubation, the formazan absorbance was measured at 450 nm by the Multiskan GO microplate spectrophotometer (Thermofisher Scientific) using 620 nm as reference wavelength. Control values, represented by cells incubated with medium alone, were set at 100% viable and all values were expressed as a percentage of the control. Cell viability was measured after 5, 24, 48 and 72 h of incubation with ZnO NCs.

5.2.4 Internalization assay

ZnO NCs uptake in KB cells was measured with a Guava Easycyte 6-2L flow cytometer (Merck Millipore). Briefly, cells were seeded into a 6-well TC treated culture plate (Corning) with cell culture medium 24 h before the assay ($1x10^5$ cells/well). Then, culture medium was replaced with freshly prepared medium containing ZnO NCs labelled with Atto633-NHS (10 μg/mL). A control well, containing untreated cells, was on the contrary filled with fresh medium without NCs. ZnO NCs progressive uptake was then measured at different time points (5-24 h). Cells were washed twice with phosphate saline buffer (PBS), trypsinized and centrifuged at 130 g for 5 minutes. Cell pellets were then re-suspended in 1 mL PBS and immediately analyzed with the flow cytometer. $1x10^4$ gated events were considered excluding cellular debris, characterized by low forward scatter (FSC) and side scatter (SSC), with a flow rate of 0.59 μL/s. Results are shown as the percentage of positive events, analyzed with Incyte Software (Merck Millipore). In particular, a threshold of positivity upon control cell histogram was set. The percentage of events characterized by a shift in Red-R fluorescence intensity (emission filter 661/15 nm), due to the Atto633 attached on NCs surface, was thus measured. Representative histograms were then graphed with FCS Express Software (DeNovo Software).

5.2.5 Single SW treatments

KB cells, seeded into a treated culture flask, in exponential growth phase, where trypsinized and $5x10^5$ cells per well were plated in culture medium into a 96-well plate (Corning) for the SW treatment as described by others[126,131,132].

SW was administered by the high-energy focalized SW device PW^2 (R.Wolf, ELvation Medical). According with the previously mentioned literature, energy flux density ranges, corresponding to the energy at the focal point, were set, i.e. 0.15-0.22-0.3-0.4-0.52 mJ/mm^2, corresponding to positive peak pressures (PPP) of 29.1, 39.4, 50.3, 61.7 and 74.1 MPa. Furthermore, 500 or 1000 shots were given for each treatment (4 shots/s). The therapy source FB10G4, equipped with a 4 cm thick pad, was employed to give the SW treatment. The 96-well plate containing KB cells was directly put on the top of the cap covered by a thin layer

of ultrasound gel (Stosswellen Gel 144 Bestelle, ELvation Medical) to minimize SW attenuation. Immediately after the treatment, $2x10^3$cells were seeded in 100 µL of culture medium in replicates (n=4) in a 96-well culture plate for the WST-1 proliferation assay. Control wells containing the untreated cells, plated in the same conditions of the SW-treated samples, were also prepared. As before, the values kept from the untreated cells were set at 100% viability.

The experiments were then repeated, following the same protocol, preparing two flasks of KB and pre-incubating one with a freshly prepared solution of ZnO NCs (10 µg/mL per 24 h incubation) for the evaluation of the ZnO NCs-SW combined effects. In this case, an additional control with KB cells, incubated with ZnO NCs but not irradiated with SW, was prepared.

5.2.6 Multiple SW treatments

Since adherent cells bear multiple detachments, the protocol employed for the single treatment carried out from the literature was modified similarly to what reported by Marino et al.[133,134] for the multiple treatments. Briefly, $1.5x10^3$ cells were seeded into 100 µL of culture medium in a 96-well culture plate in replicates (n=4). 24 h later, two wells were incubated with ZnO NCs (10 µg/mL) while the other two were re-filled with fresh medium. After 24 h, all the wells were washed with PBS and re-filled with 100 µL fresh culture medium. SW treatments were then performed (3 times/day, one every 4 h). 24 h after the last treatment, cell viability was carried out with the WST-1 proliferation assay.

5.2.7 ROS scavenging analysis

The observed cell death upon the sonosensitizer activation is frequently related in the literature with the ROS production[19,44]. For this reason, the experiments with ZnO NCs and multiple SW treatments were repeated by pre-incubating KB cells with two different antioxidants in order to evaluate ROS involvement in cell proliferation upon ZnO NCs incubation and SW treatment. N-acetylcysteine (NAC, Sigma) and mannitol (MAN, Sigma) were chosen as ROS scavengers for this purpose.

It is reported that NAC could enhance cell antioxidant properties through increasing intracellular GSH and interacting with radicals such as H_2O_2 and $OH^{\bullet}$ [135]MAN is instead an $OH^{\bullet}$ scavenger[136] .

For NAC the successfully employed protocol by Brazzale et al[137] was followed. Briefly, 1 h before the first SW treatment, but already after the 24 h incubation with ZnO NCs, cell medium was replaced with a solution composed by culture medium with the addition of 5 mM NAC. This solution was discarded before the first SW treatment and cells were resuspended in culture medium (100 μL). Cell viability was measured with the WST-1 assay 24 h after the last treatment, as described before. In order to exclude potential toxic effects of the antioxidant alone, a well with untreated cells without NAC was also prepared.

For MAN the concentration was 0.1 M for 30 minutes incubation before the SW application[138].

5.2.8 Kinetic evaluation of cell death

The kinetic evaluation of cell apoptosis and necrosis was performed with the RealTime-Glo Annexin V Apoptosis and Necrosis Assay (Promega). Plate signals were collected with the microplate reader Glomax (Promega).

KB cells were plated in a black 96-well plate with clear bottom (Corning) following the same protocol already mentioned for the SW multiple treatments. Control wells were also prepared with culture medium to define the background of the luminescence and the fluorescence derived from the medium without cells. These values were subtracted from the test samples as recommended by the manufacturers.

The background of the samples was measured, then 100 μL of the reaction mix containing all the substrates for the reaction were added and immediately a second reading was performed. Then the signals were measured after each SW treatment and 24 h after the last one to have a comparison with the WST-1 viability tests.

5.2.9 Statistical analysis

Measurement data were presented as mean ± standard error mean (SEM). Each assay was done at least in duplicate. One-way analysis of variance (ANOVA) was performed with the Sigmaplot software. ***$p<0.001$, **$p<0.01$ and *$p<0.05$ were considered significant. A detailed report of the statistical

analysis performed on each experiment is reported in the Supplementary Information.

5.3 Results and discussion

5.3.1 NPs Characterization

ZnO NCs characterization, post and prior to the functionalization, is described in previous section 2.3.

5.3.2 Cell viability and internalization

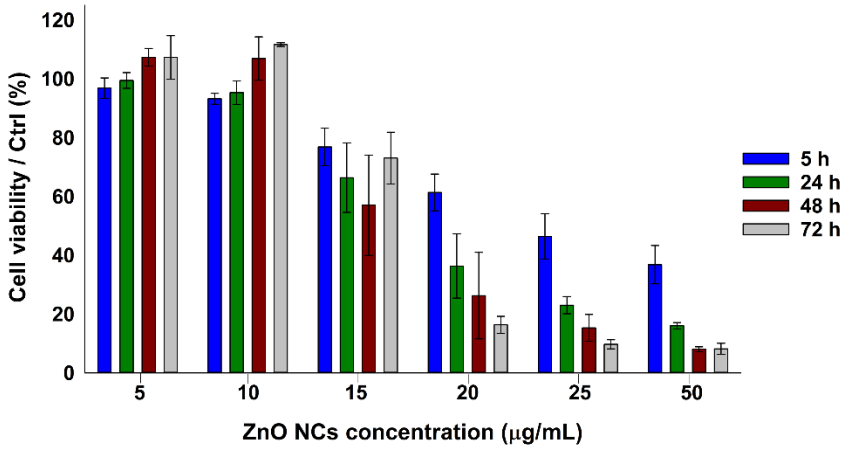

Figure 21 Cytotoxicity on KB cells at different time points detected with the WST-1 assay. KB cells were incubated with different ZnO NCs concentrations (5, 10, 15, 20, 25, and 50 μg/mL). Cell viability was measured after 5, 24, 48, and 72 h. Bars represent mean ± SEM percentages of cell viability with respect to the control cells, n = 3

The viability of KB cancer cells after the incubation with different concentrations of ZnO NCs (5, 10, 15, 20, 25, 50 μg/mL) was assessed at different time points, as depicted in Figure 21, i.e. after 5 h, 24 h, 48 h, and 72 h. A dose dependent response was indeed observed, with a progressive decrease of cell viability increasing the concentration of ZnO NCs and confirming the previous results obtained at 24 h employing the same NCs[16]. ZnO NCs at the concentrations of 5 and 10 μg/mL resulted to be non-toxic for KB cells, while the mean percentages of cell viability progressively decreased starting from 15 μg/mL at all the considered time points. Moreover, the differences in cell viability between the safest conditions, i.e. 5-10 μg/mL, and the other ones continued to increase starting from 5 h of incubation. While a mild proliferative effect was observed at the lowest dosages at 48 h, cells incubated with 20-25-50 μg/mL of

ZnO NCs never recovered and their viability drastically dropped after 24, 48, and 72 h. Interestingly, after 72 h a recovery of cells incubated with 15 μg/mL was evidenced, with percentages of cell viability increasing from 57±17 % at 48 h up to 73±9 % at 72 h. The complete statistical analysis of these data is reported in the Supplementary Information.

ZnO NCs toxicity could be ascribed to two main events: the Zn^{2+} ions release and ROS production, as previously mentioned[15]. The increase of NCs concentration exasperated both the reported effects, resulting in a marked decrease of cell growth.

The observed proliferative effect was also yet reported. Indeed, Zn^{2+} ions are involved in many cellular pathways, and thus a low dosage might enhance cell proliferation inducing key signal proliferation pathways[139] .

Dedicated analyses of NC internalization were performed with the flow cytometry, detecting the Atto633 dye labelled ZnO NCs fluorescence inside the cells at progressive time points (5 and 24 h). In particular, the internalization of ZnO NCs-Atto633 at the concentration of 10 μg/mL was monitored, as it was the highest safe concentration in the previous cytotoxicity analysis. As it is possible to observe in Figure 22, a progressive increase of cells presenting a shift of the Red-R intensity, due to the NCs internalization, was recorded. A marked shift of the green curve, representing cells incubated with ZnO NCs-Atto633 for 5 h was also observed with respect to the black curve, corresponding to the untreated cells signal, suggesting that NCs internalization occurred quite rapidly. After 24 h of incubation, the percentage of cells internalizing the NCs increased, as noticeable from the orange curve, representing the signal of cells incubated with ZnO NCs-Atto633 at 10 μg/mL for 24 h. In particular, the percentage of positive events increased from 85 ± 3 % at 5 h to 98.0 ± 0.4 % at 24 h.

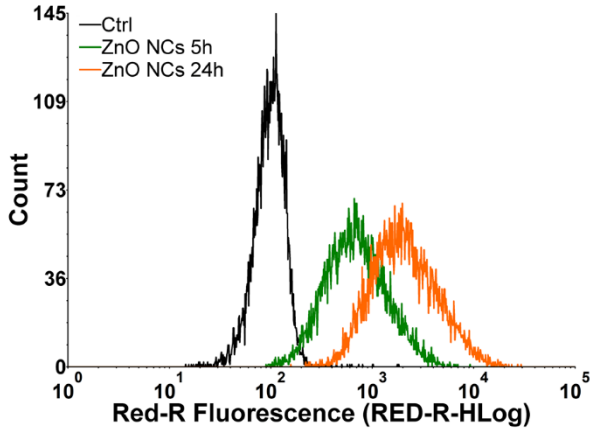

Figure 22 Representative curves of ZnO NCs uptake in KB cells at different dosages and at different time point (5–24 h) of incubation. Black curve represents untreated cells signal, green curve regards signal generated by cells incubated with ZnO NCs 10 µg/mL for 5 h and orange one by the cells incubated with ZnO NCs 10 µg/mL for 24 h.

These results suggest that ZnO NCs were rapidly internalized in KB cells and, upon a longer incubation time, i.e. 24 h, almost all cells have internalized the highest amount of NCs. This result is indicated by the higher fluorescence intensity of these cells, as it is possible to observe in the pronounced shift of the orange curve with respect to the green one.

5.3.3 SW treatments

After the ZnO NCs characterization and the first tests to assess their cytotoxicity and internalization, the non-lethal dose of 10 µg/mL was identified as a safe condition for further investigations in combination with SW. In addition, 24 h seems to be a suitable incubation time, because almost all the considered cells presented a shift in fluorescence intensity due to NCs internalization at this time point.

For the tests in combination with SW, the effects of single toward multiple SW treatments were compared.

The analyses started looking for the safest conditions for KB cells under SW stimulation in absence of ZnO NCs. Based on the previous literature investigations[126,128,131,132], a fixed number of shots (500 or 1000) was adopted, varying the PPP (29.1, 39.4, 50.3, 61.7 and 74.1 MPa). The cell viability decreased at increasing either the SW energies (from 29.1 MPa up to 79.1 MPa) or the number of shots (either 500 or 1000 shots), as evidenced in Figure 23.

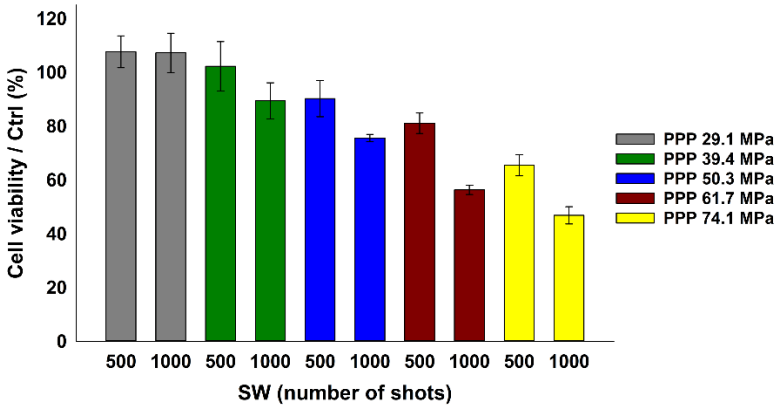

Figure 23 KB cell viability upon SW treatment measured by the WST-1 proliferation assay. KB cells were treated with SW characterized by a different PPP and number of shots, as indicated in the bars legend. Results are shown as mean ± SEM percentage of cell viability with respect to control cells. n = 3

To prove the combined effects between the SW and the ZnO NCs, the conditions where the cell viability were closest to 100 % with the sole stimulation (either SW alone or ZnO NC alone) were then selected. Cells were pre-incubated for 24 h with ZnO NCs at the concentration of 10 µg/mL and then treated with SW (ZnO NCs + SW). 24 h after the SW irradiation, cell viability was measured. The viabilities of untreated cells (Ctrl), cells incubated with ZnO NCs but not treated with SW (ZnO NCs) and cells treated only with SW in absence of ZnO NCs (SW) were also kept for comparison. The employed SW parameters were 29.1 MPa, 1000 shots (Figure 24-A), 39.4 MPa, 500 shots (Figure 24-B), 39.4 MPa, 1000 shots(Figure 24-C) and 50.3 MPa, 500 shots (Figure 24-D).

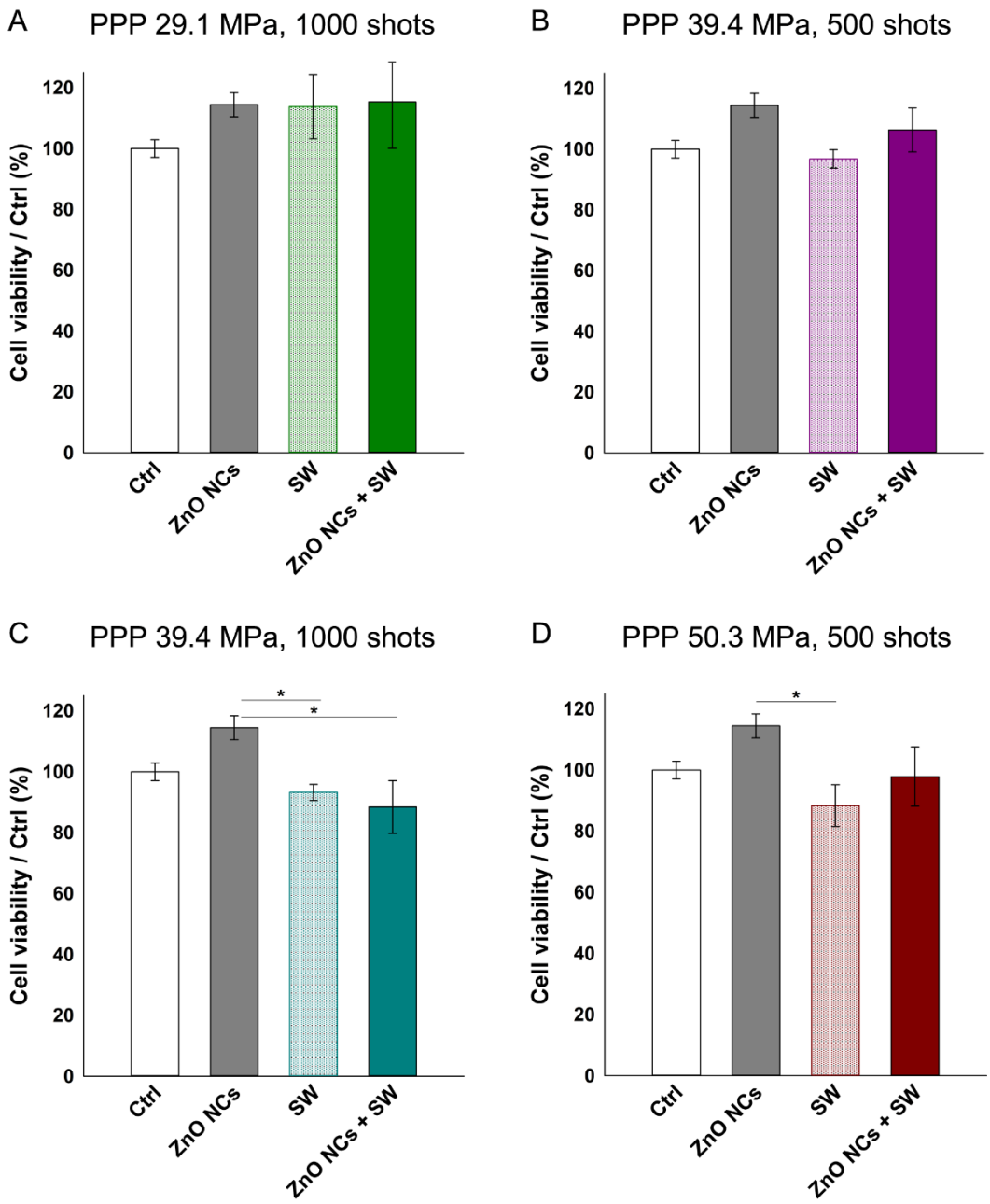

Figure 24 Study on the possible combined effect of ZnO NCs and SW. Four different samples were prepared per assay. Control untreated cells (Ctrl), cells only incubated with 10 µg/mL ZnO NCs for 24 h (ZnO NCs), cells treated with SW (SW) and cells incubated with NCs and treated with SW (ZnO NCs + SW). Cells were treated with SW at: (A) 29.1 MPa, 1000 shots, (B) 39.4 MPa, 500 shots, (C) 39.4 MPa, 1000 shots, (D) 50.3 MPa, 500 shots. Cell viability was recorded 24 h after the SW treatment with the WST-1 proliferation reagent. Data are reported as the cell viability with respect to the control referred as the 100%. Results are shown as mean ± SEM. n = 4. *$p < 0.05$

Interestingly, no differences in cell viability were evidenced between SW and ZnO NCs + SW cells, indicating that there was not a combined effect between ZnO NCs and SW with the single treatment modality.

Multiple US treatments are routinely employed alone or in combination with drugs or nanoparticles in several *in vitro*, *in vivo* and in clinical trials studies[140–145]. Marino et al. obtained positive results in terms of cell death combining barium titanate nanoparticles and multiple US treatments in an *in vitro* study. In these investigations, cells were treated 1 h/day for 4 consecutive days[133,134]. This method was indeed applied here with some modifications and using ZnO NCs and SW on KB cells. The multiple SW dose was given by irradiating the KB cells three times in a day (a treatment every 4 h). 24 h after the last irradiation, cell viability was measured with the WST-1 assay as before.

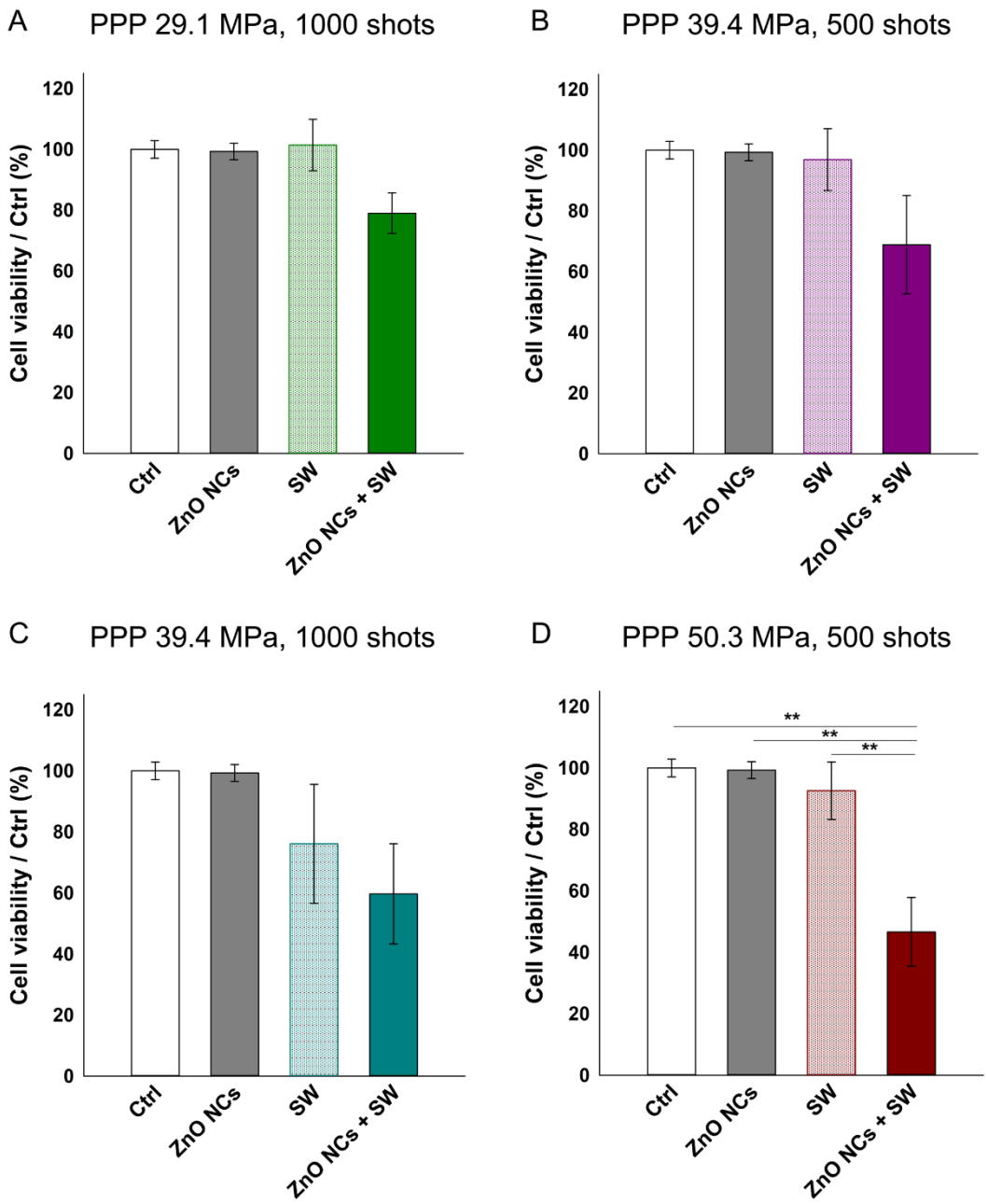

Figure 25 Study of the possible combined effect of ZnO NCs and multiple SW treatments (3 times/day). Four different samples were prepared per assay. Control untreated cells (Ctrl), cells only incubated with 10 µg/mL ZnO NCs for 24 h (ZnO NCs), cells treated with SW (SW) and cells incubated with NCs and treated with SW (ZnO NCs + SW). Cells were treated with SW at: (A) 29.1 MPa, 1000 shots, (B) 39.4 MPa, 500 shots, (C) 39.4 MPa, 1000 shots, (D) 50.3 MPa, 500 shots. Cell viability was recorded 24 h after the SW treatment with the WST-1 proliferation reagent. Data are reported as the cell viability with respect to the control referred as the 100%. Results are shown as mean ± SEM. n = 4. **$p < 0.01$

As it is possible to observe in Figure 25, the cells incubated with ZnO NCs and subjected to multiple SW treatments always showed less viability than the control ones. In the first three cases, regarding cells treated with SW 29.1 MPa-1000 shots, 39.4 MPa-500 shots and 1000 shots (reported in Figure 25-A,B,C, respectively) only those incubated with NCs and treated with SW were appreciably less viable than the controls. However, these results were not statistically different from the control experiments. Strikingly, the cells incubated with ZnO NCs and treated with SW with a PPP of 50.3 MPa and 500 shots (Figure 25-D) resulted in a significant lower cell viability (47±11 %) not only with respect to the control or to the ZnO NCs cells w/o SW (100% of viability), but also with cells treated with only SW ($p<0.01$ with a viability of 93±9 %) without NCs. Therefore, the anti-proliferative effect observed with the combination of ZnO NCs and multiple SW treatments was impressive and not found in the controls. These results suggest the existence of a powerful combined effect between ZnO NCs and SW. While a single SW treatment is not able to induce a significant variation in ZnO NCs + SW cells, three consecutive SW treatments effectively result in a reduced cell viability.

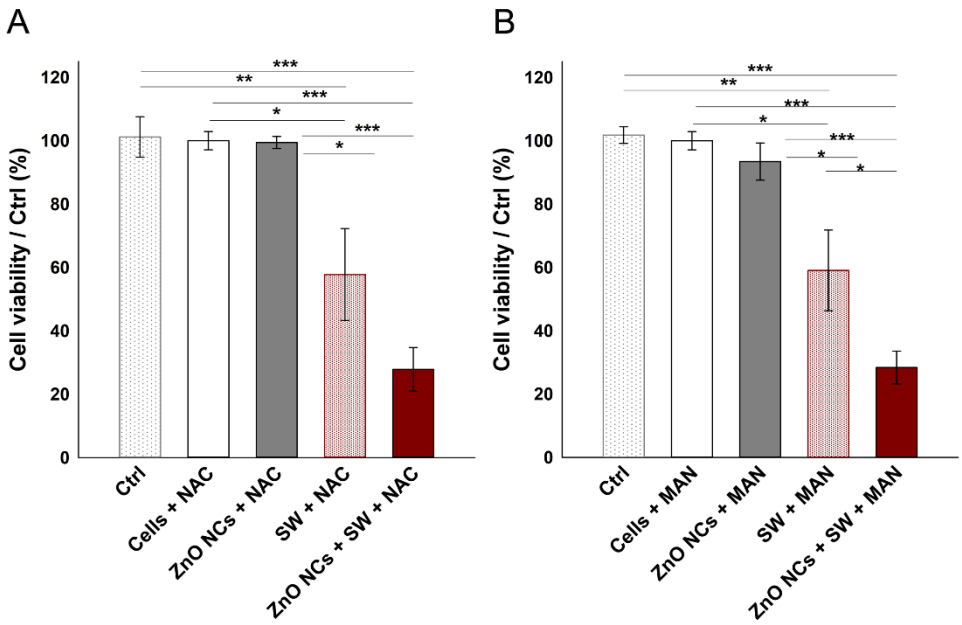

Figure 26 investigating the mechanism with ROS scavengers NAC (A) and MAN (B). Five samples were prepared per assay. Ctrl were cells without the antioxidants; Cells+NAC and Cells+MAN were cells incubated with the antioxidants; ZnO NCs+NAC or MAN were cells incubated with 10 µg/mL ZnO NCs for

24 h and then with the antioxidants; SW+NAC or MAN were cells incubated with the antioxidants and treated with SW; and ZnO NCs+SW+NAC or MAN were cells incubated with NCs and the antioxidants, and then irradiated with SW PPP 50.3 MPa, 500 shots (3 treatments/day). Data are reported as the cell viability with respect to the control referred as the 100%. Results are shown as mean ± SEM. n = 6. ***$p < 0.001$, **$p < 0.01$ and *$p < 0.05$.

Several SDT studies employ ROS scavengers to elucidate the ROS role in cell death upon the sonosensitizer activation[44,137]. In this regard, the experiments with ZnO NCs were repeated pre-incubating KB cells with two different antioxidants (NAC and MAN), using the experimental conditions where a significant difference between SW and ZnO NCs + SW cells was detected, i.e. with SW PPP 50.3 MPa, 500 shots, 3 treatments (Figure 26). Both NAC and MAN resulted to be non-toxic for KB cells in the chosen concentrations and times of incubation. Furthermore, the percentages of cell viability of ZnO NCs treated cells did not change with the addition of the antioxidants. Surprisingly, no cell viability recoveries were observed in ZnO NCs + SW samples, with both the scavengers. Furthermore, the presence of a scavenger seemed to already decrease the viability of SW-treated cells (in absence of ZnO NCs). In particular, only SW-treated cells percentage of viability shifted from 93±9 % (obtained from Figure 25-D) to 58±14 % with NAC (Figure 26-A) and to 59±13 % when pre-treated with MAN (Figure 26-B). In contrast to the previous results, SW-treated cells resulted in a significant decreased viability with respect to control cells ($p<0.01$ in both cases), to the cells with the antioxidants ($p<0.05$ in both cases), and to the cells with ZnO NCs and the antioxidants ($p<0.05$ in both cases). The same scenario was observed with the ZnO NCs + SW treated cells, where the percentage of cell viability shifted from 47±11 % (obtained from Figure 25-D) down to 28±7 % with NAC (Figure 26-A) and to 20±6 % with MAN (Figure 26-B). Also in this case, significant differences were evidenced between these samples and the control cells, the cells with the antioxidants, and the cells with ZnO NCs and the antioxidants ($p<0.001$ for all the comparisons and for both the antioxidants). Antioxidants pre-treatment seemed indeed to enhance SW cytotoxic power instead of allowing the recovery from SDT effects.

Actually, the ROS pivotal role on SDT is a debated question. From the one hand, many authors showed that the addition of an antioxidant molecule was able to protect cells from the SDT effects, thus claiming that ROS are strongly involved in the SDT mechanism of action[137,145,146]. On the contrary, other researchers proposed the mechanical stress as the main responsible of the observed cytotoxic effects[44] . Owing to these results, it seems here that ROS were not truly involved in the therapeutic effect recorded with SW. On the contrary,

ROS showed to slight sustain cells proliferation, indeed their reduction with the addition of the two antioxidants resulted in a marked decrease of cell viability in both SW and ZnO NCs + SW samples. This could be explained remembering that ROS do not play always an anti-proliferative role. Instead, it is known and reported in the literature[147] that ROS are essential for many cell functions, such as cell proliferation, innate immune responses and differentiation. Additionally, it is reported that ROS balance is strictly important to maintain cell homeostasis, because also faint imbalances could result in toxic consequences, thus their level is kept under control[148,149].

In this context, it is probable that the imbalance of ROS levels caused by NAC and MAN addition followed by multiple SW treatments resulted to be more cytotoxic, suggesting that a certain level of ROS was perhaps necessary for KB cells to recover from SW induced damages.

In addition, the obtained results discourage the hypothesis of a ZnO NCs sonoluminescent activation. The production of light flash upon inertial acoustic cavitation is actually a debated issue. Some authors proposed the possibility of the organic sonosensitizer activation through sonoluminescence[137,150,151]. In this case, an eventual light excitation of ZnO NCs has, as a result, the ROS overproduction with consequent cell death[60]. However, this phenomenon was not observed with the acoustic activation in our experiments, because a reduction in ROS burst was here associated with less cell viability and not with a recovery, as expected if the mechanism would be based on the light activation.

Here, the observed combined effect possibly lies on a mechanical injury of the enhanced bubble cavitation. Indeed, the damage could derive from bubble oscillations under non-inertial cavitation, or bubble implosion upon inertial cavitation[152]. In this view, it is reasonable to suppose that the presence of ZnO NCs in cells subsequently irradiated with SW decreased the cavitation threshold improving the number of oscillating/imploding microbubbles, increasing the mechanical stress[44]. This effect was also previously reported by our research group using amino-functionalized ZnO NC in the presence of continuous ultrasound irradiation in water media[19].

In addition, the physical motion of nanoparticles internalized into cells upon US irradiation could also contribute to the cell death, even in absence of inertial

cavitation, increasing locally the temperature and leading to mechanical destruction of the cells. This phenomenon is called “nanoscalpel effect”, where nanoparticles physically alter organelles and nuclei[153].

A further possible mechanism, in concomitance to the above-mentioned ones, can be hypothesized based on the ZnO piezoelectric properties. Actually ZnO, due to its non-centrosymmetric crystal structure[15,154] under a mechanical stimulation, is able to generate polar charges[155–157]. In this regard, the multiple and repetitive mechanical stimulation of ZnO NCs with the SW could also exert an electric stimulation in the cancer cells, resulting in a decrease of cell viability. This mechanism was also previously reported by Marino et al. with other piezoelectric nanomaterials[133,134] .

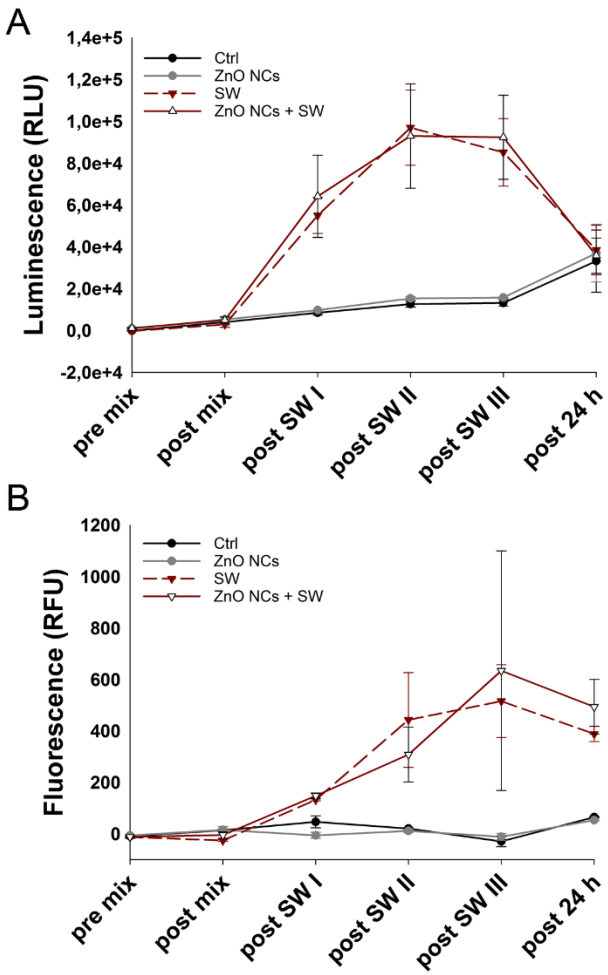

Figure 27 Kinetic of cell death in the ZnO NCs + SW experiment. (A) luminescence, expressed as relative light units (RLU), and (B) fluorescence, expressed as relative fluorescence units (RFU),

measurements. KB cells were considered alone (Ctrl), incubated with 10 μg/mL ZnO NCs for 24 h (ZnO NCs), treated with SW alone every 4 h for a total of 3 treatments in a day (SW), or incubated with ZnO NCs and then treated for three times (a treatment every 4 h) with SW (ZnO NCs + SW). Phosphatidylserine exposure (luminescence) and loss of the membrane integrity (fluorescence) were measured before the addition of the reaction mix (pre mix), after the addition but before SW treatment (post mix), after the first (post SW I), second (post SW II) and third (post SW III) SW treatment and 24 h after the last SW irradiation (post 24 h). n = 2.

To better elucidate the cell killing mechanism, the real-time measurement of both apoptotic and necrotic cells through luminescent and fluorescent signals was performed. In details, the used kit contains two annexin V fusion proteins associated with two complementary subunits of the luciferase enzyme. When the two subunits are in contact, during early apoptosis or secondary necrosis, the luciferase reacts with a substrate generating a luminescent signal. At the same time, a fluorescent intercalating DNA probe lets to precisely identify secondary necrosis. Thus, a sample negative for both signals indicates that cells are nor in apoptosis neither in necrosis. A sample positive for luminescence signal and not for fluorescence one indicates an early apoptosis, while a sample positive for both luminescence and fluorescence indicates the presence of secondary necrosis.

The recorded results of both luminescent and fluorescent signals are shown in Figure 27-A and Figure 27-B, respectively. Before the addition of the reaction mix (pre mix) and immediately before the first SW treatment (post mix), the cell basal signal in both luminescence and fluorescence channels was very low. After the first SW irradiation, the SW and the ZnO NCs + SW treated cells immediately showed a marked increment of luminescence, while the recorded fluorescence reported a slight increase. After the second treatment, the SW and ZnO NCs + SW luminescence continued to increase, as well as the fluorescence of both samples. In contrast, after the third treatment, the recorded luminescence was more or less the same of the previous time point, while the fluorescence displayed a huge increase. In particular, the signal associated to the ZnO NCs + SW treated cells was more pronounced than the one related to only SW-treated cells (Figure 27-B). After 24 h from the treatment, the luminescent signal dropped down and the four samples resulted to possess the same level of luminescence. The fluorescent signals also decreased, but to a less extend in comparison to the luminescent ones. In particular, the ZnO NCs + SW treated sample continued to possess a higher fluorescence signal than the one obtained from the cells treated with only SW. ZnO NCs-treated cells signal on the contrary showed the same trend of the control

ones, indicating that ZnO NCs at the employed concentration and time of incubation did not induce any apoptosis nor necrosis.

Together, these results suggest that multiple treatments are required indeed to exert tumor cell death. The pro-apoptotic and necrotic effects of both SW and ZnO NCs + SW treated samples increased progressively after each treatment, achieving a peak in fluorescence after the third irradiation. Additionally, the fluorescent signals associated to ZnO NCs + SW treated cells showed a difference from the SW treated sample after the third treatment. This evidence agrees with the previous experiments, where no differences between SW and ZnO NCs + SW samples after a single SW treatment was evidenced. Here it was demonstrated that at least three treatments are required in order to obtain the desired combined effect.

Moreover, analyzing the trend of the two signals in Figure 27, the presence of an early apoptosis is highlighted after the first treatment, becoming, as expected, secondary necrosis in the next steps. The progressive increase of luminescence followed by an increase of the fluorescence signal is indeed typical of an apoptotic phenotype[158]. In this case, it is suggested that an apoptotic pathway is induced in both SW and ZnO + SW treated samples. However, the combination of the two stimuli resulted in a more pronounced cell death, as it was evidenced with the WST-1 tests of Figure 26-D.

SW multiple treatments alone on KB cells were apparently able to first induce apoptosis and later, secondary necrosis. However, WST-1 results (Figure 26-D) indicate that cancer cells recovered after 24 h from the last treatment, and thus the induced damages were reverted. This result is in accordance to what reported by Canaparo et al., who already observed that SW treatment was able to improve the percentage of cells in both apoptosis and necrosis[131].

Strikingly, the cells treated with ZnO NCs + SW were not able to recover, confirming that the combined action of ZnO NCs and SW induced irreversible consequences, resulting in a loss of cell viability.

The association between apoptosis and US is largely reported in the literature, even if the mechanism driving this event is not fully understood. US are indeed able to induce this type of cell death activating various pathways[44,124,145].

Previous studies with SW associated with a photosensitizer, even if in a single dose, recorded a remarkable apoptosis and secondary necrosis caused by this combined effect[128,131,159]. However, these estimations occurred at a single time point (12/24 h after the SW treatment), while here we evaluated the trend over time at multiple SW stimulations. Anyway, Canaparo et al. observed that the percentage of apoptotic cells after the incubation with the porphyrin and the treatment with the SW reached a peak 12 h after the SW treatment, while there was a slight cell viability recovery at 24 h[159]. In the present paper, we evidenced a decrease of both the luminescent and fluorescent signals 24 h after the last SW treatment.

Based on these results and the state of the art, it is thus hypothesized here that the apoptosis is caused by cell mechanical injury upon ZnO NCs and SW co-administration. Actually, it was previously observed that mechanical stress could result in DNA damage, with the activation of the apoptotic pathway[160]. Moreover, it was reported that SW mechanotransduction could exert an apoptotic pathway[161], and the previously-cited "nanoscalpel effect" is also related to apoptosis[153] . Nevertheless, more studies are required to fully elucidate the biological mechanisms of ZnO and SW interaction.

5.4 Conclusion

Herein the effects of amino-propyl functionalized ZnO NCs in combination with SW to treat cancer cells were investigated.

After a preliminary phase dedicated to the study of the sole SW cytotoxicity, experiments involving both ZnO NCs and SW were carried out. It was discovered that a single treatment was not sufficient to achieve a significant difference in cells viability between SW and ZnO + SW stimulations. In contrast, multiple SW treatments (3 times/day) resulted to be highly cytotoxic and, strikingly, only for cells pre-incubated with ZnO NCs. Studies on the mechanism were then performed, finding that ROS role was controversial and seemed to be protective instead of being toxic. By exploring the kinetics of cell death, it was demonstrated that SW administration resulted in a pro-apoptotic stimulus. However, the ZnO NCs + SW stimuli led to high cell suffering, with an enhanced fluorescent signal associated with secondary necrosis and confirming what observed with the WST-1 viability assay. Additionally, it was highlighted that, only after the third

treatment, an increase of ZnO NCs + SW fluorescent signals occurred with respect to the sole SW ones, suggesting the importance of the combination between ZnO NCs administration and SW stimulus.

Even if the elucidation of the exact mechanism of cell death is the focus of our current studies, we proposed here the combination of various effects, including the mechanical injury due to (i) the enhanced bubble cavitation and (ii) the so-called “nanoscalpel effect”, as well as (iii) an electric change imbalance, potentially involving the piezoelectric behavior of ZnO.

Despite the previous report concerning the use of SW in presence or not with organic sonosensitizing molecules, the results showed in this chapter clearly underline a toxic behaviour of ZnO NCs in combination with SW. These results open the possibility of a future application of ZnO NCs and SW as an effective nanomedicine tool for cancer therapy.

Chapter 6

Nanotechnological engineering of extracellular vesicles for the development of actively targeted hybrid nanodevices

This chapter has been taken from the open-access publication[162], as stated in the declaration of this dissertation.

6.1 Introduction

In the last decades, an increasing number of studies allowed to unravel the biological role of extracellular vesicles (EVs), an heterogenous group of membrane-enclosed micro- and nano-structures secreted by different cell types, and to highlight their primary role in cell-to-cell communication. Starting from 2006, several groups reported that EVs could contain and transfer biomolecules present in the cytosol of originating cells[163], including mRNA and miRNA[164], proteins, lipids and metabolites[165]. The bioactive materials are protected by the vesicles from the extracellular environment and shuttled to neighboring or considerably distant cells, triggering functional changes in the recipient cells and

regulating many physiological and pathological processes[166].The discovery of their role of intercellular messengers, made EVs compelling candidates for the development of innovative therapeutic tools. Indeed, by opportunely customize their membranes and cargo, EVs can be engineered as highly biocompatible and specific cell-derived delivery tools.

Considering their lipid-bilayer structure, EVs can be assimilated to liposomes, i.e. synthetic lipid vesicles widely applied for the delivery of drugs[167], proteins[168] and inorganic nanoparticles (NPs)[169,170]. As known, the lipid bilayer could provide a suitable defensive barrier to preserve the colloidal and chemical stability of different materials in the biological environment allowing the loading of either hydrophilic and hydrophobic compounds, stable in the vesicles core or in the lipid membrane, respectively[171].

Thanks to these promising features, EVs have been recently evaluated as efficient carriers for the delivery of therapeutic cargos like small molecule drugs, nucleic acids, genes and even NPs for the treatment of various pathologies, including neurodegenerative and cardiovascular diseases, inflammation, diabetes[166], and especially cancer. According to a query done on July 2021 on the US-NIH clinical trials database, 324 clinical trials on EVs or exosomes are currently registered, 121 of which refer to their use for both diagnostic and therapeutic oncological purposes. Despite EVs loaded with anticancer drugs[172–174], recent researches evaluated the combination of cell-derived vesicles with different types of inorganic NPs with the purpose to combine the stabilizing and biomimetic EVs' features with the imaging[175,176], drug delivery[177,178] and/or therapeutic capabilities of the NPs [96].

However, the efficient encapsulation of external cargos and the maintenance of EVs integrity and functionalities after the loading processes are still the major challenges in their application as drug delivery systems[179]. Essentially, the current loading strategies can be divided in endogenous and exogenous methods, which involve respectively the engineering of parent cells for the production of pre-loaded vesicles or the direct engineering of EVs after their isolation. According to the modalities of combination between EVs and external payloads, post-isolation methods are conventionally divided into two further subcategories, i.e. passive or active loading methods[180]. In case of passive loading, the two components would simply interact on the basis of their physicochemical properties, exploiting, for instance, the presence of concentration gradients or the hydrophobicity of payloads to efficiently cross the EVs lipid membrane[171]. Although passive

strategy is generally characterized by a good preservation of EVs membrane integrity, this is often accompanied by low encapsulation efficiency in the case of large or hydrophilic payloads, that cannot easily diffuse through lipid bilayers[181]. To overcome this issue, different active methods, which involve the application of electrical, mechanical or chemical external stimuli to destabilize EVs membrane and facilitate the cargos entrance, are widely investigated[174,182]. Additionally, the engineering of EVs for drug delivery purposes is not limited to cargo customization but concerns also the biological and/or biochemical functionalization of their external surface, mainly devoted to improve their homing and target specificity. Although EVs harbor native homing and targeting properties[183], this intrinsic tropism is often insufficient to achieve an effective delivery within specific organ, tissues or cells. Concerning EVs application in oncology, single domain and monoclonal antibodies, small peptides and glycans[184] are currently investigated as ligands for biomolecular markers specific of the target cells and tumor microenvironment[185]. Furthermore, the mentioned intrinsic targeting ability and organotropism are mainly shown by tumor-derived EVs that, thanks to the presence of particular proteins and lipids in their membrane, are able to selectively home their parent tumors[186]. However, some literature studies highlighted that tumor-derived EVs are directly involved in the progression of cancer[187], metastasis promotion[188] and in the development of drug resistance phenomena[189]. Thus, their application as delivery platforms is not free of concerns and less hazardous alternatives, such as EVs derived from fruits[190], bovine milk[191] or healthy cells[192,193], are intensively investigated.

In this scenario, the present chapter focuses on the post-isolation engineering of lymphocytes-derived EVs, evaluating their surface modification with anti-CD20 monoclonal antibodies and their loading with therapeutically active zinc oxide nanocrystals (ZnO NCs). The design, construction and characterization of a hybrid nanoconstruct, named Trojan nano-horse (TNH) to convey the concept of its biomimetism and cytotoxic potential, were conducted along with the evaluation of its biocompatibility, specificity and targeted cytotoxic capability. In particular, *in vitro* studies were performed on a CD20+ human lymphoid cancer cell line (Daudi), compared to healthy CD20+ lymphocytes and CD20- human myeloid neoplastic cell line (HL60). Moreover, the therapeutic activity of the targeted TNHCD20 was exploited in combination with high-energy ultrasound

shock waves (SW), supporting the proof of concept for the development of biomimetic, selective and stimuli-responsive nanodevices for cancer treatment.

6.2 Materials and methods

6.2.1 Cell cultures

The three cell lines used were all cultured in conformity with the sterile technique and the standard mammalian cell culture protocols under a 5% CO_2 atmosphere at 37 °C.

Lymphocyte cell line (IST-EBV-TW6B) was purchased from the cell bank IRCCS AOU San Martino IST (Italy). Cells were cultured in advanced RPMI 1640 culture medium (Gibco) with 20% of heat inactivated fetal bovine serum (FBS, Gibco), 1% penicillin/streptomycin (P/S, Sigma) and 1% of L-Glutamine 200 mM (Lonza) in 75 cm^2 not treated cell culture flasks (Corning) maintaining the cell density between $9x10^{4-5}$ cells/mL.

Daudi cells (ATCC® CCL-213™), originating from a Burkitt's lymphoma patient, were cultured as reported in section 3.2.6.

HL60 cells (ATCC® CCL-240™), from an acute myeloid leukemia patient, were purchased from ATCC. They were maintained in Iscove's Modified Dulbecco's Medium (Sigma) with 20% heat inactivated FBS (Sigma), 1% Glutamine (Sigma), 1% P/S (Sigma) in 75 cm^2 not treated cell culture flasks (Corning), adjusting cell density to 1x105-6 cells/mL.

6.2.2 EVs isolation and characterization

EVs were isolated from the conditioned media of the lymphocytes cell line grown in RPMI supplemented with 20% EVs-depleted FBS, 1% glutamine and 1% P/S after 72 hours of culture. The depleted FBS was the supernatant collected from the overnight ultracentrifugation at 100'000 g (Optima Max-XP Ultracentrifuge with MLA-50 rotor, Beckman Coulter) at 4 °C of FBS.

EVs were produced by plating 1.5x105 lymphocytes/mL in a total volume of 200 mL of medium complemented with depleted FBS in 75 cm^2 untreated flasks and left in culture for three days at 37 °C under a 5% CO_2 atmosphere. Just before

the EVs extraction, lymphocytes viability was assessed via Trypan-blue (VWR) method using a TC20 TM automated cell counter (BiO-Rad Laboratories), and only samples with viability over 90% were processed to reduce the probability of apoptotic bodies' recovery. The EVs isolation protocol is adapted from the sterile differential ultracentrifugation protocol described by Thery et al.[194]. Cell culture medium was collected in 50 mL tubes and centrifuged 10 minutes at 150 g at 4°C to remove cells. Supernatants were collected and centrifuged 20 minutes at 2'000 g at 4°C to remove dead cells and cell debris. The supernatants collected were centrifuged again for 30 minutes at 10'000 g at 4 °C to discard aggregates of biopolymers, apoptotic bodies, and other structures with higher density than EVs. Supernatants were collected again, placed in ultracentrifuge polypropylene tubes (32 mL Optiseal tubes, Beckman Coulter) and ultracentrifuged at 100'000 g for 70 minutes at 4 °C. The obtained pellet was resuspended in sterile, cold, 0.1 µm filtered phosphate buffered saline (PBS) solution and ultracentrifuged for further 60 minutes at 100'000 g at 4 °C. The pellet, which contained EVs, was resuspended in 600 µl of sterile, cold, 0.1 µm filtered physiological solution (0.9% NaCl, NovaSelect), aliquoted in 50 µl cryovials and stored at -80 °C for further uses.

The concentration and the size distribution of collected EVs were measured by nanoparticle tracking analysis (NTA) technique with a NanoSight NS300 (Malvern Panalytical) equipped with λ=505 nm laser beam and a NanoSight syringe pump. Samples were diluted in a final volume of 500 µl of 0.1 µm-filtered physiological solution to meet the ideal particles per frame value (20-100 particles/frame). Different EVs aliquot were measured by capturing three videos of 60 seconds with an infusion rate of 50 a.u, and a camera level value between 14 and 16. The collected videos were then analyzed by the NTA 3.4 software (Malvern Panalytical), setting the detection threshold at 5.

The protein content of isolated EVs was measured by Bradford assay as described in literature[194]. Bradford reagent (Bio-Rad) was diluted 1:5 in bd water and added to EVs samples, diluted 1:2 in 0.1 µm-filtered PBS, and serially diluted bovine serum albumin (BSA, Sigma Aldrich) standards with known concentrations. The absorbance at 590 nm was then recorded using a microplate spectrophotometer (Multiskan GO, Thermo Fisher Scientific) and the protein concentration of EVs samples was extrapolated comparing their absorbance

values with the calibration curve made on BSA standards. All samples were analyzed in triplicate.

The EVs morphology was analyzed trough Transmission Electron Microscopy (TEM) using a JEOL JEM-1400Plus TEM, with thermionic source (LaB6), operated at 120 kV. For TEM analyses, a drop of the sample solution was placed on a copper grid, 150 mesh, coated with amorphous carbon film; then, to highlight the EVs morphology, the EVs were stained before observation with a solution of 1% uranyl acetate in water. Energy Dispersive X-ray Spectroscopy was performed with the same instrument equipped with a JEOL-JED-2300 Energy Dispersive Spectroscopy (EDS) silicon drift type detector (area 30 mm^2).

To evaluate the presence of the CD20 surface antigen on EVs' membranes, vesicles were adsorbed on Aldehyde/Sulfate Latex Beads, 4% w/v, 3 µm (Thermo Fisher) and analyzed by flow cytometry using the Guava Easycyte 6-2L flow cytometer (Merck Millipore). In details, 10 µL of latex beads were coupled for 15 minutes at RT with a sample of EVs containing 5 µg of protein. Then, PBS was added to a final volume of 1 mL and the coupling continued for 2 hours at RT on a tube rotator with fixed speed of 20 min-1. To saturate any free binding site of the beads, 110 µL of PBS/1 M glycine were added and incubated for 30 min at RT. Then, samples were centrifuged for 3 min at 4'000 rpm, the supernatants were discarded and the bead pellets were resuspended in 1 mL PBS/0.5% BSA. Beads were washed three times before the incubation with CD20-PE antibody (Miltenyi Biotec) and the respective isotype control. Unstained beads were used to adjust instrument voltages and gate bead population to exclude debris and impurity derived from buffer solution. $5x10^3$ gated events were acquired in very low modality (0.12 µL/s flow rate) and the PE signal was excited with blue laser (488 nm). Results were analyzed with Incyte Software in term of median fluorescence intensity (MFI) of the antigen minus the MFI of the isotype control[195,196]. Each experiment was repeated three times (n=3).

6.2.3 ZnO NCs synthesis, functionalization and characterization

ZnO NCs were synthesized through a microwave-assisted approach[16] and the morphology of ZnO NCs was evaluated through Transmission Electron Microscopy using a Jeol JEM-1011 transmission electron microscope operated at 100 kV of acceleration voltage. The crystalline structure of ZnO NCs was investigated by X-ray diffraction, hydrodynamic size and the z-potential of the

ZnO NCs were determined using the dynamic light scattering (DLS) technique with a Zetasizer Nano ZS90 (Malvern Instruments), as reported in section 2.2.2.

6.2.4 TNH assembly and characterization

The EVs:ZnO NCs ratio of 1:2 used during TNH assembly was calculated starting from a model which estimates the maximum number of nanocrystals that could be geometrically encapsulated within a single vesicle. Considering the EVs concentration as part/mL and µg/mL obtained from NTA and Bradford techniques respectively, the maximum theoretical number of ZnO NCs (indicated as n°ZnO NCs), corresponding to a fixed amount of µg of EVs, was calculated as follows:

$$(n°_{\text{ZnO NCs}})_{\mu\text{g EVs}} = (n°_{\text{ZnO NCs}})_{\text{EV}} \cdot n°_{\text{EVs per }\mu\text{g}} \cdot \mu\text{g EVs}$$

where $n°_{\text{EVs per }\mu\text{g}} = \frac{\text{Conc}_{\text{EVs@NTA [part/mL]}}}{\text{Conc}_{\text{EVs@Bradford [}\mu\text{g/mL]}}}$

Finally, the mass of a single particle was calculated considering its volume (ie the volume of a sphere with diameter equal to the ZnO NC diameter, dZnO) and the ZnO density (ρZnO=5.606 g/cm^3) and the obtained value was used to determine the corresponding NCs amount expressed as µg:

$$\mu\text{g ZnO NCs} = (n°_{\text{ZnO NCs}})_{\mu\text{gEVs}} \cdot \text{mass}_{\text{ZnO NC}}$$

where $\text{mass}_{\text{ZnO NC}} = \left(\frac{\pi}{6} d^3_{\text{ZnO NC}} \cdot 10^{-21}\right) \cdot \rho_{\text{ZnO}} \cdot 10^6$

The model was then amended on the basis of experimental observations, as discussed in detail in the 5.3 section, and finally an excess of 10 µg of amino-functionalized ZnO NCs were combined with an amount of EVs corresponding to 5 µg of protein measured by Bradford assay. The encapsulation process was performed in a 1:1 (v/v) solution of 0.1 µm-filtered bd water and physiological solution, with a final concentration of 80 µg/mL for ZnO NCs and 40 µg/mL for EVs. Opportunely labeled EVs dispersed in physiological solution were rapidly frozen in liquid nitrogen for 3 minutes and thawed at RT for 15 minutes. The freeze-thaw cycle was repeated twice and then the corresponding amount of ZnO NCs in bd water was added. The obtained mixture was incubated under

continuous agitation (250 rpm) at 45 °C for 10 minutes, at 37 °C for 2 hours and then overnight (O/N) at RT. In order to redisperse the obtained TNHs in media suitable for *in vitro* tests, a final step of centrifugation was performed. The samples were centrifuged at 5'000 g for 5 minutes, suspended in the cell culture medium and redispersed by vortexing for 3 minutes.

The coupling efficiency was evaluated through fluorescence microscopy. The amino- functionalized ZnO NCs were labeled with Atto 550-NHS ester (λEx= 554 nm, ATTO-Tech), by adding 4 µg dye each mg of ZnO NCs suspension in ethanol; the solution was stirred in dark O/N and then washed twice. EVs, diluted 1:2 in physiological solution were labeled with Wheat Germ Agglutinin (WGA) conjugated with Alexa Fluor 488 (WGA488, λ_{Ex}= 495 nm, Thermo Fisher) by adding 1 µl of dye (100 µg/mL in PBS) for each EVs aliquot containing approximately 1·1010 particles. The solution was kept under agitation (180 rpm) in dark at 37°C for 30 minutes and then purified from unbound dye molecules with 50 kDa Amicon Ultra 0.5 centrifugal filter (Merck Millipore). The samples were analyzed using a wide-field fluorescence-inverted microscope (Eclipse Ti-E, Nikon) equipped with a super bright wide-spectrum source (Shutter Lambda XL), a high-resolution camera (Zyla 4.2 Plus, 4098x3264 pixels, Andor Technology) and an immersion oil 100x objective (Nikon). The collected images were analyzed with the colocalization tool of NIS-Element software (NIS-Element AR 4.5, Nikon). In brief, the spots in red and green channels (corresponding to ZnO NCs and EVs respectively) were counted and then a merge of the two images was performed, counting the spots in which the two fluorescence signals resulted superimposed. The percentage of colocalization with respect to the ZnO NCs (% co-ZnO) was then calculated doing the ratio between the number of colocalized spots and the total number of red spots. The analysis was performed on 9 regions of interest (ROIs) to evaluate the mean %co-ZnO and the results of 5 different samples were averaged to obtain the coupling efficiency at the end of TNHs assembly process. The same colocalization procedure was used to evaluate the maintenance of coupling efficiency after incubation in cell culture medium samples (advanced RPMI+20% EVs-depleted FBS, Gibco). Four different samples were analyzed at t_0 and after 1, 24 or 48 hours of incubation and the results were expressed as percentage decrease of %co-ZnO with respect to t_0.

To evaluate the TNHs morphology, a drop of the sample solution was placed on a copper grid, 150 mesh, coated with amorphous carbon film and the sample was stained with a solution of 1% uranyl acetate in water for 30 seconds. TEM

analysis in Bright Field mode were performed using a JEOL 1011 operated at 100 kV. Annular Dark-Field (ADF) imaging in Scanning Transmission Electron Microscopy (STEM) mode and EDS analysis were performed using a TEM JEM-1400 Plus, with thermionic source, operated at 120 kV of accelerating voltage and equipped with a JEOL-JED-2300 EDS silicon drift type detector (detector area $30mm^2$).

The size distribution of TNHs in bd water and physiological solution 1:1 (v/v) was assessed by NanoSight NS300 equipped with NanoSight syringe pump. The samples were diluted 1:5 and three videos of 60 seconds were recorder with camera level and detection threshold of 16 and 5, respectively. The size distribution of TNHs in advanced RPMI (Gibco) supplemented with 20% EVs-depleted FBS (Gibco) was measured in static conditions using the O-ring top plate cell with manual syringe connection. TNHs resuspended in cell culture medium (ZnO concentration 100 µg/mL) and medium alone as reference were diluted 1:10 in bd water and physiological solution 1:1 (v/v) and three videos of 30 seconds were acquired, advancing manually the samples between them. The camera level and detection threshold values were set at 15 and 6, respectively. At least two independent experiments were performed.

TNHs hemocompatibility was preliminarily evaluated through a simple turbidimetric assay as previously reported[197], using Na-citrate human recovered plasma (Zen Bio) and calcium chloride (CaCl2 0.025 M from HYPHEN BioMed) as clotting agent. Briefly, 75 µl of plasma for each sample were aliquoted in a 96 well plate and mixed with 75 µl of TNHs samples at concentration 75 µg/mL in bd water and physiological solution 1:1 (v/v). To monitor the dispersant influence, controls with the addition of 75 µl of physiological solution or bd water and physiological solution 1:1 (v/v) were also performed. Coagulation was started adding 75 µl of $CaCl_2$, and the absorbance at 405 nm was measured through a microplate UV–VIS spectrophotometer every 30 seconds for 45 minutes at constant T=37 °C. Three replicates per sample were averaged to obtain the mean absorbance at each time point and the coagulation time, was calculated as the time corresponding to the half maximal absorbance ($t_{1/2}$). Four independent experiments were conducted and the results were expressed as mean±S.E.

CD20 expression on TNH surface was evaluated by flow cytometry as described in 'EVs isolation and characterization' Paragraph. Each experiment was repeated three times (n=3).

6.2.5 TNH functionalization with targeting antibodies

To obtain TNHCD20 samples, vesicle membranes were functionalized with anti-CD20 antibody as reported[183]. After the O/N co-incubation step, TNH samples corresponding to 5 µg of EVs proteins were mixed with functionalizing antibodies, added in three consecutive incubation steps (1 hour at RT on a tube rotator with fixed speed of 20 min-1 each). In details, half of the EVs protein content measured by Bradford assay was considered equal to CD20 antigen and anti-CD20 antibody (Rituximab, Cat. n° TAB-016, Creative Biolabs, 5 mg/mL in PBS) was added in a molar ratio 4:1 with respect to the assumed antigen concentration, working in a large excess to favor antibody-antigen interaction. Then, anti-human secondary antibody (AffiniPure $F(ab')_2$ Fragment Goat Anti-Human IgG, Fcγ fragment specific, Jackson ImmunoResearch or AMCA AffiniPure $F(ab')_2$ Fragment Goat Anti-Human IgG, Fcγ fragment specific, Jackson ImmunoResearch, λEx= 450 nm) was added as cross-linker in molar ratio secondary Ab: anti-CD20=1:1. Finally, a second aliquot of anti-CD20 antibody was added in the same amount as the first incubation step. After the third hour of incubation, TNHCD20 samples were collected and centrifuged (5'000 g for 5 minutes) to remove unbound antibodies and resuspended in cell culture medium suitable for *in vitro* tests.

6.2.6 Cytotoxicity assay of TNH and TNHCD20

To evaluate the viability of lymphocytes, Daudi and HL60 cell lines treated with 5 µg/mL of TNH and TNHCD20 (considering the EVs protein content), after the centrifugation step at 5'000 g, the two TNH samples were resuspended in the required volume of cell culture medium. Then, $2x10^5$ cells for each mL of treatment were centrifuged at 130 g for 5 minutes for Daudi and HL60 and at 150 g for 5 minutes for lymphocytes, and the supernatants replaced with the treatment solutions of TNH and TNHCD20. A total volume of 100 µl was plated for each well in a 96-well flat-bottom plastic culture plate (Greiner Bio-one, 96 Well for suspension culture). After 20 and 44 hours of incubation 10 µl of WST-1 reagent was added to each well and, after further 4 hours of incubation, the formazan absorbance was detected as reported in section 3.2.6. All the experiments were

carried out at least four times for each cell line and results were normalized to the untreated control.

6.2.7 Cytofluorimetric analysis of TNH and TNHCD20 internalization

For the uptake evaluation of TNH and TNHCD20, the amino-functionalized ZnO NCs were labeled with Atto 647-NHS ester (λEx= 647 nm, ATTO-Tech) fluorescent probe as previously described, and the preparation of the TNH performed as described above. After the centrifugation steps, the two TNHs were resuspended in cell medium. $2x10^5$ lymphocytes, Daudi and HL60 cells for each mL of treatment were centrifuged and the pellets were resuspended in the TNHs' solutions. The experiment was carried out five times for TNH and in duplicate for TNHCD20. Data from untreated cells were used as reference.

Cells were cultured into not treated 96 well plates, 250 µl for each well. After 24 and 48 hours of incubation, the contents of the different wells were collected and washed twice in PBS and resuspended in 350 µl of PBS for the 24 hours and 500 µl for the 48 hours cytofluorimetric analysis. $1x10^4$ events were acquired with the flow cytometer with 0.59 µl/s flow rate, excluding cell debris. The analyses were performed using the red laser (λEx=642 nm). Positive events were characterized by a shift of Red-R fluorescence intensity (emission filter 661/15) and the percentages of positive events were evaluated with respect to untreated cells using Guava InCyte Software (Merck Millipore).

6.2.8 Fluorescence microscopy imaging of TNH and TNHCD20 internalization

For the fluorescence microscopy analysis, EVs were labelled with Wheat Germ Agglutinin (WGA) conjugated with Alexa Fluor 647 (WGA647, λEx= 650 nm, Thermo Fisher), ZnO NCs with Atto 550-NHS ester (λ_{Ex}= 554 nm, ATTO-Tech), and the TNHCD20 nanoconstruct was assembled using the AMCA AffiniPure $F(ab')_2$ Fragment Goat Anti-Human IgG, Fcγ fragment specific as secondary antibody.

Samples were treated with the same protocol used for the cytofluorimetric analysis and plated in a volume of 100 µl. After 24 and 48 hours of culturing at 37

°C, 5% CO_2 in 96 well plates, the content of each well was collected, centrifuged, resuspended in 40 µL of the correspondent medium. The 40 µl drop was spotted in a 8-well chamber slide (Thermo Scientific™ Nunc™ Lab-Tek™ II CC2™ Chamber Slide System) and placed at 37 °C, 5% CO2 for 30 minutes to allow the attachment of the cells. After that, cells were fixed using 250 µl of Image-iT™ Fixative Solution (4% formaldehyde, methanol-free, Thermo Scientific) for 10 minutes, washed in PBS and cells' membranes were labelled by incubating cells with 1.25 µl of WGA conjugated with Alexa Fluor 488 (WGA488, λex=495 nm, Thermo Fisher) for 10 minutes and washed two other times in PBS. Images were acquired using a wide-field fluorescence-inverted microscope using an immersion oil 100× objective.

6.2.9 Shock waves treatment

The cytotoxic effects of shock waves combined with both TNH and TNHCD20 treatments were evaluated on Daudi and lymphocytes cell lines.

After the centrifugation steps, the TNH and TNHCD20 were resuspended in cell culture medium. $2x10^5$ lymphocytes and Daudi for each mL of treatment were centrifuged and the pellets were resuspended in the TNH and in the TNHCD20 solutions and seeded into 96 well plates, 100 µl for each well. Untreated cells were used as reference. After 24 hours of incubation cells were treated with multiple SW (3 times/day, one treatment every 3h). Each SW treatment was composed by 250 shots of 12.5 MPa, 4 shot/s, SW were generated by PW2 device from Richard Wolf. The cell viability was measured 24 hours after the SW treatment with the WST-1 assay.

6.2.10 Statistical analysis

Plotted data are mean±S.E. The statistical analysis between the treatment groups was performed by using the two or the three-way analysis of variance (ANOVA) tools of the SIGMA Plot software's data analysis package. $^{**}p < 0.001$ and $^{*}p < 0.05$ were considered significant. Independent experiments were performed at least two times.

6.3 Results and discussion

6.3.1 EVs characterization

EVs were isolated from lymphocytes' conditioned supernatants through a sterile differential ultracentrifugation protocol and characterized in terms of size, morphology, composition and concentration. EVs, derived from different isolation rounds, were quantified with both NTA and Bradford assays, obtaining a very uniform population, with a mean particles concentration of $1 \cdot 10^{11} \pm 1 \cdot 10^{10}$ particles/mL from NTA analysis and a protein concentration of 160±11 μg/mL from Bradford assays (both concentration values are expressed as mean±S.E., considering 20 different isolations). NTA measurements also reported the hydrodynamic size distribution of EVs dispersed in physiological solution, identifying a main peak centered at approximately 100 nm, as representatively showed in Figure 28-a. The size and the morphology of EVs were analyzed more in details by TEM technique. TEM image of negatively stained EVs (as representatively depicted in Figure 28-b) showed a population of round-shaped structures with a size distribution in good accordance with NTA measurements. In particular, the presence of vesicles with dimensions of ~100 nm or slightly larger and the typical cup-shaped morphology of stained EVs[198] was clearly accounted, while the smallest entities were identified as proteins and lipoproteins co-precipitated during the isolation procedu[199]. The composition of EVs samples was evaluated through Energy Dispersive Spectroscopy. The EDS spectrum reported in Figure 28-c show the presence of carbon, oxygen, nitrogen and phosphorous, typical elements of lipid vesicles membrane, together with a consistent amount of sodium ascribable to the physiological solution used as dispersant medium.

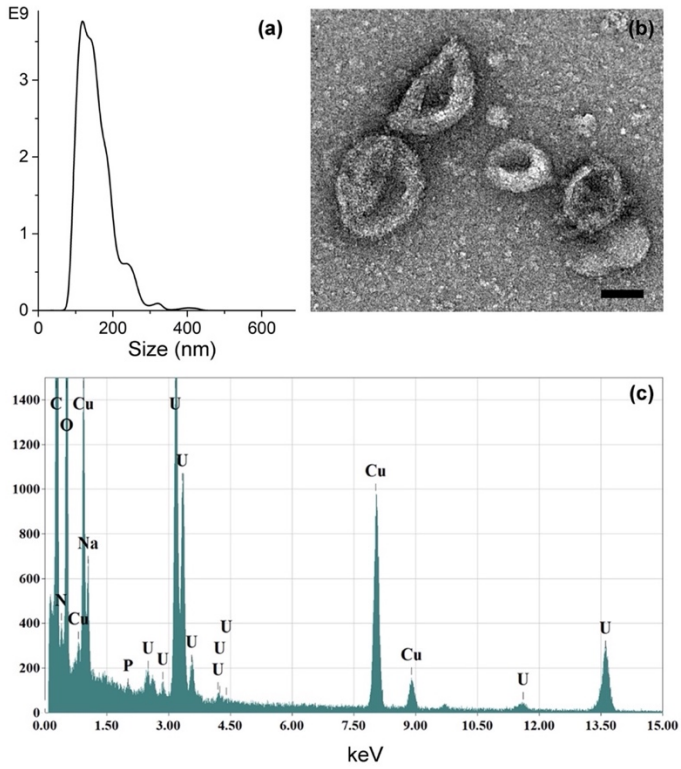

Figure 28 Characterization of lymphocytes-derived EVs. (a) Nanoparticle Tracking Analysis measurement of EVs dispersed in physiological solution. (b) BF-TEM micrograph of EVs negatively stained with uranyl acetate (scale bar: 50 nm) and (c) related EDS spectrum. Results are representative over a broad number (n>20) of EVs isolation batches.

6.3.2 ZnO NCs characterization

Thanks to their intrinsic cytotoxic properties widely explored for the treatment of different cancer cell lines[16,200–202], ZnO crystalline NPs were selected in the present study as the therapeutic payload of the EVs. As extensively reported in the literature[203–205], the cytotoxic potential of ZnO nanostructures is mainly attributed to two main mechanisms, i.e. the production of reactive oxygen species and the NPs dissolution and subsequent release of zinc cations, which are connected and affected by ZnO NPs physico-chemical properties.

The morphology and dimensions of the obtained ZnO NCs were previously reported in section 3.3.

6.3.3 TNH and TNHCD20 assembly and characterization

For the TNH assembly, a convenient coupling ratio between ZnO NCs and EVs was defined on the basis of a simple theoretical model that approximates the TNH components to hard spheres and calculates the theoretical number of nanocrystals that could be geometrically encapsulated within a single EV. Considering a packing density of ~74%, corresponding to a cubic close-packing arrangement[206], and the diameters of EVs (100 nm) and of ZnO NCs (20 nm), an amount of about 93 ZnO NCs per EVs was calculated. Based on the actual size of ZnO NCs and EVs experimentally observed by TEM analyses, it was approximately assumed that each EVs could contain up to 100 nanocrystals and the number ratio was then transformed in a mass ratio. The resulting theoretical amount was equal to ~1.5 μg of ZnO NCs for each μg of EVs proteins. To favor the probability of collision and thus the interaction between the two components, an excess of ZnO with respect to the theoretical amount was envisaged and a final experimental EVs:ZnO NCs ratio of 1:2 was set.

Concerning the encapsulation procedure, the coupling between ZnO NCs and lymphocytes-derived EVs was obtained through an optimized combination of active and passive loading methods able to maximize the loading efficiency, limit the degradation of EVs membrane and the nanocrystals aggregation. The developed procedure was based on the application of freeze-thaw cycles as active stimulus to destabilize the EVs lipid membrane and favor the coupling with the ZnO NCs[174,183]. Two freeze-thaw cycles were conducted on a solution containing only EVs, to prevent the mechanical stresses possibly induced by the presence of NCs. Following the addition of ZnO NCs, the sample was then subjected to a quick heating (45°C for 10 minutes) to promote a higher fluidity of the already weakened EVs membranes. The procedure was completed with an incubation of 2 hours at 37 °C and a further O/N incubation at RT to restore the EVs membranes integrity and microviscosity[173] and complete the encapsulation. In view of *in vitro* tests, a final centrifugation step to allow the redispersion of the obtained TNHs pellets in the cell culture medium was performed.

The successful coupling of the TNH was primarily evaluated through fluorescence microscopy, quantifying the colocalization between the labeled ZnO NCs and EVs. The two components were imaged in red and green channels, respectively, and then the images in the two different channels were superimposed

to analyze the presence of colocalized spots, corresponding to efficiently assembled TNHs nanoconstructs. The obtained average coupling efficiency, expressed as percentage of colocalized spots with respect to the total ZnO signal (%co-ZnO), was equal to 48±6%.

The morphology and elemental composition of the TNHs sample were analyzed by electron microscopy. As clearly shown by TEM (see Figure 29-a for a representative image), the original dimension and morphology of EVs were well preserved after their coupling with ZnO NCs. Furthermore, the presence of encapsulated nanocrystals was confirmed by EDS analysis, performed on the area in STEM imaging mode of Figure 29-b, together with the related EDS elemental maps (Figure 29-c,d,e,f) and spectrum (Figure 29-g). The analyzed object presented a spherical shape and the signals of oxygen, carbon and phosphorous, which are typical elements of lipid membranes, confirming its vesicular nature. In addition, the signal of zinc was detected in the same region, suggesting the encapsulation of ZnO NCs within the EVs.

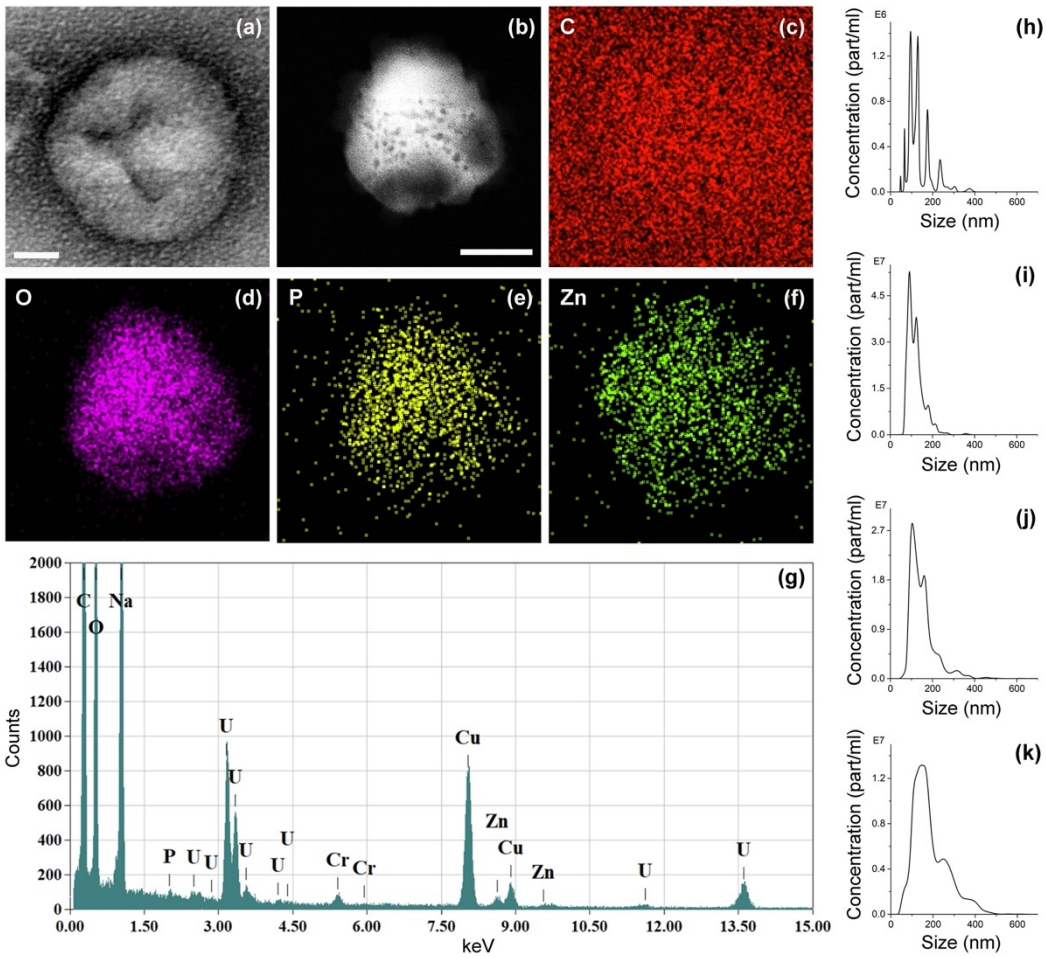

Figure 29 Characterization of TNH nanoconstructs. Representative (a) BF-TEM micrograph of TNHs negatively stained with uranyl acetate (scale bar: 20 nm); (b) ADF-STEM micrograph and (c-f) related EDS elemental maps (Scale bars: 200 nm) of Carbon (C), Oxygen (O), Phosphorous (P) and Zinc (Zn) elements; (g) EDS spectrum. Nanoparticle Tracking Analysis measurements of (h) ZnO NCs, (i) EVs, (j) TNHs before and (k) TNHs after the centrifugation step. Samples were analysed in 1:1 (v/v) of 0.1 µm-filtered bd water and physiological solution.

The colloidal stability of the TNH nanoconstructs was evaluated through NTA technique, measuring the hydrodynamic size distributions of TNHs before and after the final centrifugation step and comparing them with those of EVs and ZnO NCs individual components subjected to the same freeze-thaw cycles and co-incubation steps for consistency. The results, summarized in Figure 29 from panels h to k, confirmed the tendency of ZnO NCs to aggregate in salt-rich physiological solution. Indeed, the uncoated nanocrystals presented a wide hydrodynamic distribution with multiple peaks centered also at high size values

between 200 and 300 nm (Figure 29-h). Conversely, the EVs subjected to the same coupling procedure of the TNH counterpart, displayed good size distribution with a major peak at ~100 nm and only minor peaks at higher dimensions (Figure 29-i). These data are quite similar to the one registered for pristine EVs (see Figure 28-a), evidencing that the developed procedure slightly affected the EVs dispersion, causing only a minor extent of aggregation. The TNHs sample before the centrifugation step resulted well-dispersed in the bd water and physiological solution coupling mixture (Figure 29-j), having similar concentration and resembling the distribution of unloaded EVs with only minor peaks at larger diameters (i.e. 150 and 315 nm), thus suggesting the success of the coupling procedure. After the final centrifugation step, a slight broadening of the main peak together with a shift of minor peaks up to 250-300 nm was observed (Figure 29-k). However, despite the partial aggregation probably induced by centrifugation, the TNH maintained the same concentration as before centrifugation and suitable nanometric dimensions for biological applications. It thus constitutes a great improvement with respect to randomly-aggregated ZnO NCs, confirming the stabilization effect provided by the EVs lipid shell.

Stability in cell culture medium					
Time	***(a) Mean Size [nm]***		***(b) Concentration [part/mL]***		***(c) Percentage Decrease (as percentage) from initial t_0 value***
	Medium	***TNHs***	***Medium***	***TNHs***	***Δ%co-ZnO***
t_0	86±4	128±8	$3.88\cdot10^9\pm3.44\cdot10^8$	$3.96\cdot10^9\pm5.57\cdot10^8$	-
1h	79±5	144±4	$5.18\cdot10^9\pm1.05\cdot10^8$	$6.42\cdot10^9\pm4.25\cdot10^8$	-17±3%
24 h	78±6	138±3	$3.60\cdot10^9\pm1.50\cdot10^8$	$7.52\cdot10^9\pm1.40\cdot10^9$	-20±4%
48 h	83±4	135±13	$4.60\cdot10^9\pm7.73\cdot10^8$	$5.66\cdot10^9\pm1.23\cdot10^9$	-15±10%
(d) Clotting time in human recovered plasma					
	Ctrl (Plasma)		***Plasma+ Phys. solution***	***Plasma + Phys. Solution + water***	***Plasma + Phys. Solution + water and TNHs***
Time [min]	10.3±0.3		10.4±0.3	10.7±0.5	9.5±0.6

Table 3 Evaluation of the behaviour of TNHs nanoconstructs in biological media. (a) Mean size and (b) concentration of TNHs assessed through Nanoparticles Tracking Analysis at t_0 and after 1, 24 and 48 hours incubation at 37°C in cell culture medium. (c) Estimation of the coupling efficiency after 1, 24 and 48 hours incubation at 37°C in cell culture medium expressed as percentage decrease of %co-ZnO with respect to t_0. (d) Plasma clotting time measurements following the incubation with TNHs. The values for plasma alone, plasma/physiological solution, plasma/bd water and physiological solution 1:1 (v/v) are reported as controls. All experiments were conducted at least in duplicate.

In the perspective of biological applications, the stability of nanoconstructs in biological medium was also analyzed, monitoring over time the size distribution of TNHs maintained in cell culture medium at 37 °C to mimic the *in vitro* culture conditions. The NTA measurements, reported in Table 3 in term of mean size and particle concentration, evidenced that the TNHs efficiently maintained their hydrodynamic dimensions up to 48 hours, since there were no significant differences comparing the sizes at t_0 and 1, 24 and 48 hours. Even though a contribution ascribable to the detection of smaller medium components must be taken into account, these values confirmed also the EVs stabilizing potential, as their phospholipidic shell efficiently prevent the ZnO NCs aggregation in biological environment, as also widely investigated in a previous study[207]. Moreover, the absence of statistical differences between the concentrations at t_0, 1, 24 and 48 hours suggested a satisfactory robustness of the developed nanoconstruct, with a good over-time retain of ZnO NCs by EVs. This was further confirmed by fluorescence microscopy analysis that indicated a maximum decrease in percentage of colocalized ZnO of about -20% with respect to the one recorded at t_0 (Table 3).

A first insight of TNHs hemocompatibility was also provided through a simple turbidimetric assay able to track the kinetics of clot formation in human recovered plasma[207]. The results showed no significant differences ($p=0.276$) in the clotting time of plasma alone (10.3±0.3 min) or in presence of TNHs (9.5±0.5 min), indicating that treatment with hybrid nanoconstruct did not affect the physiological coagulation process of plasma, hint of good hemocompatibility of TNHs formulation.

6.3.4 Stability in cell culture medium

After the optimization of ZnO NCs loading procedure, the functionalization of the EVs membrane with anti-CD20 targeting ligands was explored to obtain highly selective TNHCD20 nanoconstructs towards CD20+ cells. The functionalization strategy of TNHs directly involved the use of CD20 antigen as an anchoring site. As a common marker of B cell lines[208], the presence of CD20 antigen on lymphocytes-derived EVs could be reasonably expected and its surface expression on TNH lipid shield was evaluated by flow-cytometry and compared

with that of native EVs. The obtained expression values, reported as MFI with respect to the isotype control, were equal to 19±3 and 6.7±1.1 (expressed as mean±S.E) for native EVs and TNHs, respectively. Although results confirmed that the expression of CD20 transmembrane protein significantly decrease on lymphocytes-derived EVs during the loading procedure, it was possible to proceed with functionalization and its effectiveness and selectivity were evaluated through *in vitro* tests, as described in detail in section 6.3.5.

6.3.5 Cytotoxicity and targeting capability of TNH versus TNHCD20

The results of cytotoxicity assays carried out on the three cell lines, i.e. lymphocytes, Daudi and HL60, at two different time points, 24 and 48 hours, are reported in Figure 30-a. Cells viability did not display any statistical differences when considering the time of treatment. On the contrary, significant differences in viability were observed when comparing the different cell lines at the two treatment time points. Moreover, it is worth to note that treating cells with the pristine TNH did not affect cells viability. This result highlights the high biocompatibility of the proposed TNH, similar to what measured using the native lymphocyte-derived EVs at the same concentration and time points on the three cell lines, as previously reported[183].

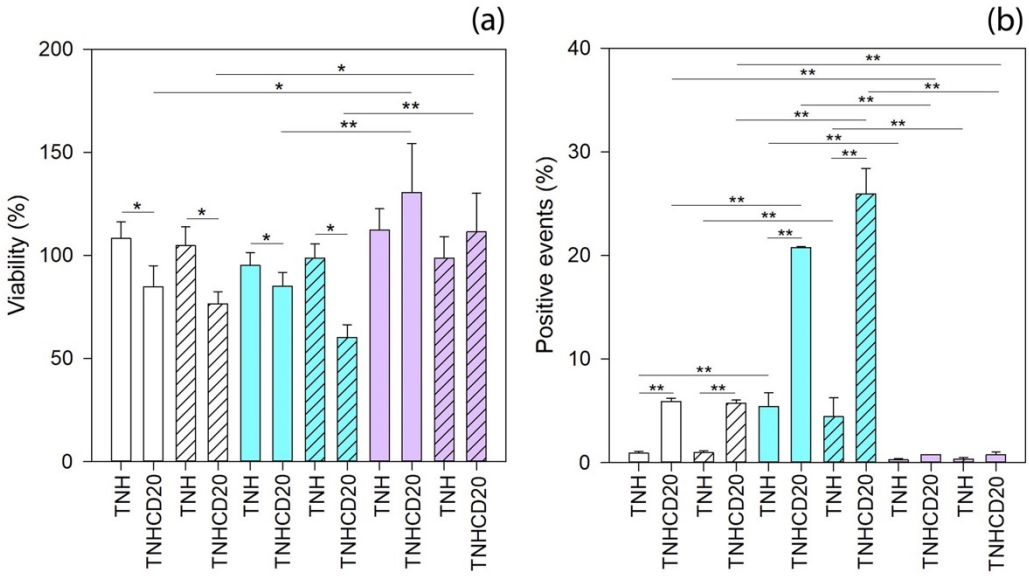

Figure 30 (a) Cytotoxicity and (b) internalization assays of TNH and TNHCD20 at 24 (solid colors bars) and 48 (dashed bars) hours in lymphocytes (white bars), Daudi (blue bars) and HL60 (purple bars).

Number of assays: $n \geq 4$ for cytotoxicity and $n \geq 2$ for internalization assay. Statistical analysis: three-way ANOVA. ** for $p \leq 0.001$, * for $p \leq 0.05$.

Differently, the TNHCD20 remarkably decreased the viability of both lymphocytes and Daudi cell lines ($p=0.021$ and $p=0.03$, respectively), but not that of CD20-HL60 ($p=0.162$) if compared to treatment with pristine TNH. Considering the different cell lines treated with TNHCD20, it was observed that the CD20-HL60 cells were not affected by the treatment, while the CD20+ cell lines, lymphocytes and Daudi, were slightly impaired ($p=0.004$ for HL60 vs. lymphocytes and $p<0.001$ for HL60 vs. Daudi).

The results of cytofluorimetric analysis of the cellular interaction with TNH and TNHCD20 are reported in Figure 30-b. As already highlighted for the cytotoxicity, there was no statistical difference between the two treatment times of 24 and 48 hours. Analyzing the cellular interaction with the nanoconstructs considering the cell lines and the two treatment times, it results that Daudi cells better interacted with the TNH nanoconstruct than lymphocytes and HL60 ($p<0.001$). Considering the TNHCD20, it interacted more with Daudi than with lymphocytes and HL60 ($p<0.001$) and more with lymphocytes than HL60 ($p=0.001$). Besides, the most noticeable difference between the pristine and the CD20-targeting nanoconstructs was the striking increase in the interaction of TNHCD20 with lymphocytes and Daudi ($p<0.001$) compared to that with HL60 cells ($p=0.704$), referable to the surface functionalization with antiCD20 antibody. This increase justifies itself in a very intuitive way, since antiCD20-engineered nanoconstruct presents on its surface moieties that can efficiently target the CD20 protein expressed on the plasma membrane of both lymphocytes and Daudi cell lines. At the same time, the TNHCD20 did not interact with HL60 cells since they these cells do not express CD20 proteins on their plasma membrane[209.]

These results clearly demonstrate the following correspondence: the increase of cellular interactions is accompanied by a consequent cytotoxicity of TNHCD20 against the target cells, as already described in the comment to Figure 30-a. These results are in agreement with the fact that anti-CD20 monoclonal antibodies, used as the key to the biofunctionalization of the proposed nanoconstruct, actually represent the main treatment to face B cell malignancies triggering cell death even without immune system effector mechanisms[210–214]. Remarkably, it must be emphasized that the treatment with the antiCD20-engineered TNH results not only

effective but also selective, as the increment in both interaction and cytotoxicity was more significant considering Daudi cancerous cells instead of lymphocytes.

The fluorescence microscopy analysis (Figure 31) qualitatively confirmed the interaction of the two nanoconstructs with the tested cell lines for both 24 and 48 hours of treatments. The images of the samples treated with the pristine TNH did not show any cellular interactions neither after 24 hours(Figure 31-a, b and c) nor after 48 hours (Figure 31-g, h and i). On the contrary, the interaction of the TNHCD20 nanoconstruct with cell membranes of both lymphocytes (Figure 31-d) and Daudi (Figure 31-e) cells was clearly evidenced already after 24 hours of treatment by the detection of blue fluorescence, related to the secondary antibody used for antiCD20 functionalization, on the plasma membrane (here in green fluorescence). Referring to the 48 hours of treatment, the close interaction was confirmed for lymphocytes (Figure 31-j) and was even more evident for the tumoral Daudi cells (Figure 31-k). In contrast, the fluorescence microscopy on tumoral HL60 cells did not evidenced any interaction of TNHCD20 with their plasma membrane (Figure 31-f and Figure 31-l for 24 and 48 hours, respectively), as already observed in the case of treatment with the non-functionalized TNH. It is interesting to observe how TNHCD20, although present in the treatment well, did not make any contact with the plasma membrane of HL60 cell even after 48 hours (Figure 31-l).

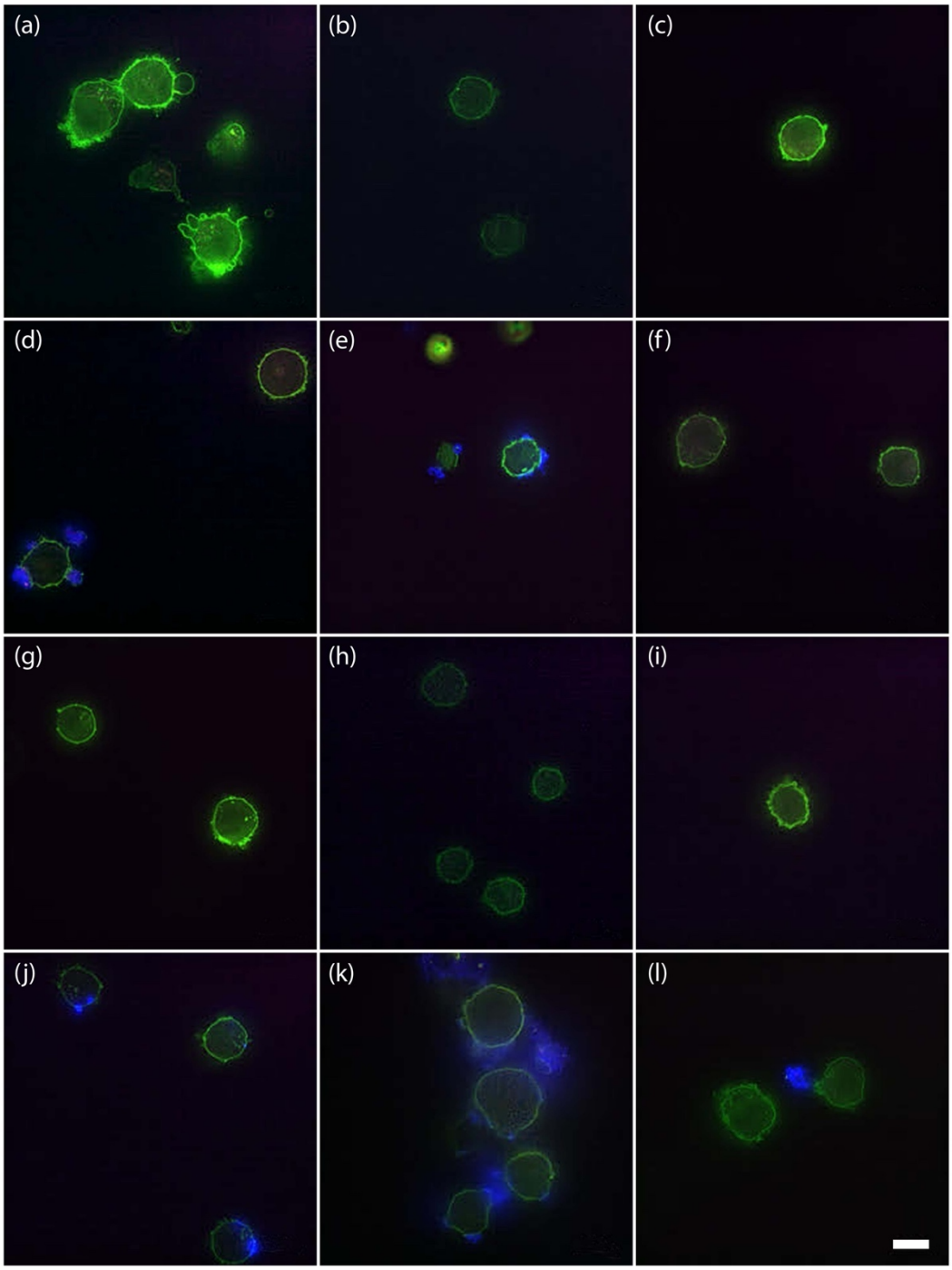

Figure 31 Fluorescence microscopy images of the internalization of the two nanoconstructs. (a) lymphocytes, (b) Daudi and (c) HL60 with TNH at 24 hours, (d) lymphocytes, (e) Daudi and f) HL60 with TNHCD20 at 24 hours, (g) lymphocytes, (h) Daudi and (i) HL60 with TNH at 48 hours, (j) lymphocytes, (k)

Daudi and (l) HL60 with TNHCD20 at 48 hours. Green represents the WGA488-labelled cells' membranes, blue the secondary antibody of the TNHCD20 nanoconstruct, purple the WGA647-labelled EVs and red the Atto550-lebelled ZnO NPs. Scale bar: 10 µm.

6.3.6 Stimuli-responsive TNH and TNHCD20 nanoconstructs with ultrasound shock waves

The obtained results suggest the possibility to employ EVs engineered as TNH and, even better, as TNHCD20 as a selective and stimuli-responsive smart nanotool for cancer treatment. Previous results have already confirmed the intrinsic cytotoxic effect of pristine ZnO NCs and the possibility to activate them by ad hoc external stimuli to further enhance their cytotoxic capability[52,65].

Several physical stimuli, such as light[40,215], magnetic fields[216,217] and acoustic waves[44,65], can be exploited to activate inorganic nanoparticles and induce a cytotoxic effect in living cells. Specifically, periodical acoustic pressure waves, like ultrasounds, or acoustic pulses, like shock waves, can produce acoustic cavitation in water-based media. Inertial cavitation can induce the formation of water-derived radicals and mechanical damages to cellular compartments and membrane[44]. Indeed, the possibilities of acoustic stimulation are many as well as challenging to be optimized. Continuous or pulsed ultrasound irradiations, highly focused or unfocused transducers use, high or low-intensity ultrasound have been broadly exploited in the literature[44]. Of prominence importance is however the use of nanomaterials, the presence of which can on the one hand reduce the cavitation threshold, thus allowing to employ low intensity ultrasound or shorter application times[19,56].On the other hand, nanomaterials can be opportunely functionalized and engineered to allow specific targeting to selected cells or tissues, thus favouring the cytotoxic action of such nanoparticles-assisted ultrasound in a specific region [218]. Motivated by the above-mentioned rationale, as a proof of concept, we proved the cytotoxic effect of TNH and TNHCD20 when activated with high-energy ultrasound shock waves (SW) on *in vitro* healthy and cancer cell line, i.e. lymphocytes and Daudi cells. As shown in Figure 32, 48 hours after the treatment, the SW alone caused a slight decrease of the cell proliferation in both lymphocytes and Daudi cells. This result accounts for the good choice of the irradiation parameters (intensity of 12.5 MPa, number of used shots - 250, number of SW applications, 3 times/day, one treatment every 3h), in terms of stimuli safety. Noticeably, the treatments with TNHCD20 presented a higher, even though not significant, cytotoxic effect on Daudi cancer cell line with respect to that on the healthy counterpart (lymphocytes). Strikingly, a larger and statistically

significant difference (p=0.014) in cell viability between Daudi and lymphocytes was measured treating cells with the combination of both TNHCD20 and SW.

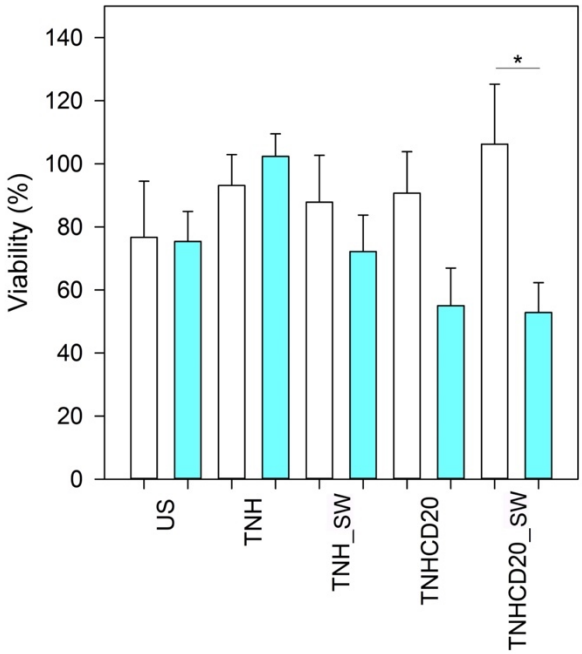

Figure 32 Viability of lymphocytes (white dashed bars) and Daudi (blue dashed bars) 24 h after the SW treatment (i.e. 48 hours after the nanoconstruct treatment). Cells were treated with SW alone, TNH, TNH in combination with SW (TNH_SW), TNH^{CD20}, and TNH^{CD20} in combination with SW (TNHCD20_SW). Each column is normalized with respect the untreated cells and the experiments were conducted with n=4. Statistical analysis: three-way ANOVA. ** for $p \leq 0.001$, * for $p \leq 0.05$. The p value obtained for TNHCD20_SW between B lymphocytes and Daudi cells is p=0.014.

Despite the full understanding of the biomolecular mechanism of the induced cell death is still the focus of our further studies and characterizations, we recall here that the observed enhanced cytotoxicity is due to the concomitant administration of the SW and of the targeting TNHCD20. In particular, the observed cytotoxicity could be caused by the combination of various concomitant effects leading to the mechanical injury of the cell structure[65] : (i) an enhanced acoustic bubble cavitation and (ii) the "nanoscalpel effect" supported by the preferred interaction of the TNHCD20 construct with the Daudi cell line. Finally the viability of the treated cells may also have been affected by an electric charge imbalance, due to the piezoelectric behavior of ZnO nanostructures[219]. The present study suggests the applicability of our hybrid nanoconstruct as a targeted anticancer tool, which not only demonstrated to be more cytotoxic to Burkitt's

lymphoma cells, but further highlighted its potential for an externally and on-demand activated therapy.

6.4 Conclusion

In this chapter it is demonstrated the possibility to efficiently engineer the EVs derived from healthy cells using inorganic nanoparticles and monoclonal antibodies. In particular, an efficient active method based on freeze-thaw cycles and mild heating to load B-cell derived EVs with a nanotherapeutic stimuli-responsive cargo, i.e. ZnO NCs is here proposed. The resulting re-engineered EVs are thus called Trojan Nano Horses (TNHs), to convey the concept of biomimetism provided by EVs and the cytotoxic potential given by the ZnO NCs on this novel nanoconstructs. Such TNHs show good hemocompatibility and high colloidal stability up to 48 hours in cell culture medium. Afterwards, TNHs are modified at their surface with anti-CD20 monoclonal antibodies to obtain a selective targeting against lymphoid cancer cell line, i.e. Daudi cells. The *in vitro* characterization has shown the high TNH biocompatibility and the remarkable selectivity of anti-CD20 engineered nanoconstructs (TNHCD20) towards the target CD20+ lymphoid Daudi cell line compared to the CD20- cancerous myeloid cells (HL60) and the healthy counterpart (lymphocytes). Furthermore, an enhanced cytotoxicity of TNHCD20 directed against Daudi cancer cells was demonstrated after the nanoconstructs activation with high-energy ultrasound shock waves. The obtained hybrid nanoconstructs can be thus on-demand activated by an external stimulation, here acoustic waves, to efficiently exploit a cytotoxic effect conveyed by the ZnO NCs cargo against selected cancer cells, while remaining highly biocompatible towards healthy B cells.

Chapter 7

CD38 Targeted Liposome Enveloping ZnO Nanocrystals in Combination with Ultrasound as Therapy for Burkitt's Lymphoma

7.1 Introduction

Extracellular vesicles (EVs) are widely studied as possible therapeutic platform due to their pivotal role in intracellular communication[220]. Despite their very high organotropism [221] and their captivating endogenous functionalities[222], EVs present some limitations. First of all, technical difficulties are encountered attempting to purify and classify the type of vesicles[221], and nowadays there is not a manufacturer method able to ensure a large-scale production[221] of any EVs-based biomedical technologies. Another major drawback is the rapid clearance from the blood demonstrated for systemically administered EVs, i.e. few minutes in healthy animals, due to the circulating phagocytic cells[223]. Even though the investigation of EVs as nanocarrier of biomolecules, drugs and nanoparticles is still in its beginning[224] and its potential is widely recognized, up to now the ability of EVs to incorporate the drug is poor and appropriate loading methods have to be

developed for biomedical applications[221,224]. In this chapter a different and fascinating approach to encapsulate ZnO NCs is proposed: the use of biomimicking liposomes.

Liposome are defined as spontaneously forming elements and they are characterized by a spherical shape, creating a lipid bilayer membrane and a hydrophilic core[225]. Their composition authorizes to consider them as the most biocompatible and least toxic artificial system[221] in nanomedicine field, and they are also able to contain moderate quantity of either hydrophobic nor hydrophilic cargo. Several drugs have been incorporated in liposomes, and although the low incorporation yield, they have already been FDA approved[226].

Liposomes are also proposed as a suitable candidate for anticancer therapy due to their physical and chemical characteristic. In particular, a high flexibility in designing liposome structure has been demonstrated, especially for chemical modifications able to easily incorporate targeting ligands with different nature[221,225], providing them with new functionalities. Indeed, liposome outer membrane can be effortlessly conjugated with PEG molecules, able to increase the blood circulation time of liposomes[227], and consequently increase the enhanced permeability and retention effect (passive targeting). As mentioned before, liposomes can also be functionalized with different elements able to perform active targeting, for example towards cancerous cells.

Fu et al. proposed liposome as drug delivery system, able to enhance Doxorubicin intracellular release for lung cancer treatments[228]. To increase the selectivity for the proposed therapy towards cancerous cells they employed arginine-glycine-aspartate (RGD) peptide as targeting agent toward integrin $\alpha_v\beta_3$ receptors, which rise the accumulation of liposome at tumor site and, together with pH responsive-degradation, demonstrate an excellent selective inhibition of tumoral cell activity *in vitro* and *in vivo*[228]. Low et al. instead focused their studies on folate-conjugated liposomal system, able to be selectively toxic against folate receptor (FR) positive cells, as for example lung, colon, kidney tumors[229]. Their doxorubicin-loaded targeted liposomes showed a 45-fold higher uptake and cytotoxicity 85-times higher when targeted liposomes were administered to FR^+ cells with respect the non-targeted counterpart[229]. With the aim to prevent cancerous cell growth and metastases formation *in vitro*, Narayanaswamy et al. presented monoclonal antibody 2C5 as targeting agent for their liposomes, which were loaded with two different chemotherapeutics[230]. They were able to demonstrate the efficacy of salinomycin and paclitaxel delivered by liposome as

selective killing agent for breast cancer cells, both for stem bulk cells of the tumor[230].

The study of liposomes as therapeutic agent in the nanomedicine field involves not only the type of surface modifications, but also the components that can be incorporated into liposome and delivered to the target element. Over the past two decades, a remarkable large variety of biomolecules, drugs and nanoparticles has been proposed as possible liposome cargo[225]. Charged structure as DNA or RNA can be successfully incorporated based on electrostatic interaction between nucleic acids, negatively charged, and phospholipids, positively charged, with the aim to prevent and treat various diseases[231]. A representative example approved for the clinical use are COVID-19 vaccines, which exploit lipidic nanoparticles to deliver mRNA to prevent infection with severe acute respiratory syndrome caused by this disease[232]. Other research groups proposed an extensive selection of nanoparticles encapsulated in a double lipidic layer, with applications in biomedical field. Lin et al. studied an innovative photoelectrochemical immunoassay for the determination of aflatoxin B_1 (AFB_1) in foodstuff, based on liposome coated mesoporous silica loaded with L-cysteine[233]. Silica nanoparticles play the main role also in the research of Liu at al, where hemoglobin was adsorbed on their surface, and the nanoparticles where encapsulated in liposomes, demonstrating an enhancement of hemogoblin release *in vitro*[234]. Gold nanoparticles were also investigated, for example by Epanchintseva et al. for the development of systems for nucleic acid delivery, to create effective therapeutics against various diseases. They were able to design and efficiently coat gold nanoparticles with lipidic shell for future biomedical purposes[235]. Kang et al. also proposed gold nanoparticles shielded by lipidic shell, demonstrating the enhancement of drug delivery toward cancerous cells and opening the possibility for external activated near-infrared photothermal treatment in synergy with anticancer drugs based on these lipid-covered gold nanoparticles[236]. Among the promising type of nanoparticles, zinc oxide is widely used in biological, chemical, and medical fields, and different research groups proposed ZnO nanoparticles shielded with liposomes as nanomedical tool. Zeng et al. investigate lipidic-coated ZnO nanoparticles and their potential role as lymphatic-targeted drug carriers, demonstrating an effective drug delivery, an enhanced internalization of nanoparticles, and a strong preferential killing capability toward cancerous cells[237]. Instead, Ancona et al. proposed lipidic-

coated ZnO nanoparticles as Reactive Oxygen Species (ROS) generator in photothermal therapy of human epithelial carcinoma cells *in vitro*. They were able to prove ROS generation in cells, and the cytotoxicity resulted from their generation under UV exposure in cancerous cells thank to their lipidic coated ZnO nanoparticles[238].

In this chapter it is proposed a targeted liposome-based system, in which the cargo are the newly synthetized zinc oxide nanocrystals. The driving idea is to design and create a lipidic biomimetic shell, resembling to certain key characteristics to natural EVs, decorated with fragmented anti-CD38, aiming at mimicking the intrinsic homing capabilities of natural EVs towards recipient cells. The cargo is composed by ZnO nanocrystals, which can be considered as therapeutically induced active nanoparticles: their killing capability becomes effective only when externally activated by ultrasound irradiation. The proposed targeted ZnO-liposomal system exhibits an efficient selectivity and cytotoxicity on-demand toward cancerous Burkitt's Lymphoma cells, without significantly affecting healthy B lymphocytes.

7.2 Materials and methods

7.2.1 Nanocrystals synthesis and functionalization

Zinc oxide nanocrystals were synthesized with a different and improved procedure with respect the one reported in the previous chapters. This new synthesis utilizes a wet chemical process, exploiting oleic acid (Sigma-Aldrich) as stabilizing agent, as reported elsewhere[108,239]. Briefly, zinc acetate dihydrate (526 mg, ACS Reagent, Sigma-Aldrich) was dissolved in 40 mL of ethanol and heated at 70 °C. Bidistilled water (1 mL, from a Direct Q3 system, Millipore, Burlington) and oleic acid (140 μL) were added to the solution. Then, tetramethylammonium hydroxide (1.044 mg, TMAH, Sigma-Aldrich) previously dissolved in bidistilled water (1.052 mL) and ethanol (10 mL), was added to the zinc precursor solution to form the NCs. After 10 minutes, the NCs were collected and centrifuged to be resuspended in fresh ethanol. The procedure was repeated three times. ZnO NCs surface was then functionalized with amino-propyl groups, adding 10 mol% of 3-aminopropyltrimethoxysilane (APTMS, Sigma-Aldrich) with respect to the molar amount of ZnO, according to the literature[16,108,218]. More in details, ZnO NCs were dispersed in ethanol at a concentration of 2.5 mg/mL and heated up to 70 °C

in nitrogen atmosphere e refluxing conditions. APTMS was added to the solution and the reaction was carried on for 6 h at 70 °C. At the end of the procedure, NCs were then collected and washed three times by a centrifugation and redispersion process. ZnO NCs were stored as ethanol colloidal suspensions, according to previous works.[108,207]

Dynamic Light Scattering (DLS) and Z-Potential measurements were carried out with Zetasizer Nano ZS90 (Malvern Instruments). The size of amino-propyl functionalized ZnO NCs was measured in bidistilled (bd) water at a concentration of 100 µg/mL. Z-Potential measurements were performed in bd water at a concentration of 100 µg/mL. Nanoparticles Tracking Analysis (NTA) measurements were executed on functionalized ZnO NCs with a NanoSight NS300 (Malvern Panalytical). To prepare the sample 6 µL of 1 mg/mL NCs solution were diluted up to 1 mL in bidistilled water. For each sample, three videos of 60 s of the samples fluxing in the instrument chamber were captured and analyzed with the NTA 3.4 software (Malvern Panalytical).

Functionalized ZnO nanocrystals were also characterized with Transmission Electron Microscopy (TEM). NCs were dispersed in water at a concentration of 50 µg/mL. Then, 10 µL of the solution were deposited onto a Lacey Carbon Support Film (300 mesh, Cu, Ted Pella Inc.) and let dry. The measurements were held with a Talos™ F200X G2 S(TEM) from Thermo Scientific at an operating voltage of 200 kV.

7.2.2 Antibody reduction and lipid coupling

The used antibody was the FDA approved Anti-CD38 Daratumumab, with a concentration equal to 20 mg/mL (CreativeBiolabs), and it was fragmented by reduction with the use of Tris(2-carboxyethyl)phosphine hydrochloride (TCEP). First, 200 µL of TCEP was centrifuged at 1000 g for 30 s in a 1.5 mL Pierce™ spin cup (Thermo Scientific); the filtered solution through the spin cup filter was discarded and the filter containing the TCEP was placed in a new spin cup container. A 100 µL of EDTA (10 mM) solution in phosphate saline buffer (PBS, Sigma-Aldrich) containing 200 µg of Anti-CD38 Daratumumab was prepared and added in the TCEP-containing filter , delicately pipetting the solution in the gel.

The spin cup was then placed for 24 h in a rotating wheel. The reduced sample was finally centrifuged at 1000 g for 1 min and the filter discarded.

To evaluate the concentration of the fragmented antibody into the solution, the Bradford protein assay, aimed at amino-acid quantification through a spectroscopic measurement, was exploited. Bovin Serum Albumin (Sigma-Aldrich) dissolved in PBS was used to build a standard curve for protein evaluation. For the sample preparation, Daratumumab and fragmented Daratumumab was diluted in PBS with a 1:16 ratio. In a 96 well plate (TC treated, Corning), 10 µL of both reference and sample solutions were added. Then, 200 µL of Coomassie brilliant blue G-250 dye (Bio-Rad) diluted 1:5 in bidistilled water was added to each well. The absorbance of the solutions at 590 nm was measured through a Multiskan GO microplate spectrophotometer (Thermo Fisher Scientific) and the obtained values were compared with the standard curve.

To verify the effectiveness of Daratumumab reduction, Sodium Dodecyl Sulphate-Polyacrylamide Gel Electrophoresis (SDS-PAGE) was performed. Criterion TGX stain free precast gel (45 µL wells, 4-15%, BioRad) was used and three sample were loaded for the test: a marker (Precision Plus Protein Dual Color Standard, BioRad), the whole anti-CD38 and the fragmented anti-CD38. Sample containing the intact antibody was prepared adding 2.25 µL of Daratumumab (1 mg/mL) to 24.75 µL of PBS and 9 µL of Laemmli Sample Buffer (BioRad); 27 µL of reduced anti-CD38 was mixed with 9 µL of Laemmli Sample Buffer. Water sample was used to separate each sample lanes, and it was composed by 27 µL of bd water and 9 µL of Laemmli Sample Buffer. To complete the samples preparation, the solutions were heated at 95 °C for 10 min. Samples were then loaded in precast gel, which was previously immersed in running buffer composed by 70 mL of 10x Tris/Glicine SDS and 630 mL of bd water, inside the electrophoresis cell. The cell was closed and connected to the power supply (PowerPac™ Basic Power Supply) at constant voltage equal to 200 V. At the end of electrophoresis process, the gel was extracted by the cell, and underwent to 3 washing steps, each lasting 5 min under orbital shake at 50 rpm. Finally, the gel was stained by pouring approximately 50 mL Coomassie solution (Coomassie, BioSafe) on it, under continuous shaking at 50 rpm for 1 h. After removing the stain, the gel was washed twice with bd water, each lasted 30 min on orbital shaking at 50 rpm. After the last washing step, the gel was left overnight in the dark on orbital shaking at 50 rpm. A picture was taken the day after, to evaluate the reduction of anti-CD38 on the electrophoretic lane, comparing molecular

weights of the whole anti-CD38 and fragmented anti-CD38 with the reference marker.

To further create a targeted liposome, the fragmented antibody was immediately conjugated with a functional phospholipid. DSPE-PEG(2000)-Maleimide (1,2-distearoyl-sn-glycero-3-phosphoethanolamine-N-[maleimide(polyethylene glycol)-2000] (from Avanti Polar Lpids, Merck, stock at 10 mg/mL in chloroform), in a molar ratio equal to 3:1 with respect to the reduced anti-CD38, was let to evaporate in a glass vial. Dimethyformamide (DMF) was added in the glass vial, in a volume equal to the volume of the reduced antybody, than the reduced anti-CD38 was added to the glass vial and left under orbital shaking at 250 rpm, at room temperature for 1 h. The conjugated anti-CD38 with DSPE-PEG(2000)-Maleimide was then stored at -20 °C.

7.2.3 Liposome formation and nanocrystals encapsulation

To enhance both the nanoparticles' stability in aqueous media and their biocompatibility, a custom made lipidic coating was designed biomimicking the natural EVs features. Briefly, a mixture of different commercially available lipids and chloroform was dried under vacuum overnight and then resuspended in a solution of ethanol and water, and then it was used to coat the nanoparticles by inducing self-assembly due to a solvent exchange technique, reported elsewhere[240].

More in detail:

- a negatively charged lipid DOPA (1,2-dioleoyl-sn-glycero-3-phosphate dissolved in chloroform, by Avanti Polar Lipids),
- a neutral lipid DOPC (1,2-dioleoyl-sn-glycero-3-phosphocholine dissolved in chloroform, by Avanti Polar Lipids),
- a PEGylated lipid DSPE-PEG(2000)-Amine (1,2-distearoyl-sn-glycero-3-phosphoethanolamine-N-[amino(polyethylene glycol)-2000] dissolved in chloroform, Avanti Polar Lipids),
- the PEGylated lipid, DSPE-PEG(2000)-Maleimide (1,2-distearoyl-sn-glycero-3-phosphoethanolamine-N-[maleimide(polyethylene glycol)-

2000], previously conjugated to the reduced anti-CD38, as described above, and
- a cholesterol solution in chloroform (Sigma Aldrich)

were mixed in a molar ratio of 50:10:1.4:0.1:38.5and dried overnight under vacuum. Afterwards, the dried mixture was resuspended in a solution made up of absolute ethanol and water, with a volume ratio of 40:60.

The lipidic solution was hence added to a pellet of previously centrifuged nanoparticles, according to an optimized NCs/lipids weight ratio of 2:1, and then the mixture was sonicated with the help a sonication bath (Branson 3800 CPXH, Branson Ultrasonics Corporation) for 3 minutes at 59 kHz to better disperse the ZnO NCs into the lipidic solution. Thereafter, following the solvent exchange technique, a volume of bidistilled water was added to allow the formation of the lipidic shell on the surface of the nanoparticles and a final 1 mg/mL concentration of NCs was achieved. A further sonication of 5 minutes was then carried out to obtain a homogeneous sample solution and to reduce the size of the newly formed lipidic shells.

Another lipid coating without the reduced anti-CD38 was also designed as control. The lipidic mixture had the final ratio of 50:10:1.5:38.5 corresponding to DOPA:DOPC:DSPE-PEG-NH2:Cholesterl. It was dried overnight and the whole process was identically repeated to coat the ZnO NCs.

DLS, Z-Potential, NTA and TEM measurements were performed on the control liposome- coated ZnO NCs (ZnO-Lip), with same methods reported in Section 7.2.1 or here above, to characterize the nanoconstruct and underline the effectiveness of the encapsulation process. The anti-CD38 targeted liposome ZnO NCs (ZnO-LipCD38) was characterized by NTA only.

7.2.4 Cell lines

Daudi (ATCC, CCL-213), B lymphocytes, IST-EBV-TW6B (IRCCS AOU San Martino), and HL60 were cultivated as reported in section 3.2.6 and 5.2.1, respectively.
The expression of CD38 antigen on cell membrane surfaces was evaluated for all the cell lines. 10^6 cells were collected and centrifuged at 150 g for 5 min and were resuspended in 1 mL PBS/0.5% BSA. Cells were incubated for 10 min in the dark at 4° degree with CD38 antibody REAfinity (Miltenyi Biotec) and the respective

isotype control. Cells were washed twice, and then resuspended in 1 mL PBS/0.5% BSA. Unstained cells were used as a control population to exclude debris and impurity derived from buffer solution.

7.2.5 Cytotoxicity and internalization tests

Cell viability was evaluated with WST-1 cell proliferation assay (Roche) after 24 h, 48 h or 72h treatments with scalar doses of ZnO NCs, or liposome coated ZnO NCs (ZnO-Lip). ZnO NCs or ZnO-Lip nanoparticles were diluted in pre-warmed cell growth media to obtain different sample solutions with different concentration: 10, 20 and 40 μg/mL were tested. 2×10^4 cells/well were seeded in 100 μL/well of prepared solution in 96 well flat bottom plates for suspension (Greiner-bio one) and incubated at 37 °C in 5% CO_2[73]. WST-1 reading was performed after 20 h, 44 h or 68 h. The same procedure was employed to test cell viability of Daudi and Lymphocytes after 24 h, 48 h or 72 h treatment with 40 μg/mL of liposome coated ZnO NCs (ZnO-Lip) and reduced anti-CD38 targeted liposome coated ZnO (ZnO-LipCD38). The experiment was performed in triplicates.

Internalization of ZnO-Lip and ZnO-LipCD38 was evaluated by flow cytometry, using with Guava Easycyte 6-2 L instrument (Merck Millipore, KGaA), as reported elsewhere[65,162]. For this assay, after the lipidic-shell formation and NCs encapsulation, liposomes were labelled with DiD, using 5 μL of DiD for 1 mg of NCs and incubated in shaking at 250 rpm at 37 °C for 30 min. 2×10^5 cells/well were plated at 1 mL/well with cell medium containing 40 μg/mL of DiD labelled ZnO-Lip or DiD labelled ZnO-LipCD38 into 24 well flat bottom plates for suspension (Thermo Scientific) and incubated at 37 °C in 5% CO_2. After 24 h, 48 h or 72 h cells were washed twice with PBS through centrifugation at 140 g for 5 min, then re-suspended in 500 μL of PBS and analyzed. The experiment was performed in duplicates.

7.2.6 Ultrasound treatments and evaluation of cell death

2×10^5 cells/well were plated at 2 mL/well. Treatment cell suspensions were: (i) cells alone, to assess the cytotoxic effects of ultrasound (US); (ii) cells with 40 μg/mL of ZnO-Lip; (iii) cells with 40 μg/mL of ZnO-LipCD38. Plated cells were

left at 37 °C in 5% CO_2 for 24 h, and then exposed to ultrasound irradiation. US were generated by LipoZero G39 (GLOBUS) at 1 MHz as frequency, 100% duty cycle, with different acoustic density generated by the transducer (0.3 and 0.45 W/cm^2) and different exposure times (30 s and 1 min), and only two wells per plate were used, to avoid cross talk among well due to unwanted US exposure. Promptly after the US treatment, 100 μL/well of cells suspension was transferred into 96 well flat bottom plates for suspension (Greiner-bio one) and incubated at 37 °C in 5% CO_2, with three technical replicates per sample. The combined cytotoxic effect of US and nanoconstruct, and cytotoxic effect of US were evaluated 24 h, 48 h and 72 h after the treatment, using WST-1 cell proliferation assay, with the same procedure previously reported. The experiments were performed in triplicate.

Further analyses were performed to evaluate apoptotic processes, which lead to the cytotoxicity of the combined US-nanoconstructs treatments. After the US treatments cells were incubated at 37 °C in 5% CO_2. After 24 h, 100 μL of cell suspension was stained with 100 μL of Guava Nexin Reagent (Guava® Nexin Reagent containing Annexin V and 7-AAD, Luminex), incubated at room temperature for 20 min and finally acquired on Guava Easycyte 6- 2 L flow cytometer.

7.2.7 Fluorescence microscopy assays

The internalization of ZnO-Lip and ZnO-LipCD38 in Daudi and Lymphocyte cells was evaluated also through spinning-disk confocal fluorescence microscopy (Ti2 Nikon equipped with Crest Large FOV laser and 60x PlanAPO objective, NA = 1.40). ZnO-Lip and ZnO-LipCD38 were labelled with DiD and 2×10^5 cells/well were plated at 2 mL/well with different treatments (controls, labelled ZnO-Lip, labelled ZnO-Lip CD38) in 24 well flat bottom plates for suspension, as reported for internalization assay with flow citometry. After 24 h of incubation at 37 °C in 5% CO_2, cells were collected and centrifuged at 140 g for 5 min and resuspended in 200 μL of PBS and then 200 μL of Image-iT Fixative Solution (4% formaldehyde, methanol-free, Thermo Scientific) was added, both PBS and fixative solution were at 4 °C. After 10 min of incubation, cells were centrifuged at 250 g for 5 min and the pellet was resuspended in 400 μL of PBS. To label the cell membrane, cells were centrifuged at 250 g for 5 min and resuspended in 250

μL of PBS, and 0.6 μL of Wheat Germ Agglutinin (WGA) conjugated with Alexa Fluor 488 (WGA488, λ_{ex} = 495 nm, Thermo Fisher) was added and incubated for 10 min at room temperature. Cells were centrifuged again at 250 g for 5 min, and resuspended in 250 μL of PBS, and 0.08 μL of Hoechst (Thermo Fisher Scientific) was added to label cell nuclei and incubate for 5 min at room temperature. Then, after two washing steps with PBS, cells are re-suspended in 250 μL of PBS and a 50 μL droplet of this cell solution was spotted in a 8-well chamber slide (Thermo Scientific Nunc Lab-Tek II CC2 Chamber Slide System) and confocal fluorescence microscopic images were acquired.

The effectiveness of the incorporation anti-CD38 fragments into the lipidic shell which cover ZnO NCs was evaluated also through spinning-disk confocal fluorescence microscopy. First of all, ZnO-LipCD38 were incubated for 1 h at room temperature on a rotating wheel with 0.7 μL of a anti-human secondary antibody (AffiniPure F(ab')2 Fragment Goat Anti-Human IgG, Fc fragment specific, 1.3 mg/mL in water, Jackson Immunoresearch)) bound to a coumarin fluorescent dye (λ_{ex} = 387 nm). This strategy ensure the interaction just with Dartumumab fragments, due to the selectivity of the secondary antibody with the anti-CD38 binding sites. Secondly, ZnO-LipCD38 were incubated with DiD, to label the liposome shell. Cells were then treated as reported above for the cytotoxicity test with 40 μg/mL of nanoconstruct. After 24 h cells were collected and resuspended in PBS and Fixative solution, as previously described, and cell membranes were labelled with WGA488 according to the procedure for the internalization studies.

To further investigate cell death mechanism after nanoconstruct and US exposure, fluorescence analyses were performed with wide-field inverted fluorescence microscope (Eclipse TiE from Nikon) equipped with 40× objective (NA = 0.60). Cells were plated and treated as reported in Section 7.2.5 for the cytotoxicity assay. After 24 h from the US exposure, cells were collected and free zinc (Zn^{2+}) was labelled with FluoZin3-AM, resuspending cell pellets in 100 μL of 1 μM solution of FluoZin-3 AM fluorescent dye in cell culture medium and let incubate for 30 min at 37 °C. The cell membrane integrity was assessed with Propidium Iodine (PI, ThermoFisher) using 100 μL of 1 μM of PI solution in cell culture medium for 5 minutes at 37 °C. Then, cells were washed two times with PBS, and finally resuspended in 200 μL of PBS. 50 μL of labelled cell suspension

were spotted in a 8-well chamber slide (Thermo Scientific Nunc Lab-Tek II CC2 Chamber Slide System) and images were acquired and analyzed.

7.2.8 Statistical analysis

Data are expressed as mean ± standard error mean (SEM) and graphed with GraphPad Prism. Statistical analysis was performed by using One-Way Anova by GraphPad Prism * $p<0.0332$, ** $p<0.0021$, *** $p<0.0002$, **** $p< 0.0001$.

7.3 Results and discussion

The morphology of ZnO NCs was assessed by High-Resolution TEM analysis. As shown in Figure 33-A, single nanocrystals with dimension ranging from 6 nm to 12 nm and an almost spherical shape were successfully synthetized. The encapsulation of ZnO NCs into the lipidic shell is visible in Figure 33-B, revealing a detail of a liposome, which contains an agglomeration of several NCs. No kind of modifications in the morphology of ZnO. It has to be noted that the analyzed sample of Figure 33-B was prepared letting it dry, without staining: this aspect can influence the shape of the lipidic vesicles on TEM analysis.

The effective lipidic shell formation is further corroborated by DLS and Z-potential results, Figure 33-C and 33-D respectively. The increase in hydrodynamic diameter in bd water from the ZnO (59 nm) to the ZnO-Lip formulation (106 nm) underlines the formation of the phospholipidic bilayer around the NCs, yet modifying the hydration layer of the particles and thus the hydrodynamic size in water.

Comparing the dimension of the single ZnO NC obtained by TEM analysis with both NTA (Figure 33-E, black line) and DLS (Figure 33-C, black line) results, a certain degree of aggregation can be hypothesized. The NTA shows in particular different size distribution peaks. However, the overall ZnO NCs colloidal stability is still good, considering the DLS data and the Z-Potential (Figure 33-D, black bar).

After the lipidic shell formation, a monodispersed size distribution is achieved, as measured by both DLS and NTA (red curves in Figures 33-C and E).

Notably, the colloidal stability in water is greatly enhanced with respect to pristine ZnO NCs, as reported in Figure 33-E (red line), presenting a majorly monodisperse population despite the increase in the hydrodynamic diameter. Z-potential data, shown in Figure 33-D, further confirm the successful encapsulation of ZnO NCs in a lipidic shell, shifting from positive z-potential of ZnO NCs to negative values of ZnO-Lip. This change can be easily reconducted to the main negative charge of the lipidic shell formulation.

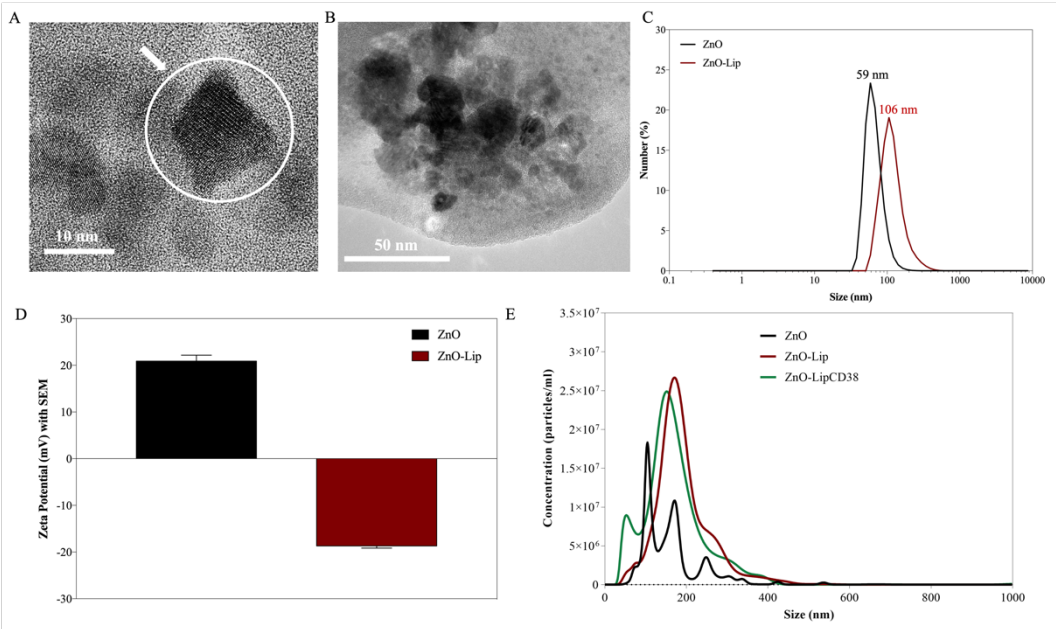

Figure 33 Transmission Electron Microscopic images of (A) ZnO NCs and (B) ZnO-Lip. (C)DLS measurements and (D) Z-potential of ZnO and ZnO-Lip (E) Nanoparticle Tracking Analysis measurements of ZnO (black curve), ZnO-Lip (red curve) and ZnO-Lip (green curve) in water

In order to functionalize the liposome coating with targeting purposes, fragments of anti-CD38 were bounded to DSPE-PEG maleimide lipids, able to create, with the same solvent-exchange method, a targeted lipidic shell.

CD38 is a human type II transmembrane glycoprotein, widely expressed on multiple immune cell populations[241,242]. The overexpression of CD38 on Daudi cells in comparison to B Lymphocytes[243,244] makes it a target of choice for therapeutic antibodies targeting nanoconstruct, as also reported in Figure 34. Acute myeloma cell line (HL60) are negative to CD38 expression, so they represents a negative control for the targeting capability of the nanoconstruct.

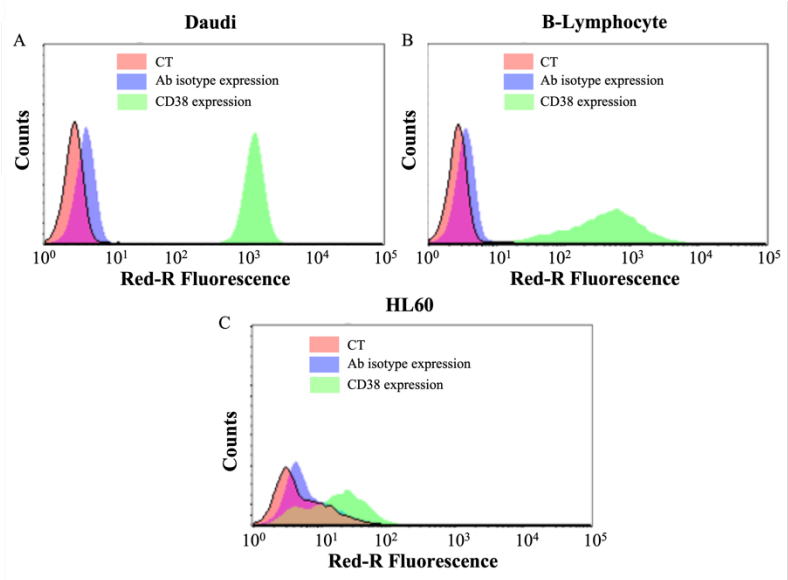

Figure 34 CD38 expression on Daudi (A), B-Lymphocytes (B) and HL60 (C) cells' membrane. Evaluation performed with flowcytometry technique.

Daratumumab is an FDA approved anti-CD38 agent, which specifically and strongly binds to CD38 epitope on Daudi cell membrane. The Daratumumab reduction process allows to expose the thiol groups of anti-CD38, which can subsequently bind to DSPE-PEG maleimide. The success of Daratumumab reduction leading to different fragments can be deduced from the gel electrophoresis results reported in Figure 35.

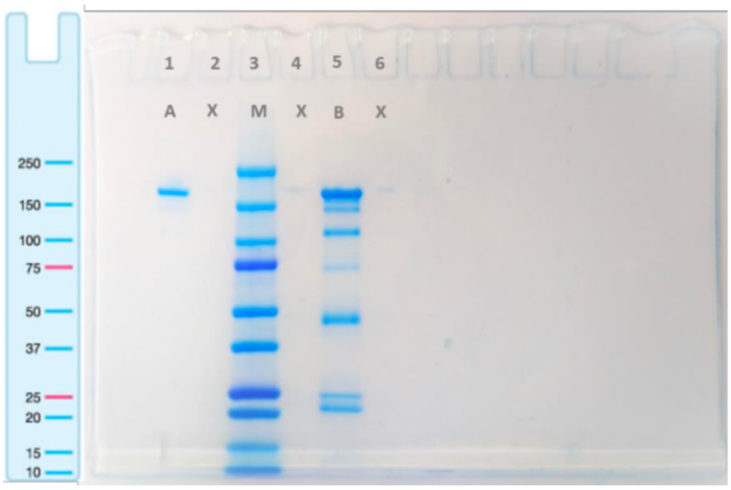

Figure 35 SDS-PAGE of anti-CD38 reduction. Non-reduced Daratumumab is represented in column A, reduced anti-CD38nis colums B, while the marcher corresponds t column M. scale unit: kDa.

NTA analyses (Figure 33-E, green line) demonstrate that in presence of anti-CD38/DSPE-PEG maleimide, no major differences can be observed in the ZnO-LipCD38 with respect to the ZnO-Lip sample, suggesting the correct formation of the lipidic shell, encapsulating ZnO NCs and improving the colloidal stability of the nanoconstruct.

The lipidic shells enclosing ZnO NCs have multiple roles, beyond the increase of colloidal stability. Biocompatibility is enhanced, and the biodegradable nature of lipids provide them with an augmented tolerance by human body[245]. Furthermore, liposomes are characterized by low toxicity, and this aspect can be exploited to deliver to cells a higher amount of ZnO NCs, which can be per se toxic in high doses, without causing any significant cytotoxic effects on *in vitro* cells.

Figure 36 demonstrates the increased biocompatibility of ZnO-Lip with respect to pristine ZnO NCs. Different concentrations (i.e. 10, 20, 40 μg/mL) of ZnO and ZnO-Lip were administered to Burkitt's lymphoma cells (Daudi, Figure 36-A,B) and healthy counterparts (B-Lymphocytes, Figure 36-C,D) and acute myeloma CD38- cells (HL60, Figure 36-E,F) and the metabolic activity of cells was evaluated with WST-1 after 24 h (Figure 36-A,C,E), and 48 h (Figure 36-B,D,F). ZnO NCs result to be toxic for Daudi cells even at low dosage (10 μg/mL), and at higher concentration the complete death of Daudi population was detected. In contrast, significant differences are noticeable when ZnO-Lip were administered. For all dosages and at all time points, cell viability of Daudi treated with ZnO-Lip is higher when compared to bare ZnO NCs, becoming significantly greater at higher dosages (both 20 and 40 μg/mL).

Different trends are demonstrated for Lymphocytes cells. The toxicity of ZnO NCs is lower per se, causing a higher metabolic activity with respect Daudi cells at any time point, in particular for 10 and 20 μg/mL. Furthermore, ZnO-Lip results to be highly biocompatible at the tested concentration also in Lymphocytes. A significant difference is evident for 40 μg/mL, where Lymphocytes viability is lower than 10 % when treated with ZnO and higher than 70 % when ZnO-Lip where administered. Acute myeloma cells demonstrated an unvaried metabolic activity at 24 h (Figure 36-E) and an increased metabolic activity at 48 h (Figure 36-F) after the administration of 10 μg /mL of ZnO.

Significant cytotoxic effects are visible at both 24 h (Figure 36-E) and 48 h (Figure 36-F) after the treatment with 20 µg /mL and 40 µg /mL of ZnO. Concerning the administration of ZnO-Lip, no significant variation in HL60 viability can be underlined for all the concentration and both the time point.

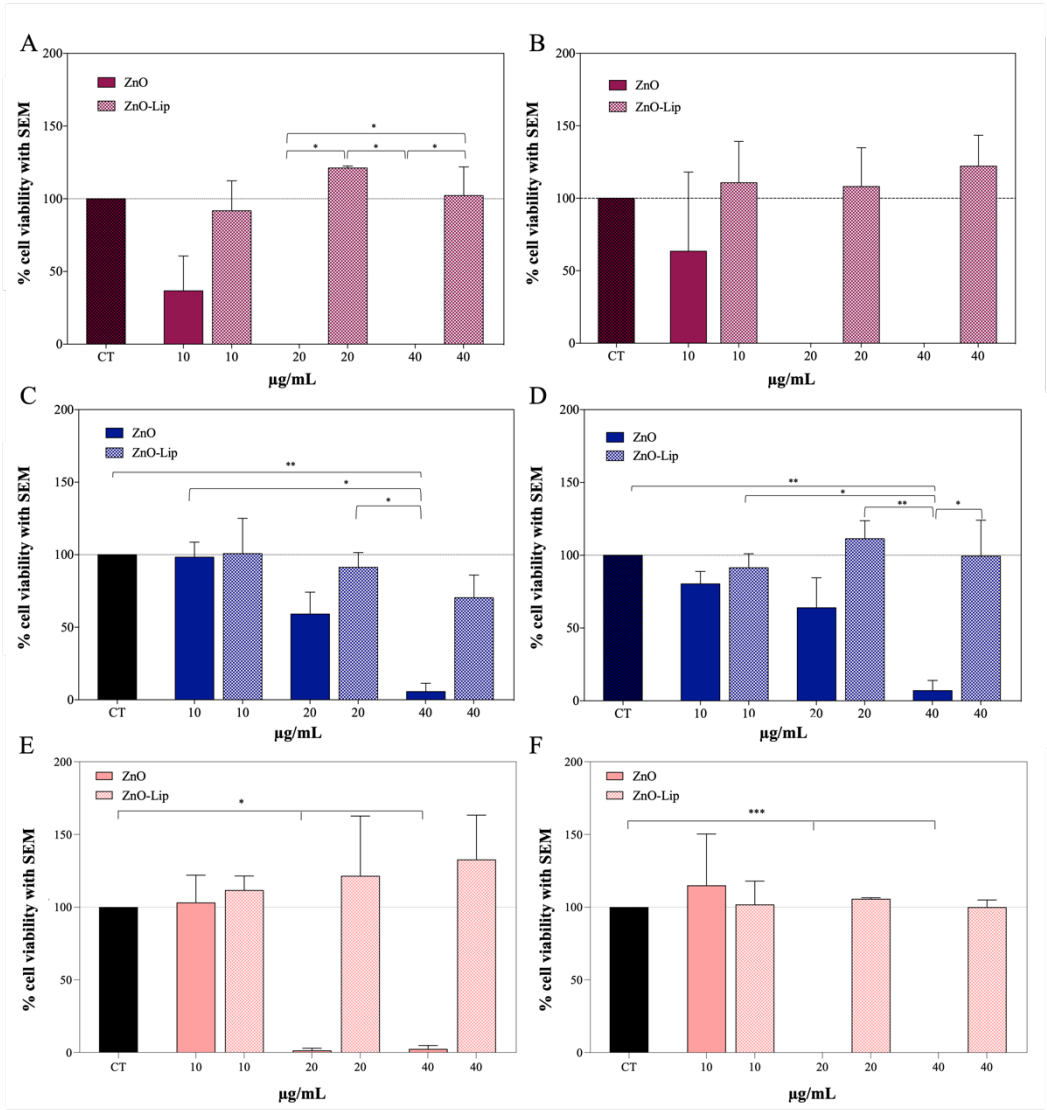

Figure 36 Cytotoxicity on Daudi cells at 24h (A), and 48h (B) of different concentrations of ZnO and ZnO-Lip. Cytotoxicity on Lymphocytes at 24h (C), and 48h (D) of different concentrations of ZnO and ZnO-Lip. Cytotoxicity on HL60 at 24h (E), and 48h (F) of different concentrations of ZnO and ZnO-Lip. All experiments were performed at least in duplicate. * $p<0.0332$, ** $p<0.0021$, *** $p<0.0002$, **** $p< 0.0001$

These results suggest that even very low concentration of ZnO NCs are characterized by an intrinsic killing selectivity toward Daudi and HL60 cells, with respect to the healthy counterparts, as reported in previous literature[108]. When

high doses of ZnO NCs are administered, large cytotoxic effects occur in both cancer and healthy cells. This intrinsic cytotoxicity makes the role of lipidic shell crucial in administering higher doses of ZnO NCs and avoiding the cytotoxic effects. These results also highlight the high biocompatibility of the ZnO-Lip nanoconstruct, even at relatively high dosages.

Therefore, the dose chosen for further treatments was the highest one, i.e. 40 µg/mL of ZnO-Lip. The cell viability and internalization in both Daudi, B-Lymphocytes and HL60 were evaluated in presence or absence of anti-CD38 fragments , bound to lipidic shell of the nanoconstruct (i.e. ZnO-LipCD38 versus ZnO-Lip), as reported in Figure 37 A and B.

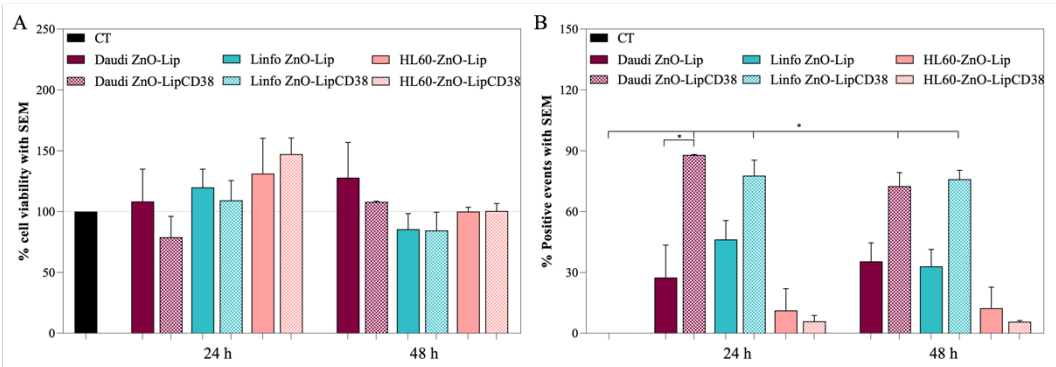

Figure 37 (A) Citotoxcity on Daudi and Lymphocytes cell lines treated with 40 ug/mL of ZnO-Lip or ZnO-LipCD38 after 24h, and 48h. (B) Internalization of ZnO-Lip or ZnO-LipCD38 after 24h, and 48h on Daudi, Lymphocytes and HL60 cell lines. Liposomes were marked with DiD, and cells were treated with 40 ug/mL of nanoconstruct. All experiments were performed at least in duplicate. * $p<0.0332$, ** $p<0.0021$, *** $p<0.0002$, **** $p< 0.0001$

The cell viability of Lymphocytes is not affected by the administration of 40 µg/mL of neither ZnO-Lip and ZnO-LipCD38 at any studied time point. The same behavior can be noted for Daudi cells, highlighting the excellent biocompatibility of the whole nanoconstruct, even in presence of Daratumumab fragments on the lipidic shell. Furthermore, the targeting action of anti-CD38 is demonstrated in Figure 37-B. The internalization of ZnO-LipCD38 is significantly higher with respect to the non-targeted counterpart in both cell lines and at any time point. This result indicate that the CD38 antigen expression in both cell lines can be efficiently targeted by the fragmented antibodies and that these fragments are correctly bound and displayed at the lipidic shell surface. It is also important to observe that the significant increase of ZnO-LipCD38 nanocontruct

internalization in Daudi cell lines with respect to the non-targeted ZnO-Lip, is in contrast not significant for Lymphocytes. This result can be considered the effect of the higher overexpression of CD38 on the Daudi membrane with respect to the B-Lymphocytes. To further corroborate this evidence, the internalization of fragmented anti-CD38 targeted nanoconstruct is extremely and significantly lower for HL60 cells (Figure 37-B), which are CD38 negative. The decrease of internalization in CD38 negative cells underlines the efficacy of the targeting capability owned by the fragmented CD38 targeted NPs. According to these results, an incubation time of the nanoconstruct equal to 24 h has been chosen on both Daudi and B-Lymphocytes for further investigations and in particular as the time point at which the external stimulus can be applied, to maximize the effect of ZnO-LipCD38 on Daudi cell line. The internalization results on HL60, provide the reason to not carry on any further experiments on this cell line.

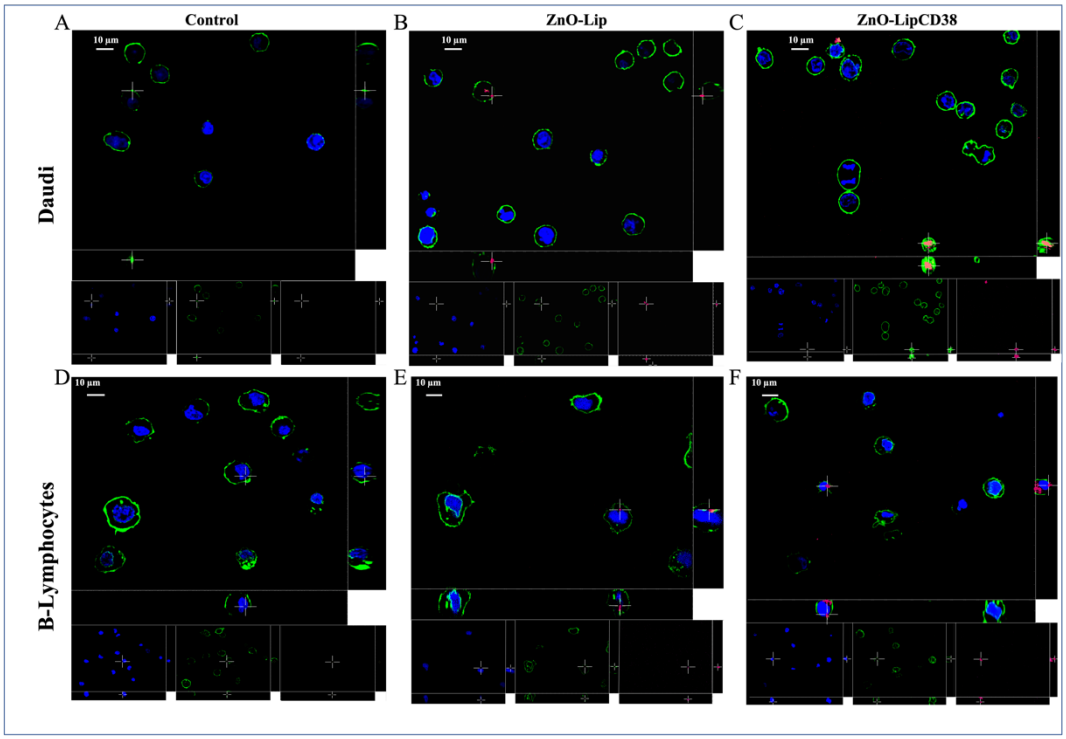

Figure 38 3D fluorescence microscopy images of Daudi (A) and B-Lymphocytes (D) control cells, Daudi treated with ZnO-Lip (B) and ZnO-LipCD38 (C) and B-Lymphocytes treated with ZnO-Lip (E) and ZnO-LipCD38 (F) after 24 h. Targeted and non-targeted liposomes containg ZnO NCs were labelled with Did (red channel); cell nuclei were labelled with Hoechst (blu channel); cell membranes were labelled with WGA488 (green channel); merged results are shown in the larger image. Cells were treated with 40 µg/mL

Further analyses were performed after 24 h from the administration of 40 µg/mL. 3D fluorescence images of Daudi and B-Lymphocytes were acquired after

the incubation with ZnO-Lip and ZnO-LipCD38. Cell membranes were given fluorescence with WGA 488 (green elements), cell nuclei were labelled with Hoechst (blue elements) and the liposomes, both targeted and not targeted, were labelled with DiD (red elements). The internalization is verified in both cell lines, and the 3D fluorescent images reported in Figure 38 show that the nanoconstructs are found to be inside the cellular membrane, but outside cell nuclei. It is possible to distinguish an increased amount of internalized red elements, which represent the nanoconstructs, when targeted ZnO-LipCD38 was administered to cells.

Fluorescent microscopy was also exploited to ensure the presence of the fragmented antiCD38 in the liposome containing ZnO NCs after the cell internalization.

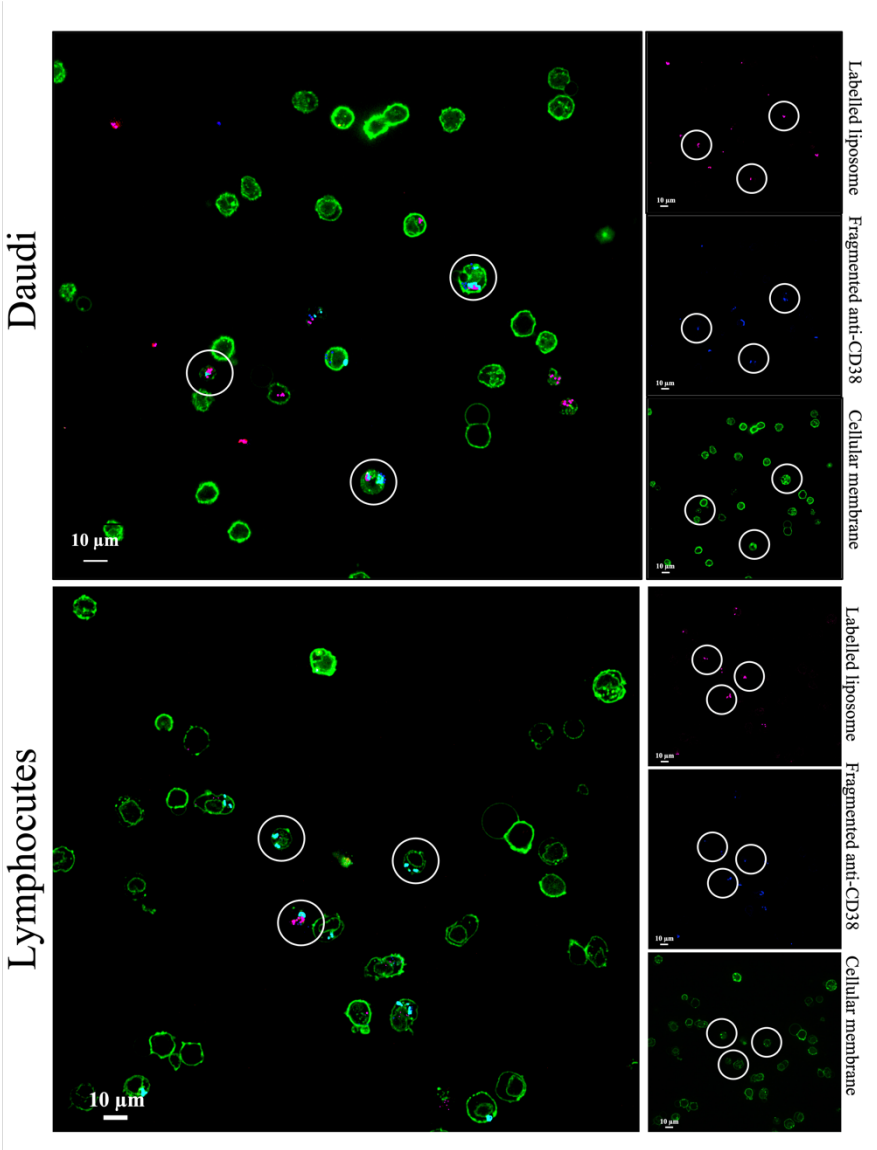

Figure 39 Fluorescence microscopy images of the internalization and colocalization of ZnO-LipCD38 nanoconstruct on Daudi and B-Lymphocytes after 24 h. Liposome containg ZnO NCs were labelled with Did (red channel); antiCD38 fragments incorporated in the lipidic shell contained ZnO NCs were labelled with Curcumin (blu channel); cell membranes were labelled with WGA488 (green channel). Cells were treated with 40 µg/mL of nanoconstruct. White circles shows significant internalization events.

In particular, Figure 39 demonstrates the colocalization of anti-CD38 fragments and the rest of the lipidic cells, and at the same time shows the internalization in cells. The liposomes were labelled with DiD (red dots, first column), while anti-CD38 fragments where selectively labelled by a secondary antibody conjugated with Coumarin dye (blu dots, second column) and cell membrane was given fluorescence with WGA 488 (green elements, third column).

The fourth column of Figure 39 represents the merge of all the three fluorescent channels, and it confirms for both Daudi and B-Lymphocytes that the nanoconstruct is inside the cell membrane, and verify the correct incorporation of antiCD38/DSPE-PEGlipid in the lipidic shell during the liposome formation process around ZnO NCs.

After ZnO-Lip and ZnO-LipCD38 characterization, the assessment of non-toxic dose (40 μg/mL) on both Daudi and B-Lymphocytes, and the correct incubation time in cells to maximize further effects, the combination of ZnO-LipCD38 and US exposure was investigated.

As reported previously in this dissertation and in the literature[17,219,246–248], ultrasounds produce different thermal and non-thermal effects, making the sonodynamic therapy an emerging approach for non-invasive treatment of less accessible lesions or tumors[249]. More in details, the periodical pressure waves provided by ultrasound irradiation can induce inertial cavitation, as described in Chapters 2 and 3, produce ROS and a large amount of mechanical stress and stream jests, which can all damage the elements nearby, as cells. The presence of nanoparticles introduces a higher number of nano bubbles, trapped on their surface, and, combined to US, can decrease the threshold for inertial cavitation to occur[55,250], permitting the decrease the US dose administered and therefore the reduction unwanted side effects, as the thermal damages in healthy tissue. ZnO represents a suitable candidate for its US response, described in previous chapters, for its bioimaging potentialities and for its piezoelectric properties[219]. In addition, considering *in vitro* systems, the physical movement of nanoparticles internalized into cells under US exposure could also contribute to the cell death, locally increasing the temperature and leading to mechanical destruction of the cells. This phenomenon is identified as "nano-scalpel effect," where nanoparticles physically alter the cell membrane, organelles and nuclei.[65]

Therefore, ultrasounds were combined with ZnO-Lip and ZnO-LipCD38 and the effects on both Daudi and B-Lymphocytes cell lines were evaluated 24 h, and 48 h, after the treatment with US. Different US input power densities (0.3 and 0.45 W/cm^2) and different exposure times (30 s and 1 min) were tested under continuous mode and with a planar US transducer (see more details in the Materials and Method section).

As visible in Figure 40-A, US alone results not to be toxic for Daudi cells after 24, and 48 from the treatments. The same result is obtained for B-Lymphocytes at all time points, suggesting that all tested doses of US do not cause any cytotoxic effect on cells. This permits to consider them as safe per se. After 24 h, the combination of ZnO-Lip and US can still be considered safe in Daudi for both 30 s and 1 min time exposures at 0.3 W/cm^2, and for 30 s exposure at 0.45 W/cm^2 (Figure 40-A). In constrast, the cell metabolic activity starts to decrease for 1 min exposure at 0.45 W/cm^2 in combination with ZnO-Lip. A recovery trend is visible after 48 h (Figure 40-B) for Daudi cells which received ZnO-Lip and 0.45 W/cm^2 for 1 min.

Noteworthy, the cytotoxic effect of ZnO-LipCD38 and US is more remarkable, starting from 1 min exposure at 0.3 W/cm^2 at 24 h (Figure 40-A). At 48 h after the treatment with 0.45 W/cm^2 and ZnO-LipCD38 (Figure 40-B), a significant difference is obtained between Daudi treated with US and the ones treated with the combination of US and targeted nanoconstruct. No significant difference is found with US and non-targeted nanoconstruct at same conditions.

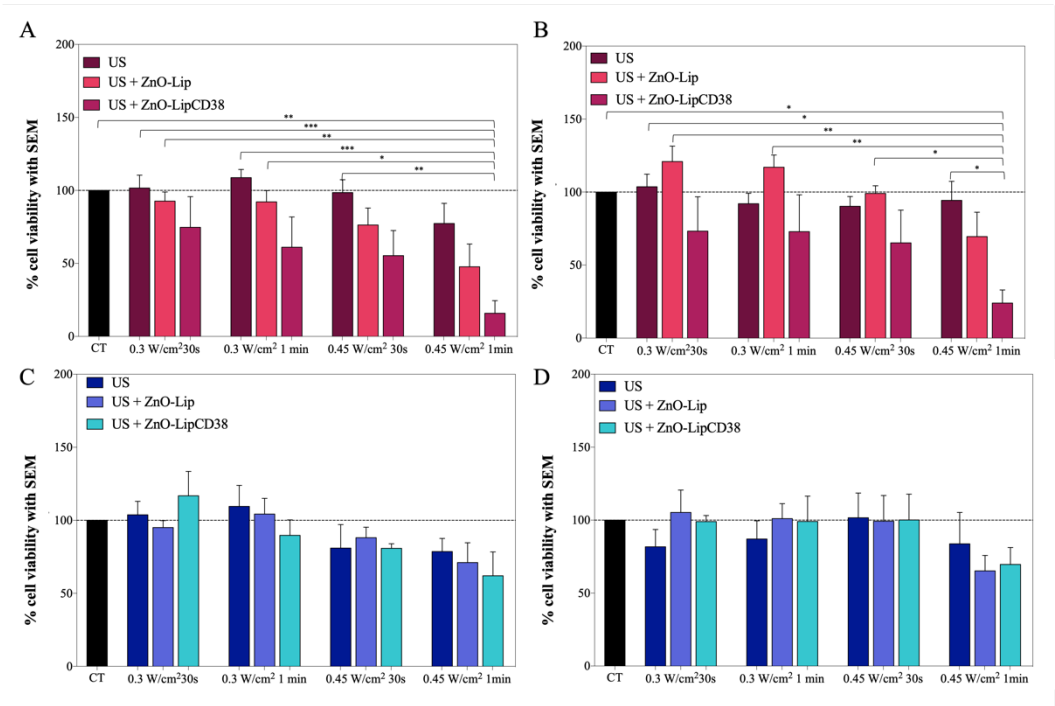

Figure 40 Cells viability of Daudi after 24h (A), and 48h (B) the treatment with US; B-Lymphocytes viability after 24h (C), 48h (D) the treatment with US. US were produced by Lipo0 transducer, at 1MHz, 100%DC. All the experiments were performed at least in triplicates. In US+ZnO-Lip and US+ZnO-LipCD38

groups, cells were previously incubated with 40 ug/mL of nanoconstructs 24h before the US treatment. * $p<0.0332$, ** $p<0.0021$, *** $p<0.0002$, **** $p< 0.0001$

B-Lymphocytes viability was evaluated at 24 h (Figure 40-C), and 48 h (Figure 40-D) after the different US treatments in combination with ZnO-Lip and ZnO-LipCD38. A small cytotoxic effect can be seen at 24 h for B-Lymphocytes treated with 0.45 W/cm^2 for 1 min in combination with both ZnO-Lip and ZnO-LipCD38. Regardless, no significant difference was obtained in B-Lymphocytes viability for all the different treatment combinations, nor for the different time points.

These results underline the effective killing capability of the combination of 1 min US exposure at 0.45 W/cm^2 and ZnO-LipCD38 towards Daudi cells, leaving the healthy counterparts, i.e. B-Lymphocytes, without any significant cytotoxic effect.

To further investigate the killing mechanism, a dual fluorescent probe strategy test was performed on Daudi and B-Lymphocytes treated with 1 min exposure at 0.45 W/cm^2 and ZnO-Lip or ZnO-LipCD38. Annexin V-PE is a fluorescent dye able to monitor the externalization of phosphatidylserine, which is translocated to the outer of cell membrane during early-stage apoptosis[251]. On the other hand, 7-AAD is a fluorescent DNA intercalator, which can permeate the cell membrane of late-stage apoptotic or death cells[252]. Outcomes of this assay are displayed in a dot-plot with quadrant-defined population. Indeed, it is possible to distinguish 4 different cell populations: non-apoptotic cells (lower left quadrant), early apoptotic cells (lower right quadrant), late stage apoptotic and dead cells (upper right quadrant), and debris (upper left quadrant). Results are shown in Figure 41 for Daudi and in Figure 42 for B-Lymphocytes, data were collected at 24 h (Figure 41/42 -A), and 48 h (Figure 41/42 -B) after the US treatments.

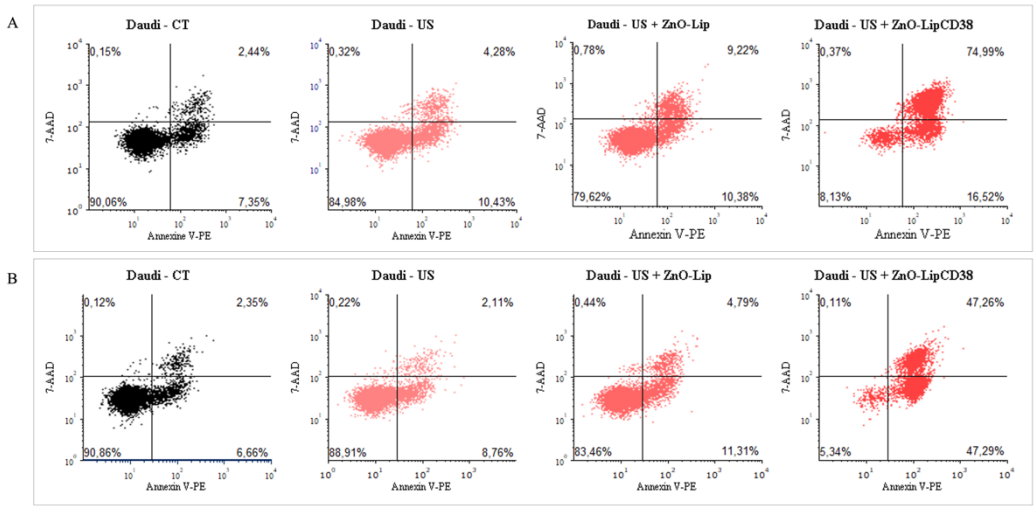

Figure 41 Evaluation of percentage of early and late apoptotic populations after 24h (A), and 48h (B) induced in Daudi cells after the US treatment with Lipo0 transducer (1MHz, 100%DC, 0.45 W/cm^2, 1 min). In US+ZnO-Lip and US+ZnO-LipCD38 groups, cells were previously incubated with 40 ug/mL of nanoconstructs 24h before the US treatment.

At 24 h, Daudi cells (Figure 41-A) were not affected by US alone and by US in combination with ZnO-Lip, but when cells were treated with US and ZnO-LipCD38, an increase in both early-stage and late-stage apoptosis is visible. More in details, for the US+ZnO-LipCD38 group, 16.5% and 75% of cell population is at early-stage and late-stage apoptosis, respectively. In contrast, for both US and US+ZnO-Lip groups just ~ 10% of cell population is in early-stage apoptosis and lower % are recorded for late apoptosis. These results suggest that during the first 24 h, mechanical stress and nano-scalpel effects caused by inertial cavitation are the main responsible for cell damages, producing the death of 75% of cell population. Instead, after 48 h (Figure 41-B) there is a progressive increase of early-stage apoptosis cells for US+ZnO-LipCD38 group, which become 47% of cell population at 48 h. In contrast, the early-stage apoptosis cell population remains stable for all the other groups at any time points. It can be assumed that the Daudi population which survived to mechanical damages after 24 h from the treatment with US+ZnO-LipCD38, activate pathways of programmed cell death, rising the killing efficacy of the combined therapy composed by external stimulus and the targeted nanoconstruct.

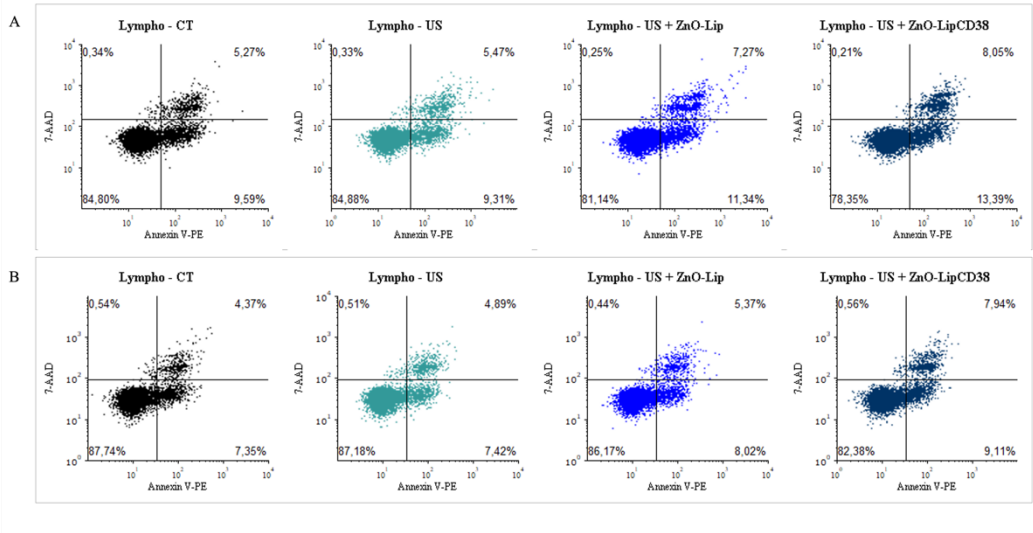

Figure 42 Evaluation of percentage of early and late apoptotic populations after 24h (A), and 48h (B) induced inB- Lymphocytes cells after the US treatment with Lipo0 transducer (1MHz, 100%DC, 0.45 W/cm^2, 1 min). In US+ZnO-Lip and US+ZnO-LipCD38 groups, cells were previously incubated with 40 ug/mL of nanoconstructs 24h before the US treatment

The results presented in Figure 42 for B-Lymphocytes are in accordance with the previously presented data. The percentage of both early-stage and late-stage apoptotic cells for US, US+ZnO-Lip and US+ZnO-LipCD38 groups are similar to the physiological values visible in the untreated cells (black dot plot, control cells) at any time point (Figure 42-A, B). These data suggest one more time the safety of the US-activated and targeted nanconstruct treatment on healthy cells, while underline its effectiveness of Burkitt's lymphoma cells. CD38-targeted liposome containing ZnO NCs is thus proved to be externally activated by US stimuli and to selectively damage only cancerous cells.

A further demonstration of the achieved results is presented in Figure 43-A,B, for Daudi cells at 24 h, and 48 h, respectively and in Figure 43-C,D for B-Lymphocytes at 24 h, and 48 h. Cells were stained with two different fluorescent dyes: Fluozin-3 dye which labels intracellular Zn^{2+} ions [253,254], and Propidium Iodine (PI) which is a DNA intercalator, impermeable to intact cell membrane[255,256] used here as detector for damaged cell membranes.

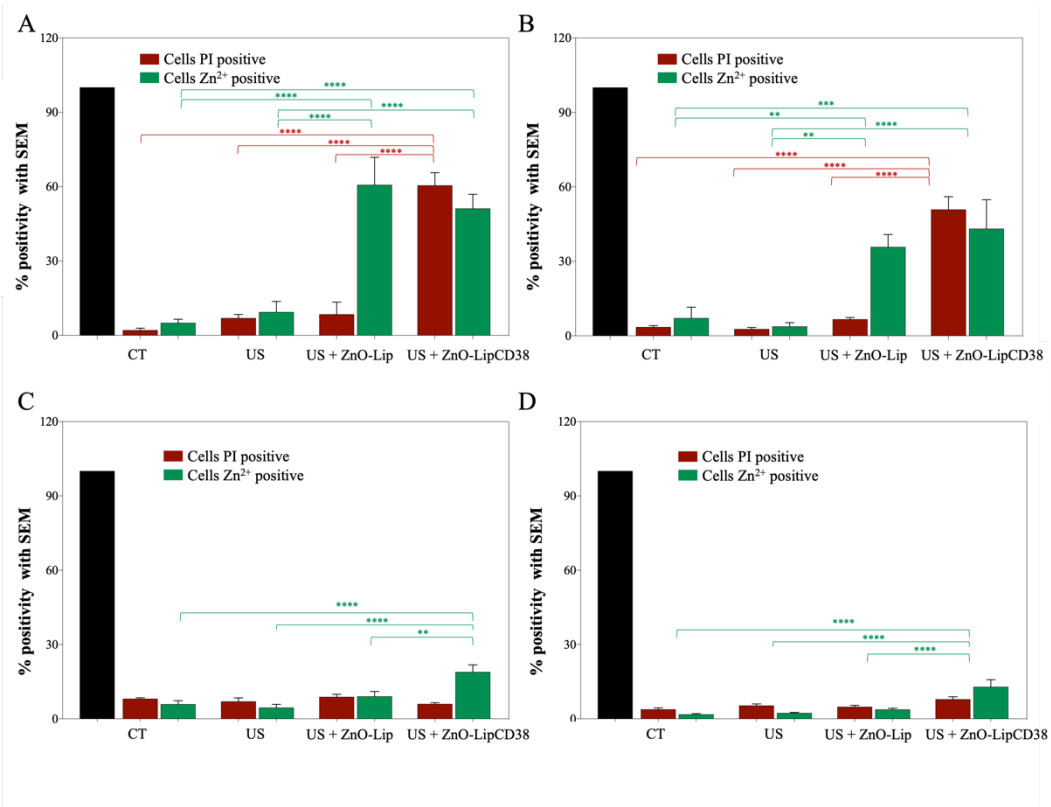

Figure 43 Cells membrane integrity was evaluated with PI dye, while Zn^{2+} presence inside cell was measured by Fluozin dye. Percentage of cells positive to PI and Fluozin is shown for Daudi cells at 24h (A), and 48h (B) after treatment with US, and for B-Lymphocytes after 24h (C), and 48h (D) the US treatment. US were produced by Lipo0 transducer, at 1MHz, 100%DC, 0.45W/cm^2, 1 min. 5 images per sample were evaluated. In US+ZnO-Lip and US+ZnO-LipCD38 groups, cells were incubated with 40 ug/mL of nanoconstructs 24h before the US treatment. * $p<0.0332$, ** $p<0.0021$, *** $p<0.0002$, **** $p< 0.0001$

The presence of Zn^{2+} ions is significantly higher in Daudi and in B-Lymphocytes which received either ZnO-Lip or ZnO-LipCD38 at any time point, as expected. However, the percentage of positive events is above 50% for Daudi, while is below 30% for B-Lymphocytes pointing out that the ZnO-Lip construct is totally safe for B-Lymphocytes, sparing them also from zinc cation cytotoxic effects. The damages in the cell membrane reflect the results obtained with all the other techniques. A significantly higher amount of PI signal was detected in Daudi cells treated with US+ZnO-LipCD38 with respect to both US and US+ZnO-Lip groups 24 h and 48 h after the treatment (Figure 43-A,B, respectively). It can be assumed that the higher cell membrane damage is directly related to the efficacy of the combined targeted therapy[257,258]. Instead, no significant results are obtained for B-Lymphocytes, in which the percentage of cells positive to PI remains close to the one measured for control (untreated) cells.

It has been reported in previous literature[19,51,259], and in the previous chapter, the enhanced ROS production generated by the ultrasound irradiation of ZnO nanoparticles, due to the increased number of inertial cavitation nuclei at NPs surface. ROS are involved in various cell signaling processes[260], and an imbalance in cellular redox homeostasis could cause cellular component damages, as well as the activation of many signal pathways liable of cell death, causing ROS-mediated apoptosis or necrosis[261]. Oxidative stress is not the only cytotoxic effect which compete to cells death, but also stress, mechanical damages, and toxic Zn^{2+} release, as confirmed by Figure 43, could be responsible for the decrease of cellular viability after the exposure to the targeted nanoconstruct and US irradiation. The results presented in Figure 42 and Figure 43-C,D suggest that the cellular metabolism of B-Lymphocytes is less sensitive to the mingling of consequences derived from US irradiation and ZnO-LipCD38 administration with respect to cancerous Daudi cells. The overall outcome is the targeted cytotoxicity of the proposed strategy toward Burkitt's lymphoma cells, without any significant effects on the healthy counterpart.

7.4 Conclusion

In this Chapter we establish a liposome-based shielding approach for newly synthetized ZnO NCs, and a successful decoration with fragmented anti-CD38 for targeting purposes. The lipidic shell has here proved to be effective in enhancing the colloidal stability of the nanoconstruct and diminishing the cytotoxicity of ZnO NCs alone in hematological cells, both cancer and normal ones. Fragmentation of commercial Daratumumab occurred in a controlled manner, allowing to bound fragments of reduced anti-CD38 with DSPE-PEG Maleimide lipids, permitting their incorporation during the self-assembly process of liposome formation around ZnO NCs. The augmented internalization of the targeted nanoconstruct in Burkitt's lymphoma cells in comparison to the one in healthy B-Lymphocytes demonstrates the targeting efficiency of anti-CD38 liposome coated ZnO NCs.

Further steps were done towards the therapeutic applicability of the nanoconstruct for antitumoral purposes. CD38-targeted liposome enveloping ZnO NCs were tested as potential therapeutic agent in combination with ultrasound exposure with Burkitt's Lymphoma cell line, demonstrating their effectiveness.

Furthermore, the nanoconstruct has proven to be highly biocompatible when is not activated, and to possess high killing capability when US activated only for cancer cells, leaving healthy B-Lymphocytes cells without any significant damage. These results open the possibility of future applications of the nanoconstruct *in vivo,* particularly for the high specificity in targeting only towards cancerous cells, avoiding unwanted damages on healthy cells.

Chapter 8

General conclusions

The results presented in this dissertation have widely proven the imaging potential and the therapeutic ability of ZnO nanocrystals, not only due to the physical and chemical properties of nanosized ZnO when remotely activated by US exposure, but also due to the mimicking and targeting strategies adopted in this work.

In particular, inertial cavitation under ultrasound exposure leads to a large reactive oxygen species (ROS) production in water, but in presence of ZnO NCs a lower threshold cavitation is set and consequently larger amount of ROS is generated in ZnO NCs solutions with respect to pure water. This phenomenon can be exploited to tune ROS production in a controlled manner. Ultrasound B-mode imaging also demonstrated the enhanced echographic signal generation of the ZnO NCs containing solutions.

The acoustic pressure field and acoustic density distribution was mathematically modeled and the formation of a symmetric and tapered focus along the central vertical axis of the water sample volume was observed, validating the qualitative sonochemiluminescence (SCL) measurements in pure water, and quantitative electron paramagnetic resonance spectroscopy (EPR) data, allowing once again to estimate the amount of produced ROS in the system in presence of ZnO NCs.

Furthermore, the optical response of ZnO NCs was deeply studied, demonstrating the ability of ZnO NCs to enhance the sonoluminescence (SL) emission under low-intensity ultrasound irradiation. This reveals also the ZnO NCs potential use as a nanocontrast agent for therapeutic applications.

Finally, the anti-cancerous potential of ZnO NCs was investigated with different cancer cell lines, with and without protective shell and targeting elements.

A preliminary phase dedicated to the study of the sole ZnO NCs cytotoxicity and shock wave (SW) response was performed on cervical adenocarcinoma cells. It was discovered that a single treatment was not sufficient to achieve a significant difference in cells viability between SW and ZnO + SW stimulations. In contrast, multiple SW treatments (3 times/day) resulted to be highly cytotoxic and, strikingly, only for cells pre-incubated with ZnO NCs. The results showed clear toxic behaviour of ZnO NCs in combination with SW.

Successively, ZnO NCs were encapsulated in EVs derived from healthy cells, which were further engineered with targeting agent, a monoclonal antibody. In particular, an efficient active method based on freeze-thaw cycles to load B-cell derived EVs with a nanotherapeutic stimuli-responsive cargo (ZnO NCs) was characterized. The *in vitro* data showed the high biocompatibility and the remarkable selectivity of anti-CD20 engineered nanoconstructs (TNH^{CD20}) towards the target CD20+ cancerous Daudi cell line compared to the CD20- cancerous myeloid cells (HL60) and the healthy counterpart (B-Lymphocytes). Furthermore, an enhanced cytotoxicity of TNH^{CD20} directed against Daudi cancer cells was demonstrated after the nanoconstructs activation with high-energy ultrasound shock waves.

Another mimicking and targeting strategy was presented in dissertation. ZnO NCs were encapsulated in artificial and self-assembled liposomes, and fragments of anti-CD38 antibody were employed as targeting agent toward cancerous Daudi cells. The biosafety of the construct itself was here proved in both healthy (B-Lymphocytes) and cancerous cell lines. The remote activation of the nanoconstruct by ultrasound exposure make it become toxic for cancerous Daudi cells, without having any significant impact on metabolic activity of healthy cells. A step further was done to understand the mechanism of cell killing: mechanical damages were created at first, then apoptotic pathways were activated increasing the therapeutic efficiency against cancerous cells.

In conclusion, this work demonstrates the multifaced potential of nanosized Zinc Oxide as biomedical imaging agent and therapeutic nanotool for anticancer applications. Further study on this nanomaterial can dramatically contribute to the evolvement of the field of medicine.

References

(1) Soares, S.; Sousa, J.; Pais, A.; Vitorino, C. Nanomedicine: Principles, Properties, and Regulatory Issues. *Front Chem* **2018**, *6* (AUG), 360. https://doi.org/10.3389/FCHEM.2018.00360/BIBTEX.

(2) Tinkle, S.; Mcneil, S. E.; Mühlebach, S.; Bawa, R.; Borchard, G.; Barenholz, Y. C.; Tamarkin, L.; Desai, N. Nanomedicines: Addressing the Scientific and Regulatory Gap. *Ann N Y Acad Sci* **2014**, *1313* (1), 35–56. https://doi.org/10.1111/NYAS.12403.

(3) Kalash, R. S.; Lakshmanan, V. K.; Cho, C. S.; Park, I. K. Theranostics. *Biomaterials Nanoarchitectonics* **2016**, 197–215. https://doi.org/10.1016/B978-0-323-37127-8.00012-1.

(4) *Cancer*. https://www.who.int/news-room/fact-sheets/detail/cancer (accessed 2022-09-28).

(5) Shi, J.; Kantoff, P. W.; Wooster, R.; Farokhzad, O. C. Cancer Nanomedicine: Progress, Challenges and Opportunities. *Nature Reviews Cancer 2016 17:1* **2016**, *17* (1), 20–37. https://doi.org/10.1038/nrc.2016.108.

(6) Chen, G.; Roy, I.; Yang, C.; Prasad, P. N. Nanochemistry and Nanomedicine for Nanoparticle-Based Diagnostics and Therapy. *Chem Rev* **2016**, *116* (5), 2826–2885. https://doi.org/10.1021/ACS.CHEMREV.5B00148/ASSET/IMAGES/LARGE/CR-2015-00148A_0029.JPEG.

(7) Khan, I.; Saeed, K.; Khan, I. Nanoparticles: Properties, Applications and Toxicities. *Arabian Journal of Chemistry* **2019**, *12* (7), 908–931. https://doi.org/10.1016/J.ARABJC.2017.05.011.

(8) Peer, D.; Karp, J. M.; Hong, S.; Farokhzad, O. C.; Margalit, R.; Langer, R. Nanocarriers as an Emerging Platform for Cancer Therapy. *Nature Nanotechnology 2007 2:12* **2007**, *2* (12), 751–760. https://doi.org/10.1038/nnano.2007.387.

(9) Sanna, V.; Sechi, M. Therapeutic Potential of Targeted Nanoparticles and Perspective on Nanotherapies. *ACS Med Chem Lett* **2020**, *11* (6), 1069–1073. https://doi.org/10.1021/ACSMEDCHEMLETT.0C00075/ASSET/IMAGES/LARGE/ML0C00075_0005.JPEG.

(10) Carofiglio, M.; Barui, S.; Cauda, V.; Laurenti, M. Doped Zinc Oxide Nanoparticles: Synthesis, Characterization and Potential Use in Nanomedicine. *Applied Sciences 2020, Vol. 10, Page 5194* **2020**, *10* (15), 5194. https://doi.org/10.3390/APP10155194.

(11) Gokduman, K.; Gok, A. In Vitro Investigation of Therapeutic Potential of Bare Magnetite (Fe_3O_4) Nanoparticles (≤100 Ppm) on Hepatocellular Carcinoma Cells. *J Nanosci Nanotechnol* **2020**, *20* (3), 1391–1400. https://doi.org/10.1166/JNN.2020.17152.

(12) Yu, J.; Chu, X.; Hou, Y. Stimuli-Responsive Cancer Therapy Based on Nanoparticles. *Chemical Communications* **2014**, *50* (79), 11614–11630. https://doi.org/10.1039/C4CC03984J.

(13) Sohail, A.; Ahmad, Z.; Bég, O. A.; Arshad, S.; Sherin, L. A Review on Hyperthermia via Nanoparticle-Mediated Therapy. *Bull Cancer* **2017**, *104* (5), 452–461. https://doi.org/10.1016/J.BULCAN.2017.02.003.

(14) Jiang, J.; Pi, J.; Cai, J. The Advancing of Zinc Oxide Nanoparticles for Biomedical Applications. *Bioinorg Chem Appl* **2018**, *2018*. https://doi.org/10.1155/2018/1062562.

(15) Racca, L.; Canta, M.; Dumontel, B.; Ancona, A.; Limongi, T.; Garino, N.; Laurenti, M.; Canavese, G.; Cauda, V. Zinc Oxide Nanostructures in Biomedicine. *Smart Nanoparticles for Biomedicine* **2018**, 171–187. https://doi.org/10.1016/B978-0-12-814156-4.00012-4.

(16) Garino, N.; Limongi, T.; Dumontel, B.; Canta, M.; Racca, L.; Laurenti, M.; Castellino, M.; Casu, A.; Falqui, A.; Cauda, V. A Microwave-Assisted Synthesis of Zinc Oxide Nanocrystals Finely Tuned for Biological Applications. *Nanomaterials 2019, Vol. 9, Page 212* **2019**, *9* (2), 212. https://doi.org/10.3390/NANO9020212.

(17) Canavese, G.; Ancona, A.; Racca, L.; Canta, M.; Dumontel, B.; Barbaresco, F.; Limongi, T.; Cauda, V. Nanoparticle-Assisted Ultrasound: A Special Focus on Sonodynamic Therapy against Cancer. *Chemical Engineering Journal* **2018**, *340*, 155–172. https://doi.org/10.1016/J.CEJ.2018.01.060.

(18) Fu, P. P.; Xia, Q.; Hwang, H. M.; Ray, P. C.; Yu, H. Mechanisms of Nanotoxicity: Generation of Reactive Oxygen Species. *J Food Drug Anal* **2014**, *22* (1), 64–75. https://doi.org/10.1016/J.JFDA.2014.01.005.

(19) Vighetto, V.; Ancona, A.; Racca, L.; Limongi, T.; Troia, A.; Canavese, G.; Cauda, V. The Synergistic Effect of Nanocrystals Combined With Ultrasound in the Generation of Reactive Oxygen Species for Biomedical Applications. *Front Bioeng Biotechnol* **2019**, *7*, 374. https://doi.org/10.3389/FBIOE.2019.00374/BIBTEX.

(20) Vighetto, V.; Troia, A.; Laurenti, M.; Carofiglio, M.; Marcucci, N.; Canavese, G.; Cauda, V. Insight into Sonoluminescence Augmented by ZnO-Functionalized Nanoparticles. *ACS Omega* **2022**, *7* (8), 6591–6600. https://doi.org/10.1021/ACSOMEGA.1C05837/ASSET/IMAGES/LARGE/AO1C05837_0008.JPEG.

(21) SHIBAGUCHI, H.; TSURU, H.; KUROKI, M.; KUROKI, M. Sonodynamic Cancer Therapy: A Non-Invasive and Repeatable Approach Using Low-Intensity Ultrasound with a Sonosensitizer. *Anticancer Res* **2011**, *31* (7), 2425.

(22) Neppiras, E. A. Acoustic Cavitation. *Phys Rep* **1980**, *61* (3), 159–251. https://doi.org/10.1016/0370-1573(80)90115-5.

(23) McMurray, H. N.; Wilson, B. P. Mechanistic and Spatial Study of Ultrasonically Induced Luminol Chemiluminescence. *Journal of Physical Chemistry A* **1999**, *103* (20), 3955–3962. https://doi.org/10.1021/JP984503R.

(24) Dayem, A. A.; Hossain, M. K.; Lee, S. bin; Kim, K.; Saha, S. K.; Yang, G. M.; Choi, H. Y.; Cho, S. G. The Role of Reactive Oxygen Species (ROS) in the Biological Activities of Metallic Nanoparticles. *International Journal of Molecular Sciences 2017, Vol. 18, Page 120* **2017**, *18* (1), 120. https://doi.org/10.3390/IJMS18010120.

(25) Dąbrowski, J. M. Reactive Oxygen Species in Photodynamic Therapy: Mechanisms of Their Generation and Potentiation. *Adv Inorg Chem* **2017**, *70*, 343–394. https://doi.org/10.1016/BS.ADIOCH.2017.03.002.

(26) Aldosari, S.; Awad, M.; Harrington, E. O.; Sellke, F. W.; Abid, M. R. Subcellular Reactive Oxygen Species (ROS) in Cardiovascular Pathophysiology. *Antioxidants 2018, Vol. 7, Page 14* **2018**, *7* (1), 14. https://doi.org/10.3390/ANTIOX7010014.

(27) Lau, A. T. Y.; Wang, Y.; Chiu, J.-F. Reactive Oxygen Species: Current Knowledge and Applications in Cancer Research and Therapeutic. *J Cell Biochem* **2008**, *104* (2), 657–667. https://doi.org/10.1002/jcb.21655.

(28) Canavese, G.; Ancona, A.; Racca, L.; Canta, M.; Dumontel, B.; Barbaresco, F.; Limongi, T.; Cauda, V. Nanoparticle-Assisted Ultrasound: A Special Focus on Sonodynamic Therapy against Cancer. *Chemical Engineering Journal* **2018**, *340*, 155–172. https://doi.org/10.1016/J.CEJ.2018.01.060.

(29) Kim, Y. M.; Kim, S. J.; Tatsunami, R.; Yamamura, H.; Fukai, T.; Fukai, M. U. ROS-Induced ROS Release Orchestrated by Nox4, Nox2, and Mitochondria in VEGF Signaling and Angiogenesis. *Am J Physiol Cell Physiol* **2017**, *312* (6), C749–C764. https://doi.org/10.1152/AJPCELL.00346.2016.

(30) Urao, N.; Inomata, H.; Razvi, M.; Kim, H. W.; Wary, K.; McKinney, R.; Fukai, T.; Ushio-Fukai, M. Role of Nox2-Based NADPH Oxidase in Bone Marrow and Progenitor Cell Function Involved in Neovascularization Induced by Hindlimb Ischemia. *Circ Res* **2008**, *103* (2), 212. https://doi.org/10.1161/CIRCRESAHA.108.176230.

(31) Osumi, K.; Matsuda, S.; Fujimura, N.; Matsubara, K.; Kitago, M.; Itano, O.; Ogino, C.; Shimizu, N.; Obara, H.; Kitagawa, Y. Acceleration of Wound Healing by Ultrasound Activation of TiO2 in Escherichia Coli-Infected Wounds in Mice. *J Biomed Mater Res B Appl Biomater* **2017**, *105* (8), 2344–2351. https://doi.org/10.1002/JBM.B.33774.

(32) Pelicano, H.; Carney, D.; Huang, P. ROS Stress in Cancer Cells and Therapeutic Implications. *Drug Resistance Updates* **2004**, *7* (2), 97–110. https://doi.org/10.1016/J.DRUP.2004.01.004.

(33) Nogueira, V.; Hay, N. Molecular Pathways: Reactive Oxygen Species Homeostasis in Cancer Cells and Implications for Cancer Therapy. *Clin Cancer Res* **2013**, *19* (16), 4309–4314. https://doi.org/10.1158/1078-0432.CCR-12-1424.

(34) Tong, L.; Chuang, C. C.; Wu, S.; Zuo, L. Reactive Oxygen Species in Redox Cancer Therapy. *Cancer Lett* **2015**, *367* (1), 18–25. https://doi.org/10.1016/J.CANLET.2015.07.008.

(35) Gonzalez, L.; Lison, D.; Kirsch-Volders, M. Genotoxicity of Engineered Nanomaterials: A Critical Review. *http://dx.doi.org/10.1080/17435390802464986* **2009**, *2* (4), 252–273. https://doi.org/10.1080/17435390802464986.

(36) Dayem, A. A.; Hossain, M. K.; Lee, S. bin; Kim, K.; Saha, S. K.; Yang, G. M.; Choi, H. Y.; Cho, S. G. The Role of Reactive Oxygen Species (ROS) in the Biological Activities of Metallic Nanoparticles. *Int J Mol Sci* **2017**, *18* (1). https://doi.org/10.3390/IJMS18010120.

(37) Carlson, C.; Hussein, S. M.; Schrand, A. M.; Braydich-Stolle, L. K.; Hess, K. L.; Jones, R. L.; Schlager, J. J. Unique Cellular Interaction of Silver Nanoparticles: Size-Dependent Generation of Reactive Oxygen Species. *Journal of Physical Chemistry B* **2008**, *112* (43), 13608–13619. https://doi.org/10.1021/JP712087M/ASSET/IMAGES/LARGE/JP-2007-12087M_0001.JPEG.

(38) Ancona, A.; Dumontel, B.; Garino, N.; Demarco, B.; Chatzitheodoridou, D.; Fazzini, W.; Engelke, H.; Cauda, V. Lipid-Coated Zinc Oxide Nanoparticles as Innovative ROS-Generators for Photodynamic Therapy in Cancer Cells. *Nanomaterials (Basel)* **2018**, *8* (3). https://doi.org/10.3390/NANO8030143.

(39) Dougherty, T. J.; Gomer, C. J.; Henderson, B. W.; Jori, G.; Kessel, D.; Korbelik, M.; Moan, J.; Peng, Q. Photodynamic Therapy. *J Natl Cancer Inst* **1998**, *90* (12), 889–905. https://doi.org/10.1093/JNCI/90.12.889.

(40) Dolmans, D. E. J. G. J.; Fukumura, D.; Jain, R. K. Photodynamic Therapy for Cancer. *Nature Reviews Cancer 2003 3:5* **2003**, *3* (5), 380–387. https://doi.org/10.1038/nrc1071.

(41) dos Santos, A. F.; de Almeida, D. R. Q.; Terra, L. F.; Baptista, M. S.; Labriola, L. Photodynamic Therapy in Cancer Treatment - an Update Review. *J Cancer Metastasis Treat* **2019**, *5*, 25. https://doi.org/10.20517/2394-4722.2018.83.

(42) McHale, A. P.; Callan, J. F.; Nomikou, N.; Fowley, C.; Callan, B. Sonodynamic Therapy: Concept, Mechanism and Application to Cancer Treatment. *Adv Exp Med Biol* **2016**, *880*, 429–450. https://doi.org/10.1007/978-3-319-22536-4_22.

(43) Yasuda, J.; Miyashita, T.; Taguchi, K.; Yoshizawa, S.; Umemura, S. I. Quantitative Assessment of Reactive Oxygen Sonochemically Generated by Cavitation Bubbles. *Jpn J Appl Phys* **2015**, *54* (7), 07HF21. https://doi.org/10.7567/JJAP.54.07HF21.

(44) Canavese, G.; Ancona, A.; Racca, L.; Canta, M.; Dumontel, B.; Barbaresco, F.; Limongi, T.; Cauda, V. Nanoparticle-Assisted Ultrasound: A Special Focus on Sonodynamic Therapy against Cancer. *Chemical Engineering Journal* **2018**, *340*, 155–172. https://doi.org/10.1016/J.CEJ.2018.01.060.

(45) van Straten, D.; Mashayekhi, V.; de Bruijn, H. S.; Oliveira, S.; Robinson, D. J. Oncologic Photodynamic Therapy: Basic Principles, Current Clinical Status and Future Directions. *Cancers 2017, Vol. 9, Page 19* **2017**, *9* (2), 19. https://doi.org/10.3390/CANCERS9020019.

(46) Zhang, H.; Chen, B.; Jiang, H.; Wang, C.; Wang, H.; Wang, X. A Strategy for ZnO Nanorod Mediated Multi-Mode Cancer Treatment. *Biomaterials* **2011**, *32* (7), 1906–1914. https://doi.org/10.1016/J.BIOMATERIALS.2010.11.027.

(47) Firdous, S. Development and Imaging of Zinc Oxide Nanorods as a Photosensitizer for the Diagnosis and Treatment of Cancer Using Lasers1.

Laser Phys Lett **2018**, *15* (9), 095604. https://doi.org/10.1088/1612-202X/AAD28C.

(48) Albanese, A.; Tang, P. S.; Chan, W. C. W. The Effect of Nanoparticle Size, Shape, and Surface Chemistry on Biological Systems. *http://dx.doi.org/10.1146/annurev-bioeng-071811-150124* **2012**, *14*, 1–16. https://doi.org/10.1146/ANNUREV-BIOENG-071811-150124.

(49) Yu, S. Y.; Jing, H.; Cao, Z.; Su, H. Q. The Luminescent Properties and Toxicity Controllability Investigation of Novel ZnO Quantum Dots with Schiff Base Complexes Modification. *J Nanosci Nanotechnol* **2014**, *14* (5), 3299–3304. https://doi.org/10.1166/JNN.2014.7990.

(50) Lau, A. T. Y.; Wang, Y.; Chiu, J. F. Reactive Oxygen Species: Current Knowledge and Applications in Cancer Research and Therapeutic. *J Cell Biochem* **2008**, *104* (2), 657–667. https://doi.org/10.1002/JCB.21655.

(51) Tamboia, G.; Campanini, M.; Vighetto, V.; Racca, L.; Spigarelli, L.; Canavese, G.; Cauda, V. A Comparative Analysis of Low Intensity Ultrasound Effects on Living Cells: From Simulation to Experiments. *Biomed Microdevices* **2022**, *24* (4), 35. https://doi.org/10.1007/s10544-022-00635-x.

(52) Racca, L.; Cauda, V. Remotely Activated Nanoparticles for Anticancer Therapy. *Nano-Micro Letters 2020 13:1* **2020**, *13* (1), 1–34. https://doi.org/10.1007/S40820-020-00537-8.

(53) Battaglini, M.; Marino, A.; Carmignani, A.; Tapeinos, C.; Cauda, V.; Ancona, A.; Garino, N.; Vighetto, V.; la Rosa, G.; Sinibaldi, E.; Ciofani, G. Polydopamine Nanoparticles as an Organic and Biodegradable Multitasking Tool for Neuroprotection and Remote Neuronal Stimulation. *ACS Appl Mater Interfaces* **2020**, *12* (32), 35782–35798. https://doi.org/10.1021/ACSAMI.0C05497/SUPPL_FILE/AM0C05497_SI_001.PDF.

(54) Carmignani, A.; Battaglini, M.; Sinibaldi, E.; Marino, A.; Vighetto, V.; Cauda, V.; Ciofani, G. In Vitro and Ex Vivo Investigation of the Effects of Polydopamine Nanoparticle Size on Their Antioxidant and Photothermal Properties: Implications for Biomedical Applications. *ACS Appl Nano Mater* **2022**, *5* (1), 1702–1713.

https://doi.org/10.1021/ACSANM.1C04536/SUPPL_FILE/AN1C04536_SI_002.MP4.

(55) Matos, J. C.; Laurenti, M.; Vighetto, V.; Pereira, L. C. J.; Waerenborgh, J. C.; Gonçalves, M. C.; Cauda, V. Biomimetic Amorphous Titania Nanoparticles as Ultrasound Responding Agents to Improve Cavitation and ROS Production for Sonodynamic Therapy. *Applied Sciences 2020, Vol. 10, Page 8479* **2020**, *10* (23), 8479. https://doi.org/10.3390/APP10238479.

(56) Ancona, A.; Troia, A.; Garino, N.; Dumontel, B.; Cauda, V.; Canavese, G. Leveraging Re-Chargeable Nanobubbles on Amine-Functionalized ZnO Nanocrystals for Sustained Ultrasound Cavitation towards Echographic Imaging. *Ultrason Sonochem* **2020**, *67*, 105132. https://doi.org/10.1016/J.ULTSONCH.2020.105132.

(57) Lops, C.; Ancona, A.; di Cesare, K.; Dumontel, B.; Garino, N.; Canavese, G.; Hérnandez, S.; Cauda, V. Sonophotocatalytic Degradation Mechanisms of Rhodamine B Dye via Radicals Generation by Micro- and Nano-Particles of ZnO. *Appl Catal B* **2019**, *243*, 629–640. https://doi.org/10.1016/J.APCATB.2018.10.078.

(58) Canaparo, R.; Foglietta, F.; Limongi, T.; Serpe, L. Biomedical Applications of Reactive Oxygen Species Generation by Metal Nanoparticles. *Materials 2021, Vol. 14, Page 53* **2020**, *14* (1), 53. https://doi.org/10.3390/MA14010053.

(59) Tiong, T. J.; Chandesa, T.; Yap, Y. H. Comparison of Sonochemiluminescence Images Using Image Analysis Techniques and Identification of Acoustic Pressure Fields via Simulation. *Ultrason Sonochem* **2017**, *36*, 78–87. https://doi.org/10.1016/J.ULTSONCH.2016.11.003.

(60) Ancona, A.; Dumontel, B.; Garino, N.; Demarco, B.; Chatzitheodoridou, D.; Fazzini, W.; Engelke, H.; Cauda, V. Lipid-Coated Zinc Oxide Nanoparticles as Innovative ROS-Generators for Photodynamic Therapy in Cancer Cells. *Nanomaterials 2018, Vol. 8, Page 143* **2018**, *8* (3), 143. https://doi.org/10.3390/NANO8030143.

(61) Lipovsky, A.; Tzitrinovich, Z.; Friedmann, H.; Applerot, G.; Gedanken, A.; Lubart, R. EPR Study of Visible Light-Induced ROS Generation by Nanoparticles of ZnO. *Journal of Physical Chemistry C* **2009**, *113* (36), 15997–16001. https://doi.org/10.1021/JP904864G.

(62) Mojović, M.; Vuletić, M.; Bačić, G. G. Detection of Oxygen-Centered Radicals Using EPR Spin-Trap DEPMPO: The Effect of Oxygen. *Ann N Y Acad Sci* **2005**, *1048*, 471–475. https://doi.org/10.1196/ANNALS.1342.069.

(63) Wei, Z.; Weavers, L. K. Combining COMSOL Modeling with Acoustic Pressure Maps to Design Sono-Reactors. *Ultrason Sonochem* **2016**, *31*, 490–498. https://doi.org/10.1016/J.ULTSONCH.2016.01.036.

(64) Fontana, F.; Iberite, F.; Cafarelli, A.; Aliperta, A.; Baldi, G.; Gabusi, E.; Dolzani, P.; Cristino, S.; Lisignoli, G.; Pratellesi, T.; Dumont, E.; Ricotti, L. Development and Validation of Low-Intensity Pulsed Ultrasound Systems for Highly Controlled in Vitro Cell Stimulation. *Ultrasonics* **2021**, *116*, 106495. https://doi.org/10.1016/J.ULTRAS.2021.106495.

(65) Racca, L.; Limongi, T.; Vighetto, V.; Dumontel, B.; Ancona, A.; Canta, M.; Canavese, G.; Garino, N.; Cauda, V. Zinc Oxide Nanocrystals and High-Energy Shock Waves: A New Synergy for the Treatment of Cancer Cells. *Front Bioeng Biotechnol* **2020**, *8*. https://doi.org/10.3389/FBIOE.2020.00577.

(66) Lei, J.; Hill, M.; Glynne-Jones, P. Numerical Simulation of 3D Boundary-Driven Acoustic Streaming in Microfluidic Devices. *Lab Chip* **2013**, *14* (3), 532–541. https://doi.org/10.1039/C3LC50985K.

(67) Spigarelli, L.; Vasile, N. S.; Pirri, C. F.; Canavese, G. Numerical Study of the Effect of Channel Aspect Ratio on Particle Focusing in Acoustophoretic Devices. *Sci Rep* **2020**, *10* (1). https://doi.org/10.1038/S41598-020-76367-W.

(68) Comsol. The Acoustics Module User's Guide. **2020**.

(69) *The Acoustic Bubble - 1st Edition*. https://www.elsevier.com/books/the-acoustic-bubble/leighton/978-0-08-051876-3 (accessed 2022-07-05).

(70) Takagi, Y.; Hosokawa, T.; Hoshikawa, K.; Kobayashi, H.; Hiki, Y. Relaxation of Polystyrene near the Glass Transition Temperature Studied by Acoustic Measurements. *http://dx.doi.org/10.1143/JPSJ.76.024604* **2007**, *76* (2). https://doi.org/10.1143/JPSJ.76.024604.

(71) Shih, H.; Shih, H. Oxidation Kinetics of Aluminum Powders in a Gas Fluidized Bed Reactor in the Potential Application of Surge Arresting Materials. *Materials Sciences and Applications* **2019**, *10* (3), 253–292. https://doi.org/10.4236/MSA.2019.103021.

(72) Dhiren M. Joshi. *Living Science Physics 9*.

(73) Vighetto, V.; Racca, L.; Canta, M.; Matos, J. C.; Dumontel, B.; Gonçalves, M. C.; Cauda, V. Smart Shockwave Responsive Titania-Based Nanoparticles for Cancer Treatment. *Pharmaceutics* **2021**, *13* (9). https://doi.org/10.3390/PHARMACEUTICS13091423.

(74) Podbevšek, D.; Ledoux, G.; Dular, M. Investigation of Hydrodynamic Cavitation Induced Reactive Oxygen Species Production in Microchannels via Chemiluminescent Luminol Oxidation Reactions. *Water Res* **2022**, *220*, 118628. https://doi.org/10.1016/J.WATRES.2022.118628.

(75) Fu, P. P.; Xia, Q.; Hwang, H. M.; Ray, P. C.; Yu, H. Mechanisms of Nanotoxicity: Generation of Reactive Oxygen Species. *J Food Drug Anal* **2014**, *22* (1), 64–75. https://doi.org/10.1016/J.JFDA.2014.01.005.

(76) Özgür, Ü.; Alivov, Y. I.; Liu, C.; Teke, A.; Reshchikov, M. A.; Doğan, S.; Avrutin, V.; Cho, S. J.; Morkǫ, H. A Comprehensive Review of ZnO Materials and Devices. *J Appl Phys* **2005**, *98* (4), 041301. https://doi.org/10.1063/1.1992666.

(77) Kwan, J. J.; Graham, S.; Myers, R.; Carlisle, R.; Stride, E.; Coussios, C. C. Ultrasound-Induced Inertial Cavitation from Gas-Stabilizing Nanoparticles. *Phys Rev E Stat Nonlin Soft Matter Phys* **2015**, *92* (2), 023019. https://doi.org/10.1103/PHYSREVE.92.023019/FIGURES/4/MEDIUM.

(78) Suslick, K. S.; Flannigan, D. J. Inside a Collapsing Bubble: Sonoluminescence and the Conditions during Cavitation. *Annu Rev Phys*

Chem **2008**, *59*, 659–683. https://doi.org/10.1146/ANNUREV.PHYSCHEM.59.032607.093739.

(79) Salehipour, M.; Rezaei, S.; Mosafer, J.; Pakdin-Parizi, Z.; Motaharian, A.; Mogharabi-Manzari, M. Recent Advances in Polymer-Coated Iron Oxide Nanoparticles as Magnetic Resonance Imaging Contrast Agents. *Journal of Nanoparticle Research 2021 23:2* **2021**, *23* (2), 1–35. https://doi.org/10.1007/S11051-021-05156-X.

(80) Cao, X.; Gu, L.; Hu, S.; Mukhtar, A.; Wu, K. Fe/Mn Multilayer Nanowires as High-Performance T1-T2 Dual Modal MRI Contrast Agents. *Materials 2021, Vol. 14, Page 2238* **2021**, *14* (9), 2238. https://doi.org/10.3390/MA14092238.

(81) Sharma, B.; Grandjean, J.; Phillips, M.; Kumar, A.; Mandino, F.; Yeow, L. Y.; Jia, K.; Low, Y.; Nandwana, V.; Dravid, V. P.; Bengang, X.; Lim, S.; Pervushin, K. Lipocalin-Type Prostaglandin d Synthase Conjugates as Magnetic Resonance Imaging Contrast Agents for Detecting Amyloid β-Rich Regions in the Brain of Live Alzheimer's Disease Mice. *Adv Nanobiomed Res* **2021**, *1* (11), 2100019. https://doi.org/10.1002/ANBR.202100019.

(82) Menon, J. U.; Jadeja, P.; Tambe, P.; Vu, K.; Yuan, B.; Nguyen, K. T. Nanomaterials for Photo-Based Diagnostic and Therapeutic Applications. *Theranostics* **2013**, *3* (3), 152–166. https://doi.org/10.7150/THNO.5327.

(83) Hassanpour, S.; Baradaran, B.; de la Guardia, M.; Baghbanzadeh, A.; Mosafer, J.; Hejazi, M.; Mokhtarzadeh, A.; Hasanzadeh, M. Diagnosis of Hepatitis via Nanomaterial-Based Electrochemical, Optical or Piezoelectrical Biosensors: A Review on Recent Advancements. *Microchimica Acta 2018 185:12* **2018**, *185* (12), 1–24. https://doi.org/10.1007/S00604-018-3088-8.

(84) Neves, A. A.; Brindle, K. M. Assessing Responses to Cancer Therapy Using Molecular Imaging. *Biochimica et Biophysica Acta (BBA) - Reviews on Cancer* **2006**, *1766* (2), 242–261. https://doi.org/10.1016/J.BBCAN.2006.10.002.

(85) Torigian, D. A.; Huang, S. S.; Houseni, M.; Alavi, A. Functional Imaging of Cancer with Emphasis on Molecular Techniques. *CA Cancer J Clin* **2007**, *57* (4), 206–224. https://doi.org/10.3322/CANJCLIN.57.4.206.

(86) Kang, K. M.; Kim, H. W.; Shim, I. W.; Kwak, H. Y. Syntheses of Specialty Nanomaterials at the Multibubble Sonoluminescence Condition. *ASME International Mechanical Engineering Congress and Exposition, Proceedings* **2009**, *15*, 101–103. https://doi.org/10.1115/IMECE2008-68320.

(87) Park, J.; Hwang, C. H.; Lee, W. Y.; Kim, Y.; Kim, H.; Shim, I. W. Preparation of Size-Tunable SnS Nanoparticles by a Sonochemical Method under Multibubble Sonoluminescence Conditions. *Mater Lett* **2014**, *117*, 188–191. https://doi.org/10.1016/J.MATLET.2013.11.115.

(88) Ballou, B. Quantum Dot Surfaces for Use In Vivo and In Vitro. *Curr Top Dev Biol* **2005**, *70*, 103–120. https://doi.org/10.1016/S0070-2153(05)70005-3.

(89) Michalet, X.; Pinaud, F. F.; Bentolila, L. A.; Tsay, J. M.; Doose, S.; Li, J. J.; Sundaresan, G.; Wu, A. M.; Gambhir, S. S.; Weiss, S. Quantum Dots for Live Cells, in Vivo Imaging, and Diagnostics. *Science (1979)* **2005**, *307* (5709), 538–544. https://doi.org/10.1126/SCIENCE.1104274/SUPPL_FILE/MICHALET.SOM.PDF.

(90) Bilan, R.; Fleury, F.; Nabiev, I.; Sukhanova, A. Quantum Dot Surface Chemistry and Functionalization for Cell Targeting and Imaging. *Bioconjug Chem* **2015**, *26* (4), 609–624. https://doi.org/10.1021/ACS.BIOCONJCHEM.5B00069/ASSET/IMAGES/MEDIUM/BC-2015-00069M_0001.GIF.

(91) Al-Jamal, W. A. T.; Al-Jamal, K. T.; Tian, B.; Cakebread, A.; Halket, J. M.; Kostarelos, K. Tumor Targeting of Functionalized Quantum Dot Liposome Hybrids by Intravenous Administration. *Mol Pharm* **2009**, *6* (2), 520–530.

https://doi.org/10.1021/MP800187D/SUPPL_FILE/MP800187D_SI_001.PDF.

(92) Shi, H.; Sun, Y.; Yan, R.; Liu, S.; Zhu, L.; Liu, S.; Feng, Y.; Wang, P.; He, J.; Zhou, Z.; Ye, D. Magnetic Semiconductor Gd-Doping CuS Nanoparticles as Activatable Nanoprobes for Bimodal Imaging and Targeted Photothermal Therapy of Gastric Tumors. *Nano Lett* **2019**, *19* (2), 937–947. https://doi.org/10.1021/ACS.NANOLETT.8B04179/SUPPL_FILE/NL8B04179_SI_001.PDF.

(93) Wei, W.; Zhang, X.; Zhang, S.; Wei, G.; Su, Z. Biomedical and Bioactive Engineered Nanomaterials for Targeted Tumor Photothermal Therapy: A Review. *Materials Science and Engineering: C* **2019**, *104*, 109891. https://doi.org/10.1016/J.MSEC.2019.109891.

(94) Kairdolf, B. A.; Qian, X.; Nie, S. Bioconjugated Nanoparticles for Biosensing, in Vivo Imaging, and Medical Diagnostics. *Anal Chem* **2017**, *89* (2), 1015–1031. https://doi.org/10.1021/ACS.ANALCHEM.6B04873/ASSET/IMAGES/ACS.ANALCHEM.6B04873.SOCIAL.JPEG_V03.

(95) Stahl, T.; Bofinger, R.; Lam, I.; Fallon, K. J.; Johnson, P.; Ogunlade, O.; Vassileva, V.; Pedley, R. B.; Beard, P. C.; Hailes, H. C.; Bronstein, H.; Tabor, A. B. Tunable Semiconducting Polymer Nanoparticles with INDT-Based Conjugated Polymers for Photoacoustic Molecular Imaging. *Bioconjug Chem* **2017**, *28* (6), 1734–1740. https://doi.org/10.1021/ACS.BIOCONJCHEM.7B00185/ASSET/IMAGES/BC-2017-00185S_M001.GIF.

(96) Dumontel, B.; Susa, F.; Limongi, T.; Canta, M.; Racca, L.; Chiodoni, A.; Garino, N.; Chiabotto, G.; Centomo, M. L.; Pignochino, Y.; Cauda, V. ZnO Nanocrystals Shuttled by Extracellular Vesicles as Effective Trojan Nano-Horses against Cancer Cells. *Nanomedicine* **2019**, *14* (21), 2815–2833. https://doi.org/10.2217/NNM-2019-0231/ASSET/IMAGES/LARGE/FIGURE6.JPEG.

(97) Dumontel, B.; Canta, M.; Engelke, H.; Chiodoni, A.; Racca, L.; Ancona, A.; Limongi, T.; Canavese, G.; Cauda, V. Enhanced Biostability and

Cellular Uptake of Zinc Oxide Nanocrystals Shielded with a Phospholipid Bilayer. *J Mater Chem B* **2017**, *5* (44), 8799–8813. https://doi.org/10.1039/C7TB02229H.

(98) Crum, L. A. Resource Paper: Sonoluminescence. *J Acoust Soc Am* **2015**, *138* (4), 2181. https://doi.org/10.1121/1.4929687.

(99) Eastwood, L. M.; Watmough, D. J. Sonoluminescence, in Water and in Human Blood Plasma, Generated Using Ultrasonic Therapy Equipment. *Ultrasound Med Biol* **1977**, *2* (4), 319–323. https://doi.org/10.1016/0301-5629(77)90033-3.

(100) Dezhkunov, N. v.; Francescutto, A.; Serpe, L.; Canaparo, R.; Cravotto, G. Sonoluminescence and Acoustic Emission Spectra at Different Stages of Cavitation Zone Development. *Ultrason Sonochem* **2018**, *40*, 104–109. https://doi.org/10.1016/J.ULTSONCH.2017.04.004.

(101) Cochran, S. A.; Prausnitz, M. R. Sonoluminescence as an Indicator of Cell Membrane Disruption by Acoustic Cavitation. *Ultrasound Med Biol* **2001**, *27* (6), 841–850. https://doi.org/10.1016/S0301-5629(01)00382-9.

(102) Pflieger, R.; Nikitenko, S. I.; Ashokkumar, M. Effect of NaCl Salt on Sonochemistry and Sonoluminescence in Aqueous Solutions. *Ultrason Sonochem* **2019**, *59*, 104753. https://doi.org/10.1016/J.ULTSONCH.2019.104753.

(103) Stöber, W.; Fink, A.; Bohn, E. Controlled Growth of Monodisperse Silica Spheres in the Micron Size Range. *J Colloid Interface Sci* **1968**, *26* (1), 62–69. https://doi.org/10.1016/0021-9797(68)90272-5.

(104) Bogush, G. H.; Tracy, M. A.; Zukoski IV, C. F. Preparation of Monodisperse Silica Particles: Control of Size and Mass Fraction. *J Non Cryst Solids* **1988**, *104* (1), 95–106. https://doi.org/10.1016/0022-3093(88)90187-1.

(105) Kopac, T. Protein Corona, Understanding the Nanoparticle–Protein Interactions and Future Perspectives: A Critical Review. *Int J Biol*

Macromol **2021**, *169*, 290–301. https://doi.org/10.1016/J.IJBIOMAC.2020.12.108.

(106) He, Y.; Xing, D.; Tan, S.; Tang, Y.; Ueda, K. I. In Vivo Sonoluminescence Imaging with the Assistance of FCLA. *Phys Med Biol* **2002**, *47* (9), 1535. https://doi.org/10.1088/0031-9155/47/9/308.

(107) Lafond, M.; Yoshizawa, S.; Umemura, S. ichiro. Sonodynamic Therapy: Advances and Challenges in Clinical Translation. *Journal of Ultrasound in Medicine* **2019**, *38* (3), 567–580. https://doi.org/10.1002/JUM.14733.

(108) Carofiglio, M.; Laurenti, M.; Vighetto, V.; Racca, L.; Barui, S.; Garino, N.; Gerbaldo, R.; Laviano, F.; Cauda, V. Iron-Doped ZnO Nanoparticles as Multifunctional Nanoplatforms for Theranostics. *Nanomaterials 2021, Vol. 11, Page 2628* **2021**, *11* (10), 2628. https://doi.org/10.3390/NANO11102628.

(109) Shi, J.; Kantoff, P. W.; Wooster, R.; Farokhzad, O. C. Cancer Nanomedicine: Progress, Challenges and Opportunities. *Nature Reviews Cancer 2016 17:1* **2016**, *17* (1), 20–37. https://doi.org/10.1038/nrc.2016.108.

(110) Zavaleta, C.; Ho, D.; Chung, E. J. Theranostic Nanoparticles for Tracking and Monitoring Disease State. *SLAS Technol* **2018**, *23* (3), 281–293. https://doi.org/10.1177/2472630317738699.

(111) Tran, S.; DeGiovanni, P.-J.; Piel, B.; Rai, P. Cancer Nanomedicine: A Review of Recent Success in Drug Delivery. *Clin Transl Med* **2017**, *6* (1), e44. https://doi.org/10.1186/S40169-017-0175-0.

(112) Chugh, H.; Sood, D.; Chandra, I.; Tomar, V.; Dhawan, G.; Chandra, R. Role of Gold and Silver Nanoparticles in Cancer Nano-Medicine. *https://doi.org/10.1080/21691401.2018.1449118* **2018**, *46* (sup1), 1210–1220. https://doi.org/10.1080/21691401.2018.1449118.

(113) Bisht, G.; Rayamajhi, S. ZnO Nanoparticles: A Promising Anticancer Agent. *Nanobiomedicine (Rij)* **2016**, *3*, 9. https://doi.org/10.5772/63437.

(114) Lim, E. K.; Kim, T.; Paik, S.; Haam, S.; Huh, Y. M.; Lee, K. Nanomaterials for Theranostics: Recent Advances and Future Challenges.

Chem Rev **2015**, *115* (1), 327–394. https://doi.org/10.1021/CR300213B/ASSET/IMAGES/CR300213B.SOCIAL.JPEG_V03.

(115) Jiang, J.; Pi, J.; Cai, J. The Advancing of Zinc Oxide Nanoparticles for Biomedical Applications. *Bioinorg Chem Appl* **2018**, *2018*. https://doi.org/10.1155/2018/1062562.

(116) Jiang, H.; Wang, H.; Wang, X. Facile and Mild Preparation of Fluorescent ZnO Nanosheets and Their Bioimaging Applications. *Appl Surf Sci* **2011**, *257* (15), 6991–6995. https://doi.org/10.1016/J.APSUSC.2011.03.053.

(117) Sanginario, A.; Cauda, V.; Bonanno, A.; Bejtka, K.; Sapienza, S.; Demarchi, D. An Electronic Platform for Real-Time Detection of Bovine Serum Albumin by Means of Amine-Functionalized Zinc Oxide Microwires. *RSC Adv* **2015**, *6* (2), 891–897. https://doi.org/10.1039/C5RA15787K.

(118) Shanmugam, N. R.; Muthukumar, S.; Prasad, S. A Review on ZnO-Based Electrical Biosensors for Cardiac Biomarker Detection. *Future Sci OA* **2017**, *3* (4). https://doi.org/10.4155/FSOA-2017-0006/ASSET/IMAGES/LARGE/FIGURE5.JPEG.

(119) Stassi, S.; Chiadò, A.; Cauda, V.; Palmara, G.; Canavese, G.; Laurenti, M.; Ricciardi, C. Functionalized ZnO Nanowires for Microcantilever Biosensors with Enhanced Binding Capability. *Anal Bioanal Chem* **2017**, *409* (10), 2615–2625. https://doi.org/10.1007/S00216-017-0204-2/TABLES/1.

(120) Laurenti, M.; Cauda, V. ZnO Nanostructures for Tissue Engineering Applications. *Nanomaterials 2017, Vol. 7, Page 374* **2017**, *7* (11), 374. https://doi.org/10.3390/NANO7110374.

(121) Laurenti, M.; Cauda, V. Gentamicin-Releasing Mesoporous ZnO Structures. *Materials 2018, Vol. 11, Page 314* **2018**, *11* (2), 314. https://doi.org/10.3390/MA11020314.

(122) Martínez-Carmona, M.; Gun'Ko, Y.; Vallet-Regí, M. ZnO Nanostructures for Drug Delivery and Theranostic Applications. *Nanomaterials 2018, Vol. 8, Page 268* **2018**, *8* (4), 268. https://doi.org/10.3390/NANO8040268.

(123) Singh, S. Zinc Oxide Nanoparticles Impacts: Cytotoxicity, Genotoxicity, Developmental Toxicity, and Neurotoxicity. *https://doi.org/10.1080/15376516.2018.1553221* **2019**, *29* (4), 300–311. https://doi.org/10.1080/15376516.2018.1553221.

(124) Wan, G. Y.; Liu, Y.; Chen, B. W.; Liu, Y. Y.; Wang, Y. S.; Zhang, N. Recent Advances of Sonodynamic Therapy in Cancer Treatment. *Cancer Biol Med* **2016**, *13* (3), 325–338. https://doi.org/10.20892/J.ISSN.2095-3941.2016.0068.

(125) Ogden, J. A.; Tóth-Kischkat, A.; Schultheiss, R. Principles of Shock Wave Therapy. *Clin Orthop Relat Res* **2001**, *387* (387), 8–17. https://doi.org/10.1097/00003086-200106000-00003.

(126) Canaparo, R.; Serpe, L.; Zara, G. P.; Chiarle, R.; Berta, L.; Frairia, R. High Energy Shock Waves (HESW) Increase Paclitaxel Efficacy in a Syngeneic Model of Breast Cancer. *Technol Cancer Res Treat* **2008**, *7* (2), 117–124. https://doi.org/10.1177/153303460800700204.

(127) Zhang, J.; Shrivastava, S.; Cleveland, R. O.; Rabbitts, T. H. Lipid-MRNA Nanoparticle Designed to Enhance Intracellular Delivery Mediated by Shock Waves. *ACS Appl Mater Interfaces* **2019**, *11* (11), 10481–10491. https://doi.org/10.1021/ACSAMI.8B21398/ASSET/IMAGES/LARGE/AM-2018-21398H_0006.JPEG.

(128) Serpe, L.; Canaparo, R.; Berta, L.; Bargoni, A.; Zara, G. P.; Frairia, R. High Energy Shock Waves and 5-Aminolevulinic for Sonodynamic Therapy: Effects in a Syngeneic Model of Colon Cancer. *Technol Cancer Res Treat* **2011**, *10* (1), 85–93. https://doi.org/10.7785/tcrt.2012.500182.

(129) *Sonodynamic Treatment as an Innovative Bimodal Anticancer Approach: Shock Wave-mediated Tumor Growth Inhibition in a Syngeneic Breast Cancer Model - Federica Foglietta - Discovery Medicine*. https://www.discoverymedicine.com/Federica-Foglietta/2015/10/sonodynamic-treatment-as-an-innovative-bimodal-

anticancer-approach-shock-wave-mediated-tumor-growth-inhibition-in-a-syngeneic-breast-cancer-model/ (accessed 2022-08-19).

(130) Varchi, G.; Foglietta, F.; Canaparo, R.; Ballestri, M.; Arena, F.; Sotgiu, G.; Guerrini, A.; Nanni, C.; Cicoria, G.; Cravotto, G.; Fanti, S.; Serpe, L. Engineered Porphyrin Loaded Core-Shell Nanoparticles for Selective Sonodynamic Anticancer Treatment. *https://doi.org/10.2217/nnm.15.150* **2015**, *10* (23), 3483–3494. https://doi.org/10.2217/NNM.15.150.

(131) Canaparo, R.; Varchi, G.; Ballestri, M.; Foglietta, F.; Sotgiu, G.; Guerrini, A.; Francovich, A.; Civera, P.; Frairia, R.; Serpe, L. Polymeric Nanoparticles Enhance the Sonodynamic Activity of Meso-Tetrakis (4-Sulfonatophenyl) Porphyrin in an in Vitro Neuroblastoma Model. *Int J Nanomedicine* **2013**, *8* (1), 4247–4263. https://doi.org/10.2147/IJN.S51070.

(132) Foglietta, F.; Duchi, S.; Canaparo, R.; Varchi, G.; Lucarelli, E.; Dozza, B.; Serpe, L. Selective Sensitiveness of Mesenchymal Stem Cells to Shock Waves Leads to Anticancer Effect in Human Cancer Cell Co-Cultures. *Life Sci* **2017**, *173*, 28–35. https://doi.org/10.1016/J.LFS.2017.01.009.

(133) Marino, A.; Almici, E.; Migliorin, S.; Tapeinos, C.; Battaglini, M.; Cappello, V.; Marchetti, M.; de Vito, G.; Cicchi, R.; Pavone, F. S.; Ciofani, G. Piezoelectric Barium Titanate Nanostimulators for the Treatment of Glioblastoma Multiforme. *J Colloid Interface Sci* **2019**, *538*, 449–461. https://doi.org/10.1016/J.JCIS.2018.12.014.

(134) Marino, A.; Battaglini, M.; de Pasquale, D.; Degl'Innocenti, A.; Ciofani, G. Ultrasound-Activated Piezoelectric Nanoparticles Inhibit Proliferation of Breast Cancer Cells. *Scientific Reports 2018 8:1* **2018**, *8* (1), 1–13. https://doi.org/10.1038/s41598-018-24697-1.

(135) Aruoma, O. I.; Halliwell, B.; Hoey, B. M.; Butler, J. The Antioxidant Action of N-Acetylcysteine: Its Reaction with Hydrogen Peroxide, Hydroxyl Radical, Superoxide, and Hypochlorous Acid. *Free Radic Biol Med* **1989**, *6* (6), 593–597. https://doi.org/10.1016/0891-5849(89)90066-X.

(136) Goldstein, S.; Czapski, G. Mannitol as an OH· Scavenger in Aqueous Solutions and in Biological Systems.

http://dx.doi.org/10.1080/09553008414551961 **2009**, *46* (6), 725–729. https://doi.org/10.1080/09553008414551961.

(137) Brazzale, C.; Canaparo, R.; Racca, L.; Foglietta, F.; Durando, G.; Fantozzi, R.; Caliceti, P.; Salmaso, S.; Serpe, L. Enhanced Selective Sonosensitizing Efficacy of Ultrasound-Based Anticancer Treatment by Targeted Gold Nanoparticles. *https://doi.org/10.2217/nnm-2016-0293* **2016**, *12* (23), 3053–3070. https://doi.org/10.2217/NNM-2016-0293.

(138) Yumita, N.; Iwase, Y.; Nishi, K.; Ikeda, T.; Umemura, S. I.; Sakata, I.; Momose, Y. Sonodynamically Induced Cell Damage and Membrane Lipid Peroxidation by Novel Porphyrin Derivative, DCPH-P-Na(I). *Anticancer Res* **2010**, *30* (6), 2241–2246.

(139) Liu, J.; Kang, Y.; Zheng, W.; Song, B.; Wei, L.; Chen, L.; Shao, L. From the Cover: Ion-Shedding Zinc Oxide Nanoparticles Induce Microglial BV2 Cell Proliferation via the ERK and Akt Signaling Pathways. *Toxicological Sciences* **2017**, *156* (1), 167–178. https://doi.org/10.1093/TOXSCI/KFW241.

(140) Ramirez, A.; Schwane, J. A.; McFarland, C.; Starcher, B. The Effect of Ultrasound on Collagen Synthesis and Fibroblast Proliferation in Vitro. *Med Sci Sports Exerc* **1997**, *29* (3), 326–332. https://doi.org/10.1097/00005768-199703000-00007.

(141) Hill, G. E.; Fenwick, S.; Matthews, B. J.; Chivers, R. A.; Southgate, J. The Effect of Low-Intensity Pulsed Ultrasound on Repair of Epithelial Cell Monolayers in Vitro. *Ultrasound Med Biol* **2005**, *31* (12), 1701–1706. https://doi.org/10.1016/J.ULTRASMEDBIO.2005.08.001.

(142) Wang, X. J.; Mitchell, D.; Lewis, T. J. Primary Clinical Use of Sonodynamic Therapy (SDT) for Advanced Breast Cancer. *https://doi.org/10.1200/jco.2008.26.15_suppl.12029* **2008**, *26* (15_suppl), 12029–12029. https://doi.org/10.1200/JCO.2008.26.15_SUPPL.12029.

(143) Ninomiya, K.; Ogino, C.; Oshima, S.; Sonoke, S.; Kuroda, S. I.; Shimizu, N. Targeted Sonodynamic Therapy Using Protein-Modified TiO2 Nanoparticles. *Ultrason Sonochem* **2012**, *19* (3), 607–614. https://doi.org/10.1016/J.ULTSONCH.2011.09.009.

(144) Katiyar, A.; Duncan, R. L.; Sarkar, K. Ultrasound Stimulation Increases Proliferation of MC3T3-E1 Preosteoblast-like Cells. *J Ther Ultrasound* **2014**, *2* (1), 1–10. https://doi.org/10.1186/2050-5736-2-1/FIGURES/6.

(145) Huang, J.; Liu, F.; Han, X.; Zhang, L.; Hu, Z.; Jiang, Q.; Wang, Z.; Ran, H.; Wang, D.; Li, P. Nanosonosensitizers for Highly Efficient Sonodynamic Cancer Theranostics. *Theranostics* **2018**, *8* (22), 6178–6194. https://doi.org/10.7150/THNO.29569.

(146) Li, Y.; Wang, P.; Zhao, P.; Zhu, S.; Wang, X.; Liu, Q. Apoptosis Induced by Sonodynamic Treatment by Protoporphyrin IX on MDA-MB-231 Cells. *Ultrasonics* **2012**, *52* (4), 490–496. https://doi.org/10.1016/J.ULTRAS.2011.10.013.

(147) Mittler, R. ROS Are Good. *Trends Plant Sci* **2017**, *22* (1), 11–19. https://doi.org/10.1016/J.TPLANTS.2016.08.002/ATTACHMENT/9FF8BEA2-B7BE-4EFA-9559-B99BBE252ACB/MMC1.MP4.

(148) Singh, K.; Bhori, M.; Kasu, Y. A.; Bhat, G.; Marar, T. Antioxidants as Precision Weapons in War against Cancer Chemotherapy Induced Toxicity – Exploring the Armoury of Obscurity. *Saudi Pharmaceutical Journal* **2018**, *26* (2), 177–190. https://doi.org/10.1016/J.JSPS.2017.12.013.

(149) Asadi-Samani, M.; Farkhad, N. K.; Mahmoudian-Sani, M. R.; Shirzad, H. Antioxidants as a Double-Edged Sword in the Treatment of Cancer. *Antioxidants* **2019**. https://doi.org/10.5772/INTECHOPEN.85468.

(150) Ninomiya, K.; Noda, K.; Ogino, C.; Kuroda, S. I.; Shimizu, N. Enhanced OH Radical Generation by Dual-Frequency Ultrasound with TiO2 Nanoparticles: Its Application to Targeted Sonodynamic Therapy. *Ultrason Sonochem* **2014**, *21* (1), 289–294. https://doi.org/10.1016/J.ULTSONCH.2013.05.005.

(151) Beguin, E.; Shrivastava, S.; Dezhkunov, N. v.; Mchale, A. P.; Callan, J. F.; Stride, E. Direct Evidence of Multibubble Sonoluminescence Using Therapeutic Ultrasound and Microbubbles. *ACS Appl Mater Interfaces* **2019**, *11* (22), 19913–19919.

https://doi.org/10.1021/ACSAMI.9B07084/ASSET/IMAGES/LARGE/AM-2019-070845_0005.JPEG.

(152) Izadifar, Z.; Babyn, P.; Chapman, D. Mechanical and Biological Effects of Ultrasound: A Review of Present Knowledge. *Ultrasound Med Biol* **2017**, *43* (6), 1085–1104. https://doi.org/10.1016/J.ULTRASMEDBIO.2017.01.023.

(153) Osminkina, L. A.; Nikolaev, A. L.; Sviridov, A. P.; Andronova, N. v.; Tamarov, K. P.; Gongalsky, M. B.; Kudryavtsev, A. A.; Treshalina, H. M.; Timoshenko, V. Y. Porous Silicon Nanoparticles as Efficient Sensitizers for Sonodynamic Therapy of Cancer. *Microporous and Mesoporous Materials* **2015**, *210*, 169–175. https://doi.org/10.1016/J.MICROMESO.2015.02.037.

(154) Cauda, V.; Gazia, R.; Porro, S.; Stassi, S.; Canavese, G.; Roppolo, I.; Chiolerio, A. Nanostructured ZnO Materials: Synthesis, Properties and Applications. *Handbook of Nanomaterials Properties* **2014**, 137–177. https://doi.org/10.1007/978-3-642-31107-9_32.

(155) Cauda, V.; Stassi, S.; Lamberti, A.; Morello, M.; Fabrizio Pirri, C.; Canavese, G. Leveraging ZnO Morphologies in Piezoelectric Composites for Mechanical Energy Harvesting. *Nano Energy* **2015**, *18*, 212–221. https://doi.org/10.1016/J.NANOEN.2015.10.021.

(156) Laurenti, M.; Stassi, S.; Lorenzoni, M.; Fontana, M.; Canavese, G.; Cauda, V.; Pirri, C. F. Evaluation of the Piezoelectric Properties and Voltage Generation of Flexible Zinc Oxide Thin Films. *Nanotechnology* **2015**, *26* (21), 215704. https://doi.org/10.1088/0957-4484/26/21/215704.

(157) Laurenti, M.; Canavese, G.; Stassi, S.; Fontana, M.; Castellino, M.; Pirri, C. F.; Cauda, V. A Porous Nanobranched Structure: An Effective Way to Improve Piezoelectricity in Sputtered ZnO Thin Films. *RSC Adv* **2016**, *6* (80), 76996–77004. https://doi.org/10.1039/C6RA17319E.

(158) Hassan, F.; Ni, S.; Arnett, T. C.; McKell, M. C.; Kennedy, M. A. Adenovirus-Mediated Delivery of Decoy Hyper Binding Sites Targeting Oncogenic HMGA1 Reduces Pancreatic and Liver Cancer Cell Viability. *Mol Ther Oncolytics* **2018**, *8*, 52–61.

https://doi.org/10.1016/J.OMTO.2018.01.002/ATTACHMENT/F436F543-D983-4C91-A821-F114A24F98AD/MMC1.PDF.

(159) *(4) (PDF) High energy shock waves (HESW) for sonodynamic therapy: Effects on HT-29 human colon cancer cells*. https://www.researchgate.net/publication/6703737_High_energy_shock_waves_HESW_for_sonodynamic_therapy_Effects_on_HT-29_human_colon_cancer_cells (accessed 2022-08-19).

(160) Furusawa, Y.; Kondo, T. Citation: Furusawa Y, Kondo T (2017) DNA Damage Induced by Ultrasound and Cellular Responses. *Mol Biol* **2017**, *6* (2), 188. https://doi.org/10.4172/2168-9547.1000188.

(161) d'Agostino, M. C.; Craig, K.; Tibalt, E.; Respizzi, S. Shock Wave as Biological Therapeutic Tool: From Mechanical Stimulation to Recovery and Healing, through Mechanotransduction. *International Journal of Surgery* **2015**, *24*, 147–153. https://doi.org/10.1016/J.IJSU.2015.11.030.

(162) Dumontel, B.; Susa, F.; Limongi, T.; Vighetto, V.; Debellis, D.; Canta, M.; Cauda, V. Nanotechnological Engineering of Extracellular Vesicles for the Development of Actively Targeted Hybrid Nanodevices. *Cell & Bioscience 2022 12:1* **2022**, *12* (1), 1–18. https://doi.org/10.1186/S13578-022-00784-9.

(163) Ratajczak, J.; Wysoczynski, M.; Hayek, F.; Janowska-Wieczorek, A.; Ratajczak, M. Z. Membrane-Derived Microvesicles: Important and Underappreciated Mediators of Cell-to-Cell Communication. *Leukemia* **2006**, *20* (9), 1487–1495. https://doi.org/10.1038/SJ.LEU.2404296.

(164) Valadi, H.; Ekström, K.; Bossios, A.; Sjöstrand, M.; Lee, J. J.; Lötvall, J. O. Exosome-Mediated Transfer of MRNAs and MicroRNAs Is a Novel Mechanism of Genetic Exchange between Cells. *Nat Cell Biol* **2007**, *9* (6), 654–659. https://doi.org/10.1038/NCB1596.

(165) Maas, S. L. N.; Breakefield, X. O.; Weaver, A. M. Extracellular Vesicles: Unique Intercellular Delivery Vehicles. *Trends Cell Biol* **2017**, *27* (3), 172–188. https://doi.org/10.1016/J.TCB.2016.11.003.

(166) Zhao, Y.; Li, X.; Zhang, W.; Yu, L.; Wang, Y.; Deng, Z.; Liu, M.; Mo, S.; Wang, R.; Zhao, J.; Liu, S.; Hao, Y.; Wang, X.; Ji, T.; Zhang, L.; Wang, C. Trends in the Biological Functions and Medical Applications of Extracellular Vesicles and Analogues. *Acta Pharm Sin B* **2021**, *11* (8), 2114–2135. https://doi.org/10.1016/J.APSB.2021.03.012.

(167) Petre, C. E.; Dittmer, D. P.; Ellen, M.; Bldg, J. Liposomal Daunorubicin as Treatment for Kaposi's Sarcoma. *Int J Nanomedicine* **2007**, *2* (3), 277.

(168) Chatin, B.; Mével, M.; Devallière, J.; Dallet, L.; Haudebourg, T.; Peuziat, P.; Colombani, T.; Berchel, M.; Lambert, O.; Edelman, A.; Pitard, B. Liposome-Based Formulation for Intracellular Delivery of Functional Proteins. *Mol Ther Nucleic Acids* **2015**, *4*, e244. https://doi.org/10.1038/MTNA.2015.17.

(169) Limongi, T.; Susa, F.; Marini, M.; Allione, M.; Torre, B.; Pisano, R.; di Fabrizio, E. Lipid-Based Nanovesicular Drug Delivery Systems. *Nanomaterials 2021, Vol. 11, Page 3391* **2021**, *11* (12), 3391. https://doi.org/10.3390/NANO11123391.

(170) Durfee, P. N.; Lin, Y. S.; Dunphy, D. R.; Muñiz, A. J.; Butler, K. S.; Humphrey, K. R.; Lokke, A. J.; Agola, J. O.; Chou, S. S.; Chen, I. M.; Wharton, W.; Townson, J. L.; Willman, C. L.; Brinker, C. J. Mesoporous Silica Nanoparticle-Supported Lipid Bilayers (Protocells) for Active Targeting and Delivery to Individual Leukemia Cells. *ACS Nano* **2016**, *10* (9), 8325–8345. https://doi.org/10.1021/ACSNANO.6B02819/SUPPL_FILE/NN6B02819_SI_004.AVI.

(171) Luan, X.; Sansanaphongpricha, K.; Myers, I.; Chen, H.; Yuan, H.; Sun, D. Engineering Exosomes as Refined Biological Nanoplatforms for Drug Delivery. *Acta Pharmacol Sin* **2017**, *38* (6), 754–763. https://doi.org/10.1038/APS.2017.12.

(172) Hadla, M.; Palazzolo, S.; Corona, G.; Caligiuri, I.; Canzonieri, V.; Toffoli, G.; Rizzolio, F. Exosomes Increase the Therapeutic Index of Doxorubicin in Breast and Ovarian Cancer Mouse Models. *Nanomedicine (Lond)* **2016**, *11* (18), 2431–2441. https://doi.org/10.2217/NNM-2016-0154.

(173) Kim, M. S.; Haney, M. J.; Zhao, Y.; Mahajan, V.; Deygen, I.; Klyachko, N. L.; Inskoe, E.; Piroyan, A.; Sokolsky, M.; Okolie, O.; Hingtgen, S. D.; Kabanov, A. v.; Batrakova, E. v. Development of Exosome-Encapsulated Paclitaxel to Overcome MDR in Cancer Cells. *Nanomedicine* **2016**, *12* (3), 655–664. https://doi.org/10.1016/J.NANO.2015.10.012.

(174) Haney, M. J.; Zhao, Y.; Jin, Y. S.; Li, S. M.; Bago, J. R.; Klyachko, N. L.; Kabanov, A. v.; Batrakova, E. v. Macrophage-Derived Extracellular Vesicles as Drug Delivery Systems for Triple Negative Breast Cancer (TNBC) Therapy. *J Neuroimmune Pharmacol* **2020**, *15* (3), 487–500. https://doi.org/10.1007/S11481-019-09884-9.

(175) Hood, J. L.; Scott, M. J.; Wickline, S. A. Maximizing Exosome Colloidal Stability Following Electroporation. *Anal Biochem* **2014**, *448* (1), 41–49. https://doi.org/10.1016/J.AB.2013.12.001.

(176) Betzer, O.; Perets, N.; Angel, A.; Motiei, M.; Sadan, T.; Yadid, G.; Offen, D.; Popovtzer, R. In Vivo Neuroimaging of Exosomes Using Gold Nanoparticles. *ACS Nano* **2017**, *11* (11), 10883–10893. https://doi.org/10.1021/ACSNANO.7B04495.

(177) Illes, B.; Hirschle, P.; Barnert, S.; Cauda, V.; Wuttke, S.; Engelke, H. Exosome-Coated Metal-Organic Framework Nanoparticles: An Efficient Drug Delivery Platform. *Chemistry of Materials* **2017**, *29* (19), 8042–8046. https://doi.org/10.1021/ACS.CHEMMATER.7B02358/SUPPL_FILE/CM7B02358_SI_001.PDF.

(178) Srivastava, A.; Amreddy, N.; Babu, A.; Panneerselvam, J.; Mehta, M.; Muralidharan, R.; Chen, A.; Zhao, Y. D.; Razaq, M.; Riedinger, N.; Kim, H.; Liu, S.; Wu, S.; Abdel-Mageed, A. B.; Munshi, A.; Ramesh, R. Nanosomes Carrying Doxorubicin Exhibit Potent Anticancer Activity against Human Lung Cancer Cells. *Scientific Reports 2016 6:1* **2016**, *6* (1), 1–15. https://doi.org/10.1038/srep38541.

(179) Kibria, G.; Ramos, E. K.; Wan, Y.; Gius, D. R.; Liu, H. Exosomes as a Drug Delivery System in Cancer Therapy: Potential and Challenges. *Mol*

Pharm **2018**, *15* (9), 3625–3633. https://doi.org/10.1021/ACS.MOLPHARMACEUT.8B00277.

(180) Rufino-Ramos, D.; Albuquerque, P. R.; Carmona, V.; Perfeito, R.; Nobre, R. J.; Pereira de Almeida, L. Extracellular Vesicles: Novel Promising Delivery Systems for Therapy of Brain Diseases. *J Control Release* **2017**, *262*, 247–258. https://doi.org/10.1016/J.JCONREL.2017.07.001.

(181) Vader, P.; Mol, E. A.; Pasterkamp, G.; Schiffelers, R. M. Extracellular Vesicles for Drug Delivery. *Adv Drug Deliv Rev* **2016**, *106* (Pt A), 148–156. https://doi.org/10.1016/J.ADDR.2016.02.006.

(182) Fuhrmann, G.; Serio, A.; Mazo, M.; Nair, R.; Stevens, M. M. Active Loading into Extracellular Vesicles Significantly Improves the Cellular Uptake and Photodynamic Effect of Porphyrins. *J Control Release* **2015**, *205*, 35–44. https://doi.org/10.1016/J.JCONREL.2014.11.029.

(183) Limongi, T.; Susa, F.; Dumontel, B.; Racca, L.; Perrone Donnorso, M.; Debellis, D.; Cauda, V. Extracellular Vesicles Tropism: A Comparative Study between Passive Innate Tropism and the Active Engineered Targeting Capability of Lymphocyte-Derived EVs. *Membranes (Basel)* **2021**, *11* (11). https://doi.org/10.3390/MEMBRANES11110886.

(184) Dang, X. T. T.; Kavishka, J. M.; Zhang, D. X.; Pirisinu, M.; Le, M. T. N. Extracellular Vesicles as an Efficient and Versatile System for Drug Delivery. *Cells* **2020**, *9* (10). https://doi.org/10.3390/CELLS9102191.

(185) Meng, W.; He, C.; Hao, Y.; Wang, L.; Li, L.; Zhu, G. Prospects and Challenges of Extracellular Vesicle-Based Drug Delivery System: Considering Cell Source. *Drug Deliv* **2020**, *27* (1), 585–598. https://doi.org/10.1080/10717544.2020.1748758.

(186) Qiao, L.; Hu, S.; Huang, K.; Su, T.; Li, Z.; Vandergriff, A.; Cores, J.; Dinh, P. U.; Allen, T.; Shen, D.; Liang, H.; Li, Y.; Cheng, K. Tumor Cell-Derived Exosomes Home to Their Cells of Origin and Can Be Used as Trojan Horses to Deliver Cancer Drugs. *Theranostics* **2020**, *10* (8), 3474. https://doi.org/10.7150/THNO.39434.

(187) Sun, W.; Luo, J. D.; Jiang, H.; Duan, D. D. Tumor Exosomes: A Double-Edged Sword in Cancer Therapy. *Acta Pharmacol Sin* **2018**, *39* (4), 534–541. https://doi.org/10.1038/APS.2018.17.

(188) Peinado, H.; Zhang, H.; Matei, I. R.; Costa-Silva, B.; Hoshino, A.; Rodrigues, G.; Psaila, B.; Kaplan, R. N.; Bromberg, J. F.; Kang, Y.; Bissell, M. J.; Cox, T. R.; Giaccia, A. J.; Erler, J. T.; Hiratsuka, S.; Ghajar, C. M.; Lyden, D. Pre-Metastatic Niches: Organ-Specific Homes for Metastases. *Nat Rev Cancer* **2017**, *17* (5), 302–317. https://doi.org/10.1038/NRC.2017.6.

(189) Namee, N. M.; O'Driscoll, L. Extracellular Vesicles and Anti-Cancer Drug Resistance. *Biochim Biophys Acta Rev Cancer* **2018**, *1870* (2), 123–136. https://doi.org/10.1016/J.BBCAN.2018.07.003.

(190) Rome, S. Biological Properties of Plant-Derived Extracellular Vesicles. *Food Funct* **2019**, *10* (2), 529–538. https://doi.org/10.1039/C8FO02295J.

(191) Munagala, R.; Aqil, F.; Jeyabalan, J.; Gupta, R. C. Bovine Milk-Derived Exosomes for Drug Delivery. *Cancer Lett* **2016**, *371* (1), 48–61. https://doi.org/10.1016/J.CANLET.2015.10.020.

(192) Tian, Y.; Li, S.; Song, J.; Ji, T.; Zhu, M.; Anderson, G. J.; Wei, J.; Nie, G. A Doxorubicin Delivery Platform Using Engineered Natural Membrane Vesicle Exosomes for Targeted Tumor Therapy. *Biomaterials* **2014**, *35* (7), 2383–2390. https://doi.org/10.1016/J.BIOMATERIALS.2013.11.083.

(193) Kim, M. S.; Haney, M. J.; Zhao, Y.; Yuan, D.; Deygen, I.; Klyachko, N. L.; Kabanov, A. v.; Batrakova, E. v. Engineering Macrophage-Derived Exosomes for Targeted Paclitaxel Delivery to Pulmonary Metastases: In Vitro and in Vivo Evaluations. *Nanomedicine* **2018**, *14* (1), 195–204. https://doi.org/10.1016/J.NANO.2017.09.011.

(194) Théry, C.; Amigorena, S.; Raposo, G.; Clayton, A. Isolation and Characterization of Exosomes from Cell Culture Supernatants and Biological Fluids. *Curr Protoc Cell Biol* **2006**, *Chapter 3* (1). https://doi.org/10.1002/0471143030.CB0322S30.

(195) Pugholm, L. H.; Bæk, R.; Søndergaard, E. K. L.; Revenfeld, A. L. S.; Jørgensen, M. M.; Varming, K. Phenotyping of Leukocytes and Leukocyte-Derived Extracellular Vesicles. *J Immunol Res* **2016**, *2016*. https://doi.org/10.1155/2016/6391264.

(196) Theodoraki, M. N.; Hong, C. S.; Donnenberg, V. S.; Donnenberg, A. D.; Whiteside, T. L. Evaluation of Exosome Proteins by On-Bead Flow Cytometry. *Cytometry A* **2021**, *99* (4), 372–381. https://doi.org/10.1002/CYTO.A.24193.

(197) Santos, C.; Turiel, S.; Sousa Gomes, P.; Costa, E.; Santos-Silva, A.; Quadros, P.; Duarte, J.; Battistuzzo, S.; Fernandes, M. H. Vascular Biosafety of Commercial Hydroxyapatite Particles: Discrepancy between Blood Compatibility Assays and Endothelial Cell Behavior. *J Nanobiotechnology* **2018**, *16* (1), 1–15. https://doi.org/10.1186/S12951-018-0357-Y/FIGURES/9.

(198) Jung, M. K.; Mun, J. Y. Sample Preparation and Imaging of Exosomes by Transmission Electron Microscopy. *J Vis Exp* **2018**, *2018* (131). https://doi.org/10.3791/56482.

(199) Bachurski, D.; Schuldner, M.; Nguyen, P. H.; Malz, A.; Reiners, K. S.; Grenzi, P. C.; Babatz, F.; Schauss, A. C.; Hansen, H. P.; Hallek, M.; Pogge von Strandmann, E. Extracellular Vesicle Measurements with Nanoparticle Tracking Analysis - An Accuracy and Repeatability Comparison between NanoSight NS300 and ZetaView. *J Extracell Vesicles* **2019**, *8* (1). https://doi.org/10.1080/20013078.2019.1596016.

(200) Bai Aswathanarayan, J.; Rai Vittal, R.; Muddegowda, U. Anticancer Activity of Metal Nanoparticles and Their Peptide Conjugates against Human Colon Adenorectal Carcinoma Cells. *Artif Cells Nanomed Biotechnol* **2018**, *46* (7), 1444–1451. https://doi.org/10.1080/21691401.2017.1373655.

(201) Hanley, C.; Layne, J.; Punnoose, A.; Reddy, K. M.; Coombs, I.; Coombs, A.; Feris, K.; Wingett, D. Preferential Killing of Cancer Cells and Activated Human T Cells Using ZnO Nanoparticles. *Nanotechnology* **2008**, *19* (29), 295103. https://doi.org/10.1088/0957-4484/19/29/295103.

(202) Kang, T.; Guan, R.; Chen, X.; Song, Y.; Jiang, H.; Zhao, J. In Vitro Toxicity of Different-Sized ZnO Nanoparticles in Caco-2 Cells. *Nanoscale Res Lett* **2013**, *8* (1), 1–8. https://doi.org/10.1186/1556-276X-8-496/TABLES/1.

(203) Rasmussen, J. W.; Martinez, E.; Louka, P.; Wingett, D. G. Zinc Oxide Nanoparticles for Selective Destruction of Tumor Cells and Potential for Drug Delivery Applications. *Expert Opin Drug Deliv* **2010**, *7* (9), 1063–1077. https://doi.org/10.1517/17425247.2010.502560.

(204) Canta, M.; Cauda, V. The Investigation of the Parameters Affecting the ZnO Nanoparticle Cytotoxicity Behaviour: A Tutorial Review. *Biomater Sci* **2020**, *8* (22), 6157–6174. https://doi.org/10.1039/D0BM01086C.

(205) Syama, S.; Sreekanth, P. J.; Varma, H. K.; Mohanan, P. v. Zinc Oxide Nanoparticles Induced Oxidative Stress in Mouse Bone Marrow Mesenchymal Stem Cells. *Toxicol Mech Methods* **2014**, *24* (9), 644–653. https://doi.org/10.3109/15376516.2014.956914.

(206) Conway, J. H.; Sloane, N. J. A. Sphere Packings, Lattices and Groups. **1999**, *290*. https://doi.org/10.1007/978-1-4757-6568-7.

(207) Dumontel, B.; Canta, M.; Engelke, H.; Chiodoni, A.; Racca, L.; Ancona, A.; Limongi, T.; Canavese, G.; Cauda, V. Enhanced Biostability and Cellular Uptake of Zinc Oxide Nanocrystals Shielded with a Phospholipid Bilayer. *J Mater Chem B* **2017**, *5* (44), 8799–8813. https://doi.org/10.1039/C7TB02229H.

(208) Horna, P.; Nowakowski, G.; Endell, J.; Boxhammer, R. Comparative Assessment of Surface CD19 and CD20 Expression on B-Cell Lymphomas from Clinical Biopsies: Implications for Targeted Therapies. *Blood* **2019**, *134* (Supplement_1), 5345–5345. https://doi.org/10.1182/BLOOD-2019-129600.

(209) Roscher, M.; Hormann, I.; Leib, O.; Marx, S.; Moreno, J.; Miltner, E.; Friesen, C. Targeted Alpha-Therapy Using [Bi-213]Anti-CD20 as Novel Treatment Option for Radio- and Chemoresistant Non-Hodgkin Lymphoma

Cells. *Oncotarget* **2013**, *4* (2), 218–230. https://doi.org/10.18632/ONCOTARGET.817.

(210) Payandeh, Z.; Bahrami, A. A.; Hoseinpoor, R.; Mortazavi, Y.; Rajabibazl, M.; Rahimpour, A.; Taromchi, A. H.; Khalil, S. The Applications of Anti-CD20 Antibodies to Treat Various B Cells Disorders. *Biomed Pharmacother* **2019**, *109*, 2415–2426. https://doi.org/10.1016/J.BIOPHA.2018.11.121.

(211) Kosmas, C.; Stamatopoulos, K.; Stavroyianni, N.; Tsavaris, N.; Papadaki, T. Anti-CD20-Based Therapy of B Cell Lymphoma: State of the Art. *Leukemia* **2002**, *16* (10), 2004–2015. https://doi.org/10.1038/SJ.LEU.2402639.

(212) Pierpont, T. M.; Limper, C. B.; Richards, K. L. Past, Present, and Future of Rituximab-The World's First Oncology Monoclonal Antibody Therapy. *Front Oncol* **2018**, *8* (JUN). https://doi.org/10.3389/FONC.2018.00163.

(213) Bezombes, C.; Grazide, S.; Garret, C.; Fabre, C.; Quillet-Mary, A.; Müller, S.; Jaffrézou, J. P.; Laurent, G. Rituximab Antiproliferative Effect in B-Lymphoma Cells Is Associated with Acid-Sphingomyelinase Activation in Raft Microdomains. *Blood* **2004**, *104* (4), 1166–1173. https://doi.org/10.1182/BLOOD-2004-01-0277.

(214) Seyfizadeh, N.; Seyfizadeh, N.; Hasenkamp, J.; Huerta-Yepez, S. A Molecular Perspective on Rituximab: A Monoclonal Antibody for B Cell Non Hodgkin Lymphoma and Other Affections. *Crit Rev Oncol Hematol* **2016**, *97*, 275–290. https://doi.org/10.1016/J.CRITREVONC.2015.09.001.

(215) Ancona, A.; Dumontel, B.; Garino, N.; Demarco, B.; Chatzitheodoridou, D.; Fazzini, W.; Engelke, H.; Cauda, V. Lipid-Coated Zinc Oxide Nanoparticles as Innovative ROS-Generators for Photodynamic Therapy in Cancer Cells. *Nanomaterials 2018, Vol. 8, Page 143* **2018**, *8* (3), 143. https://doi.org/10.3390/NANO8030143.

(216) Wu, K.; Su, D.; Liu, J.; Saha, R.; Wang, J. P. Magnetic Nanoparticles in Nanomedicine: A Review of Recent Advances. *Nanotechnology* **2019**, *30* (50). https://doi.org/10.1088/1361-6528/AB4241.

(217) Kafrouni, L.; Savadogo, O. Recent Progress on Magnetic Nanoparticles for Magnetic Hyperthermia. *Prog Biomater* **2016**, *5* (3–4), 147–160. https://doi.org/10.1007/S40204-016-0054-6/FIGURES/6.

(218) Barui, S.; Cauda, V. Multimodal Decorations of Mesoporous Silica Nanoparticles for Improved Cancer Therapy. *Pharmaceutics 2020, Vol. 12, Page 527* **2020**, *12* (6), 527. https://doi.org/10.3390/PHARMACEUTICS12060527.

(219) Carofiglio, M.; Laurenti, M.; Genchi, G. G.; Ciofani, G.; Grochowicz, M.; Cauda, V. Ultrasound Triggered ZnO-Based Devices for Tunable and Multifaceted Biomedical Applications. *Adv Mater Interfaces* **2021**, *8* (21), 2101021. https://doi.org/10.1002/ADMI.202101021.

(220) Song, Y.; Kim, Y.; Ha, S.; Sheller-Miller, S.; Yoo, J.; Choi, C.; Park, C. H. The Emerging Role of Exosomes as Novel Therapeutics: Biology, Technologies, Clinical Applications, and the Next. *American Journal of Reproductive Immunology* **2021**, *85* (2), e13329. https://doi.org/10.1111/AJI.13329.

(221) Antimisiaris, S. G.; Mourtas, S.; Marazioti, A. Exosomes and Exosome-Inspired Vesicles for Targeted Drug Delivery. *Pharmaceutics 2018, Vol. 10, Page 218* **2018**, *10* (4), 218. https://doi.org/10.3390/PHARMACEUTICS10040218.

(222) Yang, B.; Chen, Y.; Shi, J. Exosome Biochemistry and Advanced Nanotechnology for Next-Generation Theranostic Platforms. *Advanced Materials* **2019**, *31* (2), 1802896. https://doi.org/10.1002/ADMA.201802896.

(223) Choi, H.; Choi, Y.; Yim, H. Y.; Mirzaaghasi, A.; Yoo, J. K.; Choi, C. Biodistribution of Exosomes and Engineering Strategies for Targeted Delivery of Therapeutic Exosomes. *Tissue Eng Regen Med* **2021**, *18* (4), 499. https://doi.org/10.1007/S13770-021-00361-0.

(224) Mehryab, F.; Rabbani, S.; Shahhosseini, S.; Shekari, F.; Fatahi, Y.; Baharvand, H.; Haeri, A. Exosomes as a Next-Generation Drug Delivery System: An Update on Drug Loading Approaches, Characterization, and

Clinical Application Challenges. *Acta Biomater* **2020**, *113*, 42–62. https://doi.org/10.1016/J.ACTBIO.2020.06.036.

(225) Rommasi, F.; Esfandiari, N. Liposomal Nanomedicine: Applications for Drug Delivery in Cancer Therapy. *Nanoscale Res Lett* **2021**, *16* (1), 95. https://doi.org/10.1186/S11671-021-03553-8.

(226) Bulbake, U.; Doppalapudi, S.; Kommineni, N.; Khan, W. Liposomal Formulations in Clinical Use: An Updated Review. *Pharmaceutics* **2017**, *9* (2). https://doi.org/10.3390/PHARMACEUTICS9020012.

(227) Lukyanov, A. N.; Hartner, W. C.; Torchilin, V. P. Increased Accumulation of PEG–PE Micelles in the Area of Experimental Myocardial Infarction in Rabbits. *Journal of Controlled Release* **2004**, *94* (1), 187–193. https://doi.org/10.1016/J.JCONREL.2003.10.008.

(228) Fu, S.; Zhao, Y.; Sun, J.; Yang, T.; Zhi, D.; Zhang, E.; Zhong, F.; Zhen, Y.; Zhang, S.; Zhang, S. Integrin Avβ3-Targeted Liposomal Drug Delivery System for Enhanced Lung Cancer Therapy. *Colloids Surf B Biointerfaces* **2021**, *201*, 111623. https://doi.org/10.1016/J.COLSURFB.2021.111623.

(229) Low, P. S.; Henne, W. A.; Doorneweerd, D. D. Discovery and Development of Folic-Acid-Based Receptor Targeting for Imaging and Therapy of Cancer and Inflammatory Diseases. *Acc Chem Res* **2008**, *41* (1), 120–129. https://doi.org/10.1021/AR7000815/ASSET/IMAGES/LARGE/AR-2007-000815_0007.JPEG.

(230) Narayanaswamy, R.; Torchilin, V. P. Targeted Delivery of Combination Therapeutics Using Monoclonal Antibody 2C5-Modified Immunoliposomes for Cancer Therapy. *Pharm Res* **2021**, *38* (3), 429–450. https://doi.org/10.1007/S11095-021-02986-1/FIGURES/8.

(231) Hou, X.; Zaks, T.; Langer, R.; Dong, Y. Lipid Nanoparticles for MRNA Delivery. *Nature Reviews Materials 2021 6:12* **2021**, *6* (12), 1078–1094. https://doi.org/10.1038/s41578-021-00358-0.

(232) Anderson, E. J.; Rouphael, N. G.; Widge, A. T.; Jackson, L. A.; Roberts, P. C.; Makhene, M.; Chappell, J. D.; Denison, M. R.; Stevens, L. J.; Pruijssers, A. J.; McDermott, A. B.; Flach, B.; Lin, B. C.; Doria-Rose, N.

A.; O'Dell, S.; Schmidt, S. D.; Corbett, K. S.; Swanson, P. A.; Padilla, M.; Neuzil, K. M.; Bennett, H.; Leav, B.; Makowski, M.; Albert, J.; Cross, K.; Edara, V. V.; Floyd, K.; Suthar, M. S.; Martinez, D. R.; Baric, R.; Buchanan, W.; Luke, C. J.; Phadke, V. K.; Rostad, C. A.; Ledgerwood, J. E.; Graham, B. S.; Beigel, J. H. Safety and Immunogenicity of SARS-CoV-2 MRNA-1273 Vaccine in Older Adults. *New England Journal of Medicine* **2020**, *383* (25), 2427–2438. https://doi.org/10.1056/NEJMOA2028436/SUPPL_FILE/NEJMOA2028436_DATA-SHARING.PDF.

(233) Lin, Y.; Zhou, Q.; Zeng, Y.; Tang, D. Liposome-Coated Mesoporous Silica Nanoparticles Loaded with L-Cysteine for Photoelectrochemical Immunoassay of Aflatoxin B1. *Microchimica Acta* **2018**, *185* (6), 1–9. https://doi.org/10.1007/S00604-018-2848-9/TABLES/2.

(234) Liu, M.; Gan, L.; Chen, L.; Zhu, D.; Xu, Z.; Hao, Z.; Chen, L. A Novel Liposome-Encapsulated Hemoglobin/Silica Nanoparticle as an Oxygen Carrier. *Int J Pharm* **2012**, *427* (2), 354–357. https://doi.org/10.1016/J.IJPHARM.2012.02.019.

(235) Epanchintseva, A. v.; Poletaeva, J. E.; Dovydenko, I. S.; Chelobanov, B. P.; Pyshnyi, D. v.; Ryabchikova, E. I.; Pyshnaya, I. A. A Lipid-Coated Nanoconstruct Composed of Gold Nanoparticles Noncovalently Coated with Small Interfering RNA: Preparation, Purification and Characterization. *Nanomaterials 2021, Vol. 11, Page 2775* **2021**, *11* (11), 2775. https://doi.org/10.3390/NANO11112775.

(236) Kang, J. H.; Ko, Y. T. Lipid-Coated Gold Nanocomposites for Enhanced Cancer Therapy. *Int J Nanomedicine* **2015**, *10* (Spec Iss), 33. https://doi.org/10.2147/IJN.S88307.

(237) Zeng, K.; Li, J.; Zhang, Z.; Yan, M.; Liao, Y.; Zhang, X.; Zhao, C. Lipid-Coated ZnO Nanoparticles as Lymphatic-Targeted Drug Carriers: Study on Cell-Specific Toxicity in Vitro and Lymphatic Targeting in Vivo. *J Mater Chem B* **2015**, *3* (26), 5249–5260. https://doi.org/10.1039/C5TB00486A.

(238) Ancona, A.; Dumontel, B.; Garino, N.; Demarco, B.; Chatzitheodoridou, D.; Fazzini, W.; Engelke, H.; Cauda, V. Lipid-Coated Zinc Oxide Nanoparticles as Innovative ROS-Generators for Photodynamic Therapy in Cancer Cells. *Nanomaterials 2018, Vol. 8, Page 143* **2018**, *8* (3), 143. https://doi.org/10.3390/NANO8030143.

(239) Barui, S.; Gerbaldo, R.; Garino, N.; Brescia, R.; Laviano, F.; Cauda, V. Facile Chemical Synthesis of Doped ZnO Nanocrystals Exploiting Oleic Acid. *Nanomaterials 2020, Vol. 10, Page 1150* **2020**, *10* (6), 1150. https://doi.org/10.3390/NANO10061150.

(240) Cauda, V.; Engelke, H.; Sauer, A.; Arcizet, D.; Bräuchle, C.; Rädler, J.; Bein, T. Colchicine-Loaded Lipid Bilayer-Coated 50 Nm Mesoporous Nanoparticles Efficiently Induce Microtubule Depolymerization upon Cell Uptake. *Nano Lett* **2010**, *10* (7), 2484–2492. https://doi.org/10.1021/NL100991W/SUPPL_FILE/NL100991W_SI_002.ZIP.

(241) Kinder, M.; Bahlis, N. J.; Malavasi, F.; de Goeij, B.; Babich, A.; Sendecki, J.; Rusbuldt, J.; Bellew, K.; Kane, C.; van de Donk, N. W. C. J. Comparison of CD38 Antibodies in Vitro and Ex Vivo Mechanisms of Action in Multiple Myeloma. *Haematologica* **2021**, *106* (7), 2004. https://doi.org/10.3324/HAEMATOL.2020.268656.

(242) Krejcik, J.; Casneuf, T.; Nijhof, I. S.; Verbist, B.; Bald, J.; Plesner, T.; Syed, K.; Liu, K.; van de Donk, N. W. C. J.; Weiss, B. M.; Ahmadi, T.; Lokhorst, H. M.; Mutis, T.; Sasser, A. K. Daratumumab Depletes CD38+ Immune Regulatory Cells, Promotes T-Cell Expansion, and Skews T-Cell Repertoire in Multiple Myeloma. *Blood* **2016**, *128* (3), 384–394. https://doi.org/10.1182/BLOOD-2015-12-687749.

(243) *Cell line - CD38 - The Human Protein Atlas*. https://www.proteinatlas.org/ENSG00000004468-CD38/cell+line (accessed 2022-09-26).

(244) *Gene Set - DAUDI*. https://maayanlab.cloud/Harmonizome/gene_set/DAUDI/CCLE+Cell+Line+Gene+Expression+Profiles (accessed 2022-09-26).

(245) Ghasemiyeh, P.; Mohammadi-Samani, S. Solid Lipid Nanoparticles and Nanostructured Lipid Carriers as Novel Drug Delivery Systems: Applications, Advantages and Disadvantages. *Res Pharm Sci* **2018**, *13* (4), 288. https://doi.org/10.4103/1735-5362.235156.

(246) Rosenthal, I.; Sostaric, J. Z.; Riesz, P. Sonodynamic Therapy—a Review of the Synergistic Effects of Drugs and Ultrasound. *Ultrason Sonochem* **2004**, *11* (6), 349–363. https://doi.org/10.1016/J.ULTSONCH.2004.03.004.

(247) Alassaf, A.; Aleid, A.; Frenkel, V. In Vitro Methods for Evaluating Therapeutic Ultrasound Exposures: Present-Day Models and Future Innovations. *J Ther Ultrasound* **2013**, *1* (1), 1–8. https://doi.org/10.1186/2050-5736-1-21/TABLES/1.

(248) Snehota, M.; Vachutka, J.; ter Haar, G.; Dolezal, L.; Kolarova, H. Therapeutic Ultrasound Experiments in Vitro: Review of Factors Influencing Outcomes and Reproducibility. *Ultrasonics* **2020**, *107*, 106167. https://doi.org/10.1016/J.ULTRAS.2020.106167.

(249) McHale, A. P.; Callan, J. F.; Nomikou, N.; Fowley, C.; Callan, B. Sonodynamic Therapy: Concept, Mechanism and Application to Cancer Treatment. *Adv Exp Med Biol* **2016**, *880*, 429–450. https://doi.org/10.1007/978-3-319-22536-4_22.

(250) Vodyashkin, A. A.; Rizk, M. G. H.; Kezimana, P.; Kirichuk, A. A.; Stanishevskiy, Y. M. Application of Gold Nanoparticle-Based Materials in Cancer Therapy and Diagnostics. *ChemEngineering 2021, Vol. 5, Page 69* **2021**, *5* (4), 69. https://doi.org/10.3390/CHEMENGINEERING5040069.

(251) van Heerde, W. L.; de Groot, P. G.; Reutelingsperger, C. P. M. The Complexity of the Phospholipid Binding Protein Annexin V. *Thromb Haemost* **1995**, *73* (2), 172–179. https://doi.org/10.1055/s-0038-1653747.

(252) Schmid, I.; Krall, W. J.; Uittenbogaart, C. H.; Braun, J.; Giorgi, J. v. Dead Cell Discrimination with 7-Amino-Actinomycin D in Combination with Dual Color Immunofluorescence in Single Laser Flow Cytometry. *Cytometry* **1992**, *13* (2), 204–208. https://doi.org/10.1002/CYTO.990130216.

(253) Qian, W. J.; Peters, J. L.; Dahlgren, G. M.; Gee, K. R.; Kennedy, R. T. Simultaneous Monitoring of Zn2+ Secretion and Intracellular Ca2+ from Islets and Islet Cells by Fluorescence Microscopy. *Biotechniques* **2004**, *37* (6), 922–933. https://doi.org/10.2144/04376BI01/ASSET/IMAGES/LARGE/FIGURE5.JPEG.

(254) Qian, W. J.; Gee, K. R.; Kennedy, R. T. Imaging of Zn2+ Release from Pancreatic β-Cells at the Level of Single Exocytotic Events. *Anal Chem* **2003**, *75* (14), 3468–3475. https://doi.org/10.1021/AC0341057/ASSET/IMAGES/LARGE/AC0341057F00007.JPEG.

(255) Bevensee, M. O.; Schwiening, C. J.; Boron, W. F. Use of BCECF and Propidium Iodide to Assess Membrane Integrity of Acutely Isolated CA1 Neurons from Rat Hippocampus. *J Neurosci Methods* **1995**, *58* (1–2), 61–75. https://doi.org/10.1016/0165-0270(94)00159-E.

(256) Macklis, J. D.; Madison, R. D. Progressive Incorporation of Propidium Iodide in Cultured Mouse Neurons Correlates with Declining Electrophysiological Status: A Fluorescence Scale of Membrane Integrity. *J Neurosci Methods* **1990**, *31* (1), 43–46. https://doi.org/10.1016/0165-0270(90)90007-3.

(257) Riccardi, C.; Nicoletti, I. Analysis of Apoptosis by Propidium Iodide Staining and Flow Cytometry. *Nature Protocols 2006 1:3* **2006**, *1* (3), 1458–1461. https://doi.org/10.1038/nprot.2006.238.

(258) Crowley, L. C.; Scott, A. P.; Marfell, B. J.; Boughaba, J. A.; Chojnowski, G.; Waterhouse, N. J. Measuring Cell Death by Propidium Iodide Uptake and Flow Cytometry. *Cold Spring Harb Protoc* **2016**, *2016* (7), pdb.prot087163. https://doi.org/10.1101/PDB.PROT087163.

(259) Carofiglio, M.; Laurenti, M.; Genchi, G. G.; Ciofani, G.; Grochowicz, M.; Cauda, V. Ultrasound Triggered ZnO-Based Devices for Tunable and Multifaceted Biomedical Applications. *Adv Mater Interfaces* **2021**, *8* (21), 2101021. https://doi.org/10.1002/admi.202101021.

(260) Fu, P. P.; Xia, Q.; Hwang, H.-M.; Ray, P. C.; Yu, H. Mechanisms of Nanotoxicity: Generation of Reactive Oxygen Species. *J Food Drug Anal* **2014**, *22* (1), 64–75. https://doi.org/10.1016/j.jfda.2014.01.005.

(261) Dąbrowski, J. M. Reactive Oxygen Species in Photodynamic Therapy: Mechanisms of Their Generation and Potentiation; 2017; pp 343–394. https://doi.org/10.1016/bs.adioch.2017.03.002.

Appendix

List of publications

T. Limongi, M. Canta, L. Racca, A. Ancona, V. Vighetto, S. Tritta, V. Cauda. "**Improving dispersal of therapeutic nanoparticles in the human body**", NANOMEDICINE, 2019, doi: 10.2217/nnm-2019-0070.

V. Vighetto, A. Ancona, L. Racca, T. Limongi, A. Troia, G. Canavese, V. Cauda. "**The synergistic effect of nanocrystals combined with ultrasound in the generation of reactive oxygen species for biomedical applications**", Frontiers Bioeng. Biotechnol, 2019, doi: 10.3389/fbioe.2019.00374.

F. Susa, T. Limongi, B. Dumontel, V. Vighetto, V. Cauda. "**Engineered extracellular vesicles as a reliable tool in cancer nanomedicine**". CANCERS, 2019, doi:10.3390/cancers11121979.

L. Racca, T. Limongi, V. Vighetto, B. Dumontel, A. Ancona, M, Canta, G. Canavese, N. Garino, V. Cauda. "**Zinc Oxide Nanocrystals and High-Energy Shock Waves: A New Synergy for the Treatment of Cancer Cells**". Front. Bioeng. Biotechnol.,2020, doi: 10.3389/fbioe.2020.00577.

M. Battaglini, A. Marino, A. Carmignani, C. Tapeinos, V. Cauda, A. Ancona, N. Garino, V. Vighetto, G. La Rosa, E. Sinibaldi, G. Ciofani. "**Polydopamine Nanoparticles as an Organic and Biodegradable Multitasking Tool for Neuroprotection and Remote Neuronal Stimulatio**" ACS Applied Materials & Interfaces, 2020, doi: 10.1021/acsami.0c05497.

J. C. Matos, M. Laurenti, V. Vighetto, L.C.J. Pereira, J.C. Waerenborgh, M.C. Gonçalves, V. Cauda. "**Biomimetic amorphous titania nanoparticles as ultrasound responding agents to improve cavitation and ROS production for sonodynamic therapy**". Applied Sciences, 2020, doi: 10.3390/app10238479.

A. Pandey, V. Vighetto, N. Di Marzio, F. Ferraro, M. Hirsch, N. Ferrante, S. Mitra, A. Grattoni, C. S. Filgueira. "**Gold Nanoparticles Radio-Sensitize and**

Reduce Cell Survival in Lewis Lung Carcinoma". Nanomaterials, 2020, doi: 10.3390/nano10091717.

V. Vighetto, L. Racca, M. Canta, J. C. Matos, B. Dumontel, M. C. Gonçalves, V. Cauda. "**Smart Shockwave Responsive Titania-Based Nanoparticles for Cancer Treatment**". Pharmaceutics, 2021, doi: 10.3390/pharmaceutics13091423.

M. Carofiglio, M. Laurenti, V. Vighetto, L. Racca, S. Barui, N. Garino, R. Gerbaldo, F. Laviano V. Cauda. "**Iron-Doped ZnO Nanoparticles as Multifunctional Nanoplatforms for Theranostics**". Nanomaterials, 2021, doi: 10.3390/nano11102628.

V. Vighetto, A.Troia, M. Laurenti, M. Carofiglio, N. Marcucci, G. Canavese, V Cauda "**Insight into Sonoluminescence Augmented by ZnO-Functionalized Nanoparticles**". ACS Omega, 2022, doi: 10.1021/acsomega.1c05837.

A. Carmignani, M. Battaglini, E. Sinibaldi, A. Marino, V. Vighetto, V. Cauda, G. Ciofani. "**In Vitro and Ex Vivo Investigation of the Effects of Polydopamine Nanoparticle Size on Their Antioxidant and Photothermal Properties: Implications for Biomedical Applications**". ACS Appl. Nano Mater., 2022, doi: 10.1021/acsanm.1c04536.

B. Dumontel, F. Susa, T. Limongi, V. Vighetto, D. Debellis, M. Canta, V. Cauda. "**Nanotechnological engineering of extracellular vesicles for the development of actively targeted hybrid nanodevices**". CELL & BIOSCIENCE, 2022, doi: 10.1186/s13578-022-00784-9.

G. Tamboia, M. Campanini, V. Vighetto, L. Racca, L. Spigarelli, G. Canavese, V. Cauda. "**A comparative analysis of low intensity ultrasound effects on living cells: from simulation to experiments**". Biomed Microdevices, 2022, Doi: 10.1007/s10544-022-00635-x.

V. Cauda, S. Appendino, V. Vighetto, M. Carofiglio. "**Stimuli-responsive hybrid nanoconstructs for efficient theranostic applications in nanomedicine**". Project Repository Journal, 15, pp.44-47, 2022, doi: 10.54050/PRj1519538.

N.M. Percivalle, M. Carofiglio, M. Conte, G. Rosso, A. Bentivogli, G. Mesiano, V. Vighetto and V. Cauda. "**Artificial and Naturally Derived Phospholipidic Bilayers as Smart Coatings of Solid-state Nanoparticles: Current Works and Perspectives in Cancer Therapy**". Int. J. Mol. Sci. 2022, 23(24), 15815; doi: 10.3390/ijms232415815

Patents

"**A sonoluminescence contrast imaging method and apparatus assisted by nanoparticles in the biomedical field, in particular in the oncological field**" (Original title: "Metodo ed apparato per immagine di contrasto in sonoluminescenza assistita da nanoparticelle in ambito medico diagnostico, in particolare oncologico"). Italian Patent Application N. IT102021000005123 of 8th March 2021, Inventors: V. Cauda, V. Vighetto, M. Carofiglio, A. Ancona. **Granted.** PCT**: IB2022/051802** of 1st March 2022

Attended conferences and schools

OXCD3 - Oxford Centre for Drug Delivery Devices, Institute of Biomedical Engineering, Oxford, United Kingdom – 2019

Poster presentation: "*Controlled Generation of Reactive Oxigen Species under Ultrasound Exposure of Zinc Oxide Nanocrystals*". V. Vighetto, A. Ancona, L. Racca, T. Limongi, A. Troia, G. Canavese, V. Cauda.

School of Nanomedicine – University of Trieste, Trieste, Italy – 2019

Poster presentation: "*Controlled Generation of Reactive Oxigen Species under Ultrasound Exposure of Zinc Oxide Nanocrystals*". V. Vighetto, A. Ancona, L. Racca, T. Limongi, A. Troia, G. Canavese, V. Cauda.

CancerTO – UniTO and PoliTO conference series in cancer, Nanoscience in Cancer Immunotherapy, Turin-on live event, Italy – 2021

Oral presentation: "*Zinc Oxide Nanocrystals combined with Ultrasound for the Controlled Generationof Reactive Oxygen Species*". V. Vighetto, A. Ancona, L. Racca, T. Limongi, A. Troia, G. Canavese, V. Cauda.

NanoMedicine International Conference and Exhibition 2021 – Milano, Italy – 2021

Poster session: "*Protein-stabilized amorphous Titania Nanoparticles for Sonodynamic Therapy*". V. Vighetto, L. Racca, M. Canta, J. C. Matos, M. C. Gonçalves, V. Cauda.

American Advanced Materials Congress – International Association of Advanced Materials, Miami, USA – 2022

Poster session: "*Sonoluminescence Enhanced by Nanosized Zinc Oxide Contrast Agents*". V. Vighetto, A. Troia, M. Laurenti, M. Carofiglio, N. Marcucci, G. Canavese, V. Cauda. Best Poster Presentation award.